

**UNDERGROUND DESIGN AND DEFORMATION
BASED ON SURFACE GEOMETRY**

By

DOUGLAS MATTHEW MILNE

B.A.Sc., The University of British Columbia, 1977

M.Sc., The University of London, 1988

DIC, Imperial College, 1988

**A THESIS SUBMITTED IN PARTIAL FULFILLMENT OF
THE REQUIREMENTS FOR THE DEGREE OF
DOCTOR OF PHILOSOPHY**

in

**THE FACULTY OF GRADUATE STUDIES
DEPARTMENT OF MINING AND MINERAL PROCESS ENGINEERING**

THE UNIVERSITY OF BRITISH COLUMBIA

May 1997

© Douglas Matthew Milne, 1997



National Library
of Canada

Bibliothèque nationale
du Canada

Acquisitions and
Bibliographic Services

Acquisitions et
services bibliographiques

395 Wellington Street
Ottawa ON K1A 0N4
Canada

395, rue Wellington
Ottawa ON K1A 0N4
Canada

Your file Votre référence

Our file Notre référence

The author has granted a non-exclusive licence allowing the National Library of Canada to reproduce, loan, distribute or sell copies of this thesis in microform, paper or electronic formats.

L'auteur a accordé une licence non exclusive permettant à la Bibliothèque nationale du Canada de reproduire, prêter, distribuer ou vendre des copies de cette thèse sous la forme de microfiche/film, de reproduction sur papier ou sur format électronique.

The author retains ownership of the copyright in this thesis. Neither the thesis nor substantial extracts from it may be printed or otherwise reproduced without the author's permission.

L'auteur conserve la propriété du droit d'auteur qui protège cette thèse. Ni la thèse ni des extraits substantiels de celle-ci ne doivent être imprimés ou autrement reproduits sans son autorisation.

0-612-25117-9

Canada

ABSTRACT

This thesis presents a method for improving underground excavation design by relating geometry and deformation to the stability of hanging wall surfaces of open stopes. Instability on a stope hanging wall occurs when the opening geometry increases past a stable limit. There are no realistic methods of predicting surface deformation or projecting future deformation with continued mining. Computer models do exist which calculate deformation, however, no methods exist for obtaining realistic input parameters for the rock mass.

Both stability and deformation, for a given mining situation, are dependent on the geometry of the surface opening. Two terms have been introduced in this thesis, radius factor and effective radius factor, which are based on surface geometry. Radius factor, (RF), is related to the overall stability and maximum deformation of a surface. Effective radius factor, (ERF), is related to the local stability and deformation of a point on the stope surface. By introducing a term related to both stability and deformation, maximum allowable stable deformations can be designed for. Support practices can be tailored to provide the optimum support for the expected deformation.

Deformation has been linked to geometry with instrumented case histories from several mines. Several mechanisms driving deformation have been recognized including elastic relaxation, non-elastic fracture dilation and voussoir arch deflection. With monitoring, rates of deformation accompanying mining have been determined which allow the prediction of future movement with continued mining.

The modified stability graph design technique, which is an existing empirical design technique modified from the Mathews design method, has formed the basis for stability assessment. With this method hydraulic radius is used to assess surface geometry. The data

base behind the design method has been re-analysed using the RF term which more accurately reflects surface stability. Case histories of stope backs, where the modified stability graph design was unsuccessful in estimating stability, have been reassessed using RF values resulting in more accurate stability assessments.

This thesis successfully links hanging wall geometry with measured deformation and the onset of instability. Instrumented field movement data can be used to design support to match the predicted surface movements, as well as indicate the approach of failure. More complex geometries can now be assessed with commonly used empirical design tools.

TABLE OF CONTENTS

ABSTRACT	ii
TABLE OF CONTENTS	iv
LIST OF TABLES	x
LIST OF FIGURES	xi
LIST OF PHOTOS	xviii
ACKNOWLEDGEMENTS	xix
CHAPTER 1: INTRODUCTION	1
1.1 BACKGROUND	1
1.2 OBJECTIVES	3
1.3 OVERVIEW	4
CHAPTER 2: STABILITY DESIGN	7
2.1 INTRODUCTION	7
2.2 EMPIRICAL DESIGN METHODS	8
2.2.1 Terzaghi's Classification System	10
2.2.2 Rock Quality Designation (RQD)	11
2.2.3 NGI Classification	11
2.2.4 Rock Mass Rating Classification (RMR)	15
2.2.5 Laubscher Design Method	17
2.2.6 Mathews Design Method	18
2.2.7 Dilution Design	18
2.2.8 Modified Stability Graph Method	22
2.2.9 Bench Stability Method	22

2.3	ANALYTICAL DESIGN METHODS	24
2.3.1	Mohr-Coulomb Criterion	25
2.3.2	Hoek and Brown Criterion	27
2.3.3	Kinematic Failure	27
2.3.4	Beam Failure	28
2.3.5	Plate Theory	30
2.3.6	Voussoir Arch Failure	31
2.3.7	Key Block Theory	33
2.3.8	μ DEC and 3DEC Design	33
2.4	SUMMARY	34
CHAPTER 3: ROCK MASS DEFORMATION		36
3.1	INTRODUCTION	36
3.2	APPROACHES TO DEFORMATION ESTIMATION	38
3.2.1	Displacement Around a Cylinder (Kirsch Equation)	40
3.2.2	Displacement Around a Spherical Opening	41
3.2.3	Numerically Modelled Displacement	41
3.2.4	Beam Displacement	43
3.2.5	Plate Displacement	43
3.2.6	Voussoir Arch Displacement	44
3.2.7	Empirical Displacement Estimation	46
3.3	DEFORMATION MEASUREMENT	46
3.3.1	Closure Measurements	49
3.3.2	Extensometers	51
3.4	INTERPRETATION OF DEFORMATION	52

3.5	SUMMARY	54
CHAPTER 4: OPENING SPAN AND HYDRAULIC RADIUS		56
4.1	INTRODUCTION	56
4.2	GEOMETRICAL PROPERTIES OF HYDRAULIC RADIUS	57
4.3	DRAWBACKS TO THE HYDRAULIC RADIUS PARAMETER	59
4.4	SUMMARY	62
CHAPTER 5: RADIUS FACTOR AND EFFECTIVE RADIUS FACTOR		63
5.1	INTRODUCTION	63
5.2	GEOMETRICAL PROPERTIES OF THE EFFECTIVE RADIUS FACTOR TERM	67
5.2.1	Significance of the Effective Radius Factor for One Way Spanning	69
5.2.2	Significance of the Effective Radius Factor for Two Way Spanning	69
5.4	SUMMARY	74
CHAPTER 6: ELASTIC DEFORMATION AND EFFECTIVE RADIUS FACTOR VALUE		77
6.1	INTRODUCTION	77
6.2	INFLUENCE OF GEOMETRY ON MODELLED DEFORMATIONS AND ERF VALUES	83
6.3	VARIATION OF MODELLED DEFORMATIONS AND ERF VALUES WITH SURFACE GEOMETRY	87
6.3.1	Deformation at a Constant Distance From Surface	89
6.3.2	Elastic Deformation and Distance From the Surface	92
6.3.3	Deformation Versus ERF Values over Varied Opening Geometries	96
6.4	SUMMARY	101
CHAPTER 7: STRESS AND STRAIN NEAR OPENING SURFACES		103
7.1	INTRODUCTION	103

7.2	STRAIN AND DISPLACEMENT AROUND A SPHERE	103
7.3	ELASTIC STRAIN AND DISPLACEMENT ABOVE A PLANAR SURFACE	105
7.4	RELAXATION ZONE AND STRAIN ABOVE A PLANAR SURFACE	115
7.5	SUMMARY	118
CHAPTER 8: FIELD DATA ON HANGING WALL DEFORMATION		120
8.1	INTRODUCTION	120
8.2	APPROACH TO FIELD DATA ANALYSIS	122
8.3	MOUNT ISA MINE	123
8.3.1	Mount Isa Stope 5FP1	127
8.3.2	Mount Isa Stope 5HP1	128
8.3.3	M665 Stoping Triplet	132
8.3.4	80G3 Bench Stope Instrumentation	137
8.3.5	Summary	145
8.4	BRUNSWICK MINE	146
8.5	SUMMARY	151
CHAPTER 9: INFLUENCE OF BACKFILL ON HANGING WALL DEFORMATION		158
9.1	INTRODUCTION	158
9.2	HANGING WALL DEFORMATION IN A CONTINUOUS BACKFILLING CYCLE	162
9.3	WINSTON LAKE MINE CASE HISTORIES	165
9.3.1	Phase 1, Winston Lake Hanging Wall Deformation Stope 565 #4	166
9.3.2	Phase 3, Winston Lake Hanging Wall Deformation Stope 530 #8	173

9.4	SUMMARY	178
CHAPTER 10: RADIUS FACTOR AND SURFACE STABILITY ANALYSIS		181
10.1	INTRODUCTION	181
10.2	MODIFIED STABILITY GRAPH DATABASE	182
10.3	CASE HISTORIES	186
10.3.1	565 #8 Ground Fall	187
10.3.2	565 #6 Ground Fall	188
10.3.3	565 #3 Ground Fall	190
10.4	SUMMARY	191
CHAPTER 11: SURFACE FAILURE GEOMETRY AND EFFECTIVE RADIUS FACTOR VALUES		193
11.1	INTRODUCTION	193
11.2	THEORETICAL FAILURE GEOMETRY	193
11.2.1	Influence of Block Geometry on Ravelling Failures	194
11.2.2	Influence of Field Stresses on Ravelling Failures	195
11.2.3	Influence of Arching Action on Ravelling Failures	196
11.3	BRUNSWICK MINE HANGING WALL INSTABILITY	196
11.3.1	Stability Analysis	197
11.3.2	Failure Radius of Curvature	198
11.3.3	Hanging Wall Depth of Relaxation	202
11.3.4	Summary	202
11.4	DETOUR LAKE MINE DILUTION SURVEY	204
11.5	SUMMARY	206
CHAPTER 12: CONCLUSIONS		208

12.1	INTRODUCTION	208
12.2	CONCLUSIONS	208
12.2.1	Stability Design and Surface Geometry	209
12.2.2	Modelled Deformation and Surface Geometry	209
12.2.3	Field Deformation and Surface Geometry	210
12.2.4	Depth of Modelled Tensile Stress and Potential Failure	211
12.2.5	Influence of Backfill on Effective Opening Geometry	212
12.2.6	Summary	213
12.3	FUTURE WORK	213
12.4	FINAL REMARKS	214
	BIBLIOGRAPHY	215
	APPENDIX A - CONVERGE.EXE PROGRAM	221
	APPENDIX B - MATHEMATICAL DERIVATION OF THE RADIUS FACTOR TERM	225
	APPENDIX C - AUTOCAD PROGRAM FOR DETERMINING ERF VALUES	236

LIST OF TABLES

Table		Page
2.1	NGI Classification system (From Stacey & Page, 1986) (After Barton et al., 1974)	13
2.2	Excavation Support Ratio (From Hoek and Brown, 1980) (After Barton et al., 1976)	15
2.3	RMR Classification Charts (From Hoek and Brown, 1980)	16
11.1	Stope 16N - HW Slough for Major Blasts	201

LIST OF FIGURES

Figure	Page
1.1 General guidelines for relating movement and stability	2
1.2 Proposed application of research into deformation and design	5
2.1 Common design methods and the general input required	9
2.2 Proposed relation between RQD and rock support (After Merritt, 1972) (From Hoek and Brown, 1980)	12
2.3 Q classification related to span and support (After Barton et al., 1974) (From Hoek and Brown, 1980)	14
2.4 Graph relating stand-up time, unsupported span and rock classification (After Bieniawski, 1993, 1989) (From Hutchinson and Diederichs, 1996)	17
2.5 Laubscher design graph (After Laubscher, 1990)	19
2.6 Mathews design graph (After Mathews et al, 1981, from Nickson, 1992)	20
2.7 Input parameters used for determining N for the Mathews analysis (After Mathews et al., 1981)(From Nickson, 1992)	20
2.8 Dilution design method (From Pakalnis, 1993)	21
2.9 Input parameters used for determining N for the modified stability graph design method (After Potvin, 1988, from Nickson, 1992)	23
2.10 Modified stability graph design method (From Nickson, 1992)	23
2.11 Bench stability design chart (From Villaescusa, 1996)	24
2.12 Mohr Coulomb failure criterion (After Goodman, 1989)	26
2.13 Beam loading conditions under self weight	29
2.14 Geometry and forces acting on a voussoir beam (Evans, 1941)	32
3.1 Idealized stages of deformation in the vicinity of an underground excavation (From Internal NTC short course)	37
3.2 Kirsch solution for determining radial deformations around a circular tunnel	40

3.3	Voussoir arch deflection showing the relationship between beam thickness and deflection at the buckling point (From Hutchinson and Diederichs, 1995)	44
3.4	Design beam deflection versus beam thickness (From Hutchinson and Diederichs, 1995)	45
3.5	General voussoir arch solution showing maximum stable span versus stable lamination thickness. 10% of lamination thickness equals maximum beam deflection (From Hutchinson and Diederichs, 1995)	47
3.6	Deformation versus rock quality Q and span (From Barton, 1989)	48
3.7	Typical closure station measurement layout for mining drifts	49
3.8	Drift closure measurements along a cross drift give data similar to a hanging wall extensometer	50
3.9	General layout of a borehole extensometer	51
4.1	Influence of surface aspect ratio on hydraulic ratio	58
4.2	Hydraulic radius expressed as a distance to supporting abutments	58
4.3	Hydraulic radii calculated for various surface geometries based on area divided by perimeter and equation 4.3	60
4.4	An irregular stope back showing two estimates of hydraulic radius	61
5.1	Variation in hydraulic radius and radius factor for a constant 100 metre span and an increasing length	66
5.2	An irregular stope back showing the calculated radius factor value and an effective radius factor value (After Milne et al., 1996)	66
5.3	Rays used for calculating the harmonic radius and effective radius factor	68
5.4	Influence of pillars and raises on the determination of the radius factor of a surface (From Milne et al., 1996)	68
5.5	ERF values across a tunnel represented as a height of potential arching	70
5.6	Effective radius factor values contoured for a circular surface	72
5.7	Graph showing the surface of an elliptical paraboloid versus the ERF surface	72
5.8	Effective radius factor values contoured for a rectangular surface	73

5.9	Graphs showing the effective radius factor values across the minimum and maximum spans versus a curve for a parabola set to the maximum and minimum ERF values	73
5.10	Summary of the proposed applications of the RF and ERF parameters	75
6.1	ERF values on a 2, 3 and 4 sided surface represented as a downward deflection	78
6.2	Surface deformation due to stress normal to the surface	80
6.3	Surface deformation due to stresses parallel to the surface	80
6.4	Zones of relaxation, or stress shedding, above a sphere and a circular disc	82
6.5	The calculation of the deformation of a point above an open surface varies with the sum of the distances to the centre of equally sized elements	85
6.6	Plot of ERF values versus the sum of distances to each equidimensional element with a sketch showing where the relationship varies by $\pm 25\%$	86
6.7	General procedure for comparing modelled elastic displacements above a surface to corresponding ERF values on the surface	88
6.8	Deformations modelled 6.25m above a 50m cube in a uniaxial vertical stress field, plotted against the ERF value	90
6.9	Deformation modelled 6.25m above a 50m cube plotted against the ERF value	91
6.10	Deformation modelled 6.25m above a tabular opening 50m by 50m by 5m, plotted against ERF values	93
6.11	Deformation modelled 10m above an irregular tabular opening, plotted against the ERF value	94
6.12	Deformations modelled at various heights above a 50m by 50m plate in a hydrostatic stress field, plotted against the ERF value	95
6.13	Deformation modelled above a 50m by 50m plated in a hydrostatic stress field, plotted against the ERF value, projected to surface	97
6.14	Projected surface deformation on a 25m by 25m plate and a 50m by 50m plate, plotted against the ERF values	99
6.15	Projected surface deformations above 3 different sized openings, plotted against the ERF value	100

7.1	Deformation and strain calculations around a sphere in a hydrostatic stress field	106
7.2	Percent of maximum strain obtained between points 2 and 4 metres from the boundary of a sphere	107
7.3	General procedure used to relate the strain normal to an excavation surface and the corresponding ERF value	108
7.4	Zone of constant strain above a tabular opening in a hydrostatic stress field	109
7.5	Zone of constant strain above a cubic opening in a hydrostatic stress field	110
7.6	Zone of constant strain above an irregular opening in a hydrostatic stress field	111
7.7	Zone of constant strain above a 50m by 50m by 5m opening with stresses 30 MPa normal and 60 MPa parallel to the opening surface	112
7.8	Zone of constant strain above a 50m by 50m by 5m opening with stresses 60 MPa normal and 30 MPa parallel to the opening surface	113
7.9	Zone of constant strain above an irregular opening with stresses 60 MPa normal and 30MPa stress parallel to the opening surface	115
7.10	Excavation geometries modelled to determine the extent of the tensile zone (From Clark, 1996)	117
7.11	Maximum depth of relaxation for varied surface RF values and stress ratios (After Clark, 1996)	117
8.1	Typical field data showing deformation response to mining (From Bawden and Milne, 1987)	121
8.2	Hanging wall extensometer immediately before and after mining past the instrument - (stope "mine by")	122
8.3	General analysis approach for relating opening geometry, instrument location and resulting deformation with mining	124
8.4	Typical cross section showing parallel ore zones at the Mount Isa lead mine, (Isa Today, 1990)	126
8.5	Typical hanging wall extensometer configuration	127

8.6	Deformation versus time and ERF values for mining the 5FP1 stope	129
8.7	Deformation versus ERF values for mining in the 5HP1 stope	131
8.8	Hanging wall instrumentation for the M665 stoping block (After MIM Internal Report, 1979)	133
8.9	Extensometer deformation above the M665 open stope, plotted against the ERF value	135
8.10	Mt. Isa Mine - Stope 80G3 longitudinal view showing extensometer locations and blasting steps	138
8.11	Mt Isa Mine, stope 80G3 - Cross sections showing extensometer locations (After MIM Internal Memo)	140
8.12	80G3 Stope - Microstrain between anchors .5m to 6.5m from the hanging wall, plotted against the ERF value	142
8.13	80G3 Stope - Microstrain between anchors 6.5m to 30m from the hanging wall, plotted against the ERF value	143
8.14	Vertical longitudinal projection of the Brunswick Mine main ore zone (MOZ), (Internal Brunswick Mine Report)	147
8.15	Brunswick Mine Isometric, longitudinal and 6 sub plan view of instrumentation locations and blast steps	149
8.16	Cross section view of extensometer no. 2	148
8.17	Brunswick Mine 16N stope looking west showing longitudinal views of three stages of mining and the corresponding ERF values for the hanging wall extensometer (From Milne et al., 1996)	150
8.18	Collar to anchor deformation and microstrain between anchors, plotted against the ERF value (From Milne et al., 1996)	152
8.19	Graph showing the theoretical stages of hanging wall deformation versus ERF values	154
8.20	Proposed development of deformation stages	157
9.1	Plan view of expected hanging wall deformation with backfill only after stope completion	160
9.2	Plan view of expected form of hanging wall deformation with a continuously advancing backfill abutment	160

9.3	Plan view of a hanging wall deformation arch after a backfilling step (Ignoring backfill compression)	162
9.4	Plan view of projected deformation for a backfilling cycle with a 30 metre open span, backfilled to 10 metres then opened to 30 metres	162
9.5	Views of the Modified Avoca mining method used at Winston Lake Mine (From Winston Lake Mine - Inmet Mining Corp.)	164
9.6	True longitudinal view of the 565 #6 stope showing extensometer toe locations and approximate cable bolt locations	167
9.7	Cross section showing 60° dipping hanging wall and 37° sloping fill	167
9.8	Plan and cross section views of the instrumentation installed in the 565 #6 stope (From Maloney and Kaiser, 1993)	168
9.9	Mining as of November 25 th , 1989 showing longitudinal view of 3 methods of interpreting the effect of backfilling on the ERF value	169
9.10	ERF values versus microstrain between the bottom anchors of extensometer W565 #6. ERF values are based on three methods of assessing the effect of backfill	170
9.11	ERF values versus microstrain between anchors of extensometer I565 #6 ERF values are based on 3 methods of assessing the effect of backfill	171
9.12	ERF values versus microstrain between the bottom anchors of extensometer I565 #5. ERF values are based on 3 methods of assessing the effect of backfill	172
9.13	Plan and cross section views of the instrumentation installed in the 530 #8 stope (From Maloney and Kaiser, 1993)	174
9.14	Longitudinal view of stope 530 #8 showing 3 methods of interpreting the effect of backfill on effective radius factor	176
9.15	ERF values versus microstrain between Ext. 530 #3 anchors. ERF values are based on 3 methods of assessing backfill effect	177
10.1	Graph of the ratio between HR and RF values plotted against an increasing surface length to width ratio	183
10.2	Unsupported case histories plotted on the modified stability graph using hydraulic radius and radius factor (After Milne et al., 1996)	184

10.3	Supported case histories plotted on the modified stability graph using hydraulic radius and radius factor (After Milne et al., 1996)	185
10.4	Plan and sectional view showing the 565 #8 ground fall (From Internal Noranda Technology Centre report)	188
10.5	Modified stability graph plot of case histories, based on both the surface radius factor and hydraulic radius	189
10.6	Plan and cross section views of the 565 #6 ground fall (From NTC Internal Report)	189
10.7	Plan and cross section showing the 565 #3 ground fall (From NTC Internal Report)	191
11.1	Examples of a block failure and a ravelling failure	194
11.2	General failure geometry generated by a ravelling surface failure	195
11.3	Stability plot of the 16N stope hanging wall after major blasts	198
11.4	Plan and cross section views of hanging wall sloughing with mining	199
11.5	Relationship between maximum surface slough or overbreak and failure radius of curvature	200
11.6	Hanging wall radius of curvature versus surface radius factor for the Brunswick Mine 16N stope	201
11.7	Maximum extent of hanging wall failure compared to maximum expected extent of hanging wall relaxation	203
11.8	Longitudinal view of the west sub-level retreat stope at Detour Lake mine. The area where the ERF values are greater than 12m and significant dilution can be expected is highlighted (After Milne et al., 1996)	205
11.9	Metres of slough versus ERF values for the unsupported hanging wall between sub-levels and for supported sub-levels	206
B.1	A rectangular surface broken into sections for integration	227
B.2	Harmonic radius calculation for a circle for points not at the centre	230

LIST OF PHOTOS

Photo	Page
3.1 Typical multi-point extensometer collar	51

ACKNOWLEDGEMENTS

There are many people I should thank for technical, financial and moral support who have helped make this work possible. First I would like to thank the mines who have provided me with data and assistance for this study which include: Mount Isa Mines, Winston Lake Mine, Brunswick Mine and Detour Lake Mine, as well as the Noranda Technology Centre.

Dr. Yves Potvin deserves special thanks for his support and belief in the value of this research. Many individuals have helped me with the technical aspects of this research and some of them that deserve special mention are, Don Hausch, Per Lunder and my brother Chris. I am also indebted to the assistance and guidance of my research advisor, Dr. Rimas Pakalnis, as well as the members of my thesis committee who had many helpful suggestions to keep me on track. I should also thank the many proof readers who helped me complete this work.

Several organizations deserve thanks for their much appreciated financial support and they include:

- The Noranda Technology Centre
- Canadian Mineral Industry Education Foundation
- Energy Mines and Resources
- Natural Sciences and Engineering Research Council of Canada
- The Cy and Emerald Keyes Scholarship fund, the George Winkler Memorial Scholarship fund and the G. Vernon Hobson Bequest.

Finally I must thank my wife and children for their support. Without their assistance I wouldn't have enjoyed my studies nearly as much, though I might have finished a couple of years sooner.

CHAPTER 1

INTRODUCTION

1.1 BACKGROUND

The deformation and stability of open stope hanging wall surfaces have been correlated and form the basis of this thesis. In mining, a stope is a volume of ore delineated for excavation. Prior to the instability of a stope hanging wall, a finite amount of deformation occurs. Quantifying this critical value of deformation would greatly assist in the prediction of instability, as well as in the design of effective support. A relationship between surface stability and deformation will allow an engineer to assign a degree of stability to an opening surface that is based on the magnitude of surface deformation. This will be a significant improvement over the current subjective designation of stable, unstable or caved surface condition. Field equipment now exists for accurately quantifying the magnitude of failure or slough with quick and accurate survey data (Cavity Monitoring Survey system) (Miller et al., 1992). These data will also assist in more accurately defining degrees of instability.

The measurement of rock mass deformation with extensometers is commonly used in mines to assist in identifying impending failures and to improve design. There are no guidelines, however, to project the effect of continued mining on future movement. Only the most basic trends are recognized which suggest accelerating movement is an indication of approaching instability. An example of how field deformation data is most often interpreted is given in Figure 1.1.

Computer modelling techniques exist which will generate predicted rock mass deformation, however, there are many difficulties which combine to often make these modelling

INTERPRETATION OF MONITORING RESULTS

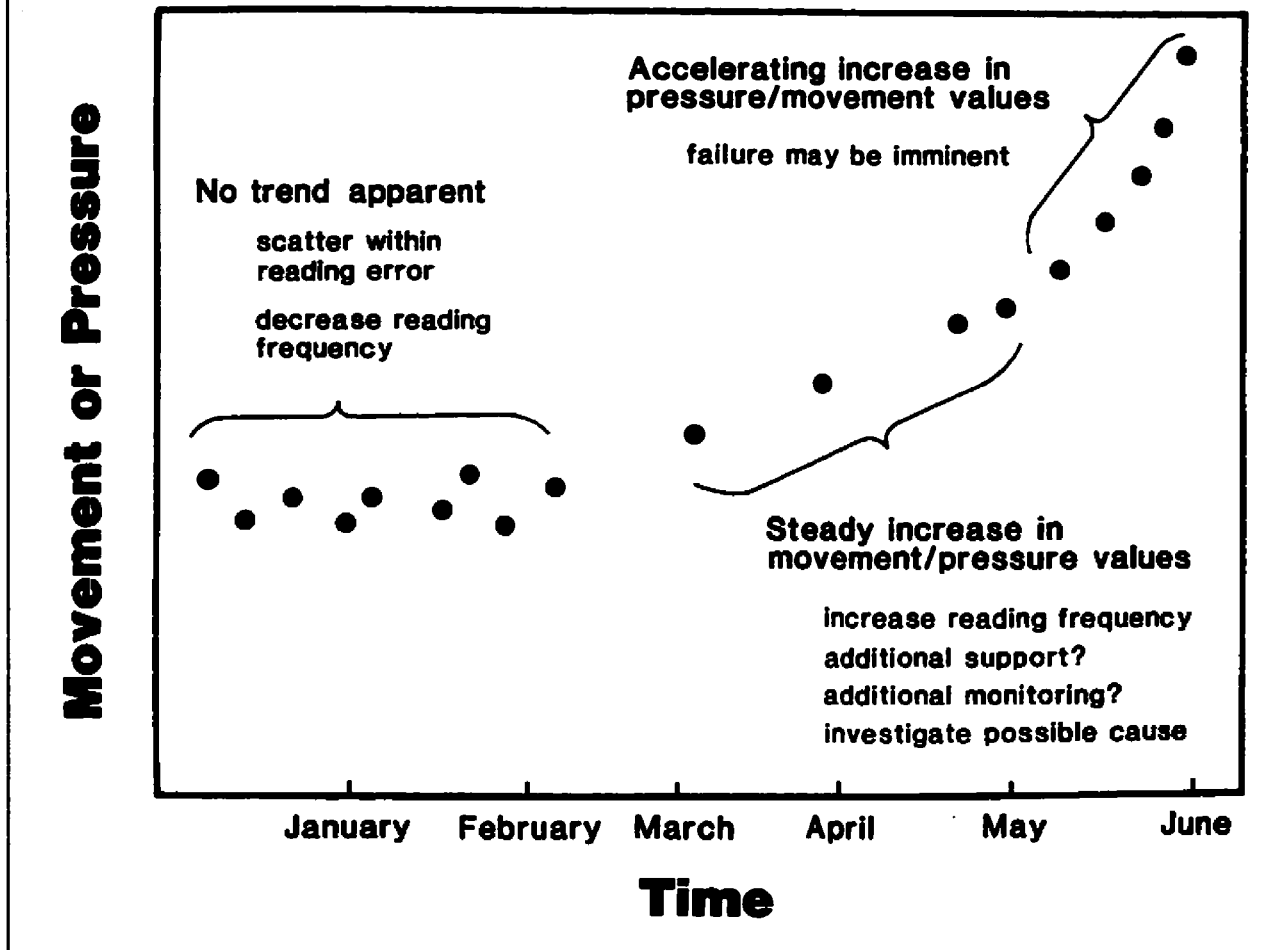


Figure 1.1 General guidelines for relating movement and stability.

approaches unsatisfactory. Assumptions must be made on the mode of deformation, as well as if and when the transition from elastic to plastic or discontinuum deformation occurs. Rock mass material properties, which cannot be readily measured in the field, must be estimated.

For stability, empirical design techniques exist which link rock mass strength and stress with surface geometry as defined by hydraulic radius, (Laubscher (1976), Mathews et al. (1981), Pakalnis (1986), Potvin (1988) and Nickson (1992)). These design techniques have widespread use in the design of underground openings and generally result in accurate assessments of

stability (Potvin and Milne, 1992). The evaluation of surface geometry with the hydraulic radius term, however, is simplistic and is not suitable for complex mining geometries. The hydraulic radius term was originally used to relate the fluid flow in square or rectangular conduits to the flow in pipes with a circular cross section. The term adequately assesses square and rectangular surface geometries, however, more complex surfaces found in mining are not adequately quantified using the hydraulic radius term. Case histories with complex surface geometries have been re-analysed where failure occurred after stability was predicted based on hydraulic radius. The new term more accurately reflected the unstable conditions.

1.2 OBJECTIVES

The main goal of this thesis is to develop an improved method of quantifying surface geometry for assessing surface stability and deformation. Current empirical stability design techniques assess surface geometry based on the surface hydraulic radius, which is defined as surface area divided by perimeter. A theoretical basis for the effectiveness of the hydraulic radius term is investigated. Based on this investigation, an improved parameter called the radius factor is introduced, which is based on the distance from the centre of a surface to the supporting abutments. The new parameter has been introduced to allow empirical design methods using the hydraulic radius term to more realistically assess irregular geometries, as well as pillars and raises intersecting the surface. The data base for a widely used empirical design method has been re-analysed based on the radius factor term and additional case histories have been analysed to determine the effectiveness of the radius factor term.

The approach for assessing surface deformation is similar to that taken for stability design. A second parameter called the effective radius factor has been introduced. This

parameter can be calculated for any point on a opening surface and is also directly related to the distance to supporting abutments. The effective radius factor values on a surface have been related to corresponding modelled elastic deformation. Deformation field data from three mines have been related to this new term. Resulting trends in deformation data allow an estimation of the critical movement prior to failure, as well as relative deformation of points on the opening surface. This allows for improved support layout and the prediction of support loads for design.

1.3 OVERVIEW

The first several chapters in this thesis consist of a review of existing methods used for the estimation of surface stability and deformation. Two new parameters, radius factor (RF) and effective radius factor (ERF), are introduced in Chapter 5 to quantify the effect of surface geometry on deformation and stability. The RF term replaces hydraulic radius as a measure of the influence of surface geometry on stability and the ERF term has been related to localized stability and deformation. These two new parameters are related to computed elastic deformation as well as field data collected at several mine sites (Chapters 7 to 9). The ability to assess field deformation and surface geometry with the same factor assists in predicting deformation from limited field data. This enables the engineer to provide the maximum possible support for the expected deformations.

A re-analysis of the Stability Graph design technique (Potvin, 1988), is done in Chapter 10 and a new chart is developed based on the radius factor replacing the hydraulic radius. Several analysed case histories showing the improved, safer evaluation of complex geometries using the RF term are given in Chapter 10.

Figure 1.2 is a schematic showing an overview of the proposed application of the

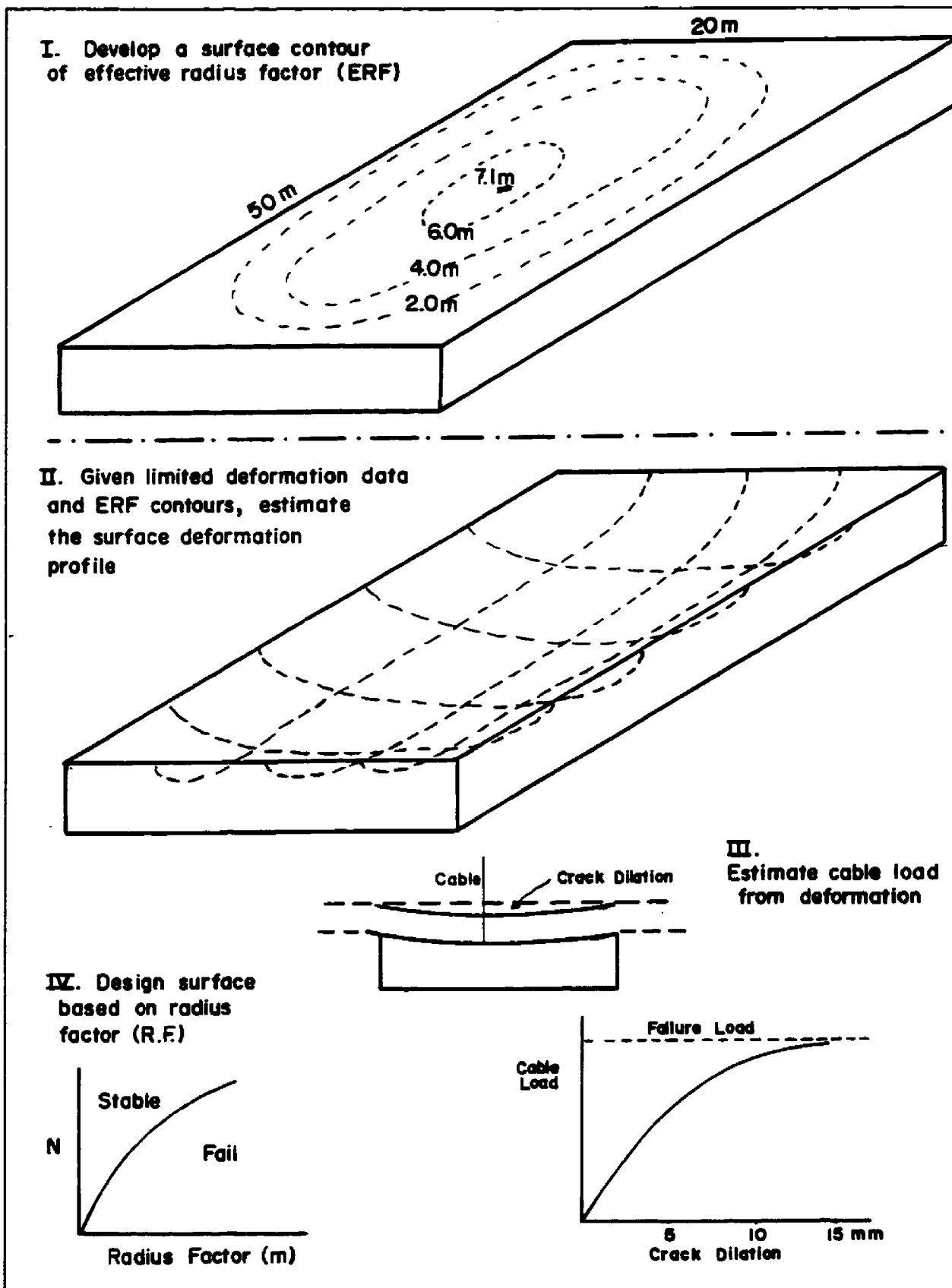


Figure 1.2 Proposed application of research into deformation and design.

research presented in this thesis, steps I through step IV. ERF values are generated for a given surface geometry and then linked to existing deformation measurements. A maximum stable surface geometry can be predicted using existing, modified design techniques, and a maximum stable deformation profile can be predicted. This predicted deformation profile can then be used to develop more effective support measures.

CHAPTER 2

STABILITY DESIGN

2.1 INTRODUCTION

Stability design methods for underground structures in rock can be broken into the two broad categories of empirical and analytical design. Both methods work on the basic engineering design approach of determining material strength and loads on the material, and then applying some failure criteria to determine stability. The primary difficulty with both categories of design is that most of the input parameters cannot be determined with a sufficient degree of accuracy.

In general, analytical design techniques are based on a theoretical failure criterion, often derived from the behaviour of intact rock. Field stresses are estimated and the influence of opening geometry on induced stresses is quantified with computer modelling techniques. A combination of lab testing and rock mass classification is often used to obtain an initial estimate of rock mass strength. Ideally, back analysis of stable and failed areas is conducted and analytical stability predictions are calibrated to actual conditions by the adjustment of rock mass strength parameters.

Empirical design techniques are based on a failure criterion derived from extensive experience. This failure criterion may consist of a design line or zone on a graph which divides stable and unstable geometries, with little or no theoretical basis. Field and induced stresses are estimated and strength parameters are commonly based on laboratory testing and rock mass classification. Back analyses of stable and failed areas are ideally conducted and the results of these back analyses may lead to modification of the failure criterion or design line used in the

empirical design technique. One drawback with empirical design is that both stable and failed case histories are required to define a failure zone. The approach of instability cannot be assessed and relies on visual observations of whether or not a surface is stable, starting to fail or caved. This study links failure with deformation so that, with experience, the engineer can follow the approach of instability based on field deformation measurements. Another drawback to empirical design is the overly simplified methods used to quantify opening geometry. This study addresses this shortcoming and introduces new factors for assessing geometry. Figure 2.1 shows some of the commonly used design methods used for mining and the general input required.

2.2 EMPIRICAL DESIGN METHODS

An underground rock mass is a natural, rather than engineered material with predetermined properties. An estimate of material properties for mining can only be obtained through testing. Jointing and discontinuities in a rock mass make strength determination highly scale dependent and the size of engineering structures in rock preclude the possibility of testing at a realistic scale. Rock mass classification forms one of the more common methods of estimating rock mass strength, as well as the basis for many empirical design techniques.

Initially, classification based empirical design techniques were developed for assessing tunnel stability for civil applications and tunnel span formed the design criteria. Stress was often not included in the design procedure since tunnels for civil application are generally at shallow depths. There are many of these combined classification and design systems and those most commonly employed will be discussed:

- Terzaghi's rock classification (Terzaghi, 1946)

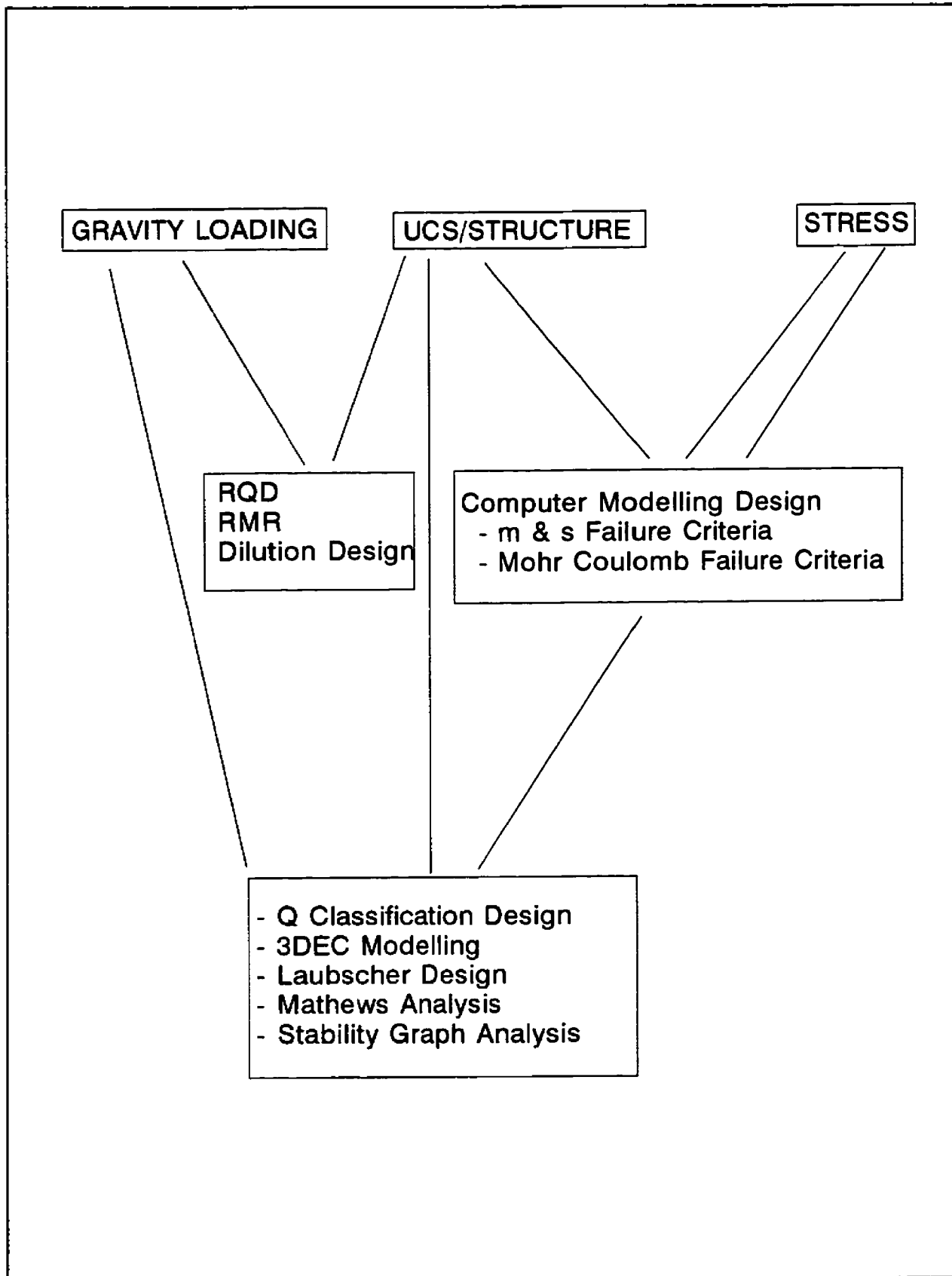


Figure 2.1 Common design methods and general input requirements.

- Rock Quality Designation (RQD) (Deere, 1964)
- NGI Classification (Barton, 1974)
- Rock Mass Rating (Bieniawski, 1974)

Much of the discussion on these classification systems is taken from Milne (1988).

Empirical mining design techniques developed from the RMR and NGI (Q) classification systems. Factors which incorporated the influence of induced stress were introduced and the span term was replaced by hydraulic radius. This term better accounts for the two way spanning often associated with mining openings. Hydraulic radius is simply the area of the exposed surface divided by the perimeter. This term still oversimplifies the opening surface geometry and chapters 4 and 5 discuss a replacement for this parameter. The most common empirical design techniques specific to mining follow:

- Mathews analysis (Mathews et al., 1981)
- Laubscher design (Laubscher, 1990)
- Dilution design (Pakalnis, 1986)
- Modified stability graph design (Potvin, 1988)
- Bench stability design (Villaescusa, 1996)

2.2.1 Terzaghi's Classification System

Terzaghi's classification system was the first system to stress the importance of discontinuities in a rock mass. It consists of several descriptions of the rock mass, primarily concerned with the nature and frequency of discontinuities (Terzaghi, 1946). Each of these descriptive categories is related to a corresponding load on the tunnel roof expressed as a function of the tunnel span and height. Stability decreases as the load on the tunnel roof increases.

The load on the tunnel roof is based on the assumption that a self supporting arch develops above a tunnel back. Below this arch the dead weight of the rock mass must be supported to prevent failure. The height of this arch increases with deteriorating ground conditions and with tunnel span.

This classification system is worth mentioning because of its historical significance. It has serious drawbacks, the primary one being that it is based entirely upon a subjective description of the rock mass. Later systems include some quantitative terms such as joint spacing and the unconfined compressive strength of the rock (Milne, 1988).

2.2.2 Rock Quality Designation (RQD)

A rock mass classification system to quantify the competence of drill core was developed by Deere (1964). This system enjoys widespread use as a parameter in many other later classification systems. The Rock Quality Designation (RQD) is defined as the total length of intact core, greater than 100mm in length, divided by the total length of core. If some core has been lost, the RQD is still based on the total length of core drilled.

Apart from acting as a factor in other classification systems, RQD has achieved widespread use as the basis for the selection of tunnel support. Figure 2.2 shows a relation suggested by Merritt (1972) for relating RQD, support requirements and tunnel span. It is worth noting that the only parameter which can relate to the load on the tunnel is the tunnel span.

2.2.3 NGI Classification

The Norwegian Geotechnical Institute (NGI) classification system expresses rock quality, Q , as a function of 6 independent variables developed by Barton, Lien and Lunde (1974). The factors considered in this classification are block size, discontinuity strength and stress effects.

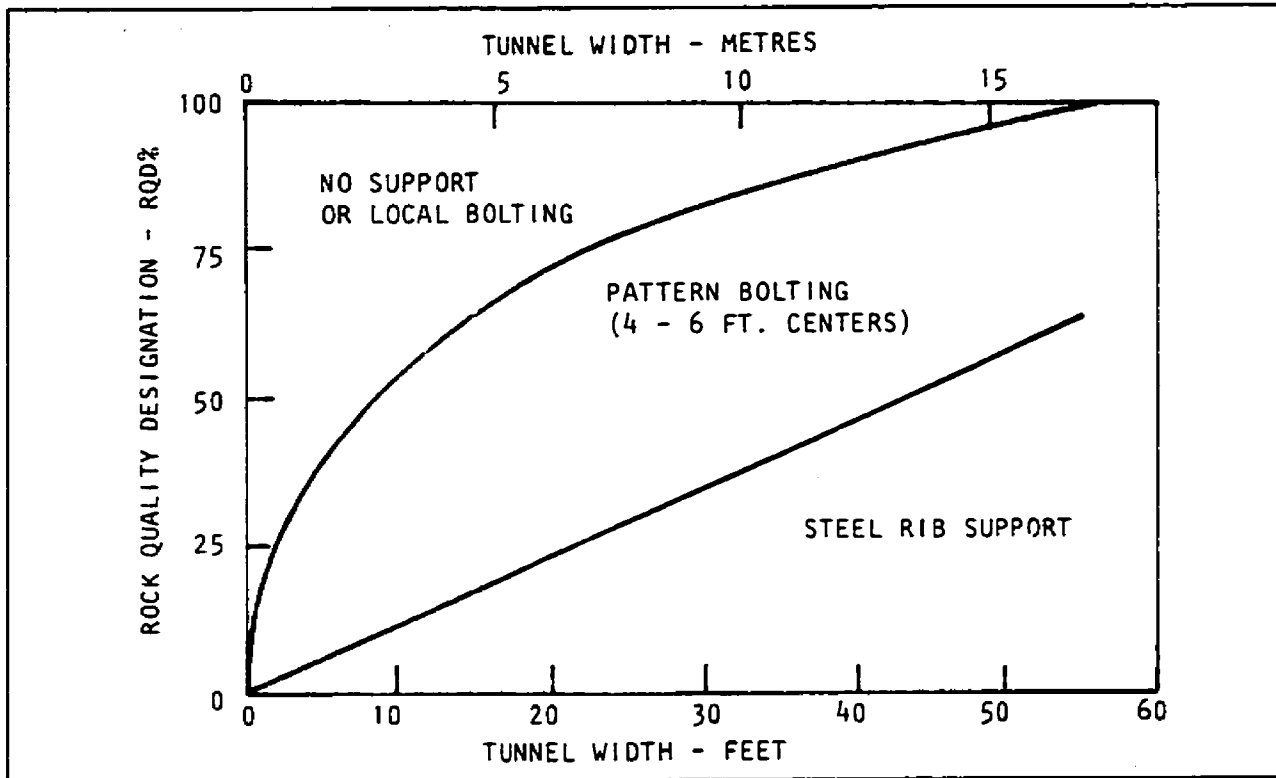


Figure 2.2 Proposed relation between RQD and rock support (After Merritt, 1972) (From Hoek and Brown, 1980)

Each of the three factors is expressed as a quotient of two of the primary controlling factors, as shown in Equation 2.1.

$$Q = \frac{RQD}{J_n} \times \frac{J_r}{J_a} \times \frac{J_w}{SRF} \quad (\text{Eq. 2.1})$$

- where:
- RQD = Rock Quality Designation
 - J_n = Joint set number
 - J_r = Joint set roughness
 - J_a = Joint set alteration number
 - J_w = Joint water reduction factor
 - SRF = Stress reduction factor

Table 2.1 summarizes the descriptions and corresponding values for determining the

Table 2.1 NGI Classification Charts

(From Stacey & Page, 1986 - After Barton et al., 1974)

Joint Set Number, J_n

<u>Description</u>	<u>J_n</u>
Massive, No or few joints	.5 - 1.0
One joint set	2.0
One joint set & random	3.0
Two joint sets	4.0
Two joint sets & random	6.0
Three joint sets	9.0
Three joint sets & random	12.0
Four or more joint sets	15.0
"Sugar Cubed"	
Crushed rock, Earth like	20.0

Joint Roughness Number J_r

<u>Description</u>	<u>J_r</u>
Discontinuous joints	4
Rough, undulating	3
Smooth, undulating	2
Slickensided, undulating	1.5
Rough, planar	1.5
Smooth, planar	1.0
Slickensided, planar	.5
Thick infill	1.0
no rock contact	

Joint Alteration Number, J_a

<u>Description</u>	<u>J_a</u>
Tightly healed	.75
Surface staining only	1.0
Low friction coating (Chlorite, talc, etc.)	4.0
Thin swelling clay	10.0
Thick swelling clay	20.0

Joint Water Reduction, J_w

<u>Description</u>	<u>J_w</u>
Dry to minor inflow	1.0
Medium inflow	.66
Large inflow	.5
Exceptionally high flow (reduces with time)	.15
Exceptionally high flow (no reduction with time)	.075

Stress Reduction Factor, SRF

<u>Description</u>	<u>SRF</u>
● Stress	
Low stress, near surface	2.5
Medium confining stress	1.0
Mild rock burst	5 - 10
Heavy rock burst	10 - 20
● Weakness zones	
Single clay free shear zone	2.5
Multiple shear zones with clay	10.0
● Squeezing rock	5 - 20
● Swelling rock	5 - 20

●NOTE: These tables are only a summary, see Hoek and Brown, 1980 for the complete descriptions.

factors given in equation 2.1. The Q value is used to estimate support requirements in civil engineering applications, as shown in Figure 2.3. Support requirements are related to a term called the Equivalent Dimension, D_e . D_e is equal to the maximum excavation span divided by the Excavation Support Ratio (ESR). The ESR term is inversely related to the required stand-up time for the structure and the degree of safety required for the opening. Table 2.2 gives typical ESR values for various underground openings. An ESR value is not provided for non-access open stopes for mining, but it may correspond to an ESR value as high as 20 (Page, 1988). It should be noted that tunnel span, shown in Figure 2.3, is the design output and is related to load on the tunnel roof.

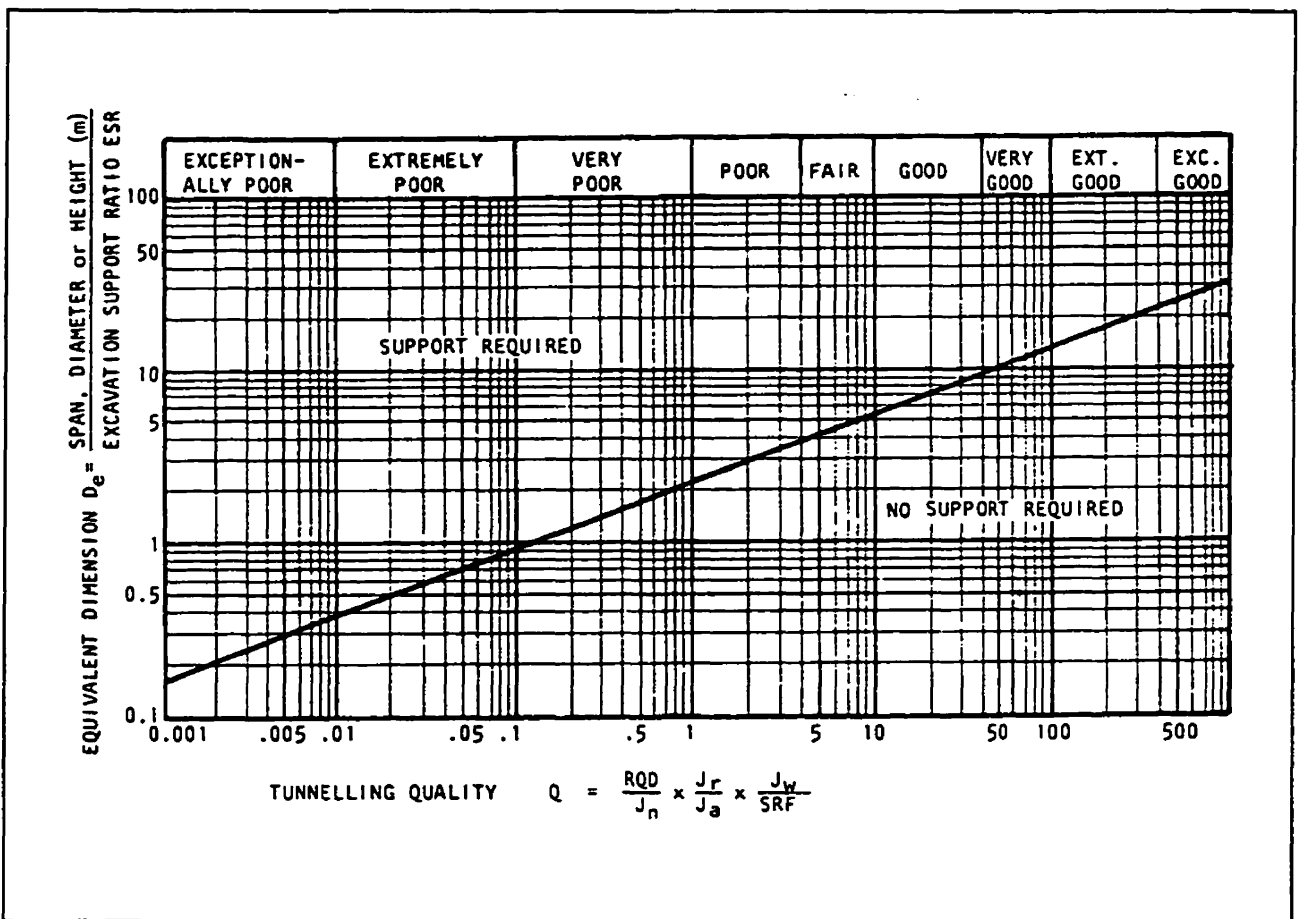


Figure 2.3 Q classification related to span and support (After Barton et al., 1974 - From Hoek and Brown, 1980).

Table 2.2
Excavation Support Ratio (ESR)

Excavation Category	ESR
A. Temporary mine openings	3-5
B. Permanent mine openings, water tunnels for hydro power (excluding high pressure penstocks) pilot tunnels, drifts and headings for large excavations.	1.6
C. Storage rooms, water treatment plants, minor road and railway tunnels, surge chambers, access tunnels.	1.3
D. Power stations, major road and railway tunnels, civil defence chambers, portals, intersections.	1.0
E. Underground nuclear power stations, railway stations, sports and public facilities, factories.	.8

(From Hoek and Brown, 1980) (After Barton et al., 1976)

2.2.4 Rock Mass Rating Classification (RMR)

The RMR classification system, devised by Bieniawski (1974), was developed for estimating support requirements for civil engineering tunnelling work. It is based on five parameters describing the properties of the rock mass. A sixth factor is added to appraise the influence of the interaction between the orientation of the engineering structure and the orientation of the discontinuity set that controls stability.

The RMR value is based on the sum of these six parameters given in Table 2.3. These parameters attempt to quantify the influence of intact rock strength, RQD, joint spacing and orientation, discontinuity strength and the presence of groundwater. The resulting sum has a value between 0 and 100 and has been related to unsupported span and stand-up time, shown in Figure 2.4. The RMR value has also been related to field elastic modulus of the overall rock

Table 2.3 RMR CLASSIFICATION CHARTS (From Hoek and Brown, 1980)

A. CLASSIFICATION PARAMETERS AND THEIR RATINGS

PARAMETER		RANGES OF VALUES					For this low range - uniaxial compressive test is preferred			
1	Strength of intact rock material	Point load strength index	> 8 MPa	4-8 MPa	2-4 MPa	1-2 MPa				
		Uniaxial compressive strength	> 200 MPa	100-200 MPa	50-100 MPa	25-50 MPa	10-25 MPa	3-10 MPa	1-3 MPa	
	Rating		15	12	7	4	2	1	0	
2	Drill core quality RQD		90%-100%	75%-90%	50%-75%	25%-50%	< 25%			
	Rating		20	17	13	8	3			
3	Spacing of joints		>3m	1-3m	0.3-1m	50-300mm	< 50mm			
	Rating		30	25	20	10	5			
4	Condition of joints		Very rough surfaces Not continuous No separation Hard joint wall rock	Slightly rough surfaces Separation < 1mm Hard joint wall rock	Slightly rough surfaces Separation < 1mm Soft joint wall rock	Slickensided surfaces Gauge < 5mm thick or Joints open 1-5mm Continuous joints	Soft gauge >5mm thick or Joints open >5mm Continuous joints			
	Rating		25	20	12	6	0			
5	Ground water	Inflow per 10m tunnel length	None		< 25 litres/min	25-125 litres/min	> 125 litres/min			
		Ratio of joint water pressure to major principal stress	OR		OR	OR	OR	OR		
		General conditions	OR		OR	OR	OR	OR		
	Rating		0		00-02	02-05	> 05			
		Completely dry		Moist only (interstitial water)	Water under moderate pressure	Severe water problems				
	Rating		10		7	4	0			

B. RATING ADJUSTMENT FOR JOINT ORIENTATIONS

Strike and dip orientations of joints		Very favourable	Favourable	Fair	Unfavourable	Very unfavourable
Ratings	Tunnels	0	-2	-5	-10	-12
	Foundations	0	-2	-7	-15	-25
	Slopes	0	-5	-25	-50	-60

C. ROCK MASS CLASSES DETERMINED FROM TOTAL RATINGS

Rating	100-81	80-61	60-41	40-21	< 20
Class No	I	II	III	IV	V
Description	Very good rock	Good rock	Fair rock	Poor rock	Very poor rock

D. MEANING OF ROCK MASS CLASSES

Class No	I	II	III	IV	V
Average stand-up time	10 years for 5m span	6 months for 4m span	1 week for 3m span	5 hours for 1.5m span	10 min. for 0.5m span
Cohesion of the rock mass	> 300 kPa	200-300 kPa	150-200 kPa	100-150 kPa	< 100 kPa
Friction angle of the rock mass	> 45°	40°-45°	35°-40°	30°-35°	< 30°

TABLE 6 - THE EFFECT OF JOINT STRIKE AND DIP ORIENTATIONS IN TUNNELLING

Strike perpendicular to tunnel axis				Strike parallel to tunnel axis		Dip 0°-20° irrespective of strike
Drive with dip		Drive against dip				
Dip 45°-90°	Dip 20°-45°	Dip 45°-90°	Dip 20°-45°	Dip 45°-90°	Dip 20°-45°	
Very favourable	Favourable	Fair	Unfavourable	Very unfavourable	Fair	Unfavourable

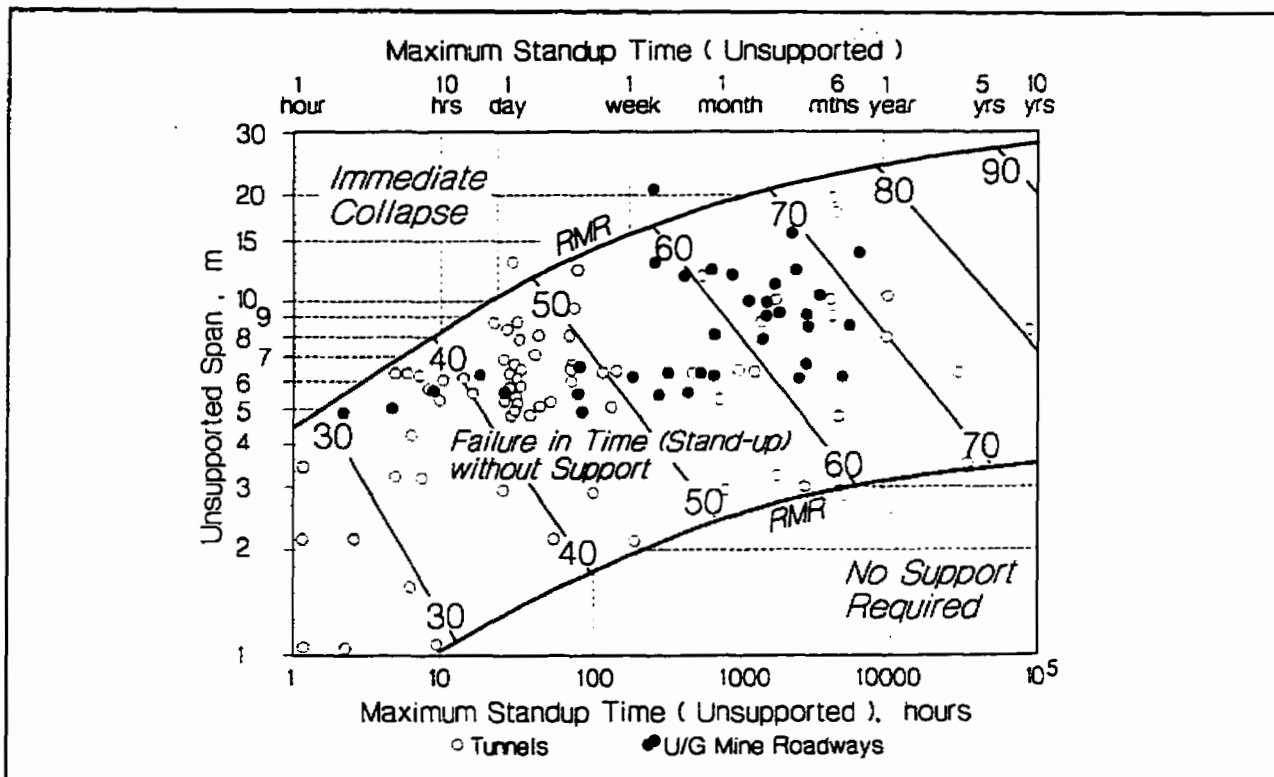


Figure 2.4 Graph relating stand-up time, unsupported span and rock classification. (After Bieniawski, 1993, 1989) (From Hutchinson and Diederichs, 1996).

mass (Bieniawski, 1978), as shown in the following equation:

$$E = 2RMR - 100 \quad (\text{Eq. 2.2})$$

The RMR and the Q systems are the two most commonly used rock mass classification methods and they have been related by the following equation (Bieniawski, 1976):

$$RMR = 9 \ln Q + 44 \quad (\text{Eq. 2.3})$$

2.2.5 Laubscher Design Method

Laubscher developed a Mining Rock Mass Classification system (MRMR), based loosely on Bieniawski's RMR system. An in situ MRMR classification is initially arrived at based on RQD, joint spacing, intact unconfined compressive strength and joint condition. Once the in situ MRMR value is determined, a series of influence factors are applied to account for weathering,

joint orientation, blasting effects and the presence of shear zones, (Laubscher, 1976). An adjusted, or weighted, rock mass rating is obtained after the application of these influence factors. This adjusted rock mass rating is then plotted against the opening surface hydraulic radius and the design surface is then determined to be stable, supportable or caving, as shown in Figure 2.5 (Laubscher, 1990). This design method has been developed and used primarily in caving mining situations and has had little application in open stoping environments.

2.2.6 Mathews Design Method

The Mathews design method was developed specifically for deep open stope surfaces (Mathews et al., 1981). This is a graphical approach which plots stability number (N) versus hydraulic radius, or shape factor, S. The graph is broken into zones labelled stable, potentially unstable and potentially caving (Fig. 2.6). The term N is based on the rock quality Q, induced stress and intact strength, joint orientation and the orientation of the surface being studied. Figure 2.7 shows graphically how the input parameters for estimating N are determined.

2.2.7 Dilution Design

The dilution design method, Pakalnis (1987), is based on the RMR classification system. It differs from other methods in that an estimate of sloughing or dilution is given rather than a stable or unstable assessment. Exposure rate is a factor used in this method to account for ground deterioration with time. Opening surface geometry is assessed by the hydraulic radius term; as the hydraulic radius increases, so does the estimated dilution. Stress effects are only accounted for indirectly as a function of the mining method. Figure 2.8 shows this graphical design method.

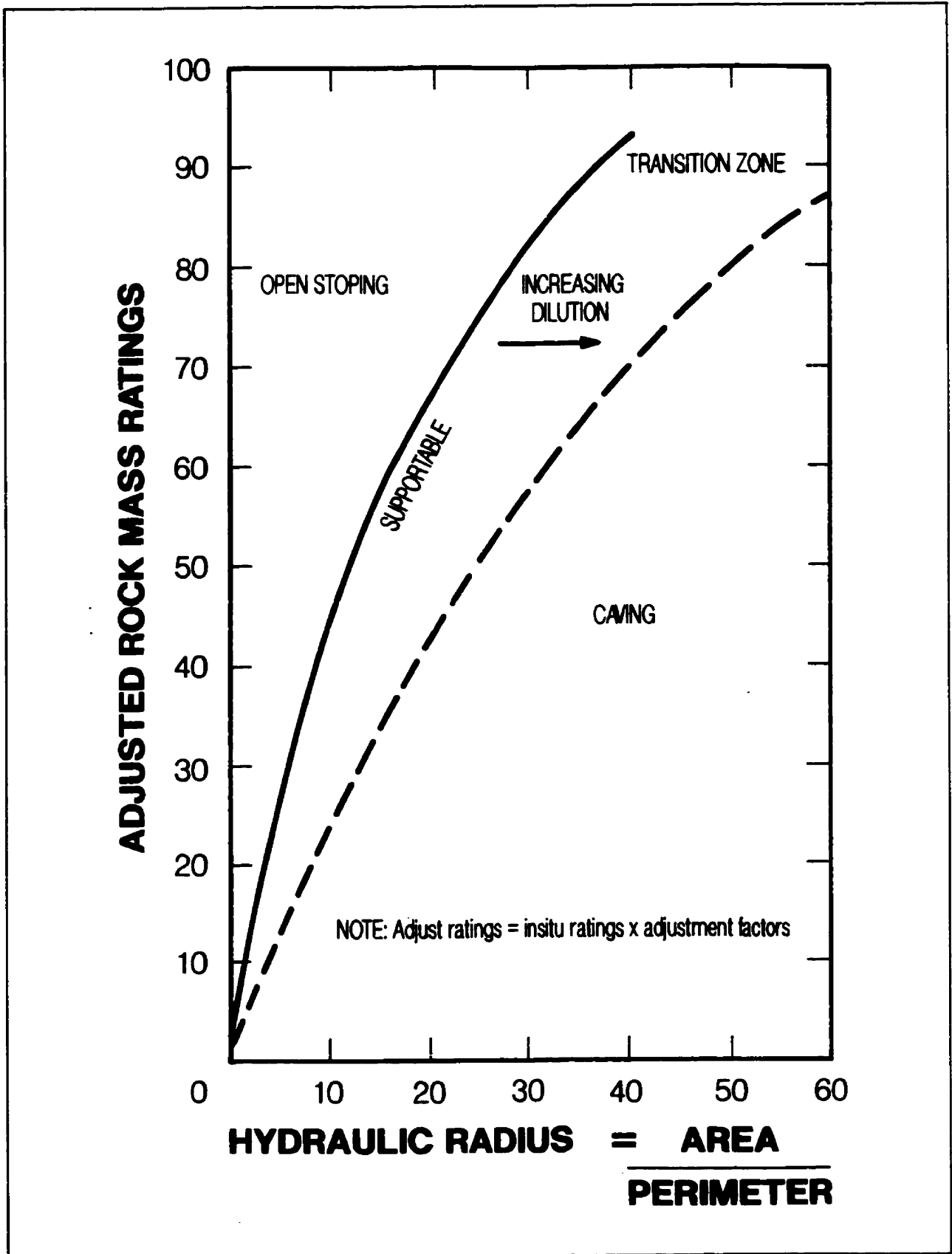


Figure 2.5 Laubscher design graph (After Laubscher, 1990)

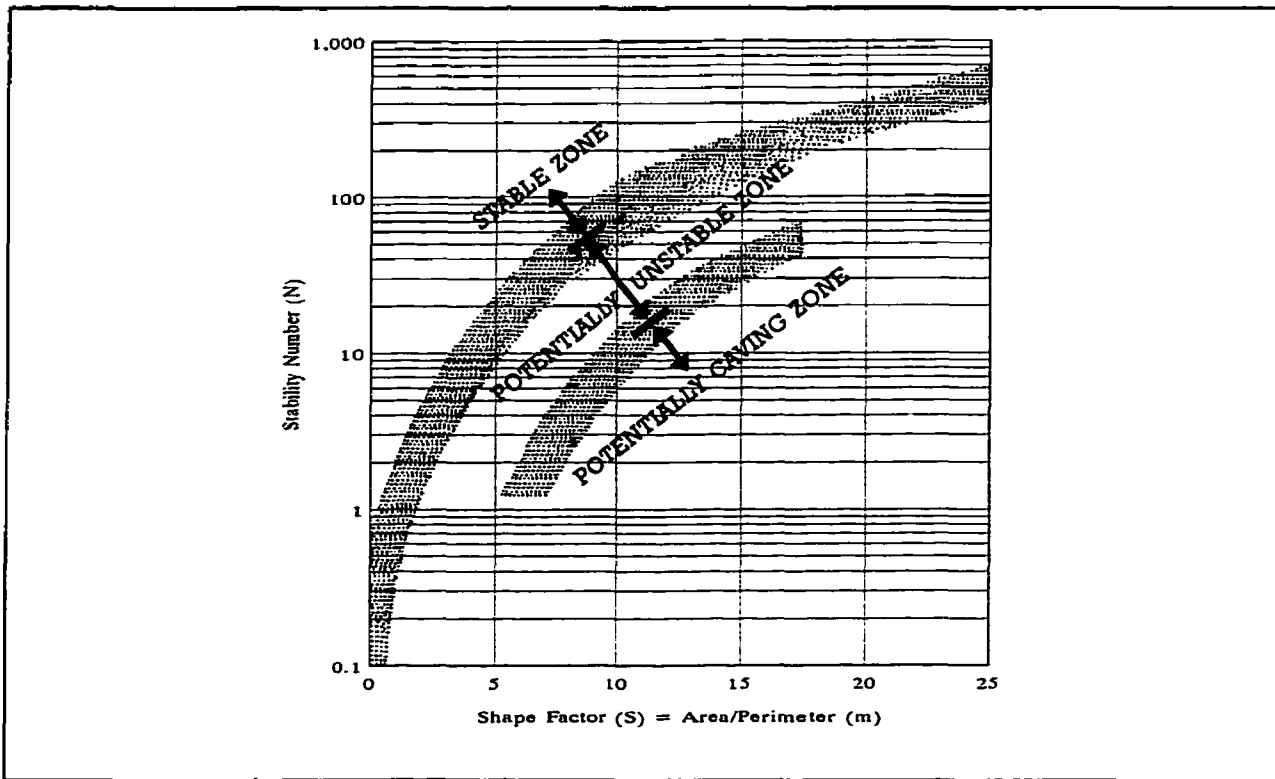


Figure 2.6 Mathews' design graph (After Mathews et al., 1981) (From Nickson, 1992)

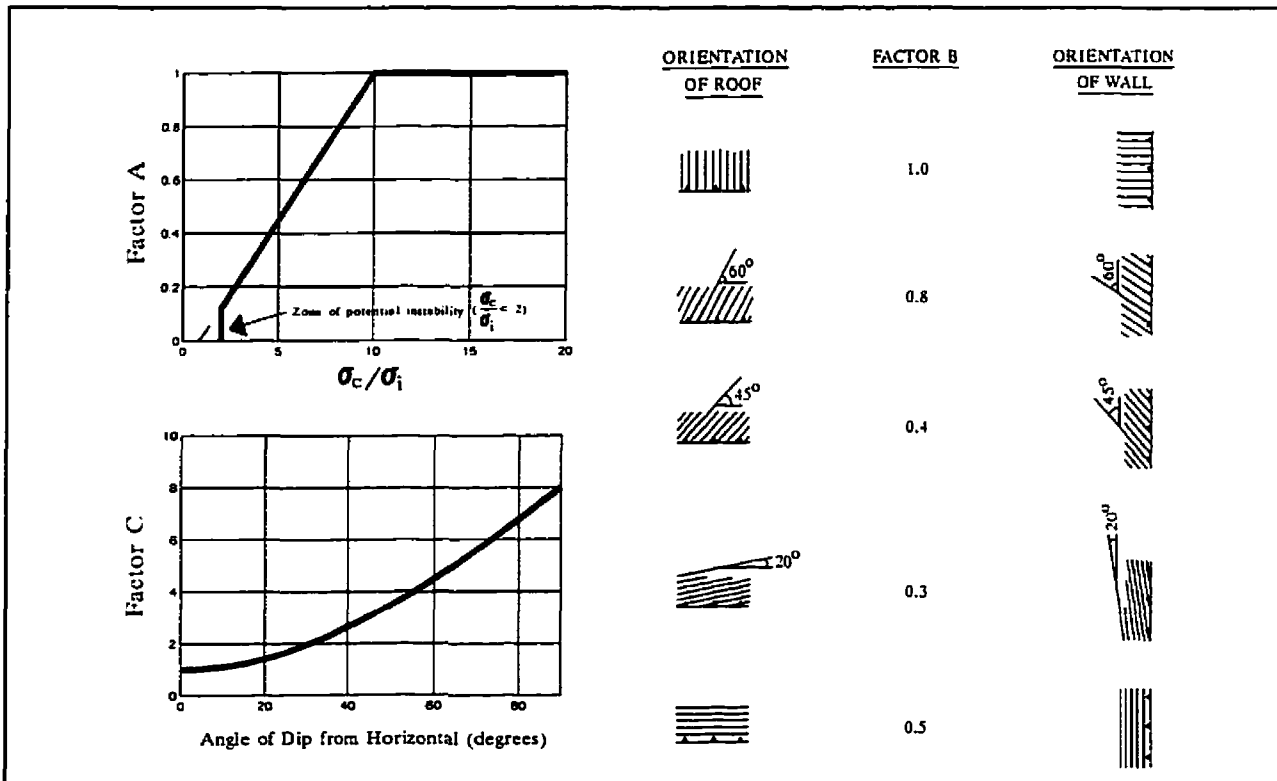
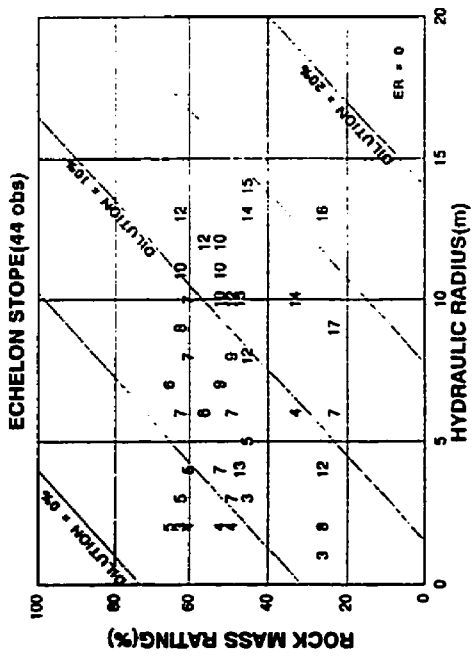
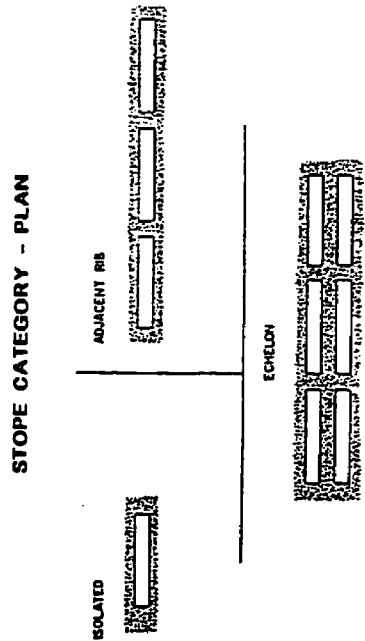
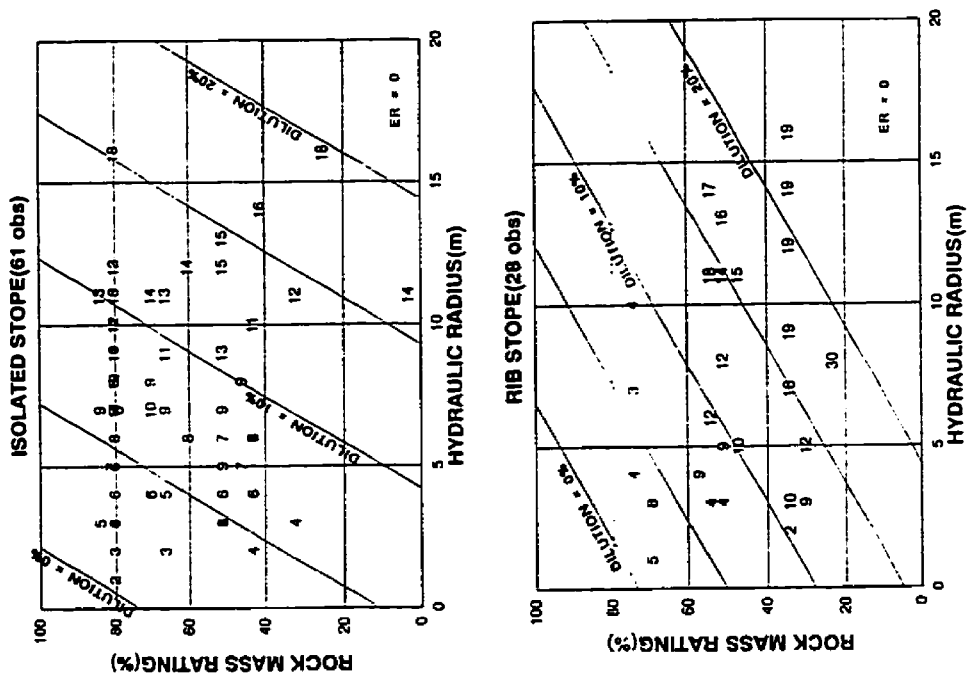


Figure 2.7 Input parameters used for determining N for the Mathews' Analysis (After Mathews et al., 1981) (From Nickson, 1992).



(5) numbers refer to dilution measured

Figure 2.8 Dilution design method (From Pakalnis, 1993)

2.2.8 Modified Stability Graph Method

The modified stability graph design technique is based on a verification and modification of the Mathews design method. It is based on 175 case histories collected from 40 underground Canadian Mines (Potvin, 1988). This design method is also graphical and plots stope surface conditions in a stable zone, caved zone or narrow transition zone. As with the Mathews' method, the graph consists of a plot of stability number N versus surface hydraulic radius. Figure 2.9 shows the modified input parameters for determining N which includes factors for assessing rock strength and stress, critical joint set orientation with respect to the surface and surface orientation. Figure 2.10 shows the modified stability graph, as revised by Nickson, 1992.

2.2.9 Bench Stability Method

This empirical stability design technique was developed by Villaescusa (1996) and is a site specific method developed for Mount Isa Mines. The design method consists of a graph of surface hydraulic radius plotted against the hanging wall ground condition. The ordinate is the ground condition term and is based on the three factors which have historically controlled the strongly laminated stopes at the Mount Isa Lead Mine. The factors consist of the following:

- rock classification based on the number of bedding plane breaks per metre and number and continuity of joint sets present.
- magnitude of stress normal to the ore body
- blasting practice.

Based on the surface hydraulic radius and calculated hanging wall ground condition, the stope surface is plotted to be in either a stable zone, dilution onset zone or failure zone (Figure 2.11).

Stability Graph Factors A, B, and C

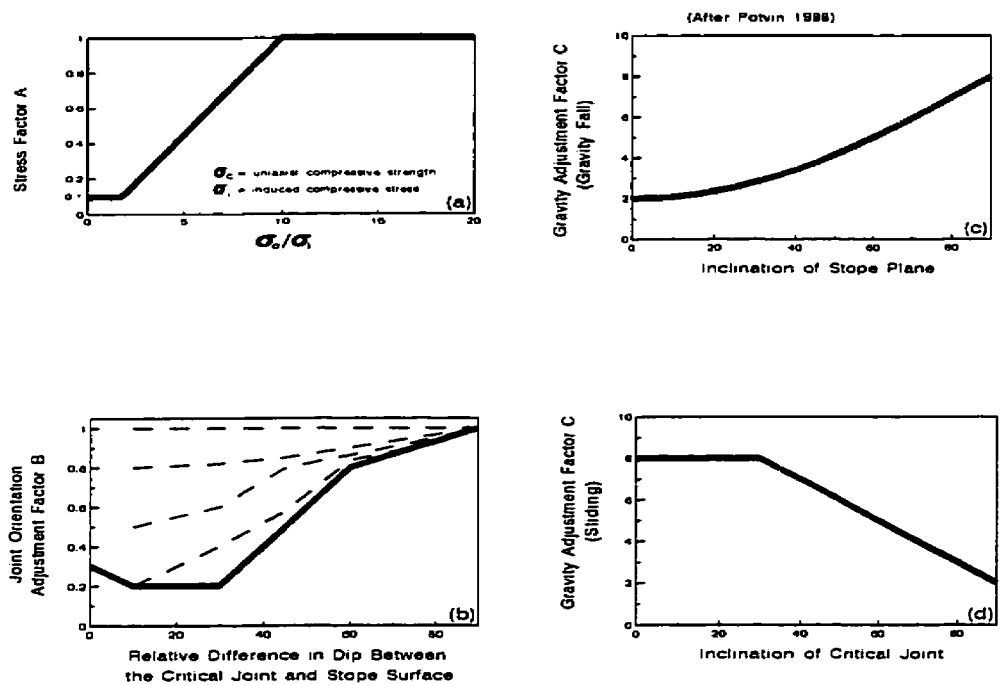


Figure 2.9 Input parameters used for determining N for the modified stability graph design method. (After Potvin, 1988) (From Nickson, 1992)

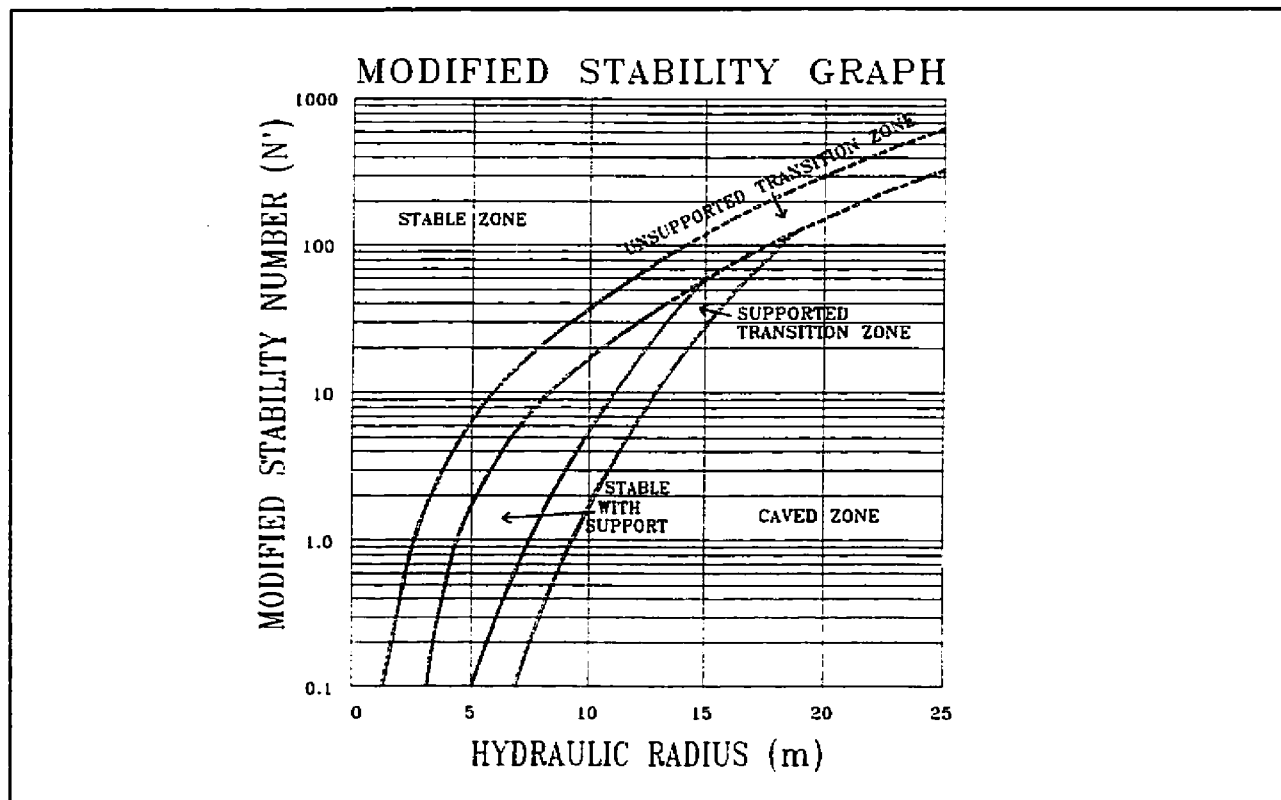


Figure 2.10 Modified stability graph design method. (From Nickson, 1992)

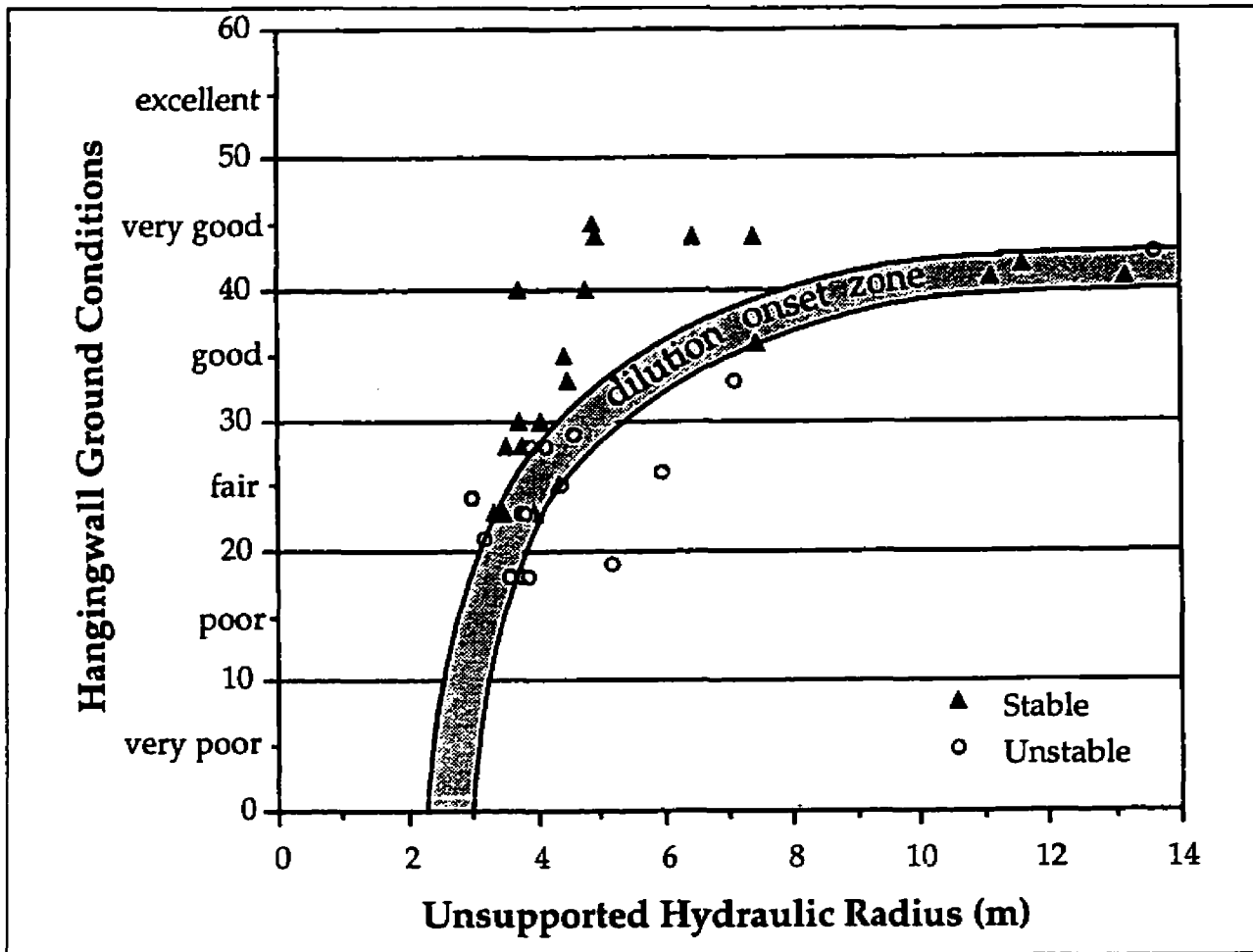


Figure 2.11 Bench stability design chart. (From Villaescusa, 1996)

2.3 ANALYTICAL DESIGN METHODS

The source of loads on underground structures includes induced stresses in the surrounding rock mass and the dead weight of the rock adjacent to the openings. The determination of stresses surrounding excavations is exacerbated by the difficulty in measuring representative far field stresses and assessing the influence of discontinuities and changing elastic properties in the rock mass. The primary difficulty with determining dead weight forces acting on the backs of openings is in estimating the limit beyond which the rock mass is self supporting through the influence of confining stress or some arching action.

Analytical design techniques can be broken into three broad categories based on the assumed failure mechanism. Stress driven failure, gravity driven failure and a combination of stress and gravity driven failure. As well as the difficulty associated with estimating loads in each of these conditions, the same difficulties exist in estimating rock mass strength properties as with empirical design methods.

Stress driven failure design only considers the strength properties of the rock mass and the stress regime. It does not consider the much more stable orientation of the floor of a drift compared to the back. Many different failure criteria have been developed, often based on strength of the intact rock. Correction factors or high safety factors are often used to reflect the weaker rock mass properties as compared to intact rock. Most failure criteria have had limited use in rock mechanics, except for the Mohr-Coulomb failure criteria, which has had wide acceptance, and the Hoek and Brown failure criterion, developed specifically for underground rock applications. All of the failure criteria are based on the magnitude of the principal stresses and some measure of the rock mass strength.

Gravity driven failure looks at only the dead weight of the material considered for design and the rock mass strength properties. Beam and plate theory originated with civil engineering and treat the immediate surface of an opening as a continuous structural member. Voussoir arch theory is also borrowed from civil engineering and looks at transmitting vertical gravity loading to a horizontal thrust acting onto the opening abutments. Kinematic failure design looks at the jointed nature of the rock mass and determines what block or wedge geometries can fall into an opening. Each of these design approaches is looked at briefly in the following sections.

2.3.1 Mohr-Coulomb Criterion

The Mohr-Coulomb failure criterion is one of the simplest and best known failure

criterion used for rock (Goodman, 1989). It is primarily used to evaluate intact rock failure, however, it has had some mining application where the input parameters have been calibrated to field conditions. This failure criterion takes into account the increased strength of the rock with increasing confinement. Figure 2.12 shows the criterion with a tensile cutoff. Failure in terms of the maximum principal stress σ_1 can be expressed by the following equation:

$$\sigma_1 = \sigma_{UCS} + \sigma_3 \tan\left(45 + \frac{\phi}{2}\right) \quad (\text{Eq. 2.4})$$

Where: σ_{UCS} = Unconfined compressive strength

ϕ = Angle of internal friction

Under very high confinements, the maximum stress at failure becomes unrealistic because a linear failure surface is generated. The Hoek and Brown failure criterion flattens the failure

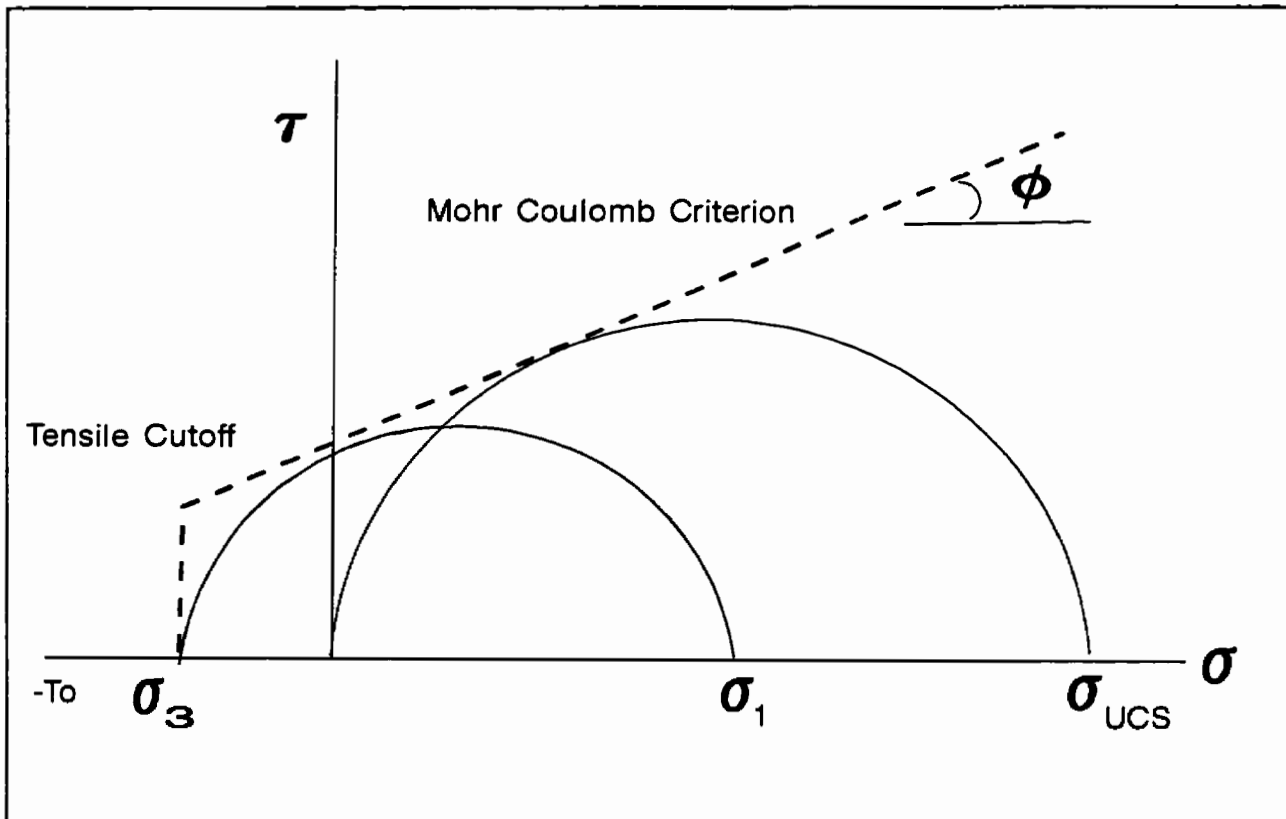


Figure 2.12 Mohr Coulomb failure criterion (After Goodman, 1989).

surface and attempts to account for the jointed nature of the rock mass (Hoek and Brown, 1980).

2.3.2 Hoek and Brown Criterion

Hoek and Brown developed an empirical relationship for the maximum failure stress for a range of confinements. The criterion introduces two constants, m and s , and is also based on the rock unconfined compressive strength (UCS) to describe the rock mass strength properties. The terms m and s are based on the rock mass properties, or classification, as well as the rock type. The equation developed to determine maximum load at failure is given below:

$$\sigma_1 = \sigma_3 + (m\sigma_3\sigma_{UCS} + s\sigma_{UCS}^2)^{\frac{1}{2}} \quad (\text{Eq. 2.5})$$

Where m & s are constants dependent on rock type and rock mass classification.

The advantage of this failure criterion is that it is related to rock classification values, RMR and Q, which take into account the jointed nature of the rock mass.

2.3.3 Kinematic Failure

Kinematic failure design considers the jointed nature of the rock mass and is based on well delineated joint sets determined from detailed mapping. For a kinematically possible block or wedge, the stability is determined by relating the joint's frictional and cohesive strength with the dead weight of the object. Often, kinematic design is based on the presence of ubiquitous joints. In this case, if a potential failure wedge or block geometry exists, it will be present regardless of the opening size. As an opening geometry increases, however, the weight of the wedge or block will increase as a cubic function, whereas the cohesive strength will increase as a square function.

2.3.4 Beam Failure

Early analysis techniques for designing mining backs attempted to apply basic theory of beams and plates to assess loads on open stope surfaces. An excellent summary of beam theory, as it applies to opening stability, is given by Obert & Duval (1967). Several assumptions are required for the application of this theory and are listed:

1. Beam length is $\geq 8t$, where t is either beam thickness or width.
2. Beam material is continuous, homogeneous, isotropic and linear elastic.
3. The beam has a uniform cross section and a longitudinal plane of symmetry.
4. Loads are applied normally to the long axis of the beam and in the plane of symmetry.
5. Plane sections in an unloaded beam remain plane during bending.

Beam theory best applies to tunnel roof conditions in a bedded or laminated rock mass. The tunnel span is equated to a beam length and the beam thickness is set to the bedding spacing. The beam ends are considered to be rigid since moments can be induced within the abutments. Under downward loading, the beam deflects. At the centre the top of the beam is put into compression and the bottom of the beam in tension.

If beam loading is assumed to be simply determined from the weight of the beam, as shown in Figure 2.13, beam loading and deflection can be determined. For bending a beam with fixed ends under self weight, the following equations govern maximum induced tensile, compressive and shear stresses, as well as maximum induced moments and deflection:

Maximum Tensile/compressive stress	$(\sigma_{Max}) = \pm(\gamma L^2)/2t$	(Eq. 2.6)
------------------------------------	---------------------------------------	-----------

Maximum Moment (Abutment)	$(M_{Max}) = \pm(\gamma L^2 t)/12$	(Eq. 2.6b)
---------------------------	------------------------------------	------------

Maximum Shear stress	$(\tau_{Max}) = (3\gamma L)/4$	(Eq. 2.6c)
----------------------	--------------------------------	------------

Maximum Deflection	$(\eta_{Max}) = (\gamma L^4)/(32Et^2)$	(Eq. 2.6d)
--------------------	--	------------

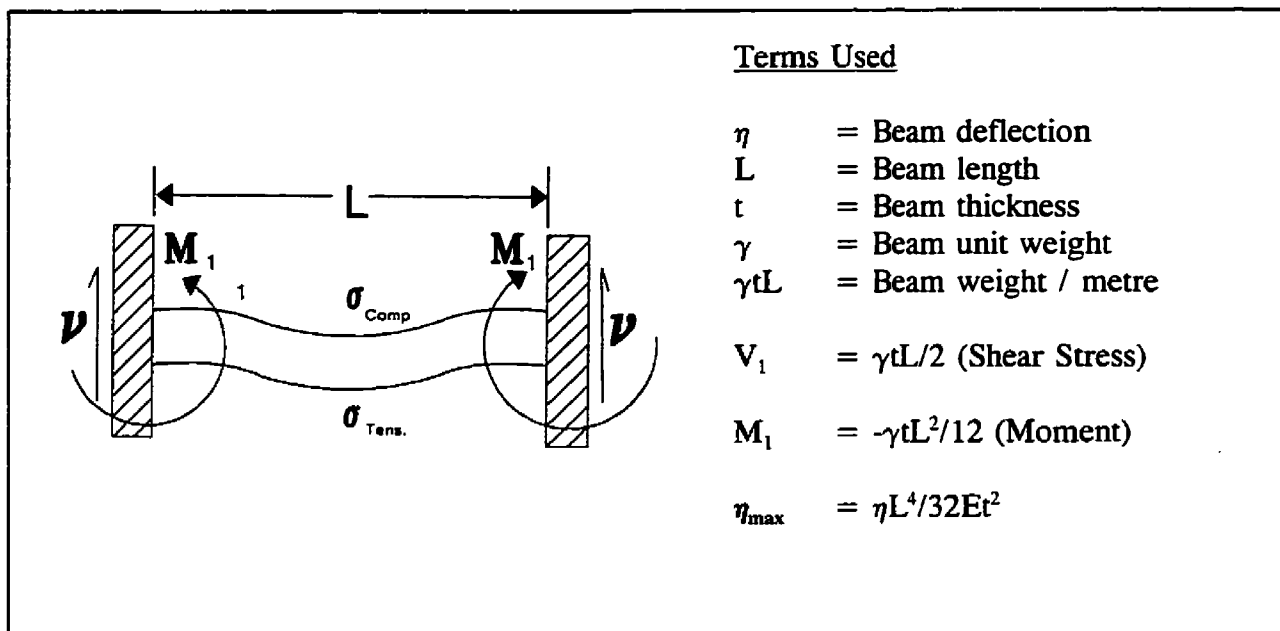


Figure 2.13 Beam loading conditions under self weight.

Using the beam approach, to design for the maximum allowable tensile strength greatly overestimates stability. In a hard rock mine, an unconfined compressive strength (UCS) of 100 MPa and a horizontal joint spacing of 1 metre are reasonable conditions. For a 100 MPa rock, a 10 MPa tensile strength could be estimated based on Griffith theory (Jaeger and Cook, 1984). These conditions would give a maximum drift span design of 27 metres (hydraulic radius ~ 14m). This hydraulic radius represents a large opening and is an optimistic design for anything other than a very competent rock mass.

The major flaw with this design approach is the assumption that the rock mass can mobilize tensile stresses. The presence of cross joints orientated perpendicular to the span makes it impossible for tensile stresses to be mobilized. Realizing the shortcomings of this design method, practitioners commonly used factors of safety as high as eight in their design, Merrill (1954).

Beam theory can only be applied in situations where the opening length is significantly greater than the width, as in tunnels and drifts. To account for other geometries such as drift

intersections and slope backs, plate theory is required.

2.3.5 Plate Theory

A good introduction to plate theory is given in Obert & Duval (1967). As mentioned above, plate theory is more applicable to design in cases where an opening length is not much greater than the width. As with beam theory, several assumptions are required for the application of this theory and they are listed below (Obert & Duval, 1967):

1. A plate is a rectangular surface whose width is at least four times the thickness.
2. The plate material is continuous, homogeneous, isotropic and linear elastic.
3. The maximum plate deflection is less than half its thickness.
4. All loads are applied normal to the surface and the central plane of the plate remains unstressed.
5. Vertical straight lines remain straight after loading, although they do become inclined.

For the analysis of a back in an underground situation, the back is analysed as a plate with 'built in edges'. Background to the theory on plate loading is given in Timoshenko (1940) and Timoshenko and Goodier (1958). The following equations can be used to determine the maximum moment, stress and deflection for a plate loaded by its weight:

$$\text{Tensile/compressive stress} \quad (\sigma_{Max}) = \pm(6\beta\gamma S^4)/t \quad (\text{Eq. 2.7a})$$

$$\text{Maximum Moment (Abutment)} \quad (M_{Max}) = \pm \beta\gamma S^2 \quad (\text{Eq. 2.7b})$$

$$\text{Maximum Deflection} \quad (\eta_{Max}) = (\alpha\gamma S^4)/Et^3 \quad (\text{Eq. 2.7c})$$

Where:

γ	=	unit weight of rock (.027 Mn/m ³)
α & β	=	Coefficients based on the span to length ratio for a $\nu = .3$
t	=	Beam thickness
S	=	Span
E	=	Young's Modulus

2.3.6 Voussoir Arch Failure

During deflection in both beam and plate theory, the base of the member is loaded in tension and the top in compression. The usually fractured nature of a rock mass makes it difficult to accept the mobilization of tensile loads in the back of an excavation. To account for the observed stability of fractured backs, a theory calling for the mobilization of a voussoir, or linear arch in the back of an opening was developed (Evans, 1941).

The mobilization of an arch or "arching action", consists of the formation of a compressional zone above an opening which transfers vertical load to the abutments on either side of the opening (Wright, 1973). Some of the assumptions found in Evans' paper concerning the depth of the compressional zone were later found to be incorrect. A summary of the voussoir arch theory is found in Brady & Brown (1985).

For a beam deflecting under dead weight, it is assumed that tensile stresses will not be developed due to the fractured nature of the rock mass. Instead, with deflection, tensile cracks will tend to form and open at the base of the centre span and the top of the beam near the abutments, coinciding with the tensile zones. Compressive stresses will develop at the base of the abutment and top of the centre span opposite the tensile zones. For a beam of thickness t , these stresses will be distributed over the portion of the beam 'nt'. Figure 2.14 summarizes the loading and forces described.

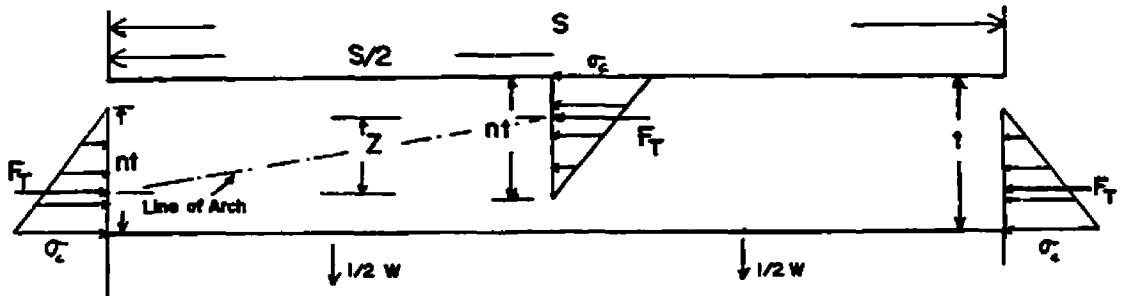
The solution of the voussoir beam problem is an iterative procedure, and, using the equations already presented above, the following steps are required (Brady & Brown, 1985).

1. n = a set initial value

2. $Z_0 = t - 2tn/3$ (Eq. 2.8a)

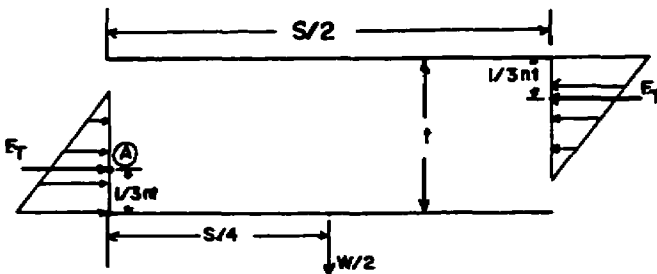
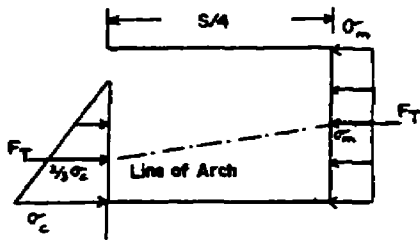
a) maximum longitudinal stress

$$\sigma_c = \{\gamma S^2\}/(4nZ) \quad \text{(Eq. 2.8b)}$$



Terms Used

- S = Beam (or tunnel span)
- t = Beam thickness
- nt = Beam thickness under compressive or tensile loads due to deflection
- σ^C = Maximum compressive or tensile stress
- F_T = Total force or thrust due to stress distribution
- W = Beam weight (γSt per unit width)
- Z = Moment couple ($t - \frac{1}{3}nt$)



Z_0 = Moment arm before deflection occurs
 $Z_0 = t(1 - \frac{1}{3}n)$
 deflection/compression reduces the moment arm

$\sum M_A : F_T * Z = \frac{1}{2}\gamma St * \frac{1}{2}S$
 where: $F_T = \frac{1}{2}\sigma_c * nt$
 $\sigma_c = \{\gamma S^2\} / (4nZ)$

Figure 2.14 Geometry and forces acting on a voussoir beam (Evans, 1941)

b) average longitudinal stress (Eq. 2.8c)

$$\sigma_{avg} = \{\sigma_c(3n + 4)/12\}$$

c) arc length of the arch (Eq. 2.8d)

$$L = S + 8/3 (Z_o^2/S)$$

d) elastic shortening of the arch (Eq. 2.8e)

$$\Delta L = (\sigma_{avg}/E) * L$$

e) arch height or moment arm (Eq. 2.8f)

$$Z = \{3S/8(8Z_c^2/3S - \Delta L)\}^{1/2}$$

Where Z_c = the value of Z from the previous iteration

f) lateral load depth ratio (Eq. 2.8g)

$$n = 3/2(1 - Z/t)$$

Note: The equation for the arc length of the arch has been corrected from the equation given in Brady and Brown (1985).

The first step is to solve an initial estimate of the compressive stress by choosing an initial value of n. Equations 'a' through 'f' are then solved and equation 'a' is started again with a new estimate of 'n' from equation 'f'. The procedure is followed until stable values of the maximum stress are obtained.

2.3.7 Key Block Theory

Key block theory, developed by Goodman and Shi (1985), initially considered the kinematic failure of blocks and wedges and determined the maximum potential failure size based on opening and block geometry constraints. Standard kinematic analysis techniques were employed to account for joint strength, orientation and block weight. The technique has been expanded and now takes into account field stresses acting on potential blocks and wedges.

2.3.8 μ DEC and 3DEC Design

μ DEC and 3DEC (Distinct Element Code) are respectively two and three dimensional distinct element computer models (Itasca Program Documentation, 1992). The rock mass is

simulated by blocks separated by discontinuities or joints. The blocks can be modelled as linear-elastic or elastic-plastic material while joints can be modelled using a Coulomb slip criterion. Shear and normal stiffness parameters of the joints are also input. The blocks and discontinuities are loaded both by stresses in the rock mass and by gravity loading.

2.4 SUMMARY

There are many analytical and empirical design techniques used in underground design. All of the methods require the input of rock mass strength, loading conditions and failure criterion. Rock mass strength is generally estimated using the Q or RMR classification system which can be a precise and repeatable, though not an accurate measure of rock mass strength. Design approaches exist such as μ DEC and 3DEC which take very detailed input parameters on rock mass strength such as shear and normal joint stiffness as well as joint continuity. Design approaches which require several input parameters which can only be estimated through back analysis have serious drawbacks for use as an on site design tool. Many well documented back analysed case histories would be required to realistically assess each input parameter.

The immediate zone of rock around an underground opening is often under low or negligible field stresses due to stress shedding around the immediate blast damaged opening surface. This local zone of rock, free from the influence of field stresses, acts primarily under the influence of gravity loading. The zone of rock around an opening, under the influence of gravity loading or field stress, can be estimated with experience and field measurements. The failure criterion for a given rock mass under given loading conditions, however, is very difficult to determine. Even after a failure has occurred under well mapped and instrumented conditions, it is difficult to determine whether stress or gravity loading played a dominant role. Many

empirical tunnel design methods have no input for the effect of stress, and span is used as some indirect measure of load.

All of the design methods require back analysis to validate them under new conditions. Ideally, this back analysis procedure should focus on a calibration of the least well understood most difficult parameters to estimate. The criteria under which a rock mass fails is arguably the most difficult parameter to estimate and, as such, is the input best calibrated or determined through back analysis. Empirical design techniques commonly consist of a broad transition zone between stable and unstable conditions which can be calibrated to specific site conditions. The modified stability graph design technique will be looked at in greater detail in Chapter 10. The next chapter covers some of the existing methods used to interpret measured rock mass deformations.

CHAPTER 3

ROCK MASS DEFORMATION

3.1 INTRODUCTION

Deformation is the most commonly measured rock mass response to the creation of underground openings. Deformation can be a precursor to instability and, frequent visual observations of movement often provide excellent information on rock mass stability. Many mechanisms may be driving the rock mass deformation and they can include the following:

- Elastic compression / tension and relaxation
- Non-elastic relaxation (decreasing rock mass modulus and/or discontinuity dilation)
- Beam or voussoir arch type deformation (combined compressive and tensile deformations)

Figure 3.1 shows a schematic of the various stages of deformation that may occur due to the creation of an underground excavation. The diagram shows a cross section of an extensometer installed to monitor stope hanging wall conditions. In stage 1 the instrument is located in the stope abutment and movement between extensometer anchors reflects compressive stresses increasing in the area. Stage 2 shows the stope and expected instrument response immediately after the stope has been mined. The movement between extensometer anchors shows elastic extension or stress relaxation. Stage 3 shows non-elastic extension which may stabilize with time as shown in stage 4a, or may increase to ultimate failure of the local hanging wall, stage 4b.

Deformation monitoring instrumentation has made great advances in recent years. The development of more accurate deformation measuring devices and the availability of continuous

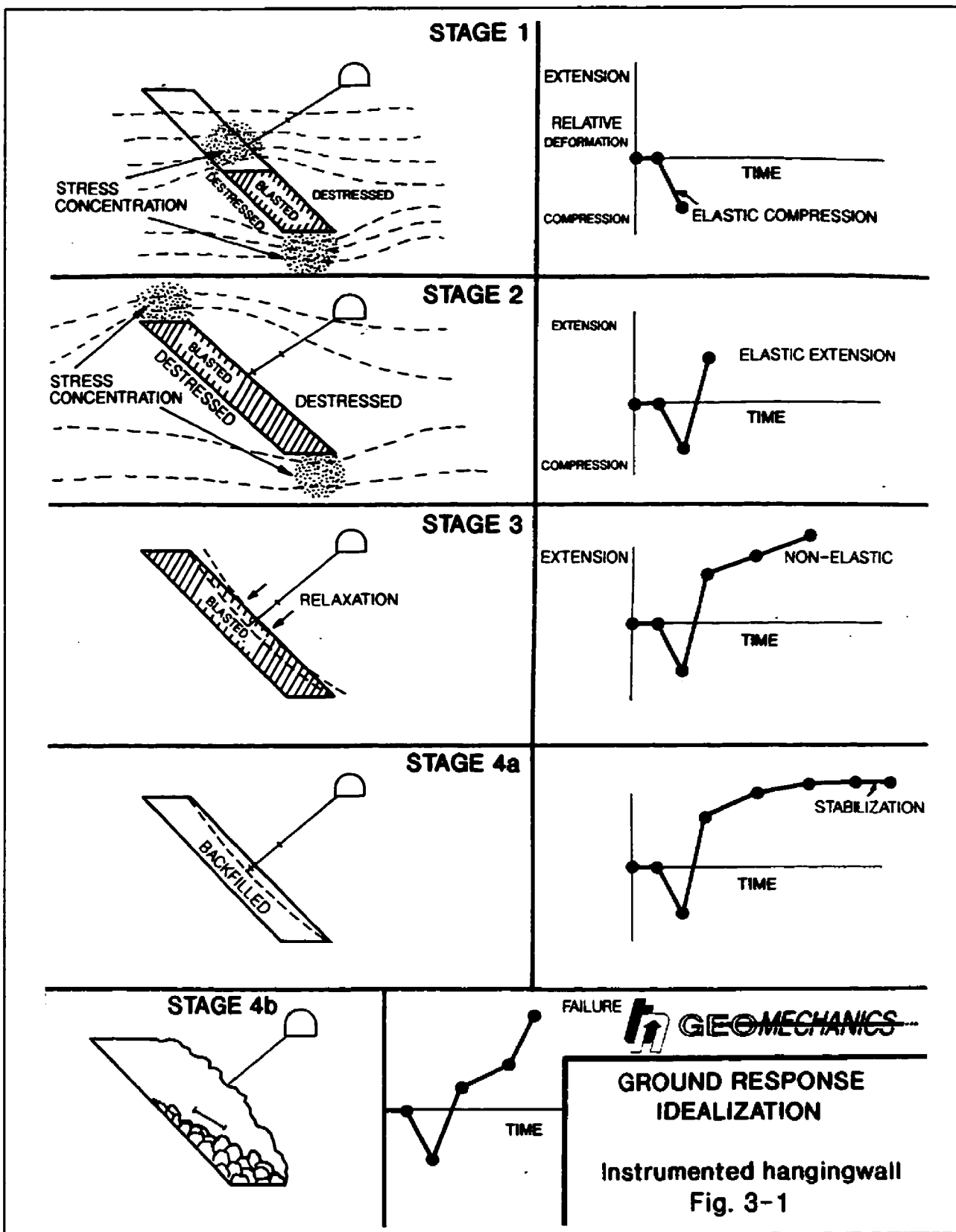


Figure 3.1 Idealized stages of deformation in the vicinity of an underground excavation (From Internal Noranda Technology Centre (NTC) short course).

automatic data recorders has greatly increased the quality of instrumentation data. The interpretation of instrumented ground movements has not kept up with the improved data. In general, the purpose of most instrumentation data collected by mines can be broken into two categories (Brady and Brown, 1985). Data can be gathered for improving safety as an indicator of approaching instability. Data can also be used to improve design by checking the accuracy of the model used to predict ground response to mining. This procedure is sometimes referred to as 'closing the design loop' and may be the only way to check design optimization, if a failure has not occurred (Bawden et al., 1988).

Few guidelines exist for determining allowable stable deformations. The on site ground control engineer is generally left to his own experience to determine safe levels of movement. Design approaches are seldom changed based on measured deformations. If an elastic model is being used to simulate non-elastic ground response to mining, instrumentation results are either ignored, or used to fit an elastic modulus to the non-elastic field deformations. This chapter reviews some of the mechanisms which can drive rock mass movements and some of the methods used in estimating these movements. Some field measuring methods and their interpretation are also discussed.

3.2 APPROACHES TO DEFORMATION ESTIMATION

Rock mass deformation is often a response to the changes in the rock mass stress field caused by the creation of openings underground. Small scale deformations are generally associated with changes in stress. When associated with stress, deformation is best expressed as strain. If two points, L metres apart, move apart ΔL metres, the strain between the points is given by Equation 3.1.

$$\epsilon = \frac{\Delta L}{L} \quad (\text{Eq. 3.1})$$

At a small scale the intact elastic rock modulus, which can be measured in the lab realistically approximates the representative field modulus. Equation 3.2 shows how deformation, expressed as strain, is caused by changing stress.

$$\epsilon_z = \frac{1}{E}(\sigma_z - \nu[\sigma_x + \sigma_y]) \quad (\text{Eq. 3.2})$$

Where: E = Young's modulus or elastic modulus and ν = Poisson's ratio (commonly .2 to .3)

At a larger scale, the shearing dilation and compression of discontinuities contribute both an elastic and non-elastic component to the deformation. Rock mass classification values have been related to elastic field modulus values (Eq. 2.2). Little back analysis, however, has been done at a mining scale to determine the accuracy of this approach.

After the rock mass around an opening has deformed elastically to adjust to the new stress regime caused by the excavation, movement may continue. This movement may be caused by plastic deformation due to a decrease in the rock mass modulus, or it may be associated with other changing loading conditions in the rock mass. A zone of low stress exists near the boundary of an opening where induced stresses parallel to the opening are shed away from the boundary. These stresses parallel to the opening act to clamp the rock mass together. As an opening surface increases in extent, the volume of rock under conditions of lower stress or confinement increases. Within this zone of low confinement, the action of gravity may no longer be overshadowed by high clamping stresses and movement along discrete structures may occur. This movement may occur as the displacement of blocks or wedges of rock, or it may take the form of a beam or voussoir arch deformation mechanism. Relatively small stresses parallel to an opening are sufficient to overcome dead weight. A horizontal stress o

approximately 0.2 MPa is sufficient to support the dead weight of a 10 metre cube of rock, assuming a 30° friction angle and zero cohesion along the sides of the cube. The following sections discuss some methods of determining deformation around an opening based on the various mechanisms which may be causing the movement.

3.2.1 Displacement Around a Cylinder (Kirsch Equation)

The elastic deformation of a surface can be estimated using closed form solutions for simple geometries, or through the use of numerical programs for more complex geometries. The Kirsch equations solve for both stresses and deformations around a cylindrical excavation, assuming plane strain conditions (Kirsch, 1898). This solution is ideal for determining displacements around tunnels and drifts, but has little practical use for stoping geometries.

Elastic stresses and strains at the boundary of a cylindrical opening are independent of size. Displacements are, however, dependent on scale. Equation 3.3 and Figure 3.2 give the Kirsch solution for deformation around a cylindrical opening.

In a mining situation, the Kirsch equation can be used to interpret drift closure

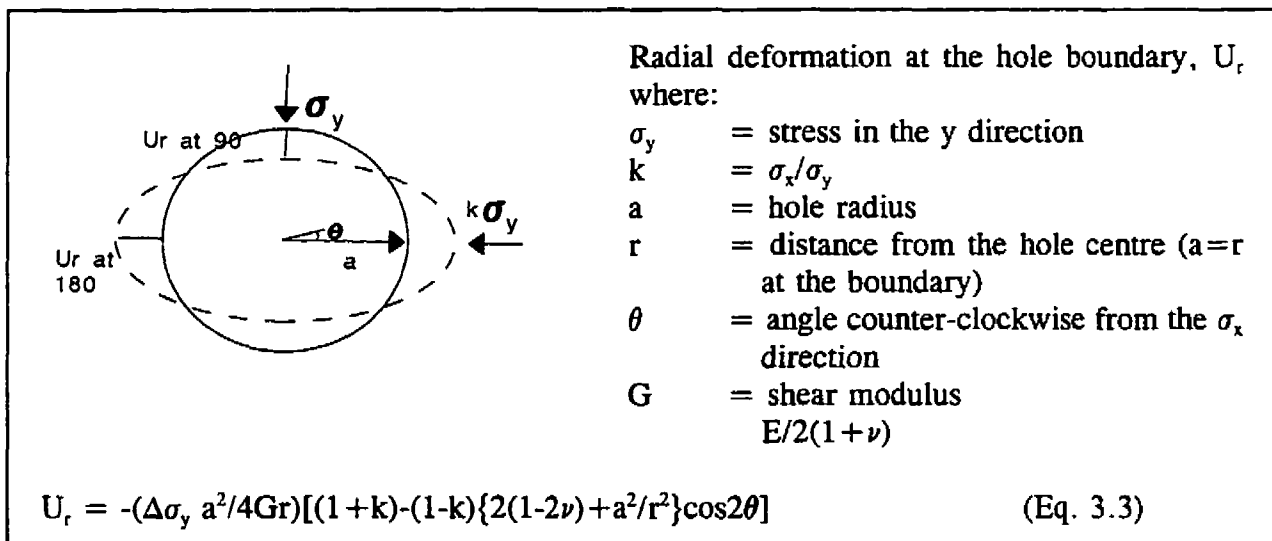


Figure 3.2 Kirsch solution for determining radial deformations around a circular tunnel.

measurements as a function of changing stress. Although drifts are not perfectly cylindrical openings, the equation provides a reasonable first approximation. It is interesting to note based on equation 3.3, that tunnel span, twice the radius of a circular tunnel, is linearly related to the maximum deformation. Appendix A presents a program based on the Kirsch equation which will resolve any three strain directions and magnitudes as principal stress change values, for given elastic rock mass properties (Milne and Milne, 1993).

3.2.2 Displacement Around a Spherical Opening

A solution for determining the displacement around a spherical opening in a hydrostatic stress field is presented in Brady and Brown (1985). All elastic displacements created by a spherical opening are radially in towards the excavation. Equation 3.4 shows that displacements at the boundary of a spherical opening are also linearly related to the opening diameter.

$$U_r = -\frac{pa^3}{4Gr^2} \quad (\text{Eq. 3.4})$$

- Where:
- U_r = Radial displacement
 - p = Hydrostatic stress field
 - a = Sphere radius
 - r = Distance from the centre of the sphere
 - G = Shear Modulus $E/2(1+\nu)$

3.2.3 Numerically Modelled Displacement

There are many numerical models available with a wide range of sophistication. In general terms, there are two predominant approaches for modelling an underground rock mass assuming either continuum or discontinuum behaviour (Potvin, 1988). The continuum approach

assumes the rock mass is a continuous medium which can behave as an elastic or non-elastic material. Discrete discontinuities can often be added to continuum models. Discontinuum models, however, treat the rock mass as a collection of discrete blocks bounded by joints, faults or other discontinuities in the rock mass. The discrete blocks can then move relative to one another based on the properties of the discontinuities and applied loads.

The discontinuum approach has the potential to more realistically model rock mass deformation. 3DEC (Three Dimensional Distinct Element Code) is a three dimensional example of this numerical modelling approach. Unfortunately, much of the input required for a computer model of this sophistication is difficult to measure in the field (Hoek, 1994). Required input includes estimates of discontinuity shear stiffness, normal stiffness, continuity, and planarity as well as spacing and orientation. Some of these parameters can be estimated in the field, though many are estimated by back analysis techniques.

There are advantages and disadvantages to both approaches. The continuum approach can realistically estimate elastic deformations resulting from stress changes which can be reasonably accurate for a small scale intact rock response to stress change. As the scale of deformation increases, however, more discontinuities are present in the rock mass and the continuum approach for estimating deformation becomes unrealistic. For example, the majority of ground falls are preceded by a period of discrete block movement which cannot be modelled with a continuum approach.

There are many continuum modelling techniques based both on finite and boundary element modelling techniques. The boundary element modelling technique is discussed in some detail in Chapter 6.2 and its application to the estimation of elastic displacement is examined.

3.2.4 Beam Displacement

Beam failure analysis was discussed in Section 2.3.4 and an equation for determining maximum beam deflection follows:

$$\eta_{\max} = \frac{\gamma L^4}{32Et^2} \quad (\text{Eq. 2.6d})$$

Where:

- η = Beam deflection
- L = Beam length
- E = Young's modulus
- t = Beam thickness
- γ = Beam unit weight (Obert and Duval, 1967)

As previously mentioned, there are several constraints to the application of this theory. The main required conditions are that the opening surface length is at least eight (8) times the width and that the beam of rock can take tensile loads. Tensile loading requires that the beam does not have any cross cutting fractures, which is usually an unrealistic assumption. In cases where opening length is not at least eight (8) times the opening width, plate theory can be applied.

3.2.5 Plate Displacement

Plate theory is discussed in section 2.3.5 and is similar to beam theory except the geometry constraint, that states the opening surface must be eight (8) time the opening width, is removed. The maximum plate deflection is given in equation 3.6.

Where:

- η = Beam deflection
- α = Coefficient based on span to length ratio (for $\nu=.3$)

$$\eta_{Max} = \frac{\alpha \gamma S^4}{Et^3} \quad (\text{Eq. 2.7c})$$

- S = Plate width
 E = Young's modulus
 t = Plate thickness
 γ = Plate unit weight (Obert and Duval, 1967)

3.2.6 Voussoir Arch Displacement

Voussoir arch failure theory was presented in section 2.3.6, based on Brady and Brown (1985). Arch deflection or displacement is not one of the direct parameters in the failure theory discussed, however, it can be determined from the calculated parameters. Figure 3.3, from Hutchinson and Diederichs (1996), shows how the mid span deflection can be related to beam thickness.

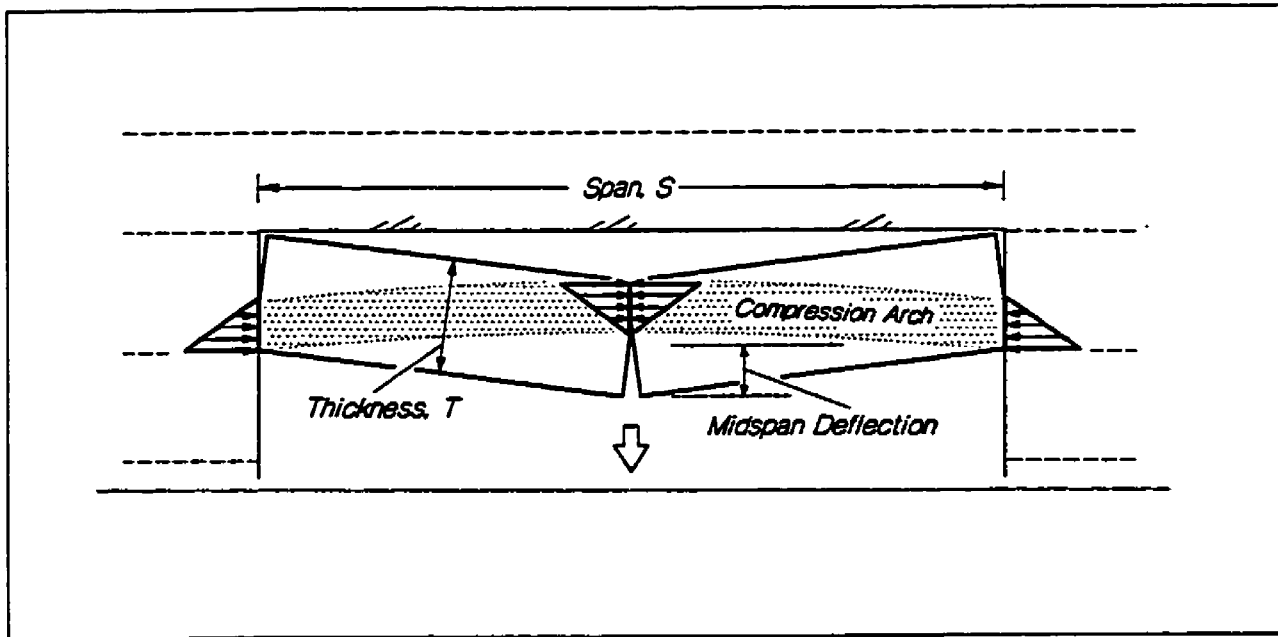


Figure 3.3 Voussoir arch deflection showing the relationship between beam thickness and deflection at the buckling point (From Hutchinson and Diederichs, 1995).

Three failure modes are possible for a voussoir arch; shear failure at the abutments, compressive failure at the abutments or at centre span and snap through or buckling failure. Brady and Brown (1985) state that buckling failure is favoured in wide roof spans with low rock mass deformation modulus. Crushing failure is unlikely in the majority of hard rock mines.

Hutchinson and Diederichs (1996) made an interesting comparison between bed thickness 't' and the midspan maximum displacement. They found that when the bedding or lamination thickness was less than ten (10) times the calculated displacement, buckling or snap-through failure become highly sensitive to a small decrease in lamination thickness. Due to the difficulty in estimating lamination thickness in the field, and to provide some aspect of conservatism to the analysis, a design limit was set where midspan displacement equals 10% of the lamination thickness (Fig. 3.4). When calculated mid-span displacement exceeded 10% of the lamination

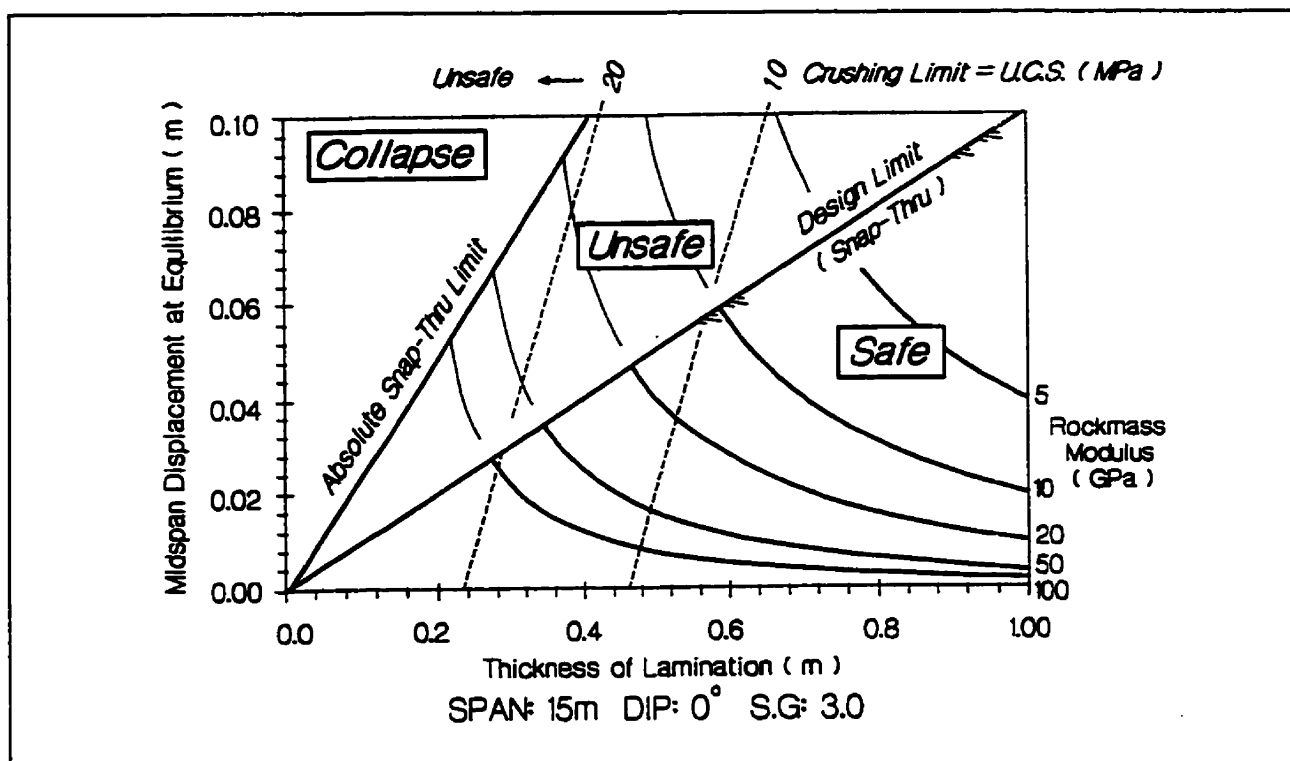


Figure 3.4 Design beam deflection versus beam thickness (From Hutchinson and Diederichs, 1995).

thickness, potential instability was assumed. Based on this buckling instability criteria, charts have been developed relating maximum stable spans and lamination thickness.

Two of these charts are presented in Figure 3.5 with maximum stable span plotted against lamination thickness. These charts relate geometries where opening length is much greater than the span (tunnels) as well as square plate geometries where the opening width and length are the same. A series of curves indicating the buckling design limit are presented in each chart. These curves represent specific conditions of rock mass modulus, specific gravity and surface orientation and they encompass the range of expected field conditions. Based on the curves representing a rock mass modulus to effective specific gravity ratio of 20 GPa, maximum stable deformations were determined for various spans and square plate geometries.

3.2.7 Empirical Displacement Estimation

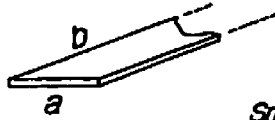
An empirical method has been introduced by Barton (1989) for relating rock quality Q , opening span and surface deformation, (Figure 3.6). The relationship shown suggests both larger opening spans and lower quality rock will result in more surface deformation. The case histories presented all used various degrees of support which reduced the surface movement by varying degrees. All of the cases presented were stable so it is not possible to predict stable limits to deformation.

3.3 DEFORMATION MEASUREMENT

As previously mentioned, deformation measurements made at a small scale can avoid rock mass fractures and can be related to stress change. Large scale movements usually include discontinuities in the rock mass and are more often related to overall behaviour of the rock mass.

Critical Span vs Thickness - General Voussoir Solution

BEAM
 $b \gg a$



$$S.G_{eff} = S.G \times \cos\alpha$$

$S.G = \text{Specific Gravity}$
 $\alpha = \text{wall dip}$

a is critical span

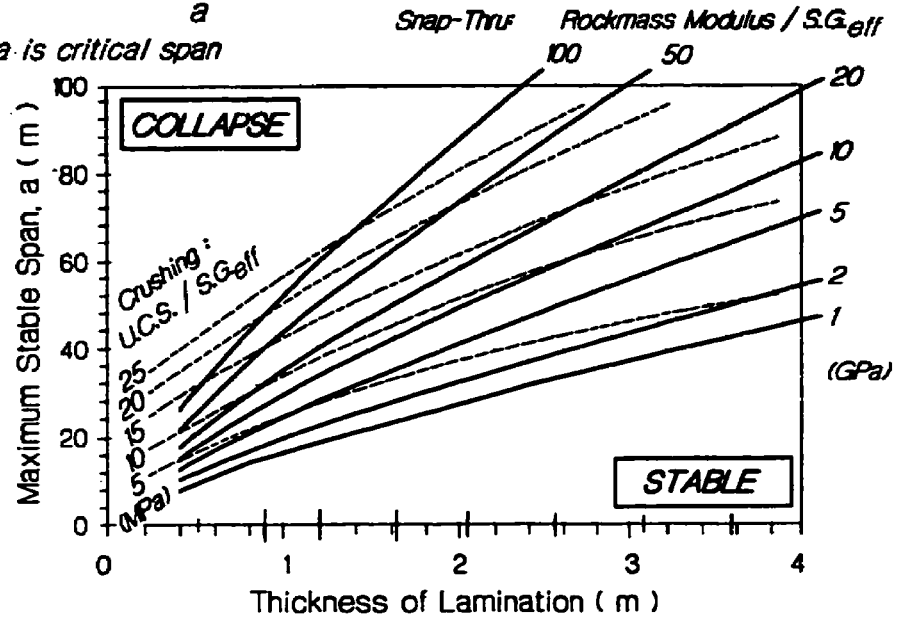


PLATE
 $b = a$

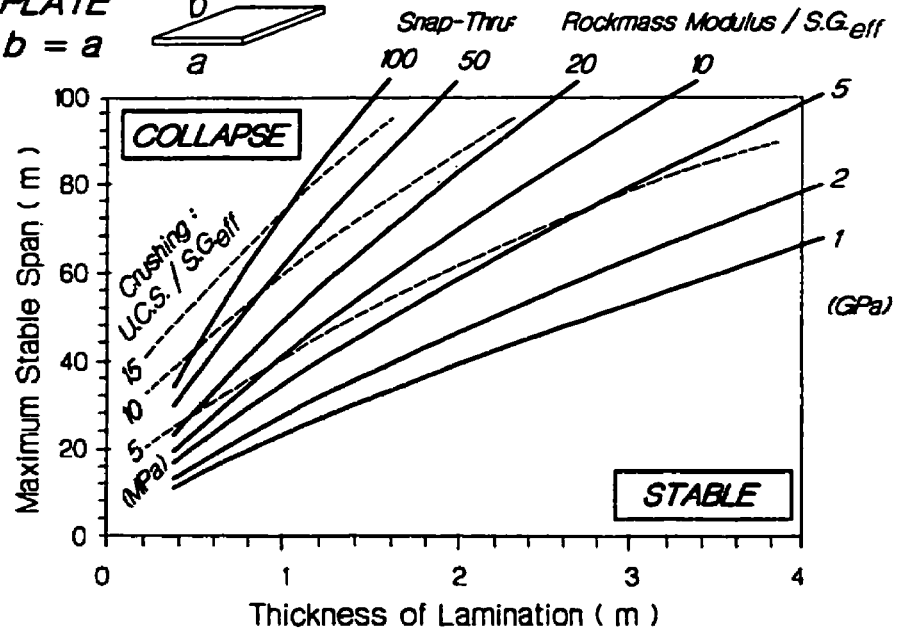


Figure 3.5 General voussoir arch solution showing maximum stable span versus stable lamination thickness. 10% of lamination thickness equals maximum beam deflection (From Hutchinson and Diederichs, 1995).

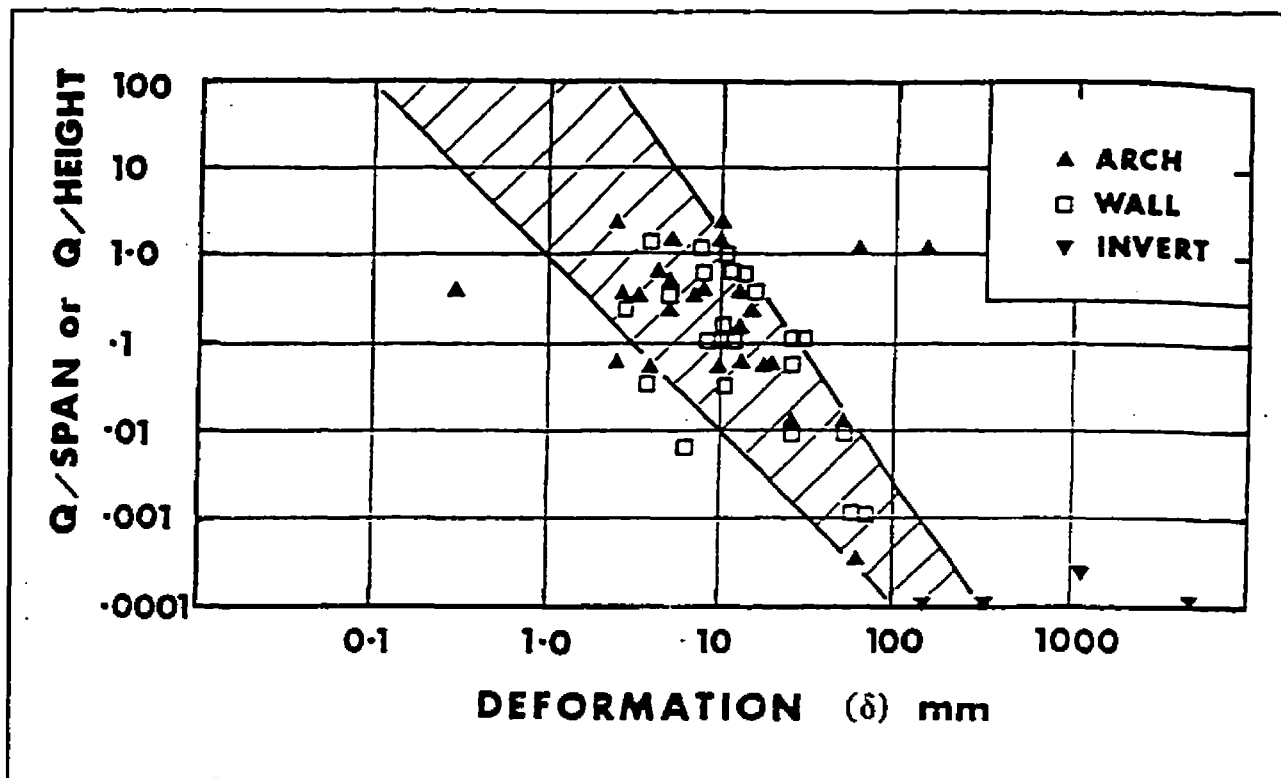


Figure 3.6 Deformation versus rock quality Q and span (From Barton, 1989)

At the small scale, strain gauges are bonded to the rock in some fashion and strain over the gauge length or between measuring points is obtained. These measurements are commonly done within a borehole and some of the common strain measuring instruments include: CSIR biaxial and triaxial gauges, CSIRO triaxial gauges and Yoke cells, vibrating wire stress cells and strain cells and USBM stress cells (Dunnicliff, 1988).

Large scale measurements of deformation are often obtained along a drill hole or through some form of surveying or direct measurement. Deformation is measured along a borehole when the area of interest is not otherwise accessible. When monitoring stope hanging wall or footwall behaviour, cross-cut drifts may provide access to the area of interest. The following sections summarize only some of the techniques for measuring large scale deformation.

3.3.1 Closure Measurements

Closure measurements are made on exposed rock surfaces underground. These measurements commonly take the form of drift closure measurements and drift surveying. The advantage to these measurements is the fact that they incur very low installation costs. Disadvantages include the fact that measurements are made in the zone of rock disturbed by drift mining and that readings are generally labour intensive.

Closure tapes can provide accurate measurements of distances between set points in the order of ten (10) metres apart. Accuracy in the order of $\pm .02\text{mm}$ can be obtained (Brady and Brown, 1985). The general application of closure tapes is for measuring relative displacement of drift walls and the back (Fig. 3.7). Interpretation of these measurements usually consists only of noting the rate and magnitude of movement and setting safe limits based on site specific experience. A great deal more information can be obtained from measurements of closure stations. Relative change in distances between measuring points can be converted to strain. For a four (4) metre wide drift, an accuracy of ± 5 microstrain can be obtained. In a 50 GPa

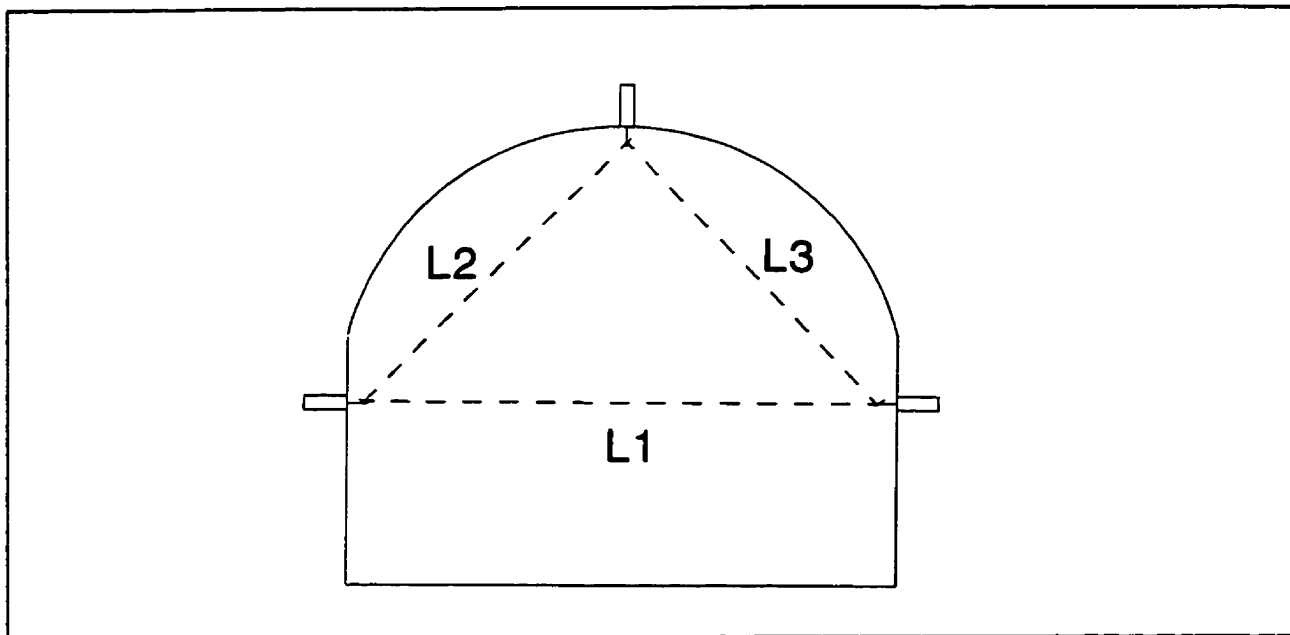


Figure 3.7 Typical closure station measurement layout for mining drifts.

modulus rock mass, this corresponds to an approximate accuracy of $\pm .25$ MPa. A program has been written, based on the Kirsch equation for a circular opening (Eq. 3.3), which converts drift closure measurements in three (3) directions to two dimensional principal stress magnitude and direction (Milne and Milne, 1993). The program makes several simplifications such as treating the drift as a circular opening, and estimating a rock mass modulus and Poisson's ratio also introduces uncertainty. The program is of value for indicating when movement has exceeded realistic elastic limits and for indicating the direction of principal movement.

Closure tapes can also be used to repeatedly measure distances along drifts to obtain estimates of drift closure or extension along the axis of the drift. Figure 3.8 shows an application of this measurement approach along the axis of a stope cross drift. If stope access is from the hanging wall, movement measurements along the cross drift can perform the same function as a hanging wall extensometer, with significant savings in drilling and equipment costs.

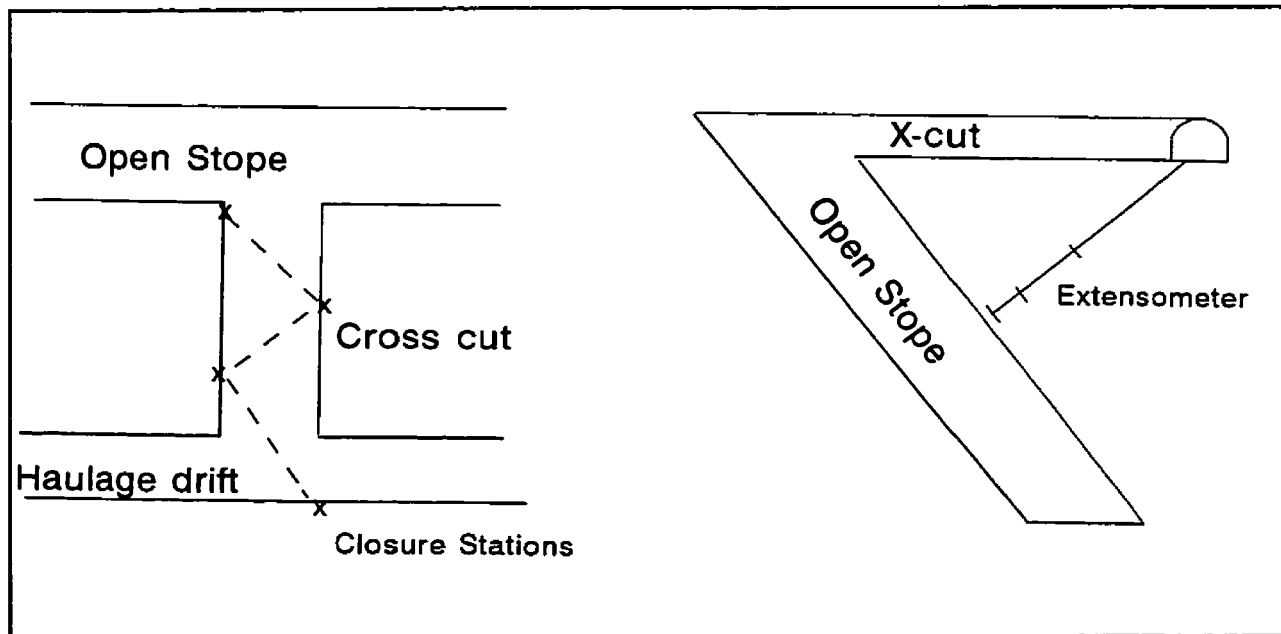


Figure 3.8 Drift closure measurements along a cross drift give data similar to a hanging wall extensometer.

3.3.2 Extensometers

Extensometers can be defined as devices installed in boreholes for monitoring the change in distance between two or more reference points located along the axis of a borehole (Dunnicliff, 1988). One of the reference points is commonly located at the borehole collar and other reference points or anchor points, are located along the drill hole in areas of interest. If only two reference points are installed, the extensometer is referred to as a single point extensometer. If more than two reference points are used the device is called a multi-point borehole extensometer (MPBXs) (Brady and Brown, 1985). One difficulty with single point extensometers is that it is not possible to determine whether the anchor or reference point is moving. Figure 3.9 and Photo 1 shows the layout of an extensometer which consists of a collar,

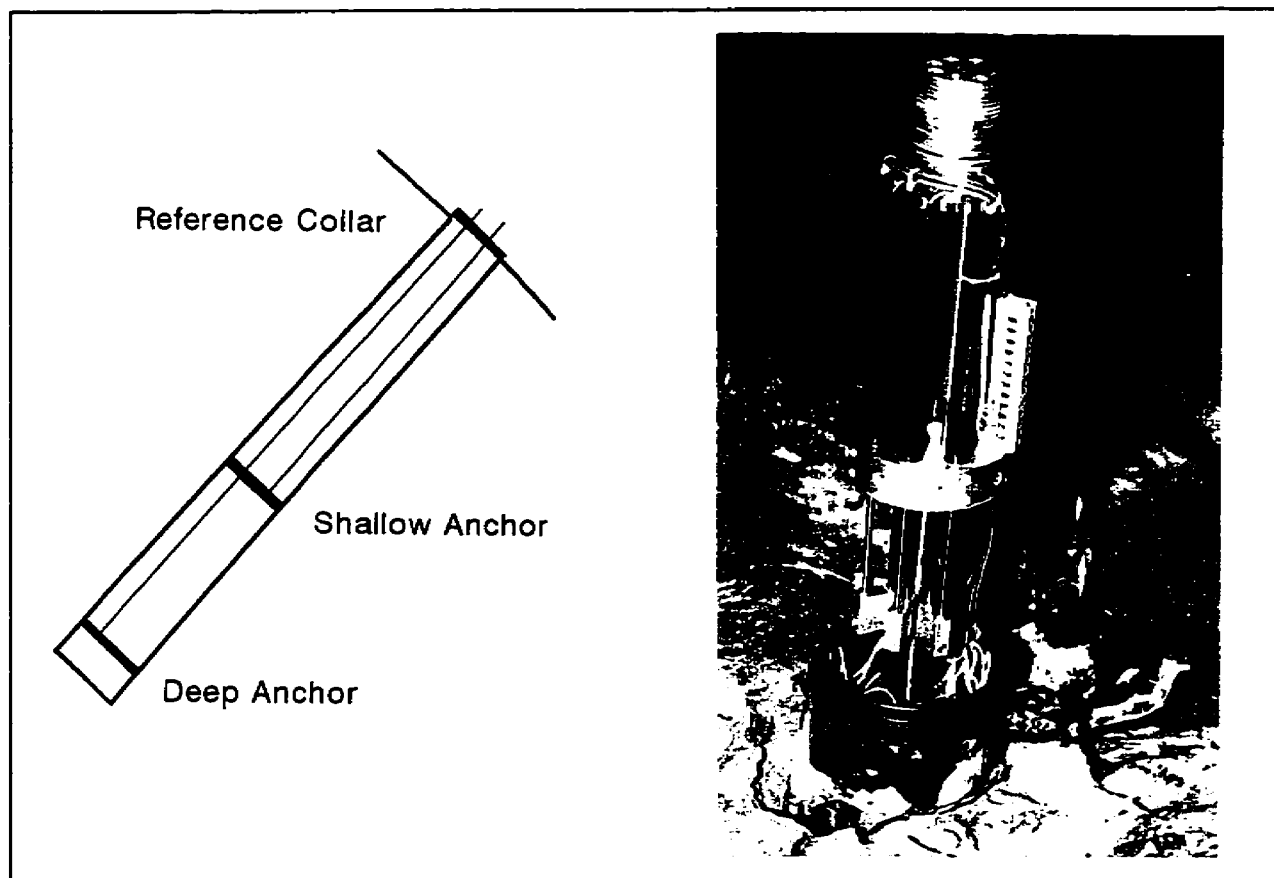


Figure 3.9 General layout of a borehole extensometer.

Photo 1 Typical multi-point extensometer collar

anchor points, and a rod or wire attached to the anchor to provide a reference between the collar and anchor.

Many types of borehole extensometers are available with the primary variation based on the use of a rod or a wire, and the anchor type. Measurements have been made relative to the extensometer collar. Both manual readings and automatic readings, through the use of linear voltage displacement transducers (LVDTs), have been obtained.

Data from extensometers are commonly plotted as change in distance, between anchor points and the collar, with time. Additional data should be provided to improve the value of this data. Pertinent mining activity should be shown on the graph and movement between anchors, as well as between each anchor and the collar, should be plotted. Deformation data can also be expressed as a strain value and then zones of elastic and non-elastic deformation can be estimated.

3.4 INTERPRETATION OF DEFORMATION

The interpretation of deformation data varies with the purpose for the monitoring. When used for safety, a maximum safe limit is commonly applied to the rate or to the magnitude of movement, and this critical value is generally based on past experience. At Detour Lake mine, a movement rate of more than 1mm per 24 hour period is set as the allowable limit for cut and fill mining after which the area is closed to access until the rate of movement diminishes (Pakalnis et al., 1993). There are no clear cut guidelines in hardrock mining which relate opening dimensions, overall rock mass strength and allowable stable deformation limits. Figure 3.6 gives measured deformations for civil structures which could be used as a deformation limit.

When instrumentation is used for calibrating design methods, measured deformations are

compared to estimated values. These deformation estimates may be based on elastic relaxation, plastic deformation, beam or plate bending, voussoir arching, empirical guidelines or some other deformation modelling technique. A back analysis can then be made comparing the measured movements to the movements expected from theory.

A hypothetical rock mass is described below so some of the various approaches for determining deformation can be compared. The rock mass has the following properties:

- Three orthogonal joint sets, each with a .5 metre spacing
- Tight, undulating, rough and clean joint surfaces
- Unconfined compressive strength of 150 MPa and a specific gravity of 2.7
- Dry conditions
- Hydrostatic in situ stresses at a magnitude of 5 MPa

Based on these input parameters and Tables 2.1 and 2.3, a Q of 33 and RMR value of 82 is determined. Based on the RMR value of 82 and Equation 2.2 relating RMR and elastic modulus E, a value of 64 GPa is estimated for the rock mass modulus. With these input parameters it is possible to estimate the maximum deformation based on the methods previously discussed. A 10 metre wide, 10 metre high by 200 metre long opening will be considered. The following techniques are considered for estimating deformations given the opening geometry and rock mass properties:

- Beam and plate theory (eq. 3.5)
- Voussoir arch theory (Figure 3.5)
- Kirsch equation (eq. 3.3)
- Map3D boundary element elastic model
- Barton's (1989) deformation versus span graph (Figure 3.6)

Beam and plate theory provide the same results for the given geometry because the

opening length is at least eight (8) times the opening width. For voussoir arch theory, the given geometry can be treated like a beam. The computer program, NTBEAM (Diederichs, 1994), has been used to calculate deformations. The program is based on the theory presented in Hutchinson and Diederichs, 1996 and summarized in Section 3.2.6. The Kirsch equation provides an estimate of the elastic deformation at the drift boundary, however, the rectangular drift cross section is treated like a circular cross section. The Map3d boundary element program was used to model the maximum elastic deformation in the back of the opening. Chapter 6.2 provides some details on the boundary element modelling approach. The empirical technique for estimating deformation consists of the graph presented in Section 3.2.7 (Figure 3.6). The deformation estimates for the case described, based on each of the approaches mentioned, is given below:

- Beam / Plate theory	.68 mm
- Voussoir arch theory	2.40 mm
- Kirsch equation	.23 mm
- Map3D modelling	.76 mm
- Barton's empirical graph	2 to 20 mm

This exercise shows a range of more than an order of magnitude for estimating maximum surface movement based on various modes of deformation. This significant discrepancy between methods of calculating deformation illustrates the need for field data.

3.5 SUMMARY

Initially, when a rock mass is influenced by the creation of an opening, the deformation response to the stress change is predominantly elastic. On a small scale, laboratory testing

provides a realistic estimate of the elastic properties of the rock. An elastic numerical model can then predict this scale and stage of deformation with some degree of confidence. On a larger scale, discontinuities act to reduce the rock mass modulus of elasticity and only rough estimates can be made of these elastic properties based on rock mass classification values and empirical data. This results in only crude approximations of elastic deformation at a mining scale. As the opening dimensions increase, non-elastic fracture opening and the movement of discrete blocks become the predominant sources of deformation.

There are many approaches to estimating deformation and the previous section showed the wide range in results that can be obtained depending on the deformation mechanism considered. Some of the approaches ignore the influence of the initial stress state on deformation and other techniques ignore the influence of discontinuities on deformation behaviour. It is obvious that both of these factors will have a significant influence on the movement around excavations in a deep mining environment. Although discontinuum modelling methods can account for both these factors, realistic methods for determining input parameters for these more advanced modelling techniques have not yet been developed (Hoek, 1994).

For each of the design techniques presented, the opening dimensions are directly related to the calculated deformation. The influence of geometry on deformation and stability is the main thrust of this research. The preceding discussion shows the importance of span on deformation. The next section looks in detail at opening span and hydraulic radius, which are the two terms most frequently used to assess the behaviour of underground stability.

CHAPTER 4

OPENING SPAN AND HYDRAULIC RADIUS

4.1 INTRODUCTION

Several empirical design techniques have been introduced which are based on opening surface span or hydraulic radius (Chapter 2). Support load was related to tunnel span as early as 1946 (Terzaghi) and many other similar design methods based on span followed (Section 2.2.1). The span term was used as an effective load determining parameter for tunnel backs. For given rock mass conditions, an arch was assumed above which the rock mass was considered to be self supporting. The dead weight of the material below this arch was assumed to be loading the support and the arch height was linearly related to the opening span. In many empirical civil tunnelling design methods, the tunnel span is the only factor that can be related to load on the rock mass. The span term can be effectively related to stability because opening span defines the distance between the major supporting elements of a tunnel back which are the tunnel side walls. The span term can be used to assess tunnel geometries because the ends of tunnels are typically far enough apart so that they do not provide support to the majority of the tunnel length.

In many mining cases, support from drift or stope ends cannot be ignored. When a rectangular opening length is less than three times the width, support provided from the opening ends is significant. Two way spanning of the opening must be considered and to assess this geometry a term called the hydraulic radius is used. The term hydraulic radius is sometimes referred to as shape factor and has been used in empirical design techniques since 1977 (Laubscher). The hydraulic radius (area/perimeter) was initially used in fluid dynamics to relate

fluid flow in square pipes to that in circular pipes. This chapter investigates why this term, which has been borrowed from fluid dynamics, should have any connection with underground rock stability.

4.2 GEOMETRICAL PROPERTIES OF HYDRAULIC RADIUS

The hydraulic radius term has an interesting mathematical property which relates it to span. Consider an opening surface with a span of S metres and a length of L metres. As the length increases towards infinity, for a constant span, the hydraulic radius converges to half the span, as shown in Equation 4.1.

$$HR = \frac{SL}{2(S+L)} \dots\dots as L \Rightarrow \infty \dots\dots = \frac{S}{2} \left(\frac{\infty}{S+\infty} \right) \approx \frac{S}{2} \quad (\text{Eq. 4.1})$$

Figure 4.1 shows how the hydraulic radius of a surface approaches half the span as the aspect ratio increases (length to span ratio). When an opening length is nine times the span, the hydraulic radius is within 90% of its maximum value of half the span. This indicates that the ends of an opening are still exerting a significant influence on the opening stability design when the length is nine times the span. The arch height of the rock mass requiring support has been related to span for tunnel geometries (Section 2.2.1). The span term cannot assess the influence of end support for short opening lengths.

Hydraulic radius can also be expressed as a distance from supporting abutments, calculated from the centre of a surface. Consider a rectangular opening of span 'a' metres and length 'b' metres. From the centre of the rectangle, the distance to each abutment is a/2 or b/2 metres away. Figure 4.2 shows the derivation of Equation 4.2 which expresses hydraulic radius as a function of distance to supporting abutments. This form of expressing hydraulic

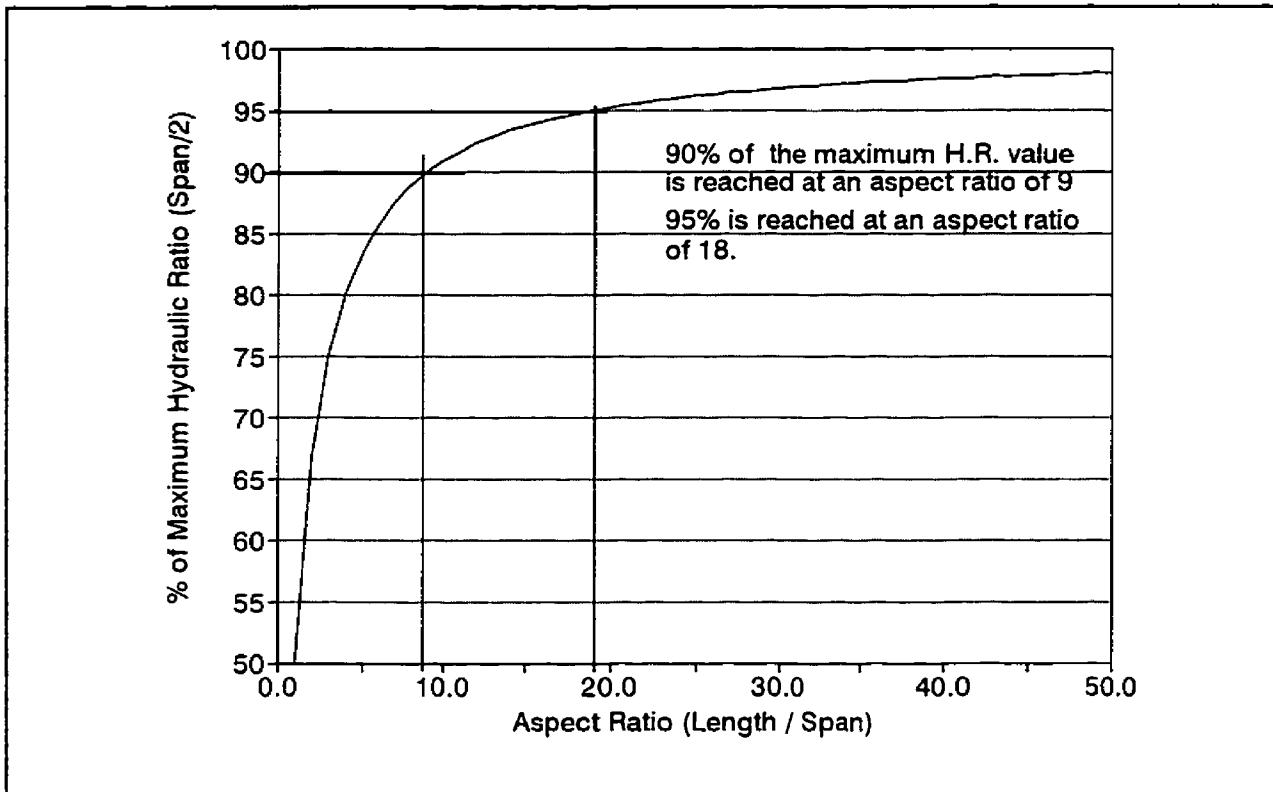


Figure 4.1 Influence of surface aspect ratio on hydraulic ratio.

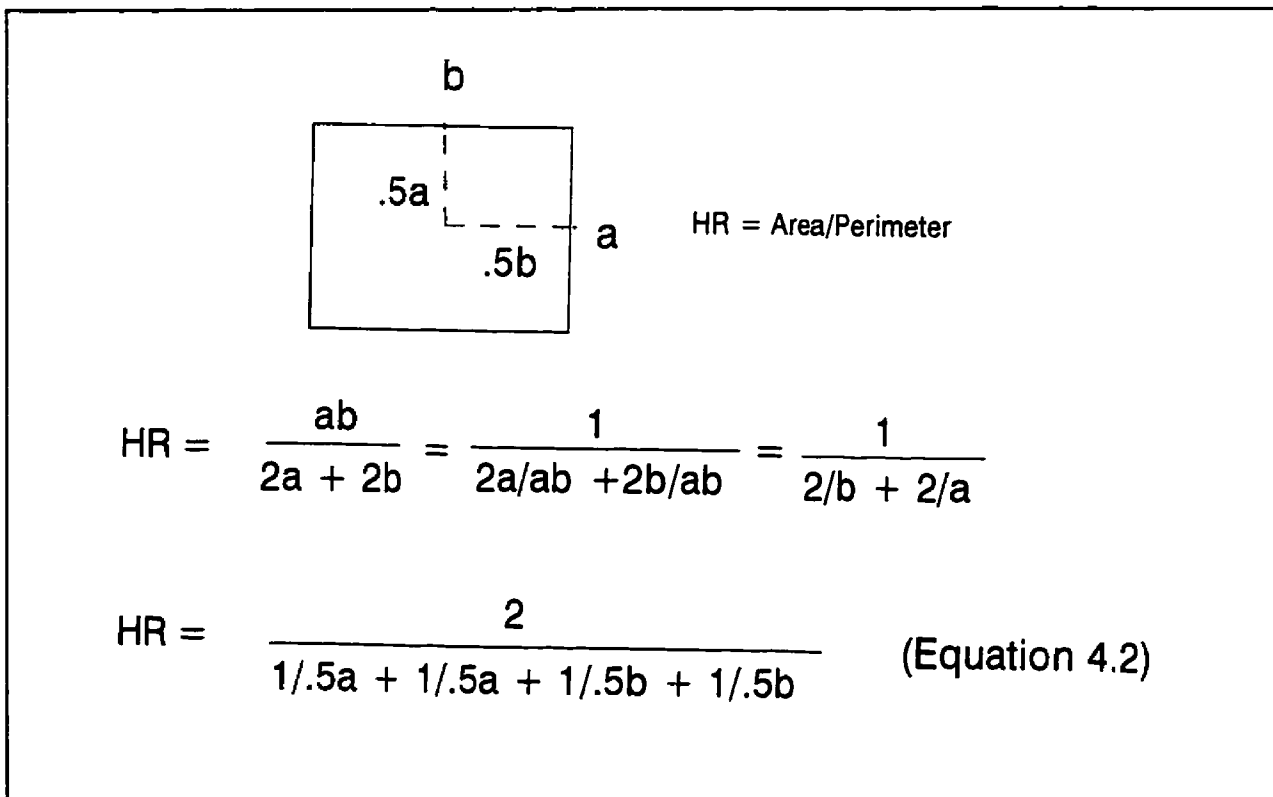


Figure 4.2 Hydraulic radius expressed as a distance to supporting abutments.

radius shows intuitively why it can be related to surface stability, far more clearly than expressing it as area divided by perimeter.

One of the main purposes of the hydraulic radius term is to allow the comparison of various surface excavation shapes. Equation 4.2 can be expressed in a more general form to allow a factor for the number of sides to the surface (Equation 4.3).

$$HR = \frac{.5s}{\sum_{n=1}^s \frac{1}{d_n}} \quad (\text{Eq. 4.3})$$

Where: s = Number of sides

d_n = Minimum distance to each side

Figure 4.3 shows the hydraulic radius calculated for various shaped openings, calculated based on area over perimeter and based on Equation 4.3.

4.3 DRAWBACKS TO THE HYDRAULIC RADIUS PARAMETER

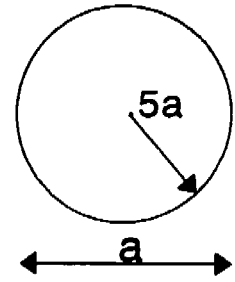
Using hydraulic radius allows us to compare the inherent stability of different opening geometries. It has proven to be an effective, empirically validated technique. There are, however, some shortcomings. Figure 4.3 shows that with similar dimensions, a circle and a square have the same hydraulic radii, as do an ellipse and a rectangle. One would intuitively think that the extra surface area of a square over a circle, or rectangle over an ellipse, would be detrimental to stability.

For a rectangular opening with a given span, the length is 9 times the span before the hydraulic radius is equal to 90% of its maximum. This implies the ends of a drift apply significant support to the centre, to a distance of 4.5 times the span. Brady & Brown (1995)

Circle

$$\text{H.R.} = \frac{\pi(.5a)^2}{2\pi(.5a)} = .25a$$

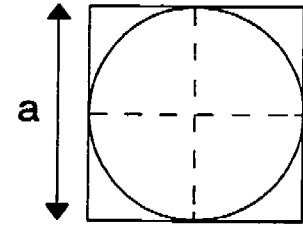
$$= \text{Area/Perimeter}$$



Square (4 sides)

$$\text{H.R.} = \frac{a^2}{4a} = .25a$$

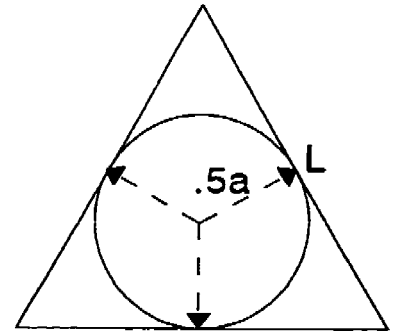
$$\text{H.R.} = \frac{\text{or } (4)(.5)}{\frac{1}{.5a} + \frac{1}{.5a} + \frac{1}{.5a} + \frac{1}{.5a}} = \frac{2(.5a)}{4} = .25a$$



Triangle (3 sides the same length)

$$\text{H.R.} = \frac{.5L^2 \sin 60^\circ}{3L} = \text{Area/Perimeter}$$

$$\text{H.R.} = \frac{\text{or } 3(.5)}{\frac{1}{.5a} + \frac{1}{.5a} + \frac{1}{.5a}} = \frac{(1.5)(.5a)}{3} = .25a$$

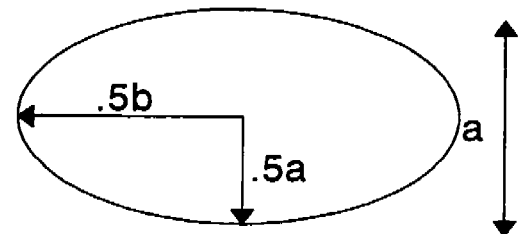


Ellipse

$$\text{H.R.} = \frac{(\pi ab)}{(2\pi(a+b))} \text{ or}$$

$$\text{H.R.} = \frac{(4)(.5)}{\frac{1}{.5a} + \frac{1}{.5a} + \frac{1}{.5b} + \frac{1}{.5b}} = \frac{2(.5a + .5b)}{(a + b)}$$

$$= \frac{axb}{2(a + b)}$$



Rectangle (4 sides)

$$\text{H.R.} = \frac{axb}{2(a+b)} \text{ or}$$

$$\text{H.R.} = \frac{(4)(.5)}{\frac{1}{.5a} + \frac{1}{.5a} + \frac{1}{.5b} + \frac{1}{.5b}}$$

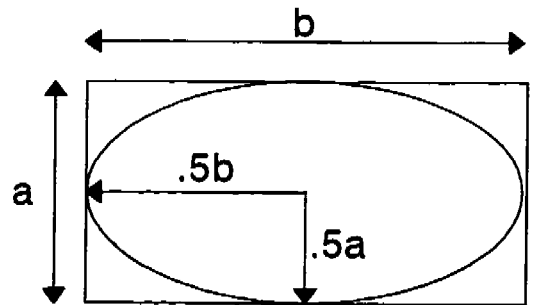


Figure 4.3 Hydraulic radii calculated for various surface geometries based on area divided by perimeter and equation 4.3.

suggest that the restraint offered by the proximity of the face in an advancing tunnel is negligible at a distance of 1.5 tunnel diameters away. This suggests that the hydraulic radius of a rectangular back should approach its maximum when the length is approximately 3 times the span as opposed to 9 times. When considering various opening geometries, it is worth questioning why a 10m by 100m drift should have the same stability as an 18.2m by 18.2m back.

Determining a hydraulic radius for an irregular mining geometry does present some difficulties. In general, the mining surface is represented by the largest possible four sided geometry which does not cross the rock abutments. In some cases the mining surface may be represented by a shape with more than four sides, though generally a four sided geometry will result in the largest representative hydraulic radius. More than one shape may be tried, as shown in Figure 4.4. The hydraulic radius term does represent an improvement over the span term for assessing mining geometries. Irregular mining geometries with the presence of brows, raises, post pillars and irregular wall geometries, however, cannot be effectively represented.

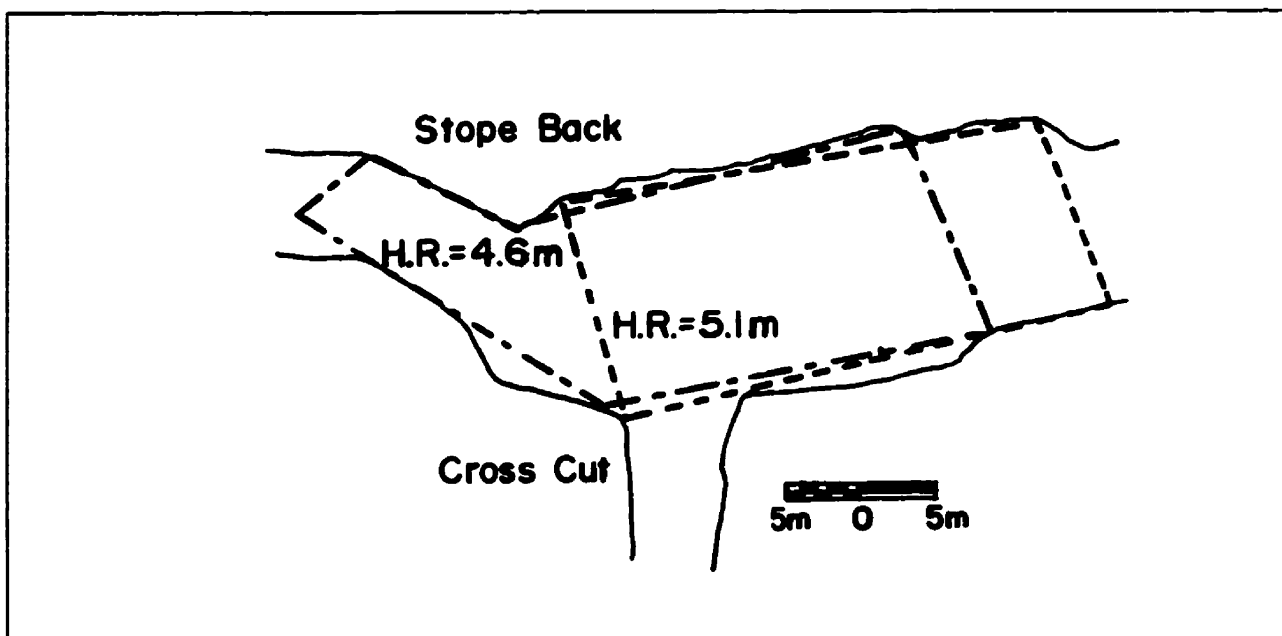


Figure 4.4 An irregular stope back showing two estimates of hydraulic radius.

4.4 SUMMARY

This section has shown the similarity between the span and hydraulic radius factors used for empirical design in the civil and mining industries. Their similarities and the wide spread application of both factors in civil and mining engineering stability assessments add credibility to their effectiveness. A more intuitive technique has been given for calculating hydraulic radius which relates it to distance from supporting abutments.

Some serious drawbacks have been highlighted in the application of hydraulic radius for determining surface stability. The next chapter introduces a new term for relating surface geometry to behaviour.

RADIUS FACTOR AND EFFECTIVE RADIUS FACTOR

5.1 INTRODUCTION

This section introduces two terms to be used for quantifying opening geometry for estimating stability and deformation. Much of the following section on radius factor and effective radius factor is taken from a paper on the subject by Milne, Pakalnis and Lunder (1996).

The previous section discussed the hydraulic radius factor, which is frequently used to quantify surface geometry for assessing underground stability. Hydraulic radius, as calculated in equation 4.2 can also be expressed as follows:

$$HR = \frac{ab}{2(a+b)} = \frac{2}{\left(\frac{1}{.5a} + \frac{1}{.5b} + \frac{1}{.5a} + \frac{1}{.5b}\right)} = \left[\frac{.5}{\frac{1}{4}\left(\frac{1}{.5a} + \frac{1}{.5b} + \frac{1}{.5a} + \frac{1}{.5b}\right)}\right] \quad (\text{Eq. 5.1})$$

where a and b are the sides of a rectangle and .5a and .5b are the minimum distances to the sides of the rectangle, measured from the centre.

The second factor in equation 5.1 is the average minimum abutment distance.

$$\frac{1}{\frac{1}{4}\left(\frac{1}{.5a} + \frac{1}{.5b} + \frac{1}{.5a} + \frac{1}{.5b}\right)} = \text{Average Minimum Abutment Distance} \quad (\text{Eq. 5.2})$$

This factor equals two times the hydraulic radius. This form of an average is called a harmonic average or harmonic mean. It was suggested (McGaughey, 1994) that this approximation of the average distance to abutments could be better quantified by taking distance measurements to abutments at small angular increments. From the centre of a surface, the following equation

gives the harmonic average radius, R_h , or average distance to the abutments.

$$\frac{1}{R_h} = \frac{1}{n} \sum_{\theta=1}^n \frac{1}{r_\theta} \quad \therefore \quad R_h = \frac{1}{\frac{1}{n} \sum_{\theta=1}^n \frac{1}{r_\theta}} \approx \frac{1}{\frac{1}{4} \left(\frac{1}{.5a} + \frac{1}{.5b} + \frac{1}{.5a} + \frac{1}{.5b} \right)} \quad (\text{Eq. 5.3})$$

Where r_θ = Distance from the surface centre to the abutments at angle θ and n = Number of rays measured to the surface edge

With the introduction of the term harmonic average radius R_h , a much more accurate assessment of surface geometry can be made. The R_h parameter can be determined from the centre of a surface by averaging the reciprocal of the distance to the abutments at very small angular increments. From equations 5.1 and 5.3, $R_h/2$ is similar to the hydraulic radius. A new parameter called the radius factor (RF) is proposed as a replacement to hydraulic radius. This new term is simply half the harmonic average radius of a surface, measured from the surface centre:

$$RF = \frac{.5}{\frac{1}{n} \sum_{\theta=1}^n \frac{1}{r_\theta}} = .5R_h \quad (\text{Eq. 5.4})$$

It is interesting to note that a circle with a diameter of 10m has the same hydraulic radius as a 10m by 10m square. For a circular surface the RF is equal to the HR. For a square, the RF is 1.1 times the HR, due to the increased distance to the abutment in the corners. The radius factor, or half the harmonic radius, takes the harmonic average radius of a surface and treats it like an equivalent circular opening of radius R_h . The radius factor, calculated at the surface centre, does not correspond directly with hydraulic radius, since it accounts for more complex geometries.

The hydraulic radius (HR) of an infinitely long rectangle (tunnel) with span 'a', is twice the HR of a square with sides 'a'. The radius factor (RF) does not vary in the same fashion.

A tunnel of span 'a' has a RF value of $\sqrt{2}$ times that for a square opening with sides 'a'. As previously mentioned, when the length of an opening is 18 times the span, the HR value reaches 95% of its maximum for a given span. The RF value, on the other hand, reaches 95% of its maximum value when the length is three times the span, which agrees with the suggested zone of increased support provided by the end of a drift based on modelled elastic deformation (Brady and Brown, 1985). Figure 5.1 shows the change in hydraulic radius and radius factor, with lengthening rectangular geometries. For rectangular geometries, both HR and RF can be expressed in terms of the length and span of the surface (Equations 5.4 and 5.5)

$$HR = .5\left(\frac{L \times S}{L + S}\right) \quad (\text{Eq. 5.5})$$

$$RF = \frac{\pi}{8} \left(\frac{L \times S}{\sqrt{L^2 + S^2}} \right) \quad (\text{Eq. 5.6})$$

The radius factor calculation or harmonic radius can be determined at any point on a surface. The maximum value of RF and R_h is determined at the centre of a surface and the value drops to zero at the abutments. To avoid confusion, for a given surface all values of RF less than the maximum will be referred to as effective radius factor values (ERF). For irregular geometries where the surface centre cannot easily be determined, the maximum ERF value is taken as the RF value. Figure 5.2 shows the same stope back as was given in Figure 4.4 with the RF value and an ERF value calculated. Intuitively, surface stability is at a maximum near the abutments and this is reflected by the harmonic radius and radius factor values. Appendix B discusses the mathematical derivation of the ERF term, (Hausch, 1995).

A program has been written by P. Lunder at the Noranda Technology Centre (NTC) which automatically calculates radius factor values for any point on a surface, or on a grid pattern. The program has been written to run within AutoCad (Autodesk, Inc.). It recognizes

100 x 100 m		H.R. = 25.0 R.F. = 27.8
100 x 150 m		H.R. = 30.0 R.F. = 32.7
100 x 200 m		H.R. = 33.3 R.F. = 35.1
100 x 300 m		H.R. = 37.5 R.F. = 37.3
100 x 500 m		H.R. = 41.7 R.F. = 38.5
100 x Inf.	+	H.R. = 50.0 R.F. = 39.3

Figure 5.1 Variation in hydraulic radius and radius factor for a constant 100 metre span and increasing length.

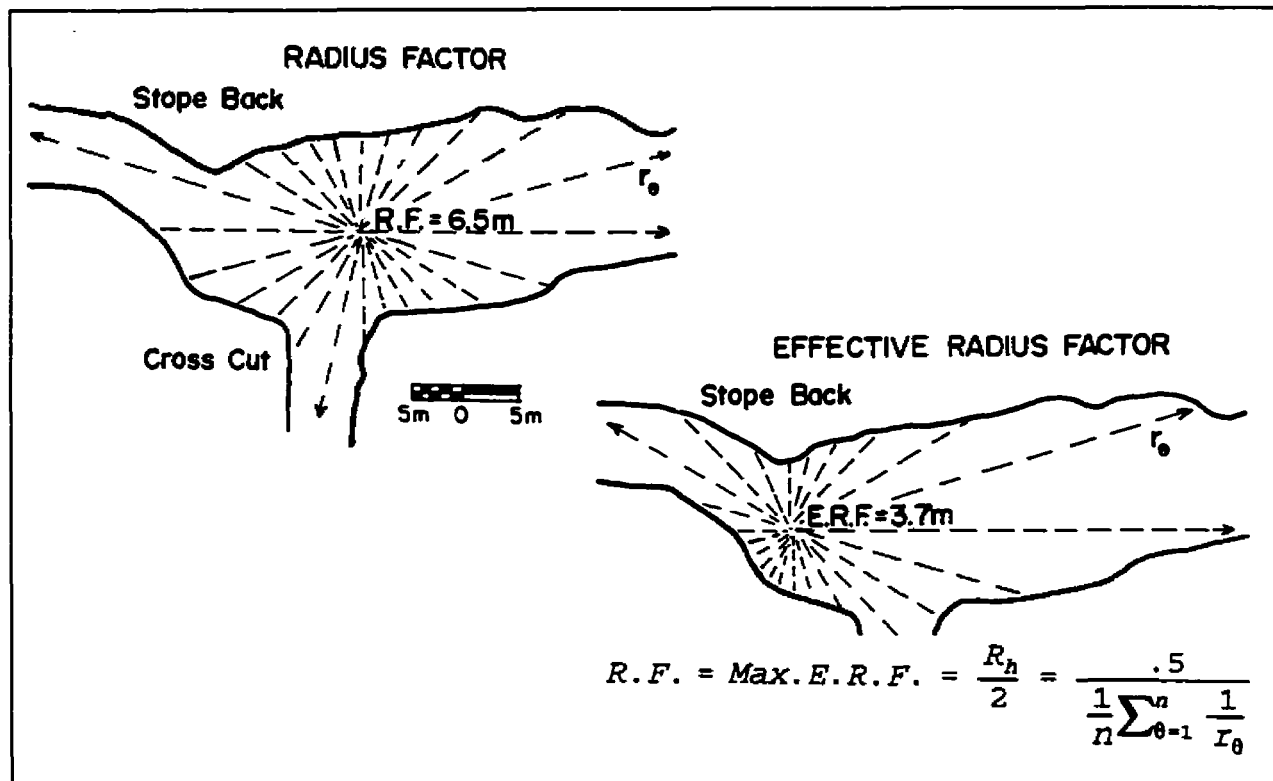


Figure 5.2 An irregular stope back showing the calculated radius factor value and an effective radius factor value (After Milne et al., 1996).

the presence of pillars, raises or brows and calculates the RF value using any angular increment desired for determining the average harmonic radius. Appendix C lists the program.

The next section looks at the geometrical significance of the radius factor term.

5.2 GEOMETRICAL PROPERTIES OF THE EFFECTIVE RADIUS FACTOR TERM

One of the primary goals of this research is to relate the stability and deformation of an underground surface to the radius factor and effective radius factor terms. Before attempting to use this term for assessing underground stability and deformation in hard rock mines, the geometrical significance of this term should first be investigated.

Figure 5.3 shows how the harmonic radius, which is twice the ERF value, would be calculated for a given block of rock located anywhere in the back of an opening. Lines of support are measured, at small angular increments, from a point in the back to the abutments. As the calculation point moves closer to the abutments, the shorter lines of support result in the calculation of smaller ERF values reflecting the higher degree of stability near supporting surfaces and abutments. At the abutments, the ERF value is zero.

Figure 5.4 shows how the RF and ERF values are influenced by raises and pillars which cannot easily be assessed by the hydraulic radius term. Any rays which intersect a pillar, treat the pillar as an abutment. For any rays which intersect a raise, the distance to the supporting abutment is treated as being of infinite length. The ERF value should not be calculated less than the average rock mass block size away from a raise. If the ERF value is calculated at the boundary of a raise, slot or even a drill hole, the results would be the same, since in each case 180° of rays would intersect the hole at the boundary. Calculating the ERF value at least one block size away from a slot or raise adds a realistic element of scale dependency. The following

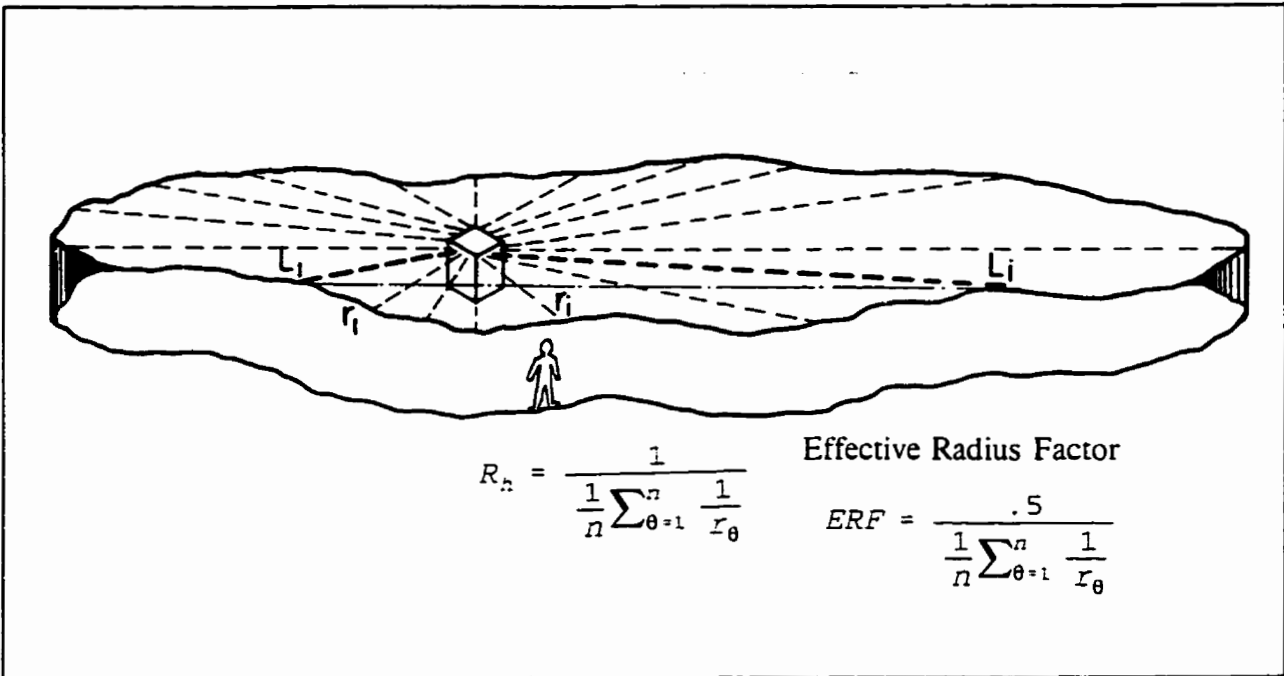


Figure 5.3 Rays used for calculating the harmonic radius and effective radius factor.

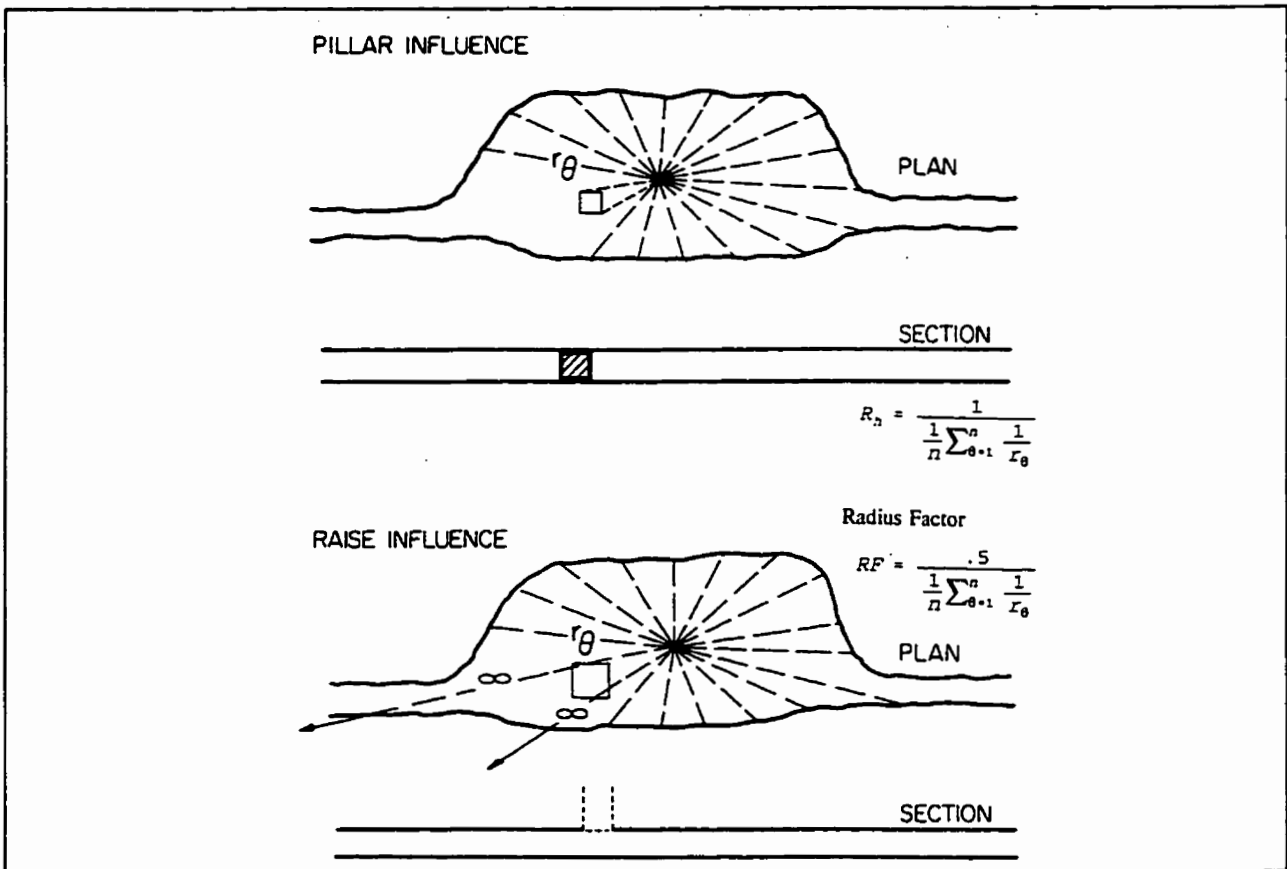


Figure 5.4 Influence of pillars and raises on the determination of the radius factor of a surface (From Milne et al., 1996).

sections look at how ERF values vary across a two dimensional opening (tunnel) and simplified three dimensional openings.

5.2.1 Significance of the Effective Radius Factor for One Way Spanning

To initially simplify the effective radius factor term, a tunnel case of one way spanning is considered. Figure 5.5 shows a 200 metre long and ten (10) metre wide tunnel. ERF values are determined along the span of the tunnel 100 metres from each end of the tunnel, so tunnel end effects are insignificant. The maximum ERF value, or radius factor, occurs at centre span and equals 3.93 metres. The ERF values decrease to zero at each abutment. The calculated ERF values along the tunnel span are shown as a height above the tunnel corresponding to a potential arch (Fig. 5.5). This potential arch corresponding to ERF values equals the equation of a parabola, as shown in Figure 5.5.

The parabola has a great deal of application in rock mechanics. Voussoir arch theory is one of the earlier methods of explaining the behaviour of a horizontally jointed rock back (Section 2.3.6). This theory assumes that a supporting lateral load is transmitted through the rock following a parabolic arch (Brady and Brown, 1985). Below this arch the rock mass is loaded under dead weight only and may be unstable.

5.2.2 Significance of the Effective Radius Factor for Two Way Spanning

Openings with similar lengths and widths are common in mining so the influence of two way spanning on ERF values must be considered. The simplest two way spanning geometry corresponds to a circular surface and this geometry will be initially considered. As in the previous section, ERF values on the surface will be represented as a height of potential arching. In the case of the tunnel, the ERF values could be represented above the surface by a parabola.

TUNNEL PLAN VIEW

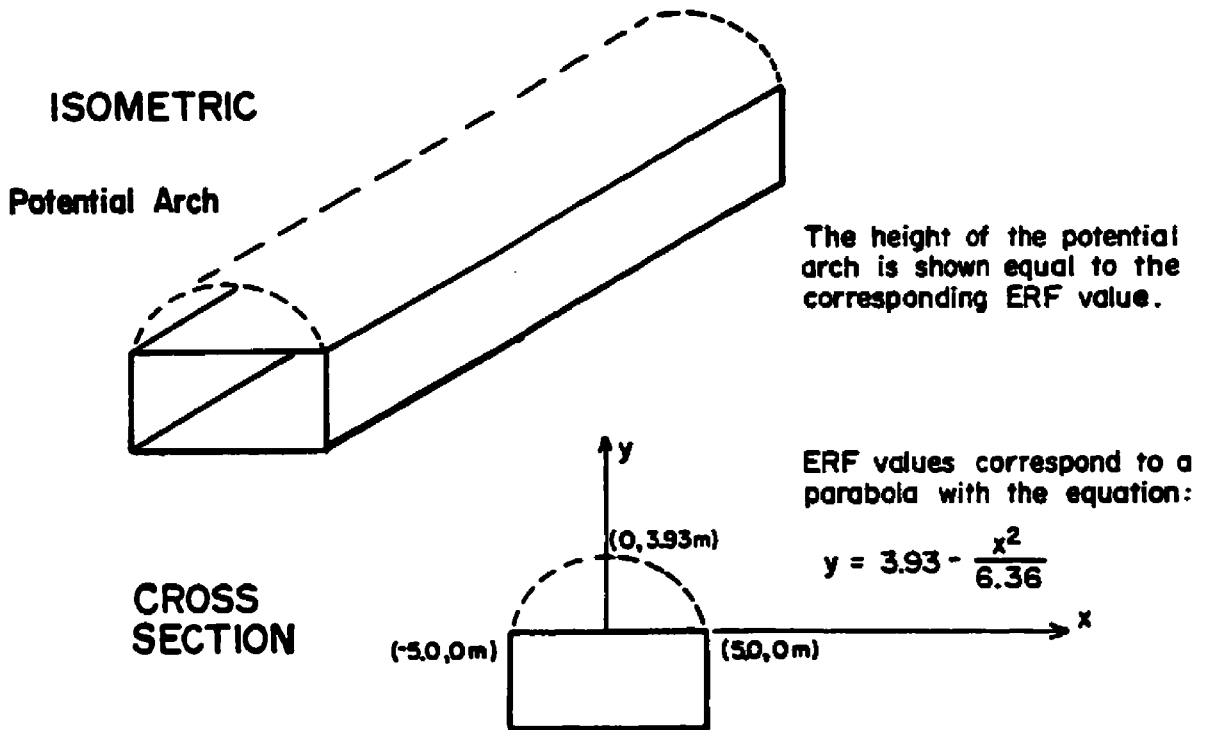
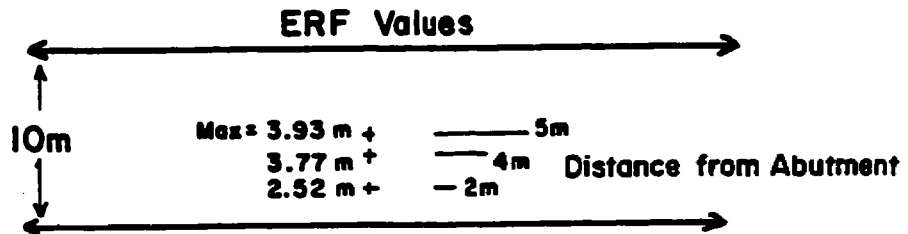
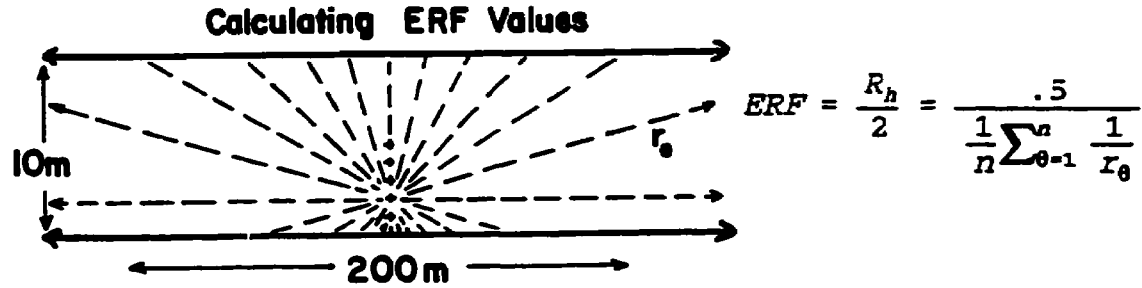


Figure 5.5 ERF values across a tunnel represented as a height of potential arching.

For the case of a circular surface, the arch generated by ERF values will be compared to a surface defined by the equation of a paraboloid. Figure 5.6 shows plan and isometric views of ERF values above a circle with a 50m radius. Figure 5.7 shows a graph of these values plotted against the values for a paraboloid. The paraboloid has been normalized to coincide to the maximum and minimum ERF values. The general equation for a paraboloid is given below (Thomas and Finney, 1984):

$$\frac{x^2}{a^2} + \frac{y^2}{b^2} = \frac{z}{c} \quad (\text{Eq. 5.7})$$

Where a, b and c are constants

A close correlation between the surface defined by a paraboloid and that defined by ERF values is shown in Figure 5.7. It has long been recognized that cavities in rock often remain stable if they have assumed shapes of domes or arches (Denkhaus, 1964) and a paraboloid can be used to represent a domed shape.

If a more realistic rectangular surface geometry is considered, the ERF values cannot be defined as a simple geometrical surface. However, 2-D slices through the surface can be investigated. A 20m by 50m rectangular surface is considered and the ERF contours are shown in Figure 5.8. The ERF values can again be related to a height of potential arching and the general shape of this arch is similar to the top of a loaf of bread (Fig. 5.8). Figure 5.9 shows a close correlation between the ERF profile across the minimum span and a parabola, normalized to zero at the surface edge and set to the maximum at the centre. Along the maximum span, however, a much poorer correlation is observed because of the ERF values are controlled by the closer abutments paralleling the maximum span.

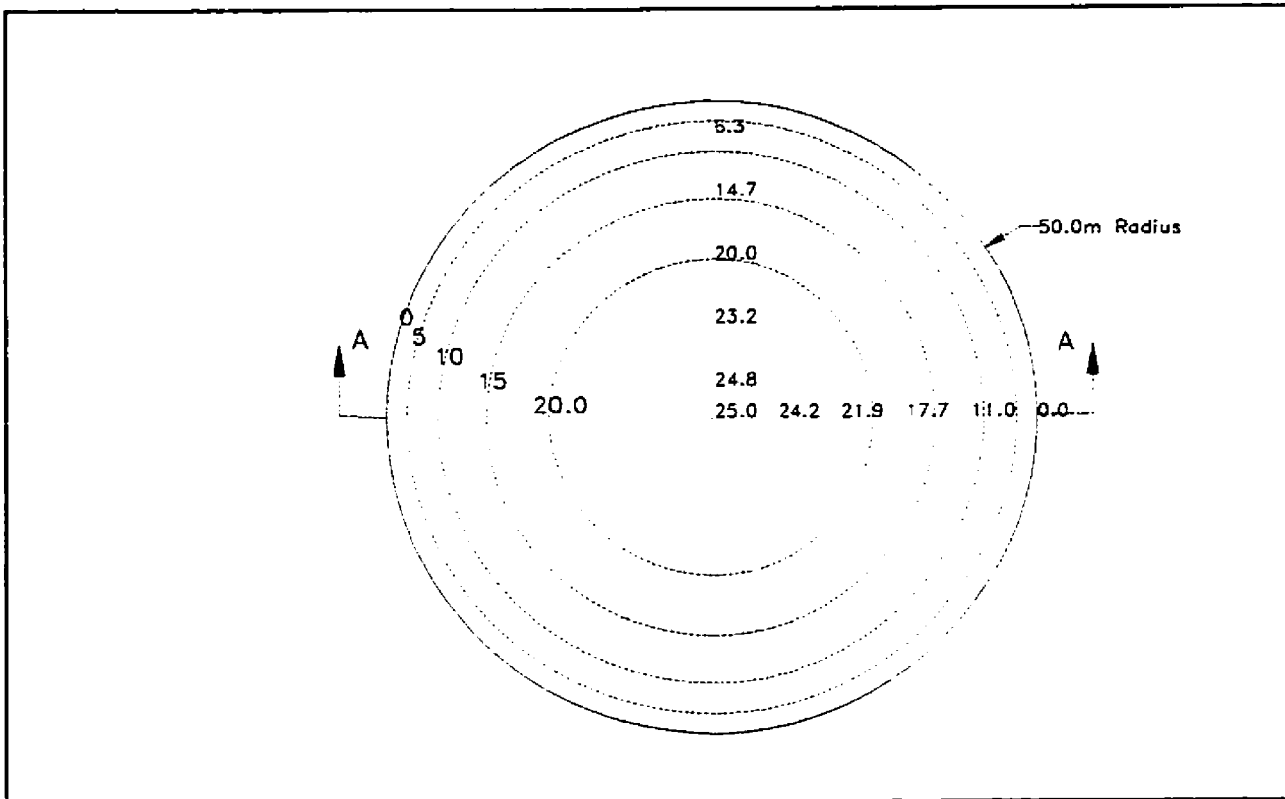


Figure 5.6 Effective radius factor values contoured for a circular surface.

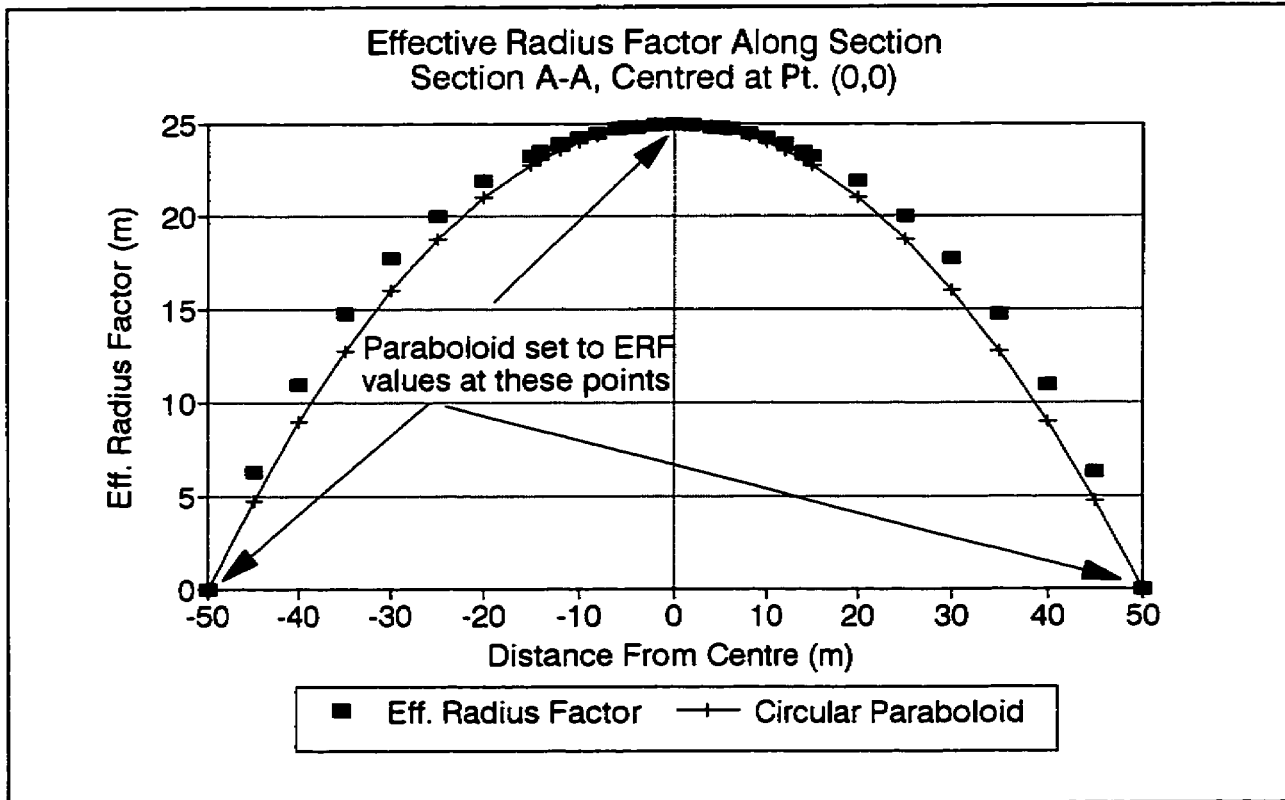


Figure 5.7 Graph showing the surface of an elliptical paraboloid versus the ERF surface.

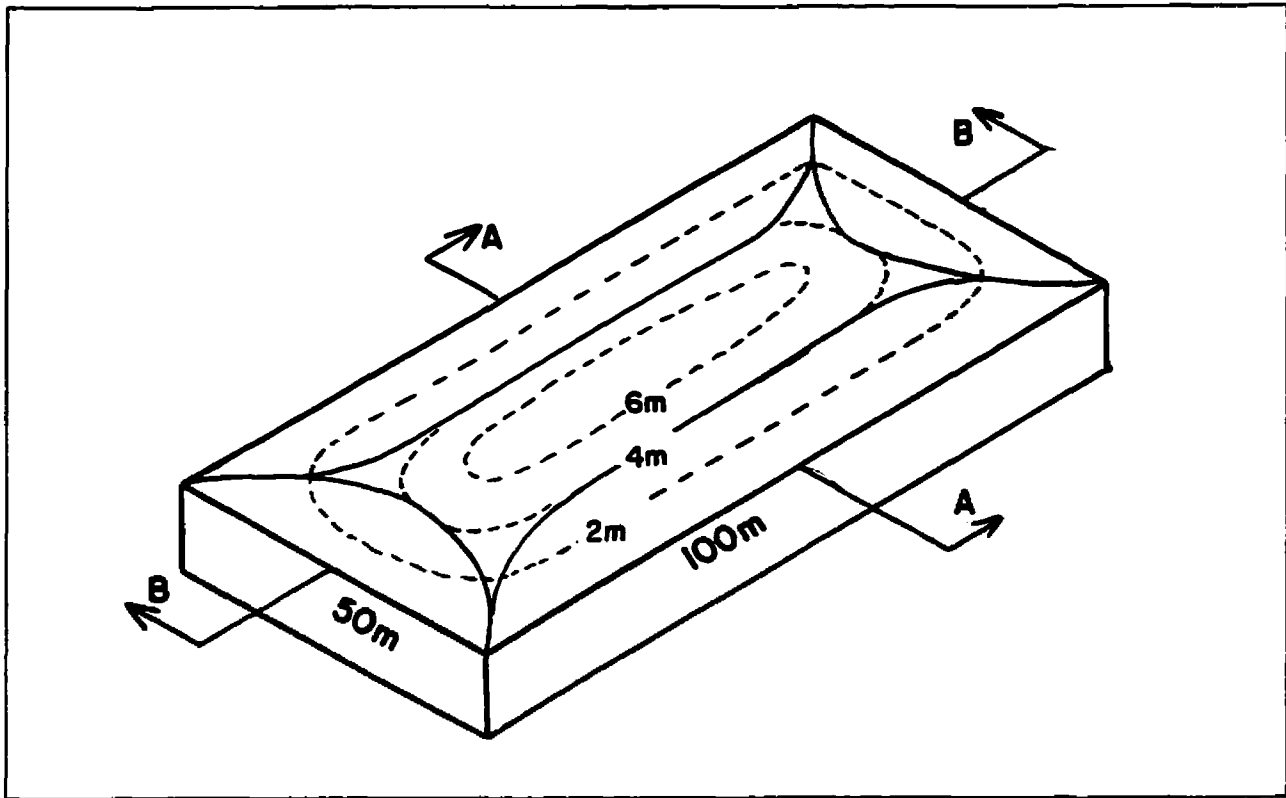


Figure 5.8 Effective radius factor values contoured for a rectangular surface.

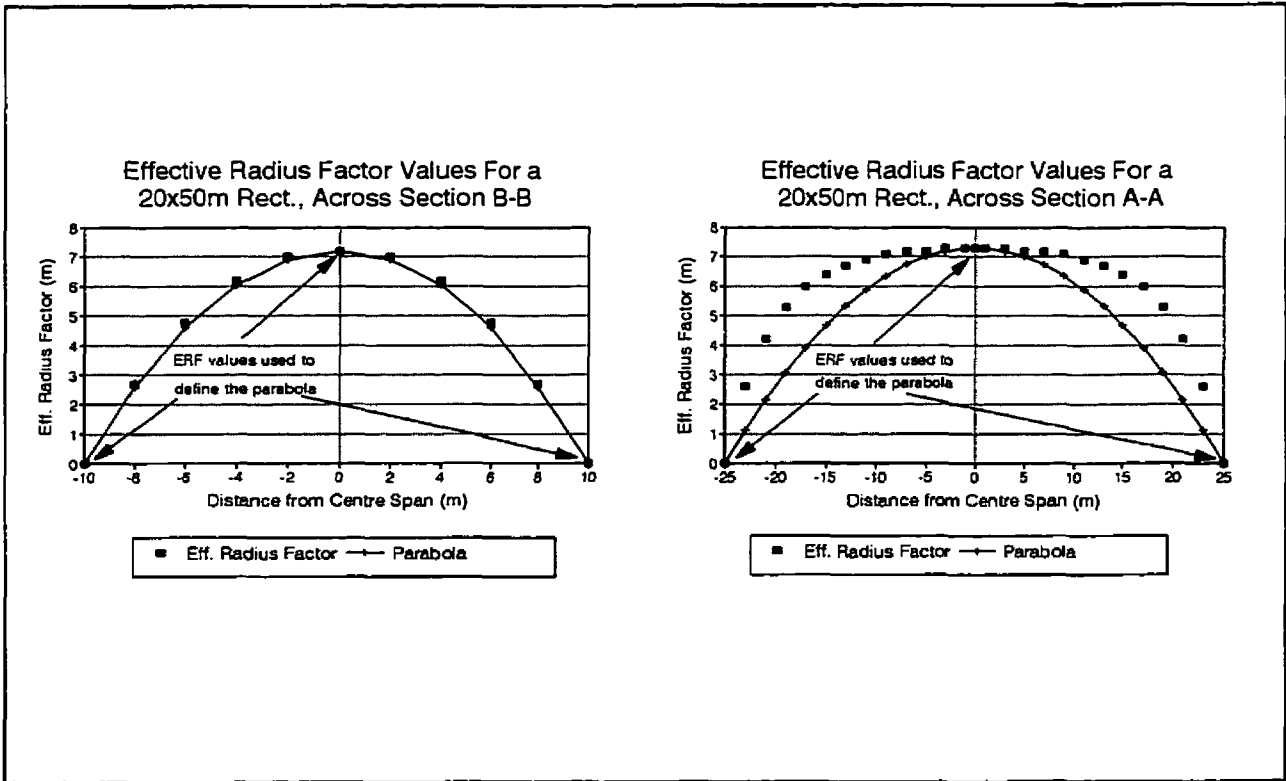


Figure 5.9 Graphs showing the effective radius factor values across the minimum and maximum spans versus a curve for a parabola set to the maximum and minimum ERF values.

5.4 SUMMARY

Three new parameters, harmonic radius, radius factor and effective radius factor have been introduced in this chapter to assist in quantifying underground surface geometry. The harmonic radius has been defined as an average distance to supporting abutments from any point on a surface, measured at small angular increments (eq. 5.3). Underground surfaces are often supported by pillars or cut by raises or brows. The pillars are treated like abutments and abutments located behind a raise or brow are taken as infinitely distant (Fig. 5.4). Half the harmonic radius value of a surface, determined from the centre of a surface, has been defined as the surface radius factor and, for simple geometries, corresponds closely with hydraulic radius. The effective radius factor can be determined from any point on a surface and equals half the harmonic radius at that point. The maximum ERF value equals the RF value for a given surface. Effective radius factor values can be contoured for any surface geometry. For a tunnel back these contour values, if assumed to equal a height of potential arching above a surface, correspond exactly to the equation of a parabola. For a rectangular geometry the ERF values across the minimum span coincide closely to the shape of a parabola.

The geometrical properties of these new parameters have been introduced and the rest of this thesis is devoted to determining if the behaviour of underground surfaces can be related to ERF and RF values. Initially, theoretical and empirical data on surface deformations will be compared to ERF values to determine if trends exist (Chapters 6 and 7). An empirical design technique based on surface hydraulic radius will then be investigated to determine if it can be recalibrated to radius factor values. Measurements of hanging wall slough will be assessed to determine if the measured depth of slough corresponds to surface ERF values. Figure 5.10 summarizes the proposed applications for ERF and RF values in the rest of this document. The

ERF And RF APPLICATIONS

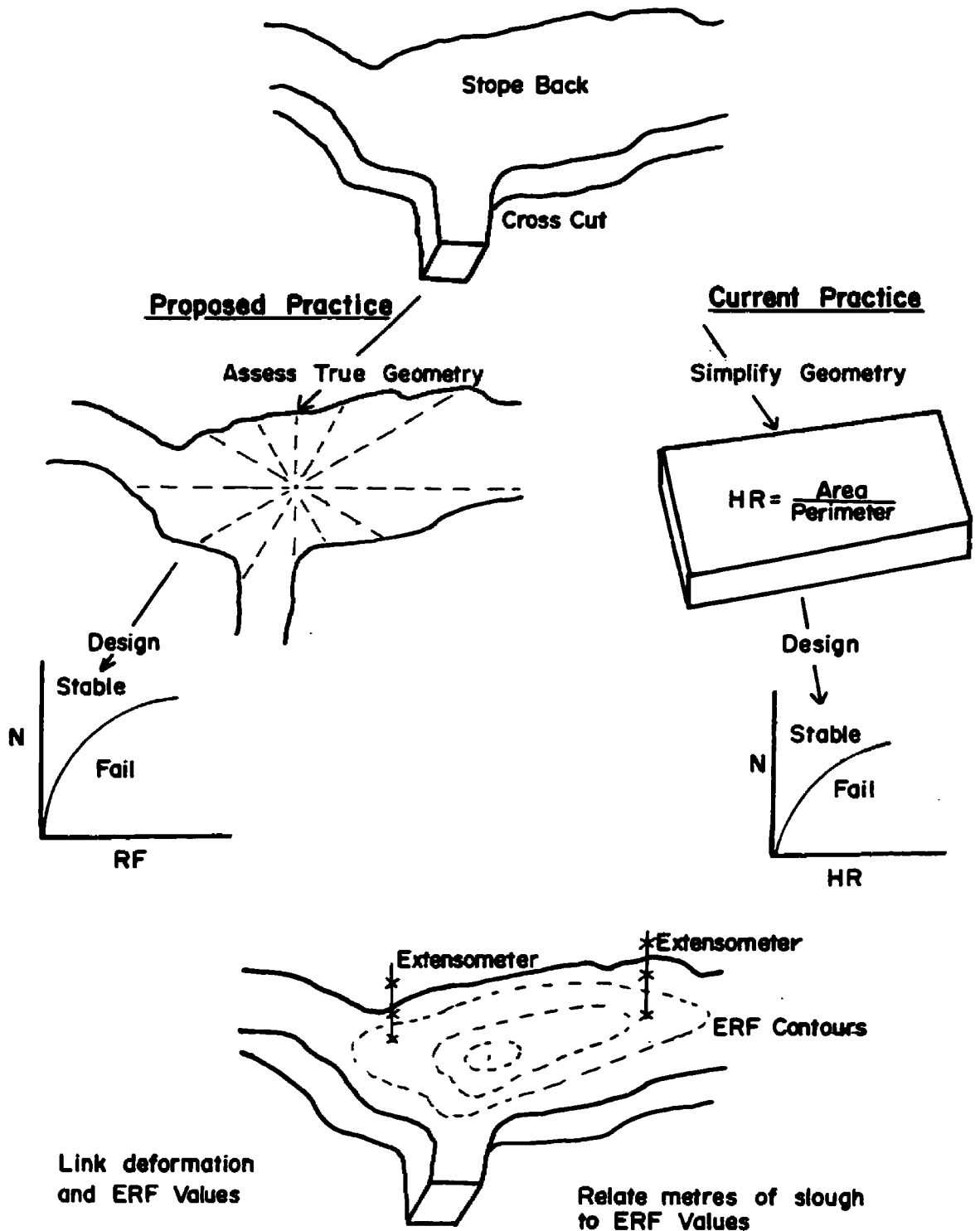


Figure 5.10 Summary of the proposed applications of the RF and ERF parameters.

next section investigates the ERF values above the surface of an underground opening and the modelled linear elastic deformation.

CHAPTER 6

ELASTIC DEFORMATION AND EFFECTIVE RADIUS FACTOR VALUE

6.1 INTRODUCTION

Initial surface deformations are elastic after the creation of an opening underground. This chapter considers this initial deformation and compares the numerically modelled distribution of deformation on a surface to the distribution of effective radius factor (ERF) values. Generally, when deformations around an excavation are modelled numerically, maximum movements occur at the centre of a surface and decrease towards the abutments. The distribution of ERF values on a surface follow the same trend. Figure 6.1 shows the general trend of ERF values on a two, three and four sided surface, represented as a downward deflection.

Before comparing modelled deformations around openings to ERF values, it is useful to first look at how changes in stress around an opening cause strain and resulting deformation on a surface. Change in strain $\Delta\epsilon_x$ is directly related to change in stress $\Delta\sigma_x$. Strain, acting over a given length, L , causes deformation (U_x), $\{U_x = L(\Delta\epsilon_x)\}$ (Eq. 3.1). For a 3-dimensional case where stress is changing, the change in strain, $\Delta\epsilon_x$, in a direction of principal stress change is given by equation 3.2:

$$\Delta\epsilon_x = \frac{1}{E}(\Delta\sigma_x - \nu(\Delta\sigma_y + \Delta\sigma_z)) \quad (\text{Eq. 3.2})$$

where ν = Poisson's ratio and E , Young's modulus and $\Delta\sigma_x$, $\Delta\sigma_y$ and $\Delta\sigma_z$ = Magnitude of principal stress change.

To simplify the complex interaction of stresses around underground openings, induced

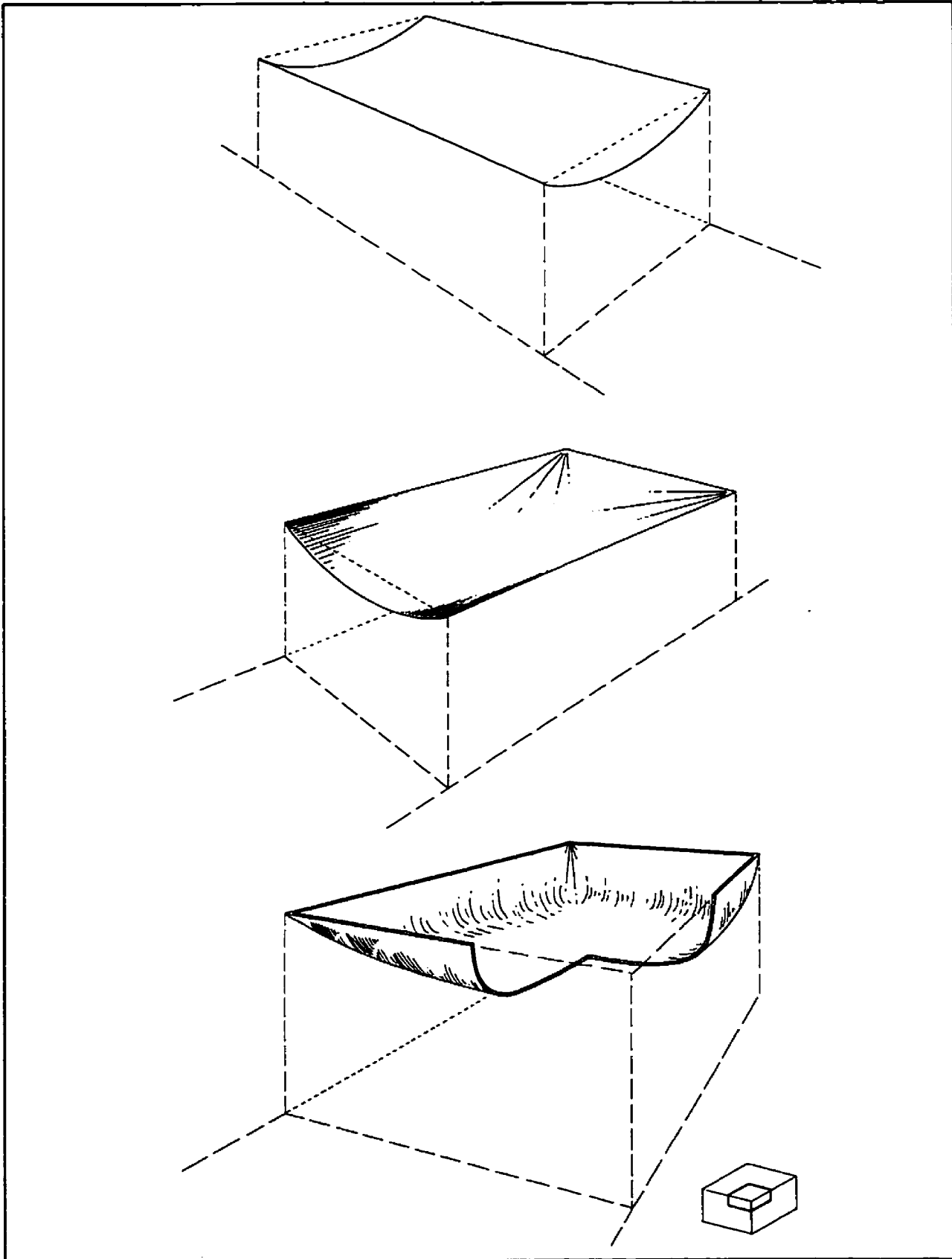


Figure 6.1 ERF values on a 2, 3 and 4 sided surface represented as a downward deflection.

stresses around a simple 2-D geometry will first be considered. Figure 6.2 shows a 3 metre by 10 metre drift with the principal stresses horizontal and vertical. Considering only the vertical stresses, two primary mechanisms cause elastic movement of the drift back:

1. A destressed zone develops in the drift back. The drop in vertical stress in this destressed zone causes a vertical expansion of the rock mass which lowers the drift back. It could, however, be argued that the vertical expansion of the rock into the excavation causes the destress zone; the result is the same. As the drift span increases, the height of the destressed zone increases, as does the downward deformation of the drift back.
2. As the vertical stresses are shed from the drift back, they are concentrated in the drift abutments (Fig. 6.2). High vertical stresses in the abutments compress the abutments and lower the back. As the height of the drift increases, the stiffness of the abutment decreases causing increased downward movement of the drift back,. For wide backs or hanging walls in narrow ore bodies, this factor is small compared to the influence of the destressed zone.

The change in horizontal stresses induced around the drift acts in two main ways to deform the drift back:

1. A destressed or tensile zone develops in the drift abutments which shed the horizontal stresses to the drift back, as shown in Figure 6.3. This increased horizontal stress in the drift back causes horizontal compression and corresponding vertical expansion proportional to $(\nu\sigma_h/E)$, causing lowering of the drift back. This factor is generally minor since it is a product of Poisson's ratio, commonly .15 to .3 (Hoek and Brown, 1980). As the drift height increases, the horizontal stresses in the drift back increase. As the drift span increases, the horizontal stress is shed further from the drift back.
2. The destressed zone in the immediate abutment caused by the shadowing of horizontal stress causes a vertical contraction of the abutment which results in a downward deformation of the

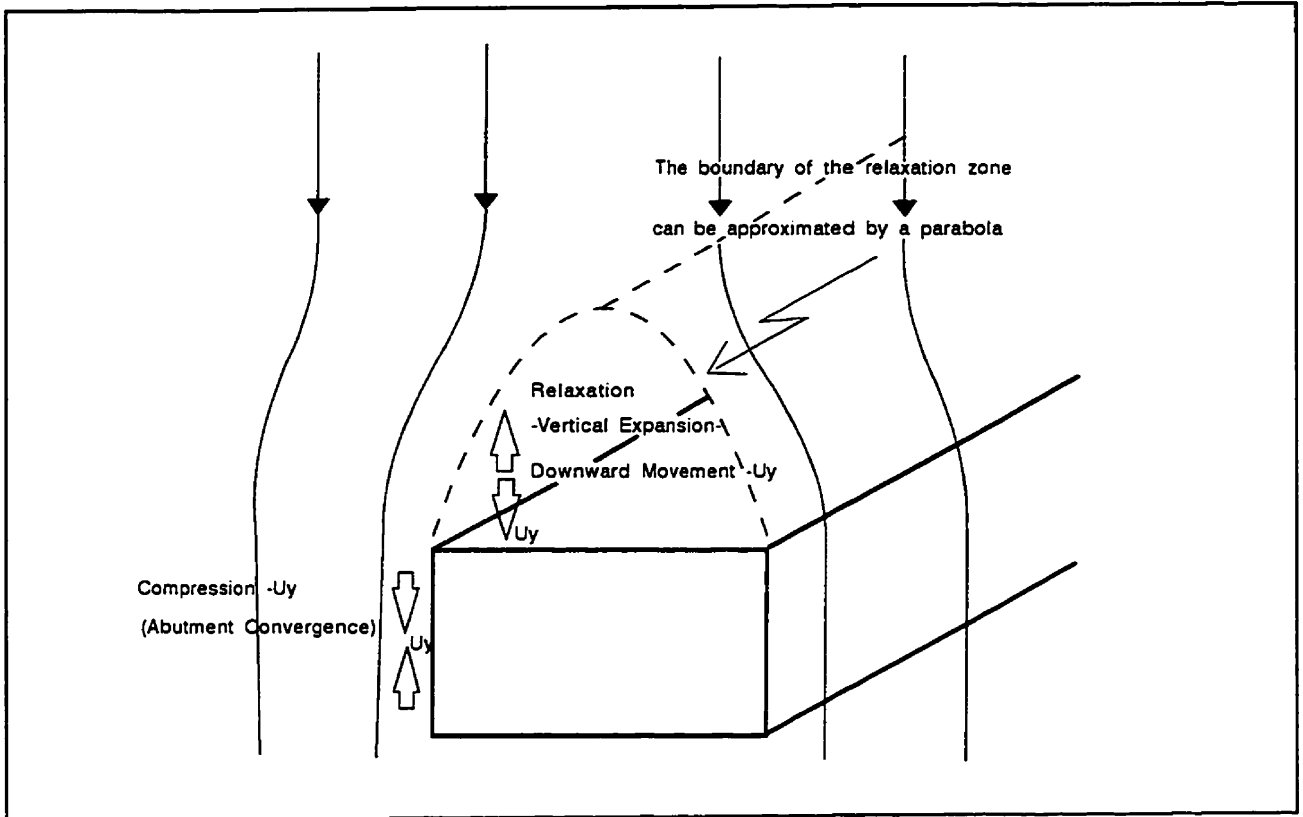


Figure 6.2 Surface deformation due to stress normal to the surface.

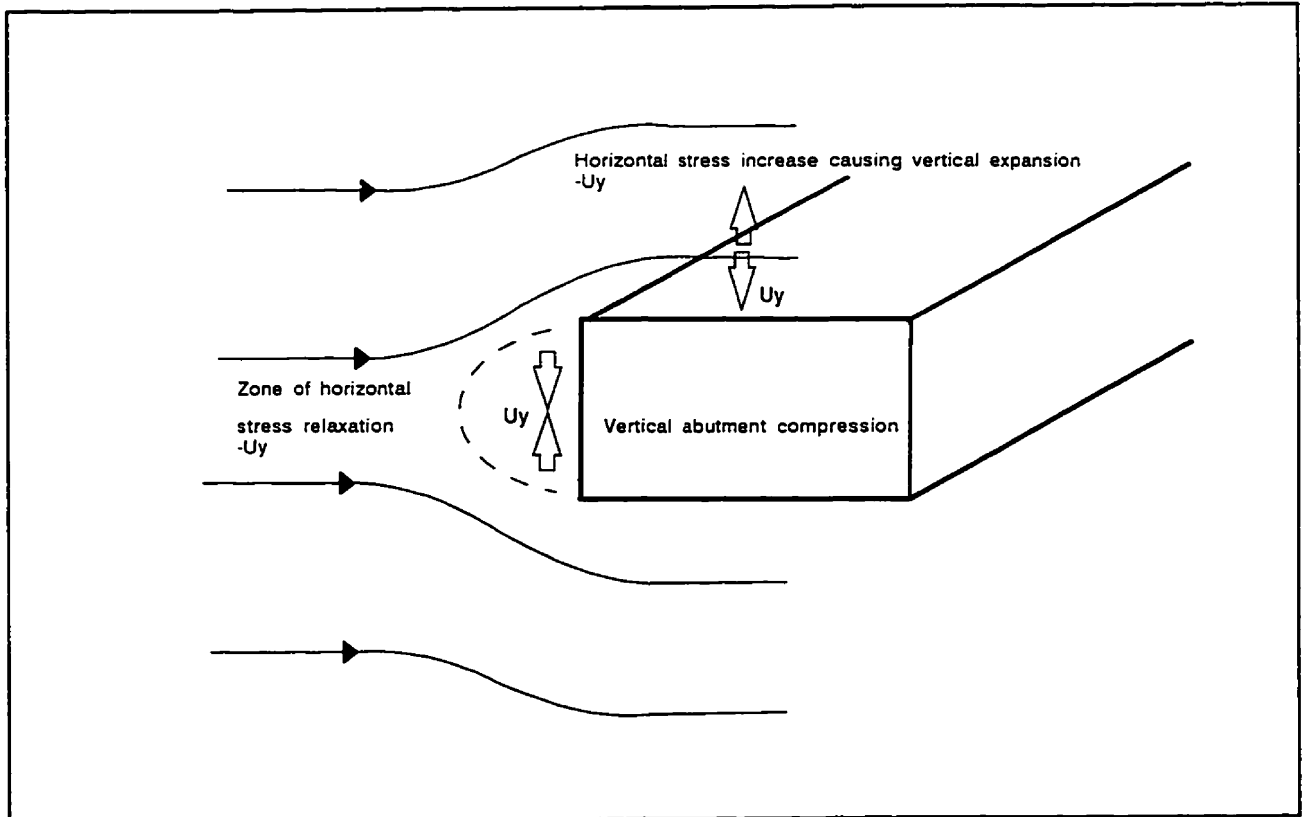


Figure 6.3 Surface deformation due to stresses parallel to the surface.

drift back. This factor is also proportional to $(\nu\sigma_n/E)$, so it is not a major factor.

The previous discussion shows that there are many factors influencing the deformation around the surface of an opening, even ignoring the presence of other openings. Some of these factors are less significant than others and it is possible to simplify the problem. In cases where the opening span is large compared to the opening height, abutment compression would not be a major factor. The influence of stresses parallel to the surface are reduced by Poisson's effect and are also not a major factor unless the abutment height is large compared to the opening span, or the parallel stresses are much greater than the normal stresses. The main factor controlling surface deformation is the zone of low stress due to the shadowing of stress normal to the opening. As an opening span to height ratio increases, the elastic deformation approaches beam bending behaviour.

A factor describing the geometry of only one surface of an opening cannot accurately predict surface deformation. However, when surface spans are large compared to opening height, as for hanging wall surfaces and stope backs in some cut and fill operations, the surface geometry is the controlling factor. The most significant factor influencing the deformation is the volume of the zone where the stresses perpendicular to the surface are destressed or shed. As such, it should be possible to compare deformation above a surface to a factor describing the surface geometry.

Insight into the relationship between opening geometry and deformation can also be obtained by considering a simple spherical excavation geometry in a hydrostatic stress field. Equation 3.4 shows the equation for deformation normal to a spherical cavity. Any one stress direction sees the spherical opening as a circular opening of radius 'a'. At the boundary of the opening, the deformation is linearly related to the radius of the opening. As described in Section 5.1, the radius factor at the centre of a circular opening equals half the radius. For irregular

geometries, the maximum effective radius factor (ERF) equates the geometry to an equivalent circular geometry with a radius of twice the ERF value. For irregular geometries where stress normal to the surface controls the majority of the deformation, the ERF value at a point on a surface may relate linearly to the surface deformation. Figure 6.4 shows the zone of stress shedding causing surface deformation above a sphere and a circular opening.

Numerically modelled displacements using the 3 dimensional boundary element model, Map3D (Wiles, 1995), will be compared to surface ERF values. Before comparing various surface geometries, it is of value to look at how boundary element models assess surface geometries.

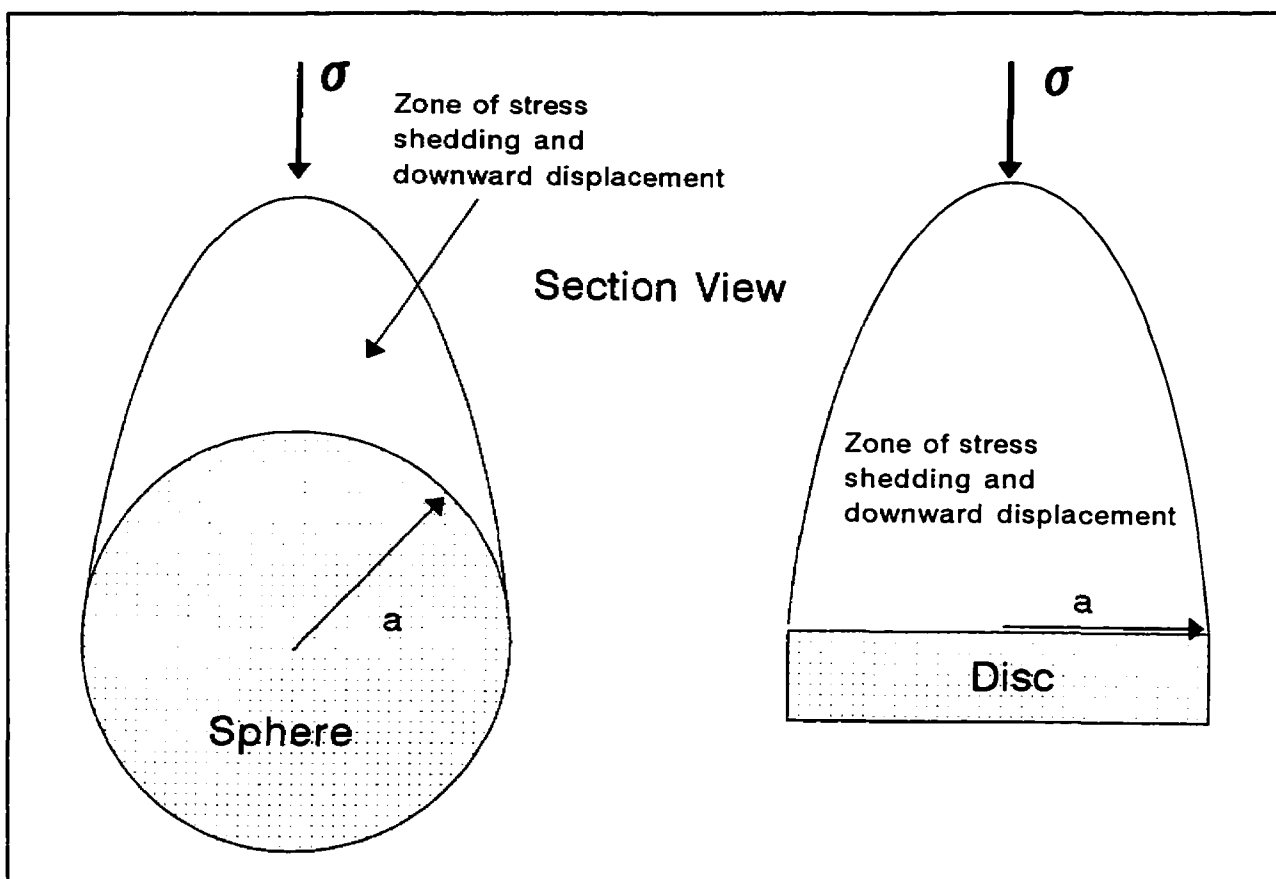


Figure 6.4 Zones of relaxation, or stress shedding, above a sphere and a circular disc.

6.2 INFLUENCE OF GEOMETRY ON MODELLED DEFORMATIONS AND ERI VALUES

The previous section discussed, in general terms, the factors affecting displacement above an opening. Close to an opening surface, deformation of a point above the surface is in a direction normal to the surface and is controlled by the surface geometry. For simplicity, a tabular opening 10 metres square is considered. Close to the 10 by 10 metre surface the deformation of a point will be governed by its position above the surface and will be in a direction perpendicular to the surface.

A simplified explanation of the procedure followed for calculating stresses and displacements around an opening excavation using a boundary element model is given in Hoel and Brown (1980), and is worth summarizing. In a given stress field, the rock mass in an area to be excavated acts to support the surrounding rock. The support provided by this rock mass can be represented by a series of normal and shear stresses which vary with the orientation of the future opening surface. These stresses are balanced by equal and opposite stresses in the surrounding rock mass. When the opening is excavated, the remaining external surface stresses must be redistributed around the surface to give zero boundary stresses normal to the opening

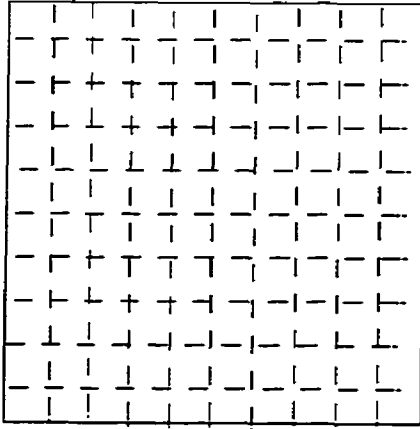
To solve for the resulting stress distribution, an imaginary situation is proposed where the surface boundary is divided into planar elements. Each element is subjected to shear and normal forces, referred to as fictitious forces. Prior to excavation, the shear and normal forces are balanced with the forces outside the excavation boundary which were equal and opposite to those within the boundary. After excavation, an iterative equation solving procedure is used to calculate displacements on each of the elements, since the displacements applied to one element influence the displacements on all the other elements. With given boundary conditions, which

include stresses normal to the excavation equalling zero, the stress state and resulting deformation can be determined anywhere around the excavation (Hoek and Brown, 1980).

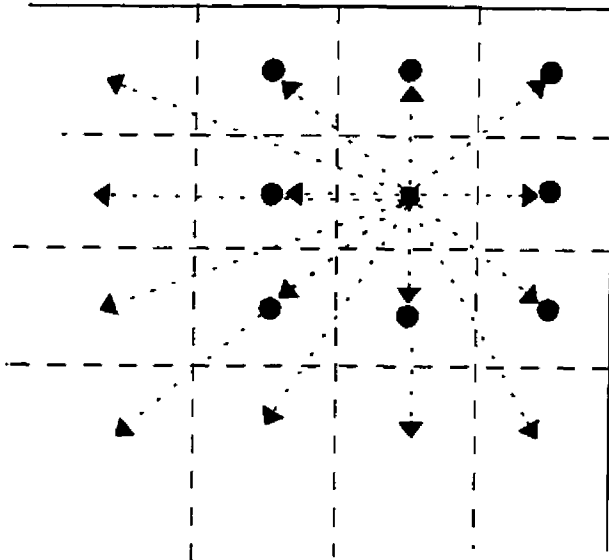
On the boundary of an opening, the normal stresses are equal to zero. In the example of a 10 by 10 metre tabular opening, divided into four hundred .5 by .5 metre elements, the normal stresses on each element are zero. Considering only the relative deformation of points at a constant distance above the surface, deformation varies with the position above the surface. A boundary element model's calculation of deformation of a point above the surface varies with the sum of the distances from the point to the centre of each of the elements (Figure 6.5). The influence of a boundary element on the displacement of a point decreases as the distance from the point to the boundary element increases (Crouch & Starfield, 1983). The distances from the centre of each element to all other elements on the surface were summed (Figure 6.5). The minimum total distance to surface elements was determined to be at the surface centre and the maximum distance was found at the corners of the square surface. As can be expected, the minimum total distance to elements occurs at the surface centre where the maximum deformation would be expected. The sum of the distance to element centres at various points was plotted against the ERF values at the points (Figure 6.6). For points along the diagonal of the square, a linear relationship was obtained. For points off of the diagonal, the sum of distances increasingly diverged from linearity, however, for the inner 90% of the surface the relationship diverged $\pm 15\%$ or less. Half way between the corners at the surface perimeter, at the maximum distance from the diagonals, the variation increased to $\pm 25\%$ (Figure 6.6). For the majority of the surface, a good trend between the ERF value and the sum of distances to element centres was obtained.

The next section discusses the results of modelled deformations at various points above a surface with the corresponding ERF values.

Boundary Element Grid



10m x 10m square divided into
1m elements



Σ Dist. to Element Centres
from a point on the
surface.

Figure 6.5 The calculation of the deformation of a point above an open surface varies with the sum of the distance to the centre of equally sized elements.

ERF Values vs Sum of Dist. to Elements 10 x 10m Surface & .5m x .5m elements

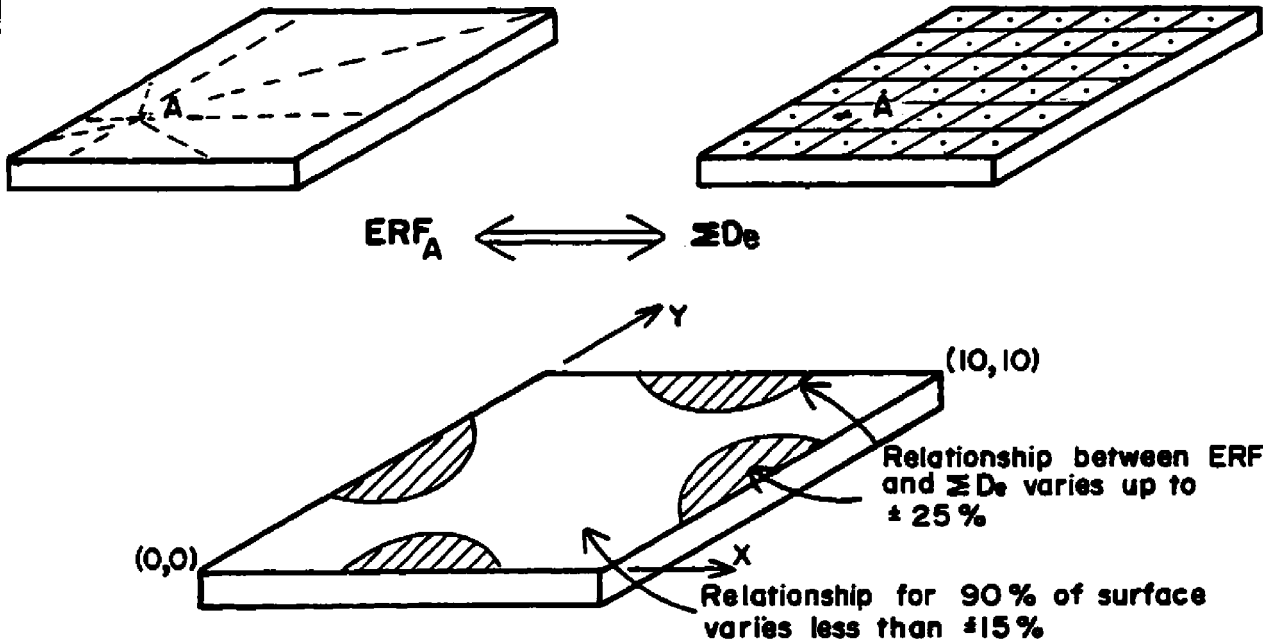
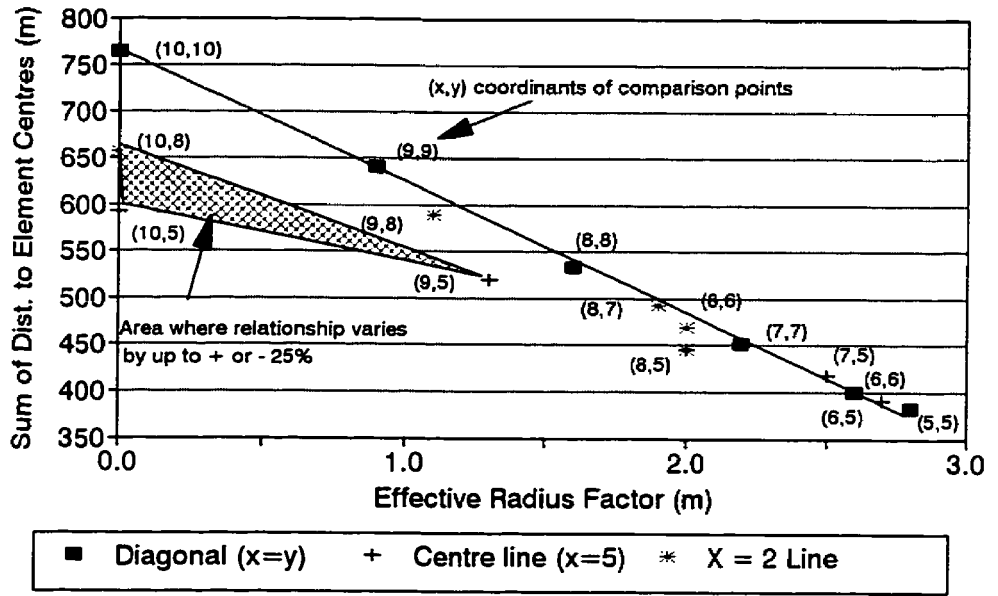


Figure 6.6 Plot of ERF values versus the sum of distances to each equidimensional element with a sketch showing where the relationship varies by $\pm 25\%$.

6.3 VARIATION OF MODELLED DEFORMATIONS AND ERF VALUES WITH SURFACE GEOMETRY

The Map3D boundary element model has been used to determine displacements above a single opening. Displacements above an opening surface vary with position, reaching a maximum above the centre of an opening. Modelling has also been done to determine if a relationship exists between the maximum ERF value and the distance from the surface the deformation is calculated. These displacements have been plotted against ERF values. Figure 6.7 shows the general procedure which has been followed throughout this chapter to compare modelled elastic deformations and surface ERF values. This procedure can be broken into a number of steps (Fig. 6.7):

1. Choose a reference plane parallel to the excavation surface being studied.
2. Cut sections through this reference plane and determine elastic deformation of points on the section.
3. Project the points on the reference plane to the excavation surface. Determine ERF values for these points.
4. On each section cut, plot the elastic deformation of points on the reference plane corresponding to ERF values on the excavation surface.

With a well defined trend between ERF values and elastic deformation it would be possible to extrapolate an elastic deformation profile for a surface given only a couple of deformation measurements on the surface. The purpose of this study is not to propose replacing numerical modelling with an empirical relationship, but is to determine if a fundamental relationship can be made between the ERF values and elastic deformations.

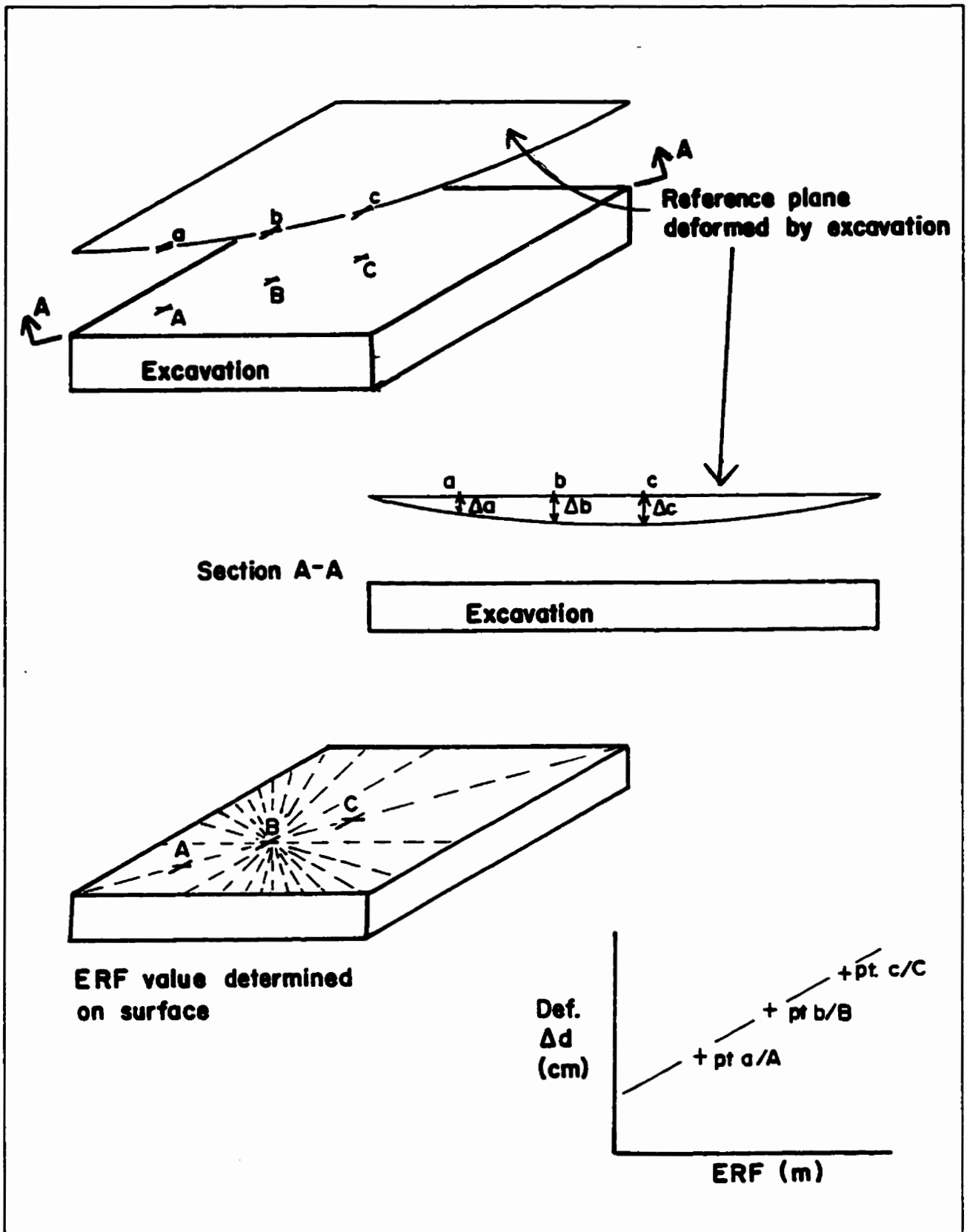


Figure 6.7 General procedure for comparing modelled elastic displacements above a surface to corresponding ERF values on the surface.

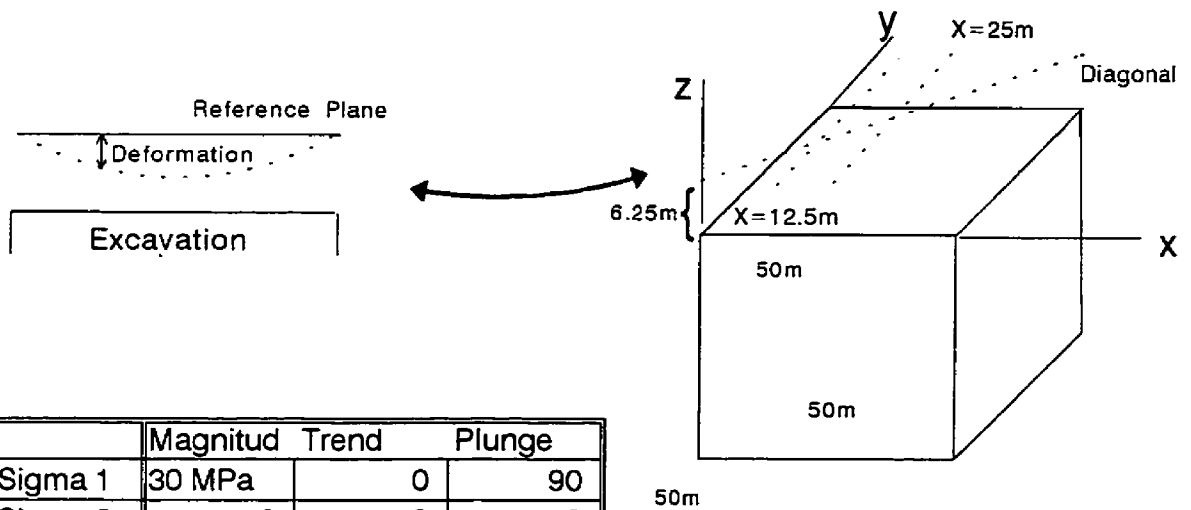
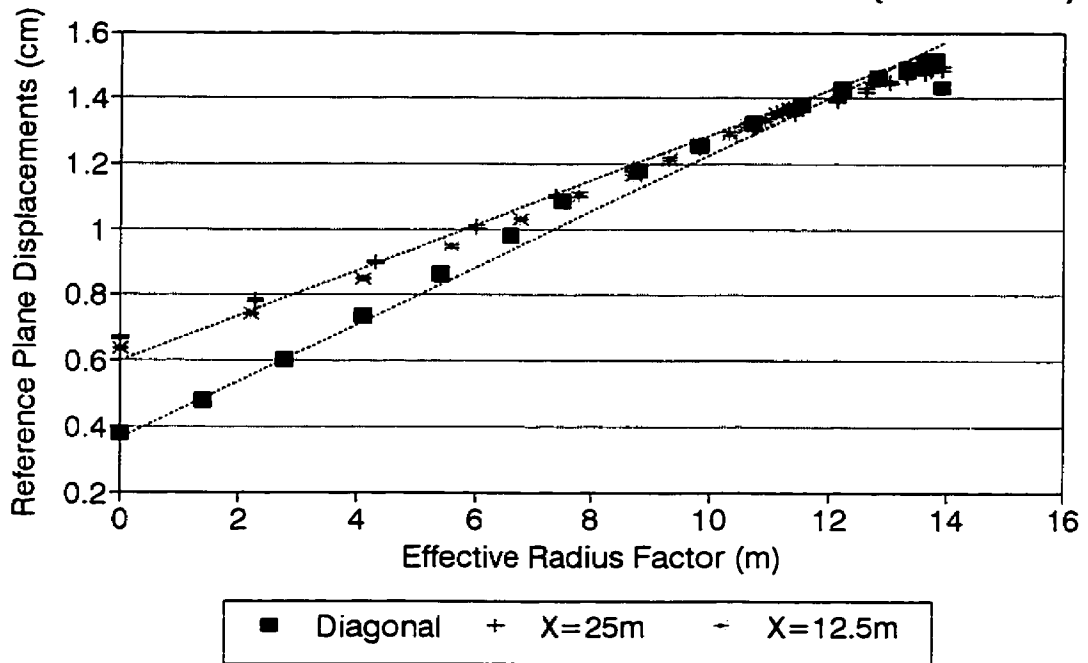
6.3.1 Deformation at a Constant Distance From Surface

Initially, deformations above a 50 metre cubic opening were modelled at a distance of 6.25m ($\frac{1}{8}$ span) away. A uniaxial stress of 30 MPa was modelled. Deformations 6.25m above the cube were determined along 3 measurement planes; diagonally across the surface, down the centre of the cube (centre span, $X = 25\text{m}$), and along the quarter span ($X = 12.5\text{m}$). Figure 6.8 shows the geometry and summarizes the results. Deformation along the 3 measurement planes were plotted against the ERF values at the modelled points on the planes. The results show a significantly linear relationship between ERF values and deformation for the three combined measurement planes. Deformations near the abutments diverged from linearity with the ERF values, probably due to the component of downward movement caused by the compression of the abutments. The least abutment compression would occur near the abutment corners and the maximum abutment compression would occur adjacent to centre span of the opening. Since ERF values are always zero at surface abutments, correlation with modelled displacement can only be expected when the variation in abutment compression is insignificant compared to back relaxation.

A second run was made with a hydrostatic stress field to better match mining conditions. This run was made to determine if a linear ERF to deformation relationship would still be obtained if stresses parallel to the opening were considered. Deformations were modelled at the same locations and the results showed less abutment compression (Figure 6.9). The decreased abutment compression in the hydrostatic stress field probably occurred because horizontal stresses were being induced and causing vertical expansion due to Poisson's effect.

It appears from Figures 6.8 and 6.9 that abutment compression detracts from the linearity between modelled surface deformation and ERF values. To determine the influence of abutment compression on the proposed relationship, additional models were run with increased abutment

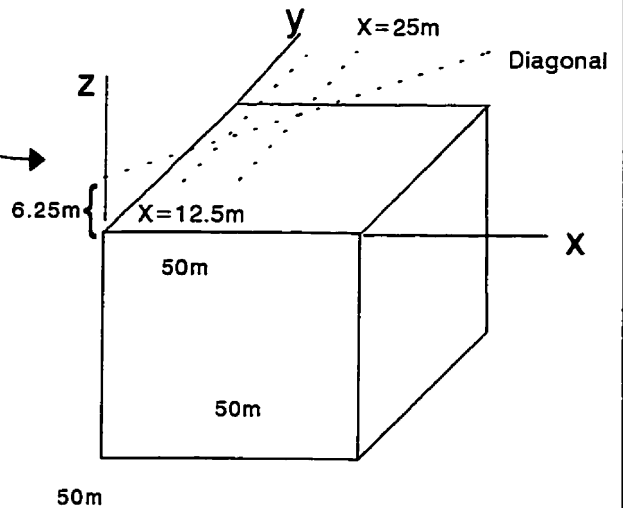
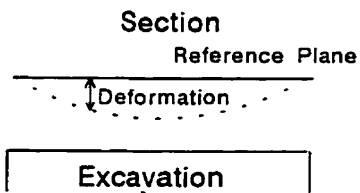
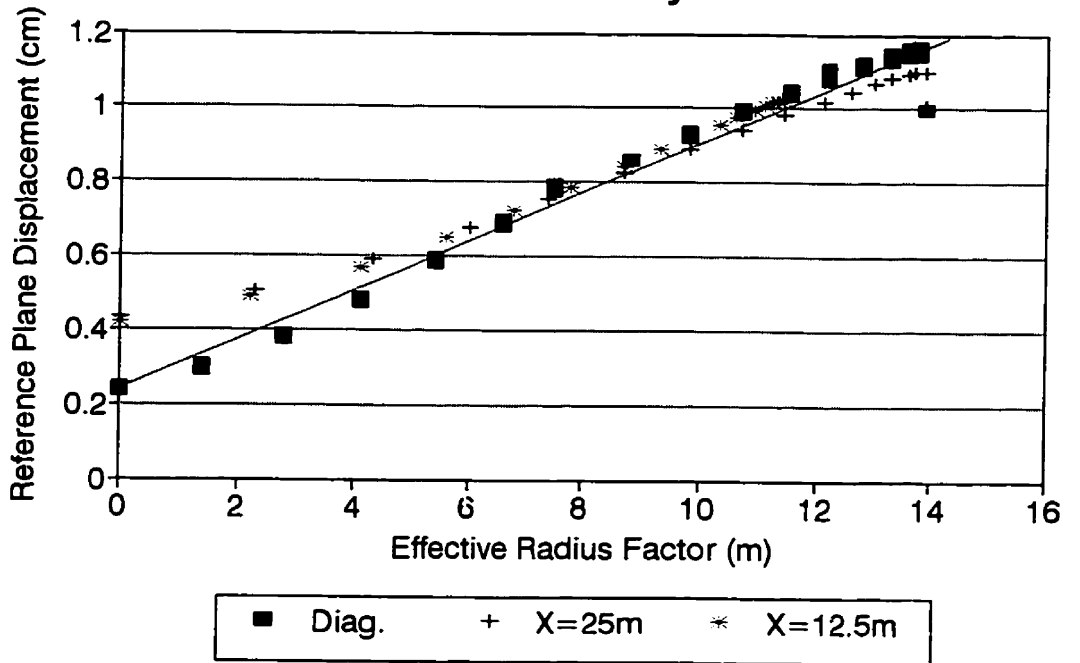
Effective Radius Factor vs Elast. Disp. 50x50x50m & 30MPa Uniaxial (+6.25m)



	Magnitud	Trend	Plunge
Sigma 1	30 MPa	0	90
Sigma 2	0	0	0
Sigma 3	0	0	0
E (GPa)	60		
Poissons	0.25		

Figure 6.8 Deformations modelled 6.25m above a 50m cube in a uniaxial vertical stress field, plotted against the ERF value.

Effective Radius Factor vs Elast. Disp. 50m Cube - 30 MPa Hydrostatic Stress



	Magnitude	Trend	Plunge
Sigma 1	30	-	-
Sigma2	30	-	-
Sigma 3	30	-	-
E (GPa)	60		
Poisson's r	0.25		

Figure 6.9 Deformation modelled 6.25m above a 50m cube plotted against the ERF value.

stiffness. The abutment thickness was decreased from 50 metres to 5 metres and a 50m by 50m by 5m tabular opening was modelled to increase abutment stiffness. Figure 6.10 shows this tabular opening modelled in a hydrostatic 30 MPa stress field. A more linear ERF to deformation relationship is shown with the modelled tabular opening in the hydrostatic stress field than with the cubical opening. There is also a slight decrease in the apparent abutment compression. Figure 6.11 considers an irregular tabular geometry and shows the same linear trend between ERF values and elastic deformation.

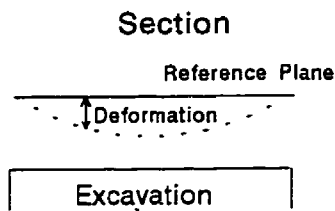
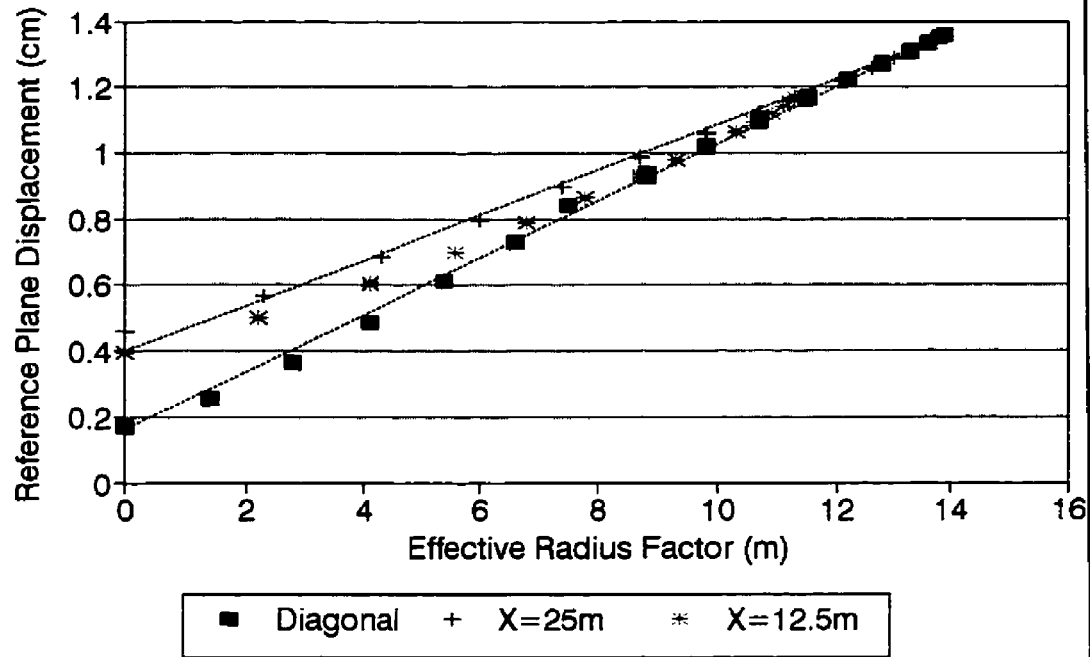
The modelled geometries have all indicated a relatively linear relationship between ERF values and elastic surface deformation, with only minor scatter near the abutments. Both hydrostatic and uniaxial stress fields were considered giving a range in stress ratio from 1 to infinity. Based on this observed relationship, field data showing a linear increase in deformation with increasing ERF value would be an indication of elastic deformation. The next section considers the variation in deformation with distance from the surface.

6.3.2 Elastic Deformation and Distance From the Surface

The previous section demonstrated that a deformation profile above an excavation surface approximately varies linearly with the ERF values on the surface. It is also of value to know how the deformation varies with distance from the opening surface. Figure 6.12 shows displacements above a 50m by 50m by 5m plate at the surface, 6.25m, 12.5m, 18.75m and 25m above the plate surface. Displacements are shown along a diagonal of the plate and are plotted against the ERF values.

From Equation 3.4 for a spherical opening, the radial deformation can be presented as follows:

Effective Radius Factor vs Elast. Disp. 50x50x5m & 30MPa Stress (6.25m Above)



	Magnitude	Trend	Plunge
Sigma 1	30 MPa	-	-
Sigma 2	30 MPa	-	-
Sigma 3	30 MPa	-	-
E (GPa)	60		
Poissons	0.25		

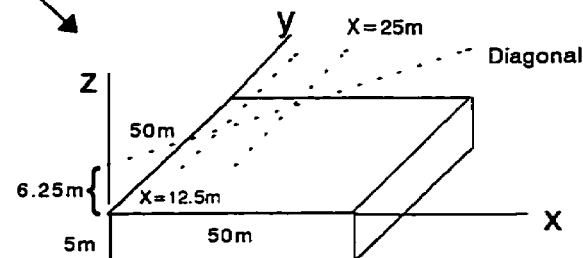
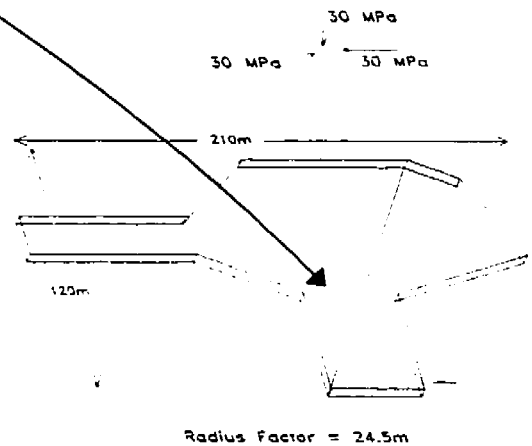
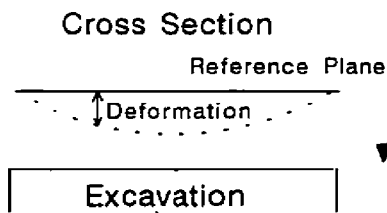
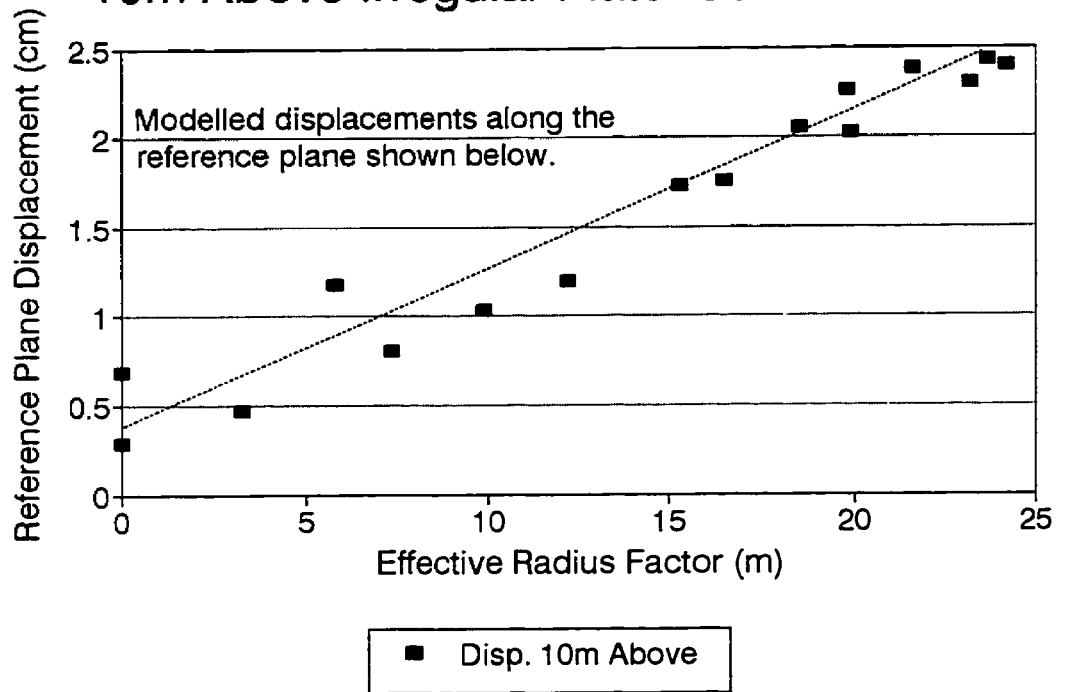


Figure 6.10 Deformation modelled 6.25m above a tabular opening 50m by 50m by 5m, plotted against ERF values.

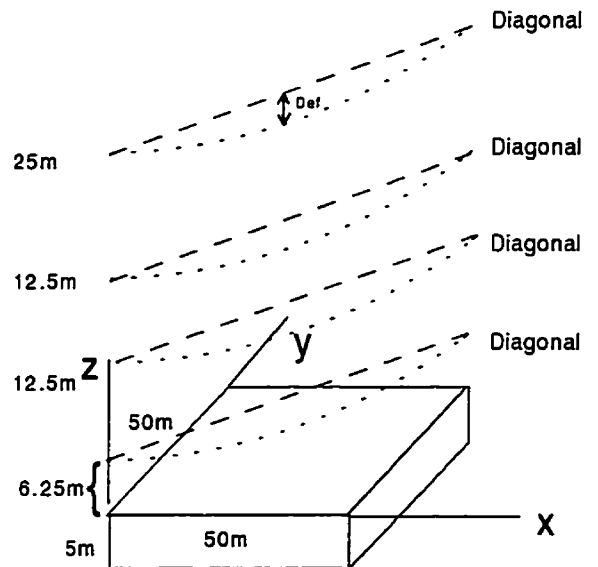
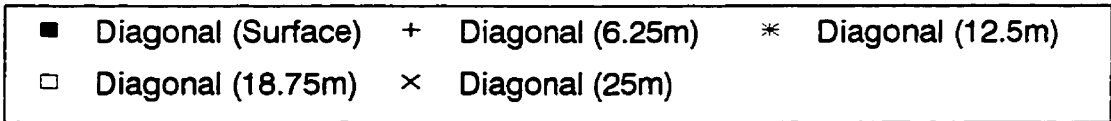
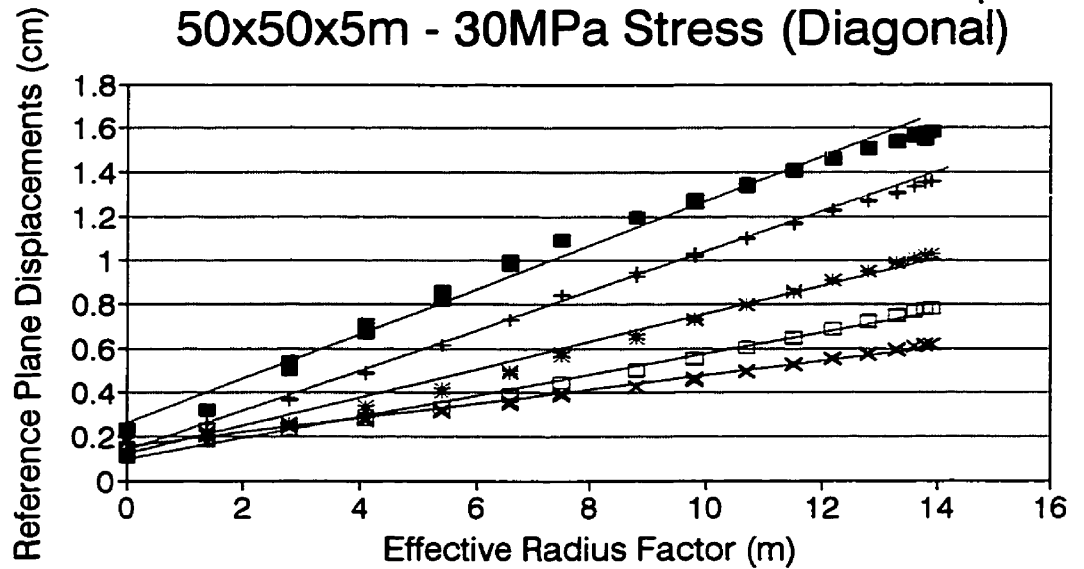
Effective Radius Factor vs Elast. Disp. 10m Above Irregular Plate -30MPa Stress



	Magnitude	Trend	Plunge
Sigma 1	30 MPa	-	-
Sigma 2	30 MPa	-	-
Sigma 3	30 MPa	-	-
E (GPa)	60		
Poissons	0.25		

Figure 6.11 Deformation modelled 10m above an irregular tabular opening, plotted against the ERF value.

Effective Radius Factor vs Elast. Disp. 50x50x5m - 30MPa Stress (Diagonal)



	Magnitude	Trend	Plunge
Sigma 1	30 MPa	-	-
Sigma 2	30 MPa	-	-
Sigma 3	30 MPa	-	-
E (GPa)	60		
Poissons	0.25		

Figure 6.12 Deformations modelled at various heights above a 50m by 50m plate in a hydrostatic stress field, plotted against the ERF value.

$$U_r \propto a \left(\frac{a^2}{r^2} \right) \quad (\text{Eq. 6.1})$$

where U_r = Deformation above the surface, a = Radius of the sphere and r = Distance from the centre of the sphere.

A similar empirical approach using the RF and ERF values is proposed for irregular geometries.

$$U_r \propto 2ERF \times \left(\frac{(2RF)^2}{(2RF+Z)^2} \right) + C \quad (\text{Eq. 6.2})$$

Where: U_r = Deformation above the surface

Z = Distance above the surface

RF = Overall surface radius factor (Maximum ERF value)

ERF = Surface radius factor at point considered

C = Constant due to abutment compression

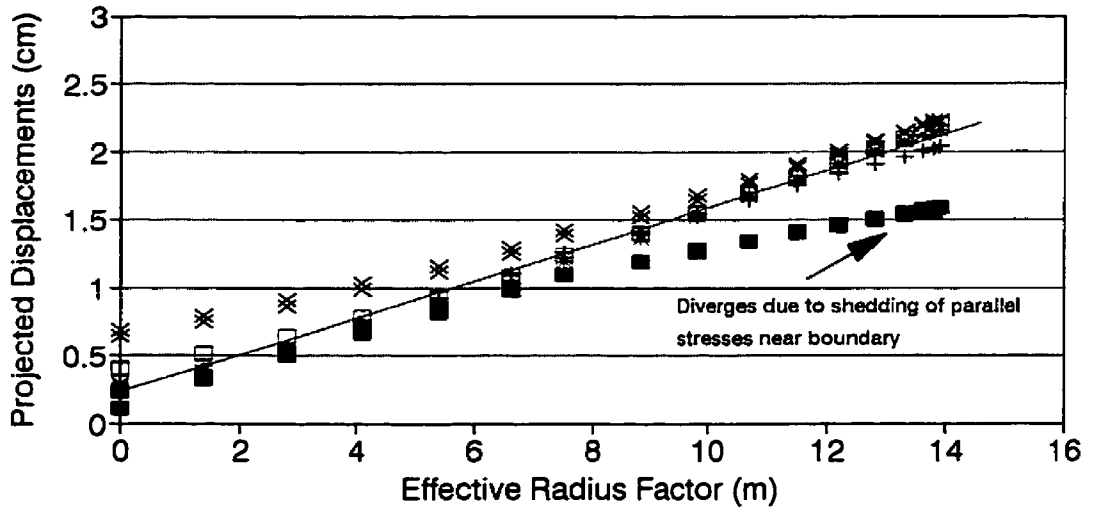
Figure 6.13 shows the deformations projected to the opening surface using Equation 6.2. The correlation is close except near centre span. The surface deformations are lower than expected, probably due to shedding of parallel stresses near the boundary. This effect cannot be accounted for based on the surface geometry alone. It should also be noted that the boundary element model does not give accurate results less than one element spacing away from the surface and the discrepancy may be a function of model accuracy.

Now that a method is presented for looking at displacements projected to the opening surface, it is possible to compare deformations on the surface of different opening geometries.

6.3.3 Deformation Versus ERF Values over Varied Opening Geometries

ERF values over the centre of a 5 metre by 5 metre surface will coincide to the ERF

Effective Radius Factor vs Elast. Disp. 50x50x5m - 30MPa Stress (Proj. to Surf)



■ Diagonal (Surface)	+ Diagonal (6.25m)	* Diagonal (12.5m)
□ Diagonal (18.75m)	× Diagonal (25m)	

	Magnitud	Trend	Plunge
Sigma 1	30 MPa	-	-
Sigma 2	30 MPa	-	-
Sigma 3	30 MPa	-	-
E (GPa)	60		
Poissons	0.25		

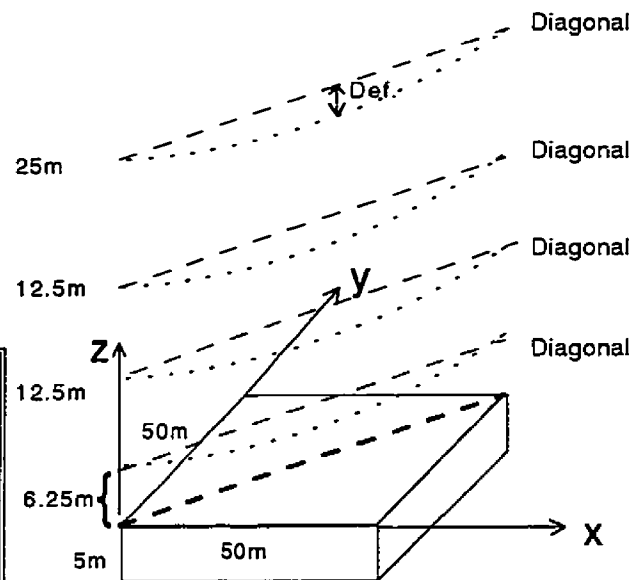


Figure 6.13 Deformation modelled above a 50m by 50m plate in a hydrostatic stress field, plotted against the ERF value, projected to surface.

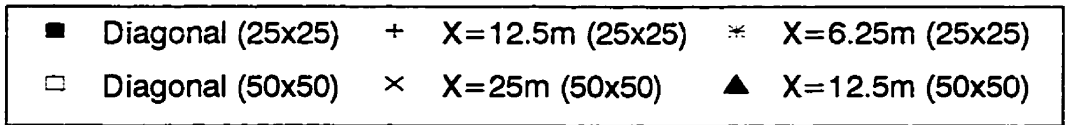
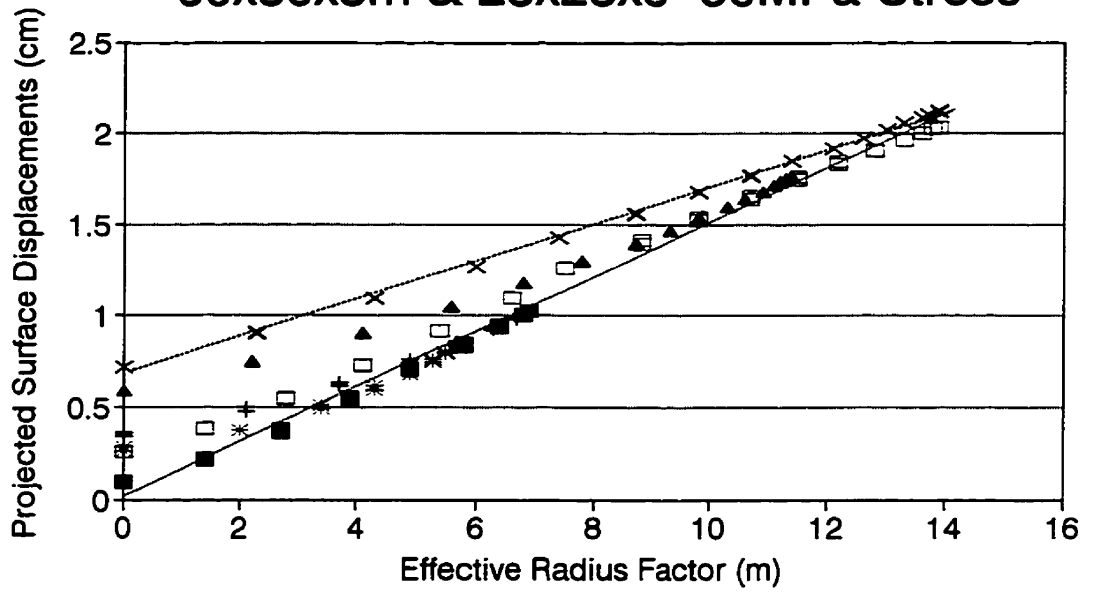
value near the abutment of a 50 metre by 50 metre surface. If ERF values can be related to the relative displacement between positions on two opening geometries, the ERF value could be used to extrapolate continued deformation adjacent to an expanding mining surface.

In order to compare various opening geometries, the ratio between opening geometry and distance from the surface must remain constant, or displacements must be compared on the opening surface. Deformations at an opening surface are often of most interest and are most frequently measured when instrumentation is installed. Unfortunately, to avoid model inaccuracies, it is necessary to compute deformations at a distance from an opening of at least one element width away. The technique proposed in Section 6.3.2 is used to project modelled deformations to the opening surface. This allows deformations to be compared without the scale effect due to the ratio between opening dimension and distance from surface (Eq. 6.1).

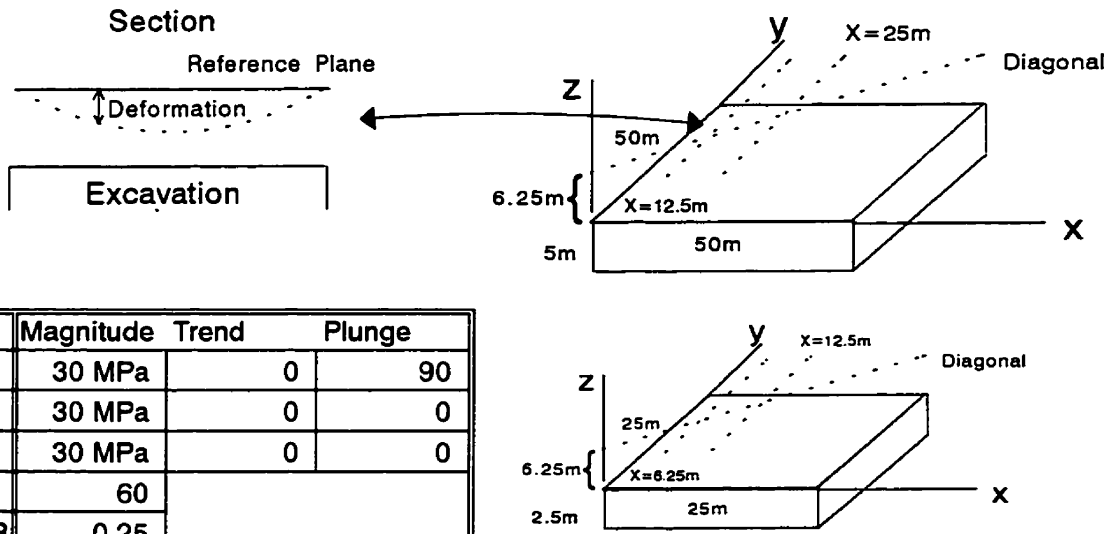
Initially, two openings 50m by 50m by 5m and 25m by 25m by 5m were modelled. For both openings, deformations were modelled 6.25m above the square surfaces under hydrostatic stresses. In order to cancel the effect of modelling deformations at proportionally different distances above the surface, the displacements were projected to the opening surface using Equation 6.2. As shown in Figure 6.14, a consistent linear trend is produced relating the surface deformation to the effective radius factor at various points above two different surface geometries.

To further verify this proposed relationship, a rectangular opening, 150m by 50m by 5m was considered. The same procedure was followed to project modelled deformations to the surface and these surface deformations were plotted against the ERF value for the rectangular opening, as well as for the two square openings. The results are shown in Figure 6.15 and show a consistently linear trend for all three geometries. The slightly smaller displacements above the 25m by 25m by 5m opening is probably due to decreased abutment compression from

Effective Radius Factor vs Elast. Disp. 50x50x5m & 25x25x5 -30MPa Stress



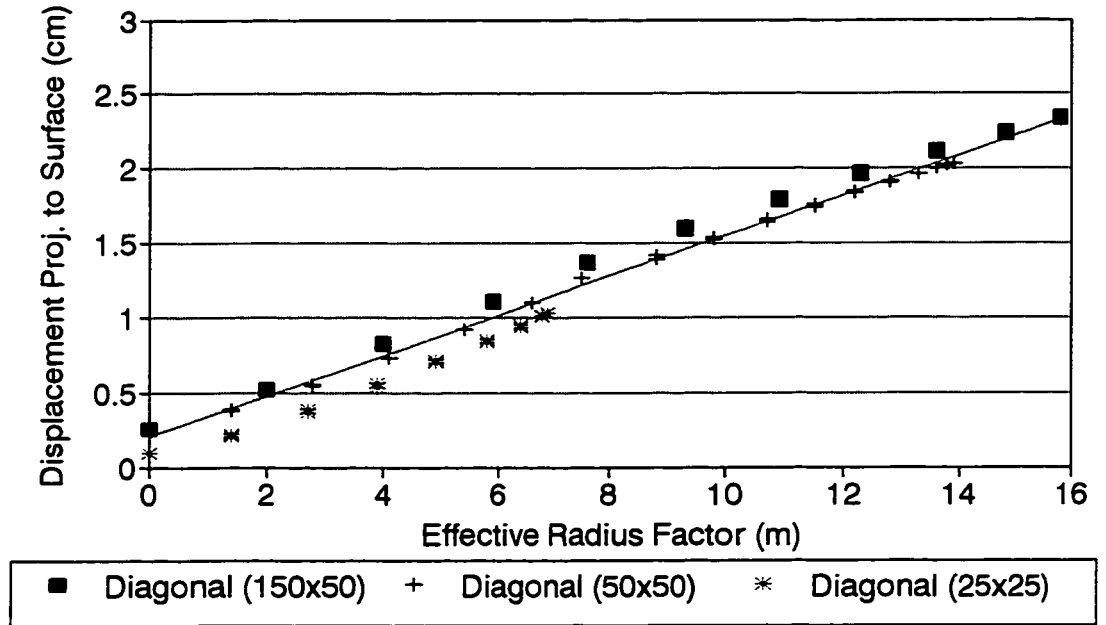
Note: Displacements have been projected to the opening surface based on the RF value and the measurement distance from the surface



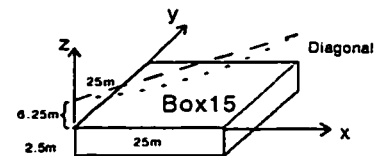
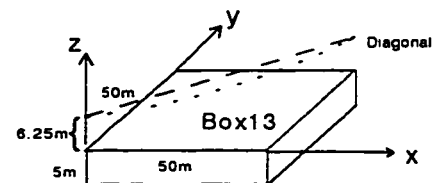
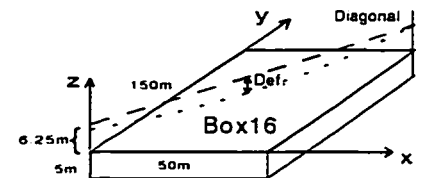
	Magnitude	Trend	Plunge
Sigma 1	30 MPa	0	90
Sigma 2	30 MPa	0	0
Sigma 3	30 MPa	0	0
E (GPa)	60		
Poissons R	0.25		

Figure 6.14 Projected surface deformation on a 25m by 25m plate and a 50m by 50m plate, plotted against the ERF values.

Effective Radius Factor vs Elast. Disp. 150x50m, 50x50m & 25x25m (Proj to Sur)



Note: Displacements above each box were projected to the surface based on a function of the surface radius factor and the distance from the modelled deformation to the surface.



	Magnitude	Trend	Plunge
Sigma 1	30 MPa	0	90
Sigma 2	30 MPa	0	0
Sigma 3	30 MPa	0	0
E (GPa)	60		
Poissons	0.25		

Figure 6.15 Projected surface deformations above 3 different sized openings, plotted against the ERF value.

reduced stress being shed from the smaller opening.

6.4 SUMMARY

The Map3D boundary element model has been used to calculate deformation at varied distances and positions above different opening geometries. These modelled elastic deformations have been compared to the corresponding ERF values on the surface. Some of the findings from this study are summarized below:

- The ERF value is approximately linearly related to the modelled deformation, with some scatter near abutments due to variable abutment compression. The relationship was accurate under both hydrostatic and uniaxial stresses normal to the opening.
- An empirical equation (Eq. 6.2) was introduced which projects deformations determined at some distance from a surface to the surface boundary.
- A reasonably linear relationship was obtained between ERF values and deformations projected to surfaces of different opening geometries.

The relationship observed between modelled elastic displacements and the corresponding ERF values does not reduce the need for computer modelling rock mass response. In cases where stresses parallel to the proposed excavation are higher than the perpendicular stresses the observed trends described will not be as accurate. The proposed relationships are most applicable to stope hanging wall conditions where the maximum stresses are most commonly normal to the hanging wall. Also, in cases where there are other openings locally influencing surface deformations, trends between ERF values and elastic deformation will not be consistent. The trends observed and the relationships developed provide insight into understanding where high elastic surface displacements can be expected and allow the engineer to predict how these

movements will change with continued mining.

The next chapter discusses how near surface elastic deformations vary and presents guidelines for determining when elastic deformations have been exceeded.

CHAPTER 7

STRESS AND STRAIN NEAR OPENING SURFACES

7.1 INTRODUCTION

The previous chapter discussed how elastic displacements vary with position near an opening surface. This chapter looks at near surface strains and how they can be related to elastic stress change. Displacements relatively close to opening surfaces are of primary concern for safety and when instrumentation is installed it is designed to obtain maximum accuracy in this area. The opening of cracks above drift and stope surfaces is an indication of decreasing surface stability and occurs when maximum elastic displacements have been exceeded. Computer modelling can be used to estimate elastic deformation, however, on a daily production basis, time constraints can make modelling impracticable. Simple guidelines are presented in the following sections to indicate when instrumented displacements are within the elastic range, or conversely, cracks are opening.

7.2 STRAIN AND DISPLACEMENT AROUND A SPHERE

Equations exist which allow calculation of displacements and stresses around a sphere in an hydrostatic stress field (Section 3.2.2). Radial displacement towards the centre of a sphere, at some distance d from the boundary of a sphere, are given in Equation 3.4 and is shown below.

$$U_r = \left(\frac{\sigma(1+\nu)}{2E}\right)\left(\frac{a^3}{(a+d)^2}\right) \quad (\text{Eq. 7.1})$$

Where: a = radius of the sphere.

d = distance from the surface of the sphere

U_r = movement radially into the sphere

E = Young's Modulus

ν = Poisson's Ratio

σ = Hydrostatic field stress

As the radius of a sphere, a , becomes large relative to the distance to the surface of the sphere, d , the term $a^3/(a+d)^2$ approaches $a-2d$. This is shown in Equations 7.2 to 7.6, given the following two approximations (Eq. 7.2 and 7.3), when $a \gg d$ (Milne, 95):

$$\frac{a-d}{a} \approx \frac{a}{a+d} \dots \text{ when } \dots a \gg d \quad (\text{eq. 7.2})$$

and

$$(a^2-2ad) \approx (a^2-2ad+d^2) \dots \text{ when } \dots a \gg d \quad (\text{Eq. 7.3})$$

therefore

$$a-2d = \frac{1}{a}(a^2-2ad) \approx \frac{1}{a}(a^2-2ad+d^2) \dots \text{ given (eq.7.3)} \quad (\text{eq. 7.4})$$

and

$$a-2d \approx \frac{1}{a}(a-d)^2 = a\left(\frac{a-d}{a}\right)^2 \approx a\left(\frac{a}{a+d}\right)^2 \dots \text{ given (eq.7.2)} \quad (\text{eq. 7.5})$$

therefore

$$a-2d \approx a\left(\frac{a}{a+d}\right)^2 = \frac{a^3}{(a+d)^2} \dots \text{ when } \dots a \gg d \quad (\text{Eq. 7.6})$$

From equation 7.6, the radial deformation around a spherical cavity, at a small distance from the opening surface relative to the opening radius, can be approximated as follows:

$$U_R = \frac{\sigma(1+\nu)}{2E}(a-2d) \quad \text{when } a > d \quad (\text{Eq. 7.7})$$

Figure 7.1 shows the calculation of normal deformation towards the centre of a sphere and the resulting strain. The strain between two points is defined as the relative movement between two points divided by the distances between the points (Eq. 3.1). The strain between two points near the surface of a large sphere, d and $d+x$ metres away, can therefore be approximated as follows, based on equation 7.7:

$$\epsilon_r = \left[\frac{\sigma(1+\nu)}{2E} \right] \left[\frac{(a-2d) - (a-2(d+x))}{x} \right] = \left[\frac{\sigma(1+\nu)}{2E} \right] \left[\frac{2x}{x} \right] \quad (\text{Eq. 7.8})$$

Where x and $(d + x) \ll a$

Which can be simplified to:

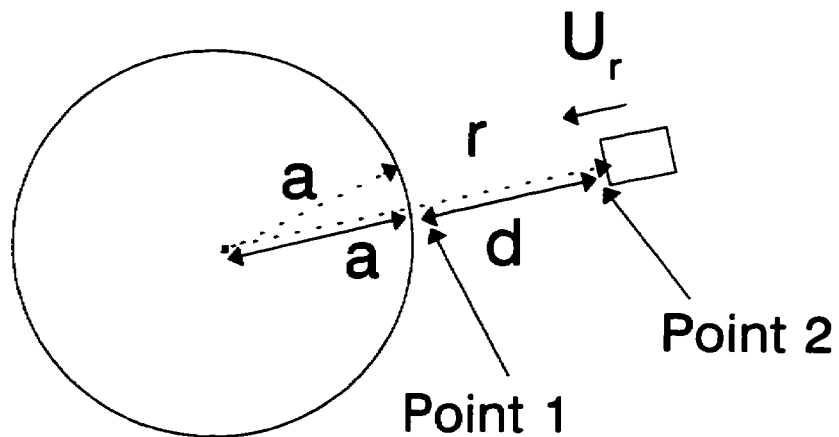
$$\epsilon_r = \left[\frac{\sigma(1+\nu)}{E} \right] \quad (\text{Eq. 7.9})$$

Equation 7.9 indicates that the strain between two points close to the surface of a sphere converges to a constant maximum value when the radius of the sphere is much greater than the distance from the sphere. This strain value can then be related to the elastic constants and stress in the medium. When this maximum strain is exceeded, the opening of cracks in the rock mass can be expected. When the radius of a sphere is twenty times the distance from the surface of the sphere to the two points considered, the strain between these points reaches 90% of the maximum (Fig. 7.2).

7.3 ELASTIC STRAIN AND DISPLACEMENT ABOVE A PLANAR SURFACE

Three dimensional modelling using the Map3D boundary element model has been conducted to determine if a similar relationship can approximate the maximum strain above a

Deformation Around a Sphere



$$U_r = - \frac{Pa^3}{4Gr^2}$$

$$\frac{P}{4G} = K$$

$P =$ Hydrostatic stress

$$G = \frac{E}{2(1+\nu)}$$

$$r = a + d$$

At pt. 1 $U_r = Ka$

At pt. 2 $U_r \approx K(a-2d)$ (When $a \gg d$)

$$\epsilon_{\text{pts. 1 to 2}} \approx K (2)$$

Figure 7.1 Deformation and strain calculations around a sphere in a hydrostatic stress field.

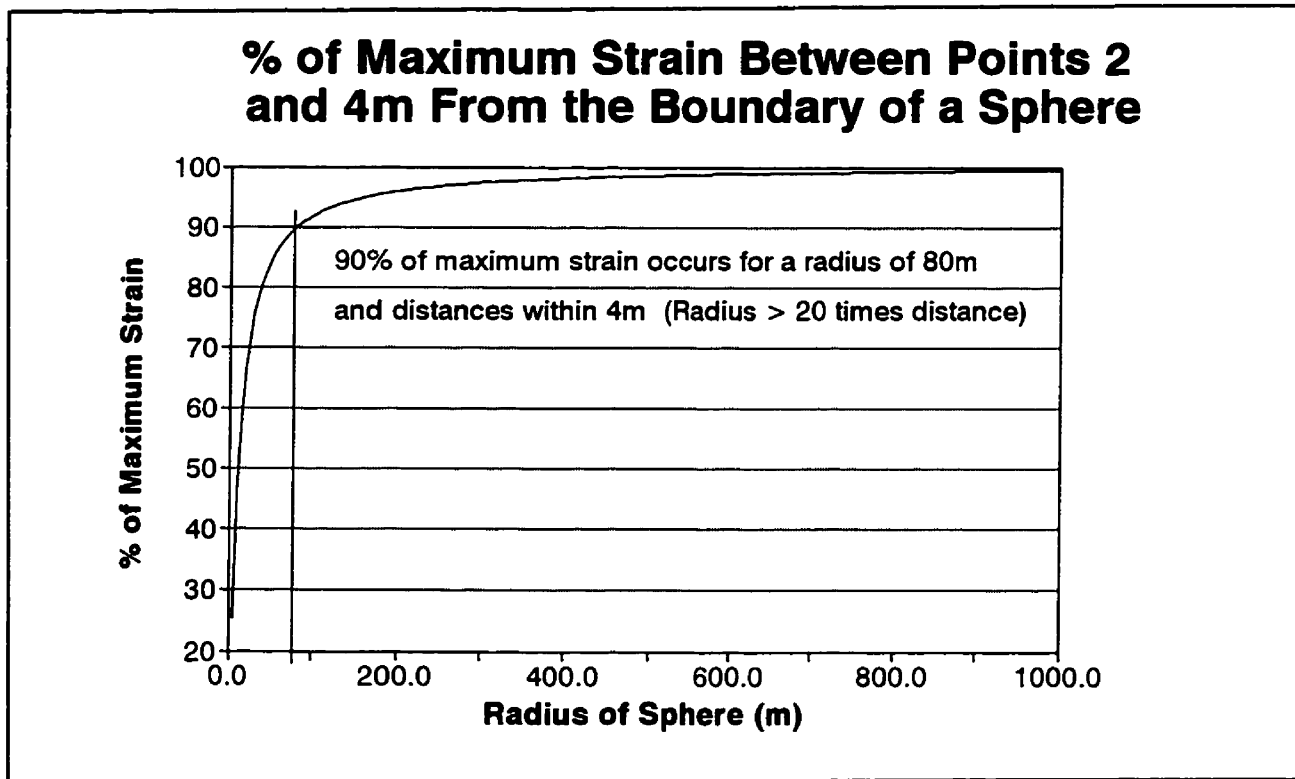


Figure 7.2 Percent of maximum strain obtained between points 2 and 4 metres from the boundary of a sphere.

planar surface in various stress fields. The calculated strain values above an excavation surface have also been compared to the corresponding ERF values on the excavation surface. Figure 7.3 shows the general procedure that has been followed to compare the strain above a surface and ERF values. Two reference planes are shown above an excavation. Prior to creating the excavation, the reference planes are 'd' metres apart. After excavating, the lower plane, plane 1, deforms towards the excavation Δd metres more than the upper plane, plane 2. The resulting strain between corresponding points on the two reference planes is plotted against the surface ERF value.

Strain above a tabular surface, a cube and an irregular surface were modelled and are shown in Figures 7.4 to 7.6. These figures shows that the microstrain between two points perpendicular and above a surface converges to a maximum when the ERF value of the points is approximately equal or greater than the maximum distance from the surface. This means that

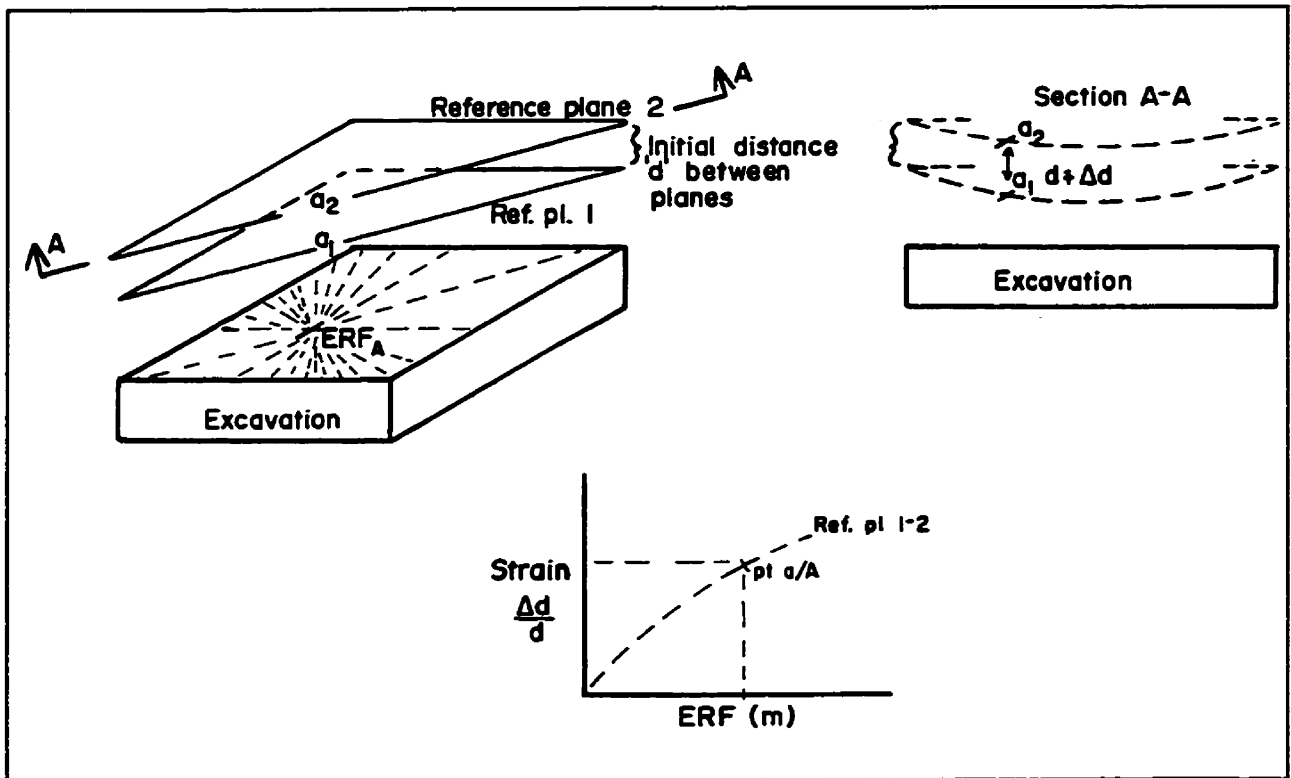
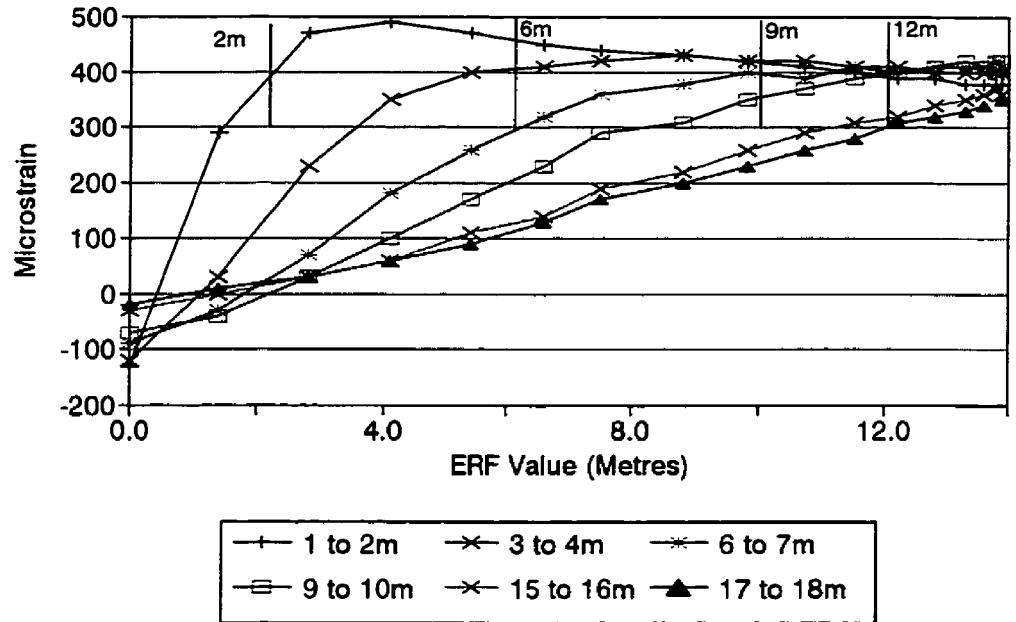


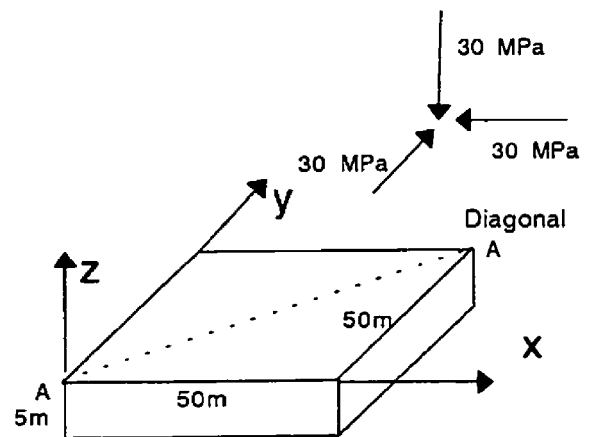
Figure 7.3 General procedure used to relate the strain normal to an excavation surface and the corresponding ERF value.

the elastic microstrain between two extensometer anchors, 3 and 5 metres above an open hanging wall, approaches a constant value when the corresponding ERF value reaches about 5m. Modelling was also done where the field stresses in the direction normal to the opening were twice the stresses parallel to the opening, as well as half the parallel stress ($k=.5$ and $k=2.0$) (Figures 7.7 to 7.9). Strains converged to a constant when the ERF value approximately equalled the distance from the modelled points to the surface. In each case the maximum strain value reached was a function of the stress normal to the opening, prior to the creation of the opening. Based on this modelling, an empirical relationship for the strain perpendicular to an opening surface was developed. This relationship follows the form of equation 7.9 for radial strain close to a spherical opening.

Elastic MStrain Above 50x50x5m Opening Versus ERF Values at Various Distances



ERF Value at maximum strain	
Anchors	ERF Value
1 to 2m	2m
3 to 4m	6m
6 to 7m	9m
9 to 10m	12m
15 to 16m	Not reached



	Magnitud	Trend	Plunge
Sigma 1	30 MPa		
Sigma 2	30 MPa		
Sigma 3	30 MPa		
E (GPa)	60 GPa		
Poisson's	.25		

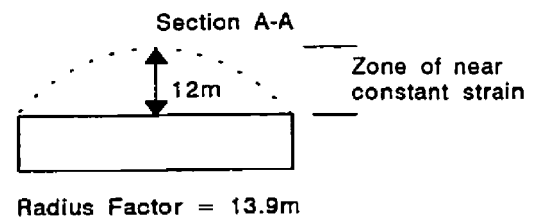
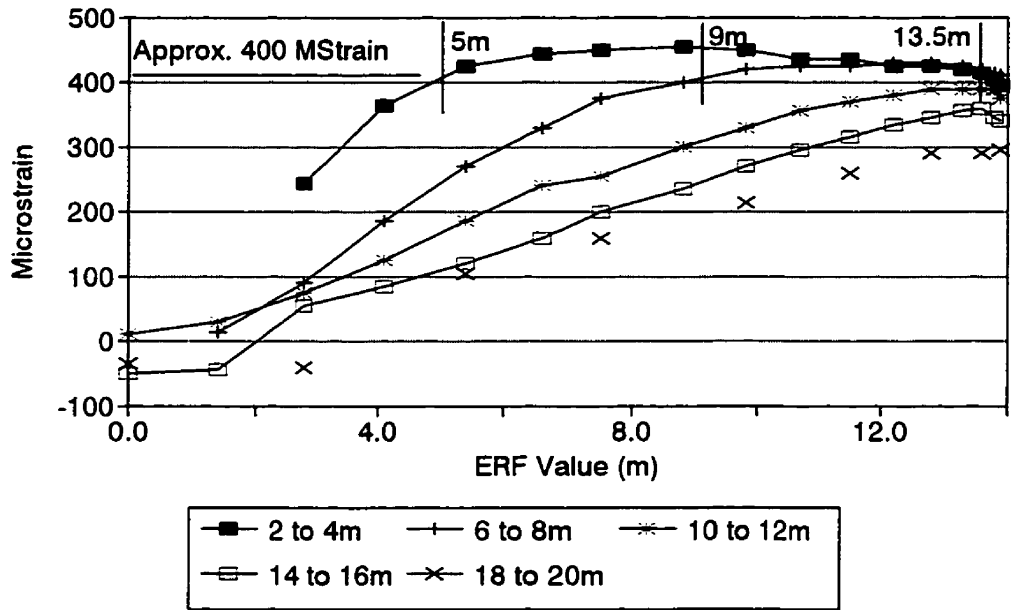


Figure 7.4 Zone of constant strain above a tabular opening in a hydrostatic stress field.

Elastic MStrain Above a 50m Cube Versus ERF Values at Various Distances



ERF Value at maximum strain	
Anchors	ERF Value
2 to 4m	5m
6 to 8m	9m
10 to 12m	13.5m
14 to 16m	Not reached
18 to 20m	Not reached

	Magnitud	Trend	Plunge
Sigma 1	30 MPa		
Sigma 2	30 MPa		
Sigma 3	30 MPa		
E (GPa)	60 GPa		
Poisson's	.25		

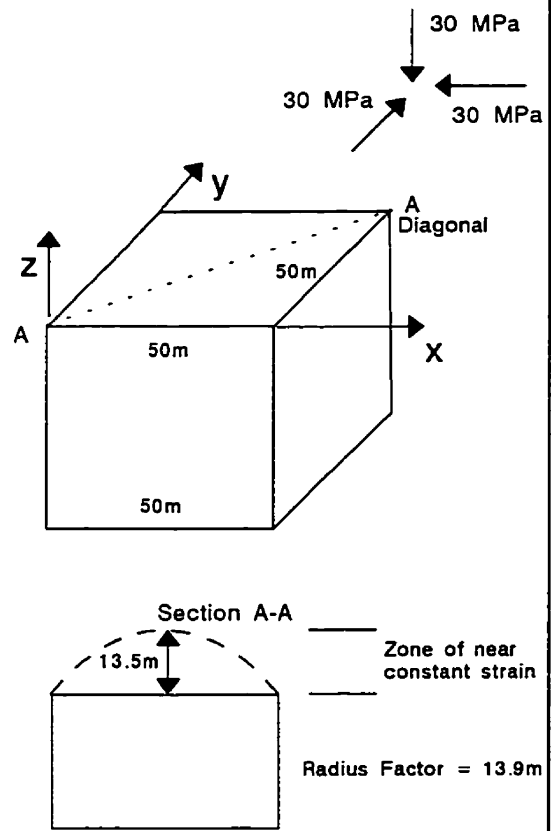
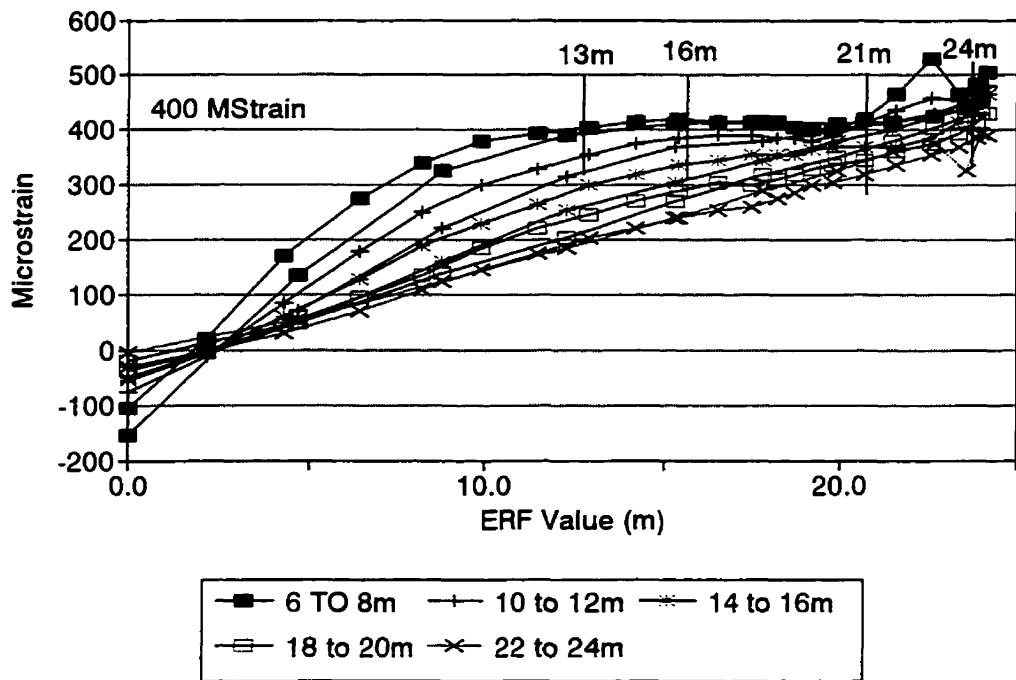


Figure 7.5 Zone of constant strain above a cubic opening in a hydrostatic stress field.

Elastic MStrain Above an Opening Vs. ERF Values Plotted at Various Distances



ERF Value at maximum strain	
Anchors	ERF Value
6 to 8m	13m
10 to 12m	16m
14 to 16m	21m
18 to 20m	24m
22 to 24m	Not reached

	Magnitud	Trend	Plunge
Sigma 1	30 MPa		
Sigma 2	30 MPa		
Sigma 3	30 MPa		
E (GPa)	60 GPa		
Poisson's	.25		

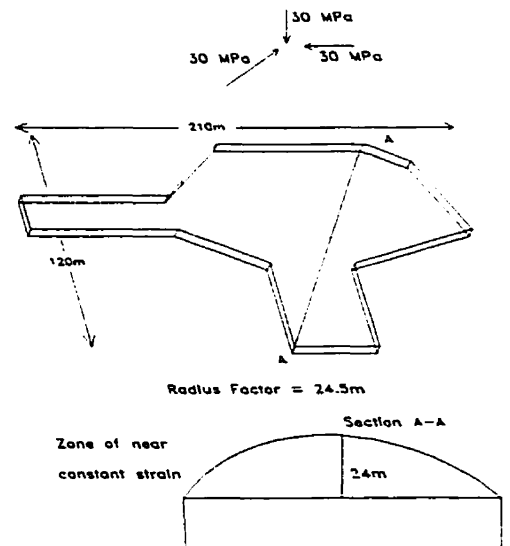
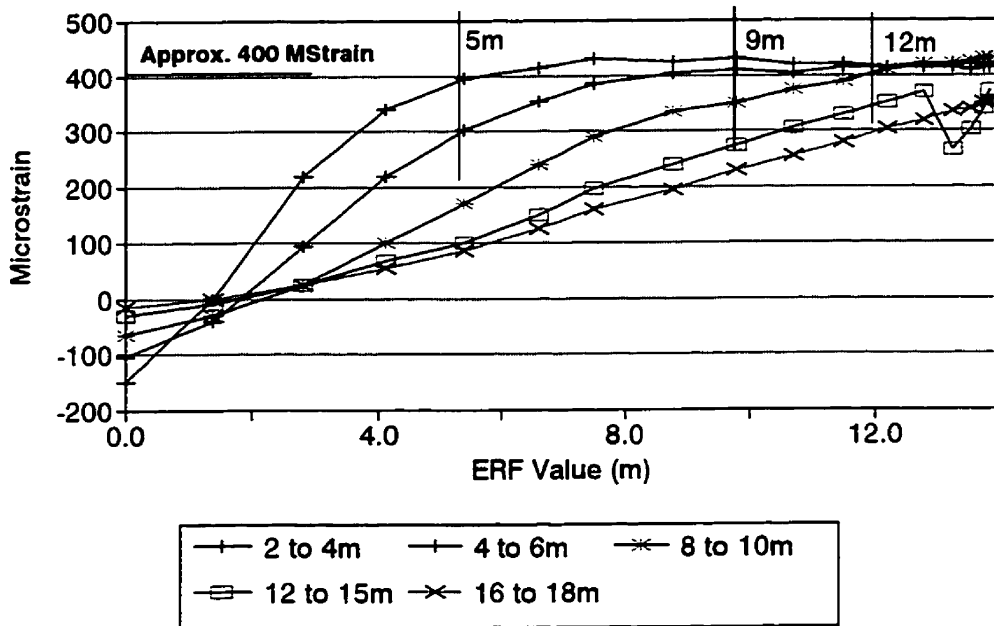


Figure 7.6 Zone of constant strain above an irregular opening in a hydrostatic stress field.

Elastic MStrain Above 50x50x5m Opening Versus ERF Values (k=.5)



ERF Value at maximum strain	
Anchors	ERF Value
2 to 4m	5m
4 to 6m	9m
8 to 10m	12m
12 to 15m	Not reached
16 to 18m	Not reached

	Magnitud	Trend	Plunge
Sigma 1	60 MPa	90	0
Sigma 2	60 MPa	180	0
Sigma 3	30 MPa		90
E (GPa)	60 GPa		
Poisson's	.25		

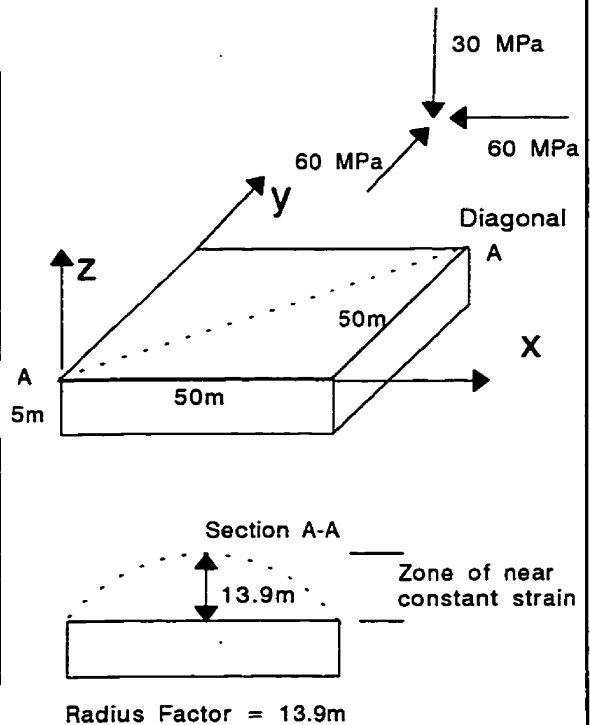
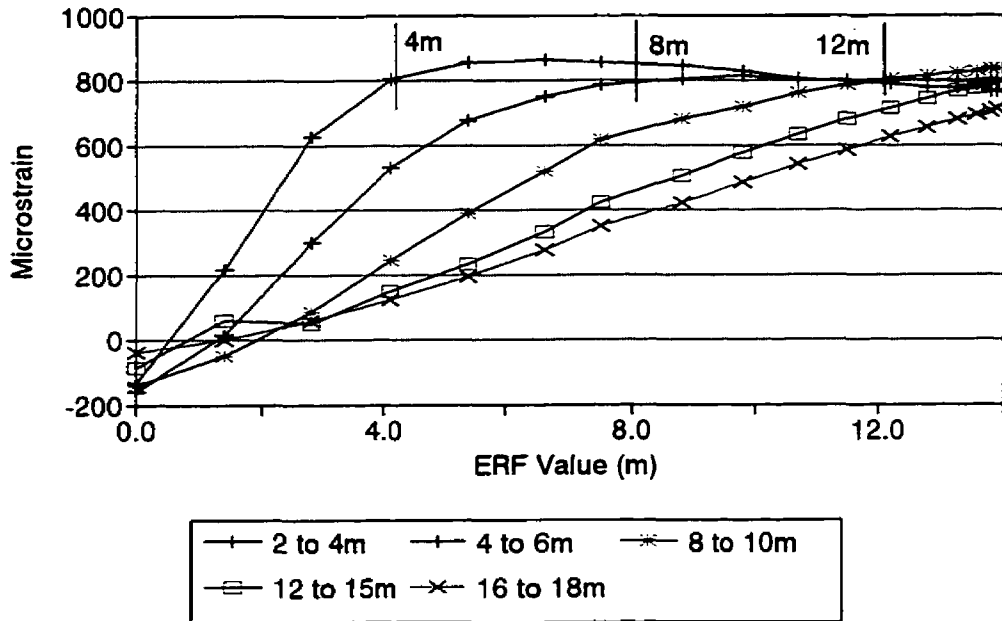


Figure 7.7 Zone of constant strain above a 50m by 50m by 5m opening with stresses 30 MPa normal and 60 MPa parallel to the opening surface.

Elastic MStrain Above 50x50x5m Opening Versus ERF Values (k=2)



ERF Value at maximum strain	
Anchors	ERF Value
2 to 4m	4m
4 to 6m	8m
8 to 10m	12m
12 to 15m	Not reached
16 to 18m	Not reached

	Magnitud	Trend	Plunge
Sigma 1	60 MPa		90
Sigma 2	30 MPa	180	0
Sigma 3	30 MPa	90	0
E (GPa)	60 GPa		
Poisson's	.25		

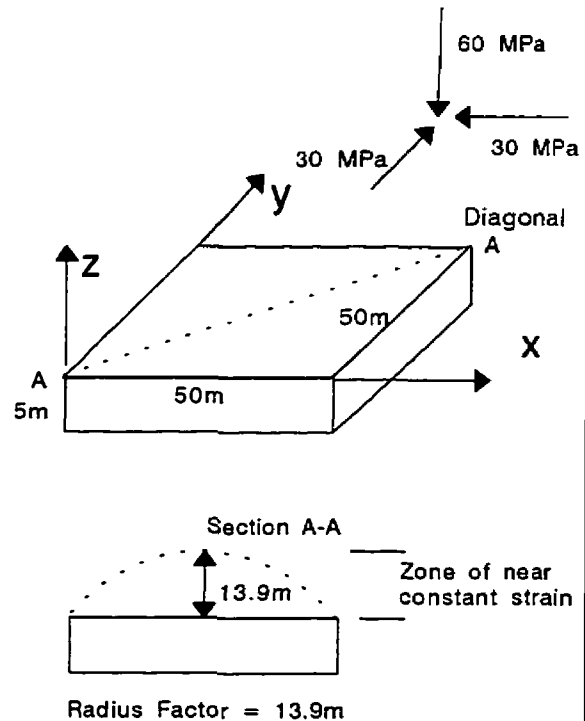
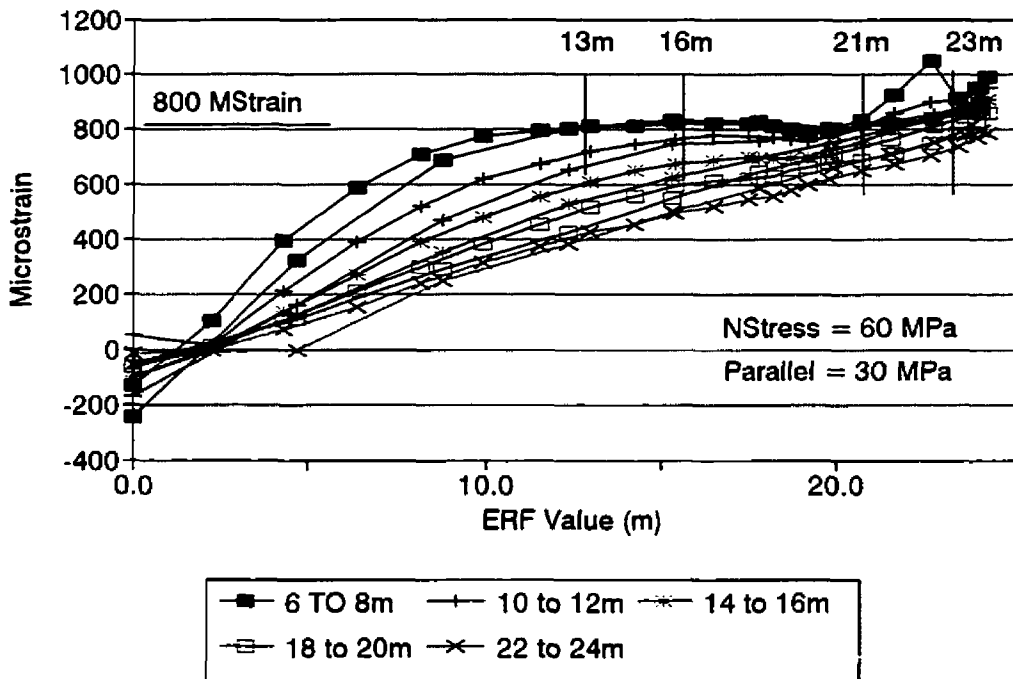


Figure 7.8 Zone of constant strain above a 50m by 50m by 5m opening with stresses 60 MPa normal and 30 MPa parallel to the opening surface.

Elastic MStrain Above an Irreg. surf. Vs ERF Plotted at Various Distances



ERF Value at maximum strain	
Anchors	ERF Value
6 to 8m	13m
10 to 12m	16m
14 to 16m	21m
18 to 20m	23m
22 to 24m	Not reached (24m?)

	Magnitud	Trend	Plunge
Sigma 1	60 MPa		90
Sigma 2	30 MPa	90	0
Sigma 3	30 MPa	180	0
E (GPa)	60 GPa		
Poisson's	.25		

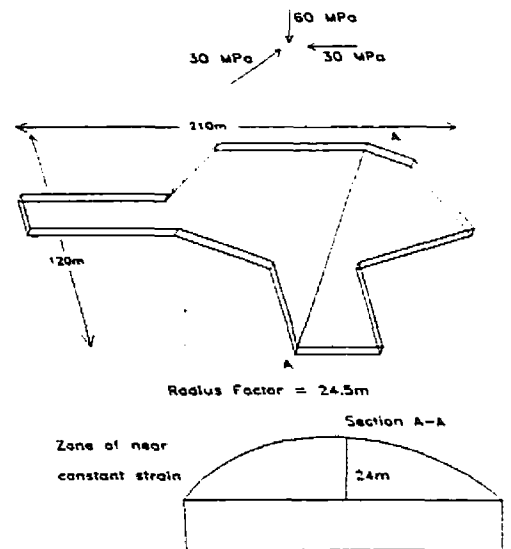


Figure 7.9 Zone of constant strain above an irregular opening with stresses 60 MPa normal and 30 MPa parallel to the opening surface.

$$\epsilon_{(a-b)} = (.64) \frac{\sigma_n(1+\nu)}{E} \quad (\text{Eq. 7.10})$$

When $ERF \geq$ distance from the surface to points 'a' and 'b'

It is interesting to compare equations 7.9 and 7.10 which suggest that the maximum strain close to an opening with a planar surface would be less than the maximum strain near a spherical opening. This difference may be partially due to higher induced tangential stresses which can be expected near a spherical surface which would create higher normal strains.

With experience, the on site engineer can develop a reasonable approximation for the elastic constants, Poisson's ratio and Young's modulus, or Young's modulus can be estimated from rock mass classification (Sect. 2.2.4). Some general modelling can give the engineer some estimate of stresses in the area of interest. Based on Equation 7.10 the engineer can quickly determine if instrumentation readings are within the probable elastic range of the rock mass and can hence be ignored. If the elastic limits are exceeded over a certain distance into the rock mass, more detailed investigation would be required. This equation is not a substitute for numerical modelling and can only give a first approximation of elastic deformation limits. Chapter 8 gives examples of field data which have been used to delineate the elastic zone of rock adjacent to a hanging wall.

7.4 RELAXATION ZONE AND STRAIN ABOVE A PLANAR SURFACE

In the immediate vicinity of large open hanging walls, the rock mass is in a state of low confinement and this zone is often referred to as the relaxation zone, or zone of tension. In the field, a fractured rock mass cannot support tensile stress so a zone of low confinement is generated. In this relaxation zone, the absence of significant clamping stresses is often cited as

one of the main reasons for instability. As discussed in Section 3.2, only .2 MPa of clamping stress can support a 10 metre cube of rock with a 30° assumed friction angle. Since very minor clamping stresses will support a substantial dead weight of rock, the relaxation zone can be treated as the volume of rock where one of the principal modelled stresses is tensile.

Work has been conducted to look at various excavation geometries in different stress fields to assess the maximum extent of tensile stresses as a distance normal to the opening surface (Clark, 1996). The maximum extent of tensile stresses occurs at a point perpendicular to the centre of the surface and the tensile stresses are oriented parallel to the excavation surface. The various geometries modelled are shown in Figure 7.10. The maximum principal stresses modelled were always perpendicular to the opening with k ratios ($\sigma_{\perp}/\sigma_{\parallel}$) of 1.5, 2.0 and 2.5. The RF value (maximum ERF value) of the excavation surfaces assessed were plotted against the corresponding maximum depth of relaxation and linear relationships were obtained for each of the stress ratios modelled. Figure 7.11 shows the plotted maximum depth of tensile stress versus the surface radius factor value. For a k ratio of 1.5, only a negligible tensile zone is indicated. For a k ratio of 2.0, the depth of relaxation is approximately .16 times the corresponding surface radius factor and for a k ratio of 2.5, the maximum depth of relaxation is approximately .3 times the surface radius factor.

Figure 7.11 has interesting ramifications when comparing the potential depth of failure and the optimum depth of support in various mining conditions. Many ore bodies consist of a single tabular planar seam. Stresses tend to be oriented parallel and perpendicular to the deposit. During the later stages of mining an area, stresses normal to the ore body increase significantly over pre-mining stress levels while the stresses parallel to the ore body tend to change much less. During the later stages of mining this results in a very high effective stress ratio k due to high induced stresses normal to the ore body. Hanging wall dilution and stability problems

MODEL GEOMETRIES EXAMINED

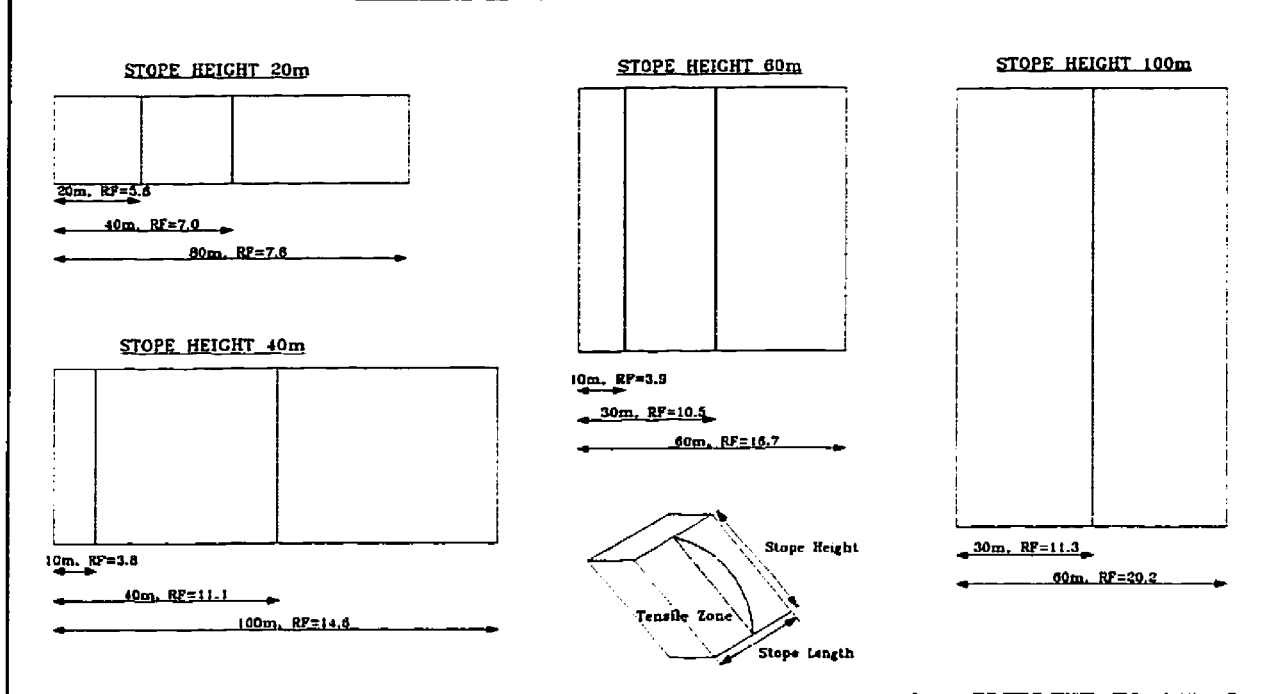


Figure 7.10. Excavation geometries modelled to determine the extent of the tensile zone (From Clark, 1996).

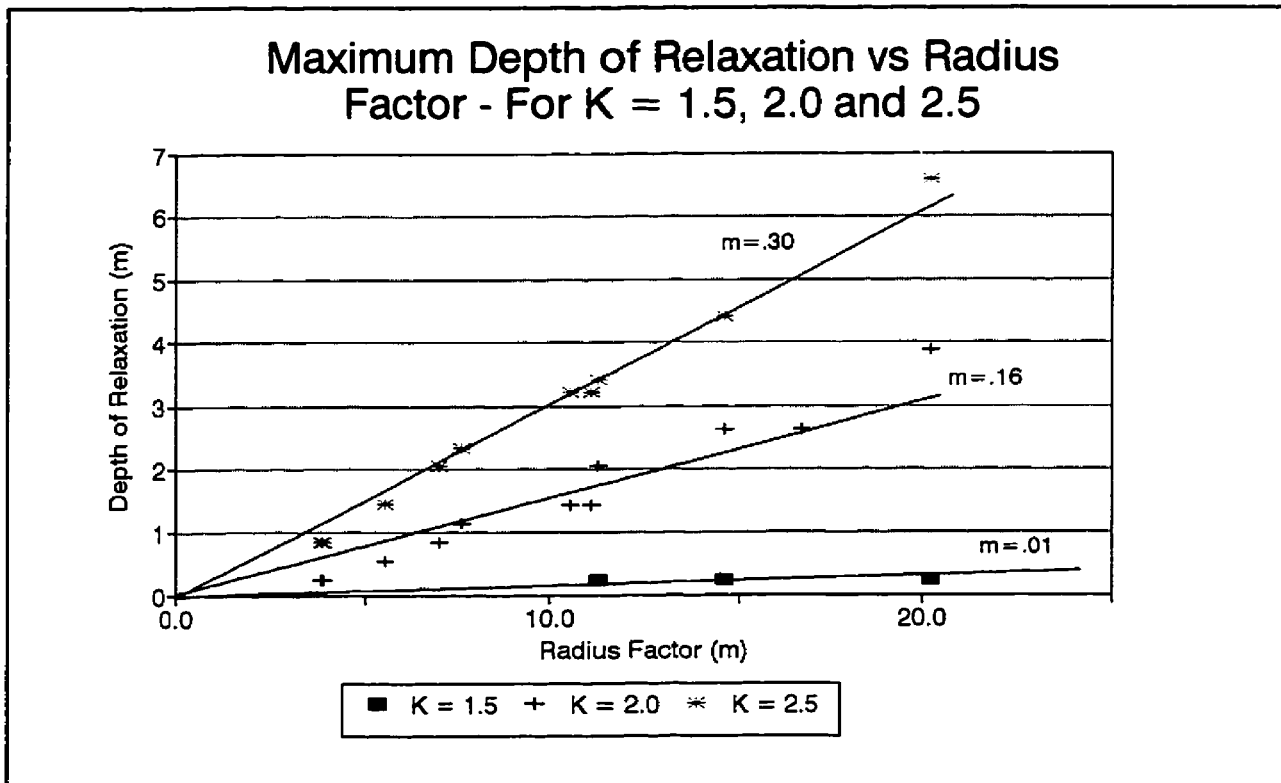


Figure 7.11 Maximum depth of relaxation for varied surface RF values and stress ratios (After Clark, 1996).

generally increase during the later mining stages (Bawden, 1996). This may partially be due to the increased tensile zone around stope hanging walls due to the high stress ratio. For secondary stopes or stopes in areas of high extraction where stresses perpendicular to the ore body are high, increased support length and density will generally be needed, compared to areas with lower stress ratios.

7.5 SUMMARY

Any deformation measurements taken between two points can be expressed as a strain value between the points. Several guidelines for interpreting strains close to an excavation have been presented in this chapter and are summarized below:

- The maximum strain, normal to an excavation surface, converges to a maximum value and this value is approximately constant when the distance from the surface is less than the effective radius factor on the surface.

- An empirical equation has been determined for relating the maximum strain between points perpendicular and near the boundary of an opening and the stress normal to the opening prior to creating the excavation. This relationship will provide the ground control engineer with the following information:

1. A quick estimate of the maximum elastic movement expected from instrumentation can be made. This gives the engineer a threshold below which instability should not be expected.

2. An approximation of field stresses normal to an excavation can be made based on simple extensometer data if a level of constant strain between anchors is reached with continued mining.

- An empirical relationship has been generated between a hanging wall radius factor, field stress ratio 'k' and the maximum extent of tensile stress. This relationship provides

insight into why hanging wall stability deteriorates in areas of high induced stress normal to the hanging wall and may also assist in deciding ground support requirements.

The empirical relationships for estimating the maximum elastic strain normal to an opening and the maximum extent of tensile stresses are not suggested as substitutes for numerical modelling. The suggested relationship between elastic strain above an opening, field stress and elastic material properties is not rigorous. It has, however, been shown to be valid for regular and irregular opening geometries and the most common range in stress ratios. For assessing movements above large open hanging walls, where the up dip and on strike opening dimensions are much greater than the width, the proposed relationships are valid. In more complex geometries with multiple openings, and above narrow stope backs where high stresses are induced parallel to the back, the approach may not be reliable and computer modelling may be indicated.

Chapter 8 presents some field data on measured deformations on open stope hanging walls. Some of the techniques for assessing deformation that have been discussed will be applied to this field data.

CHAPTER 8

FIELD DATA ON HANGING WALL DEFORMATION

8.1 INTRODUCTION

The previous chapters have looked at theoretical elastic surface deformation and how it varies with surface geometry. This chapter looks at collected field data and compares it with mining geometry. Experience is required for the interpretation of deformation data, collected primarily with extensometer instrumentation, and it is not always straight forward. It is often based on whether or not the rate of movement is increasing or decreasing with time (Figure 1.1). This approach requires sufficient data to determine if movement is stabilizing or accelerating with time. Figure 3.1 shows some typical field data plotted against time. Deformation data are collected with the goals of warning of approaching failure, improving the understanding of elastic and non elastic deformation, as well as predicting continued deformation with mining. This chapter presents an approach for interpreting deformation data with respect to opening geometry, predicting continued deformation with mining and differentiating between elastic and non elastic deformation.

Extensometer data are most often plotted as deformation versus time. The deformation can be expressed as a change in the distance from the instrument collar to the various anchor points, a change in the distance between anchors expressed in millimetres or as a microstrain occurring between anchors. If mining is occurring during the monitoring period, blasting dates are indicated on the graph. A jump in measured deformation often coincides with the mining activity (Figure 8.1). Plotting movement with time is a realistic approach for assessing the stability in areas where engineering activity is not currently changing the geometry of the area

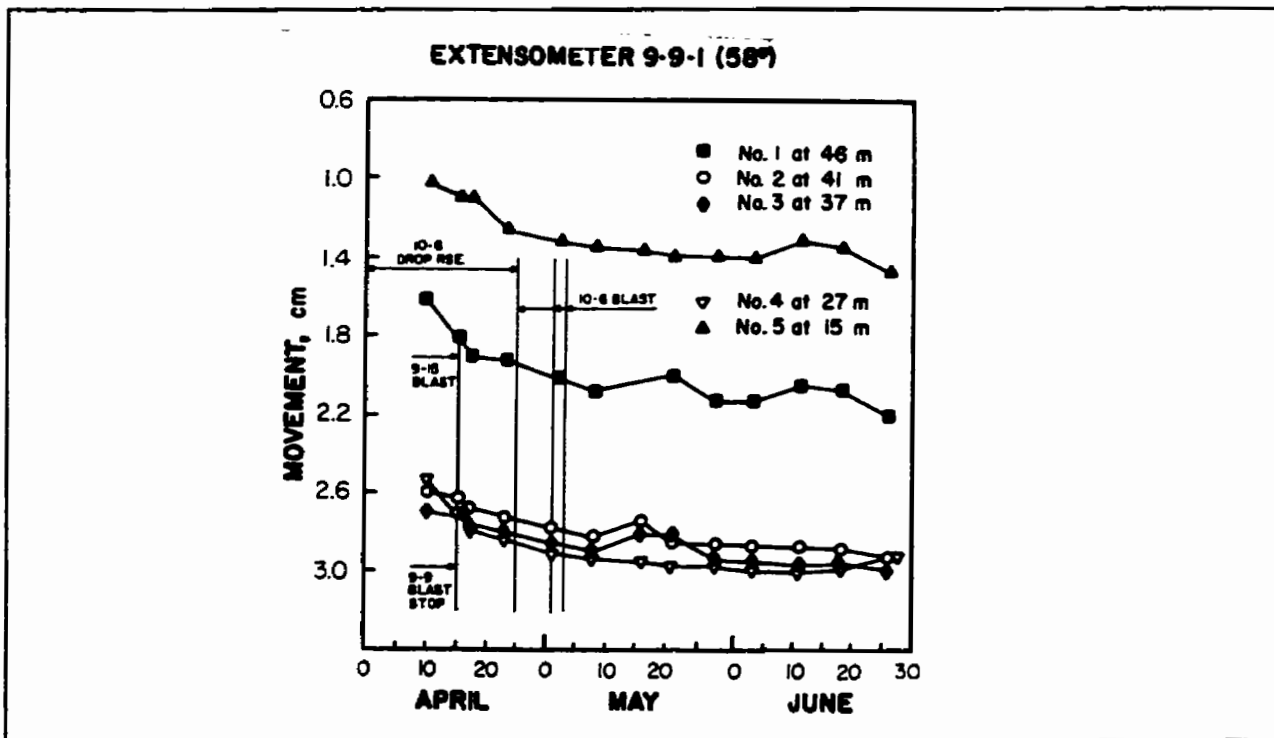


Figure 8.1 Typical field data showing deformation response to mining (From Bawden and Milne, 1987).

monitored. When local mining is occurring, this changing geometry is usually the predominant factor controlling deformation. Time dependent creep may still be occurring and the rate of this movement is important to note, however, deformation versus changing geometry should be initially considered.

Field data have been collected from several mines and data from both Mount Isa Mines and Brunswick Mine are presented in this section. Mount Isa mine is one of the largest underground mines in Australia and data have been collected from the Lead Mine section of the ore body. The data from Mount Isa mines consist of several instrumented stope case histories collected over the last 17 years. Brunswick Mine is a 10,500 tonne per day lead-zinc-copper-silver producer located in northern New Brunswick. At Brunswick mine the data set is from a study of the mining of a heavily instrumented sill pillar, funded by the Mining Research Directorate, Brunswick Mining and the Noranda Technology Centre (Hudyma et al, 1994). The

mining geometry in each of the case histories in this section consist of an advancing stoping front without the addition of backfill. The abutments for each of the stope geometries consist of rock.

8.2 APPROACH TO FIELD DATA ANALYSIS

Hanging wall deformation has not been analysed with respect to time because of the changing conditions due to continued mining. For each of the case histories, data analysis starts with the undercutting or mining by of the extensometer anchors. The term "mining by" an instrument location refers to the point at which the mining front reaches the longitudinal projection of the instrument location. Figure 8.2 shows a stope and with a hanging wall

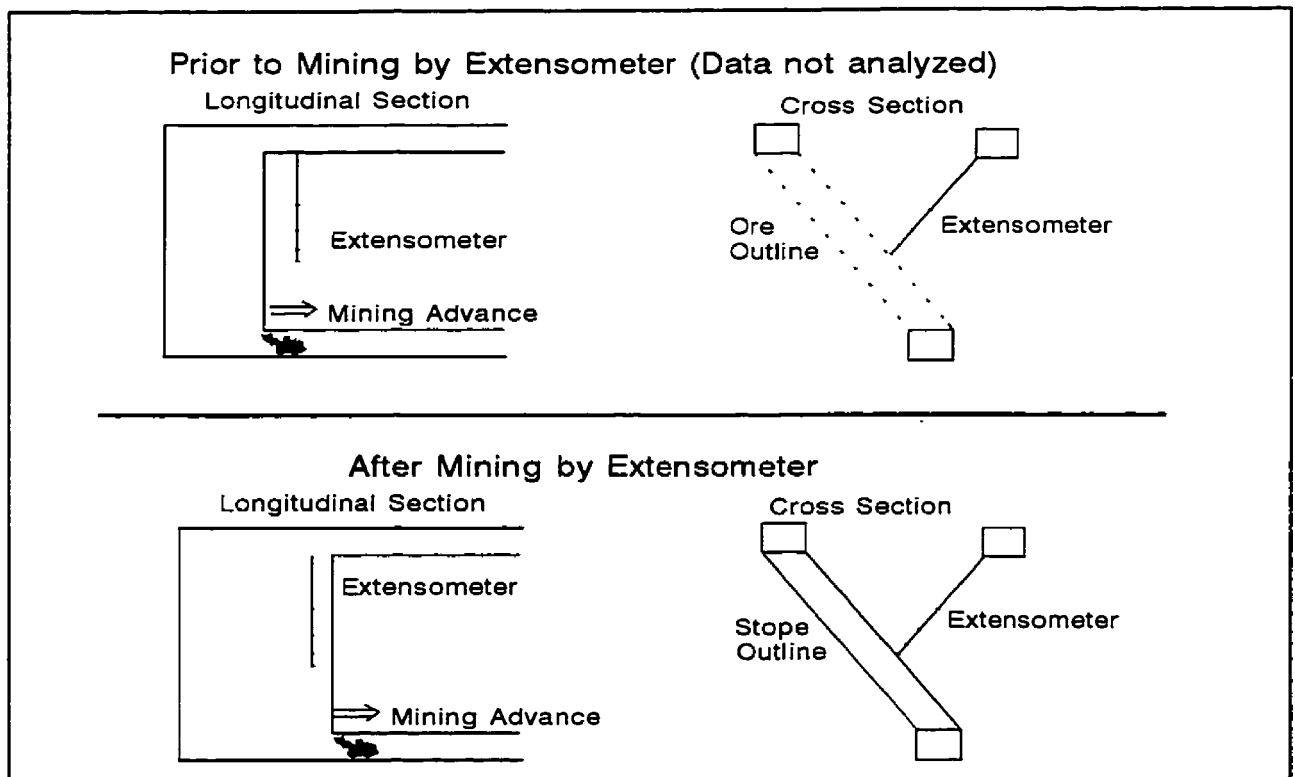


Figure 8.2 Hanging wall extensometer immediately before and after mining past the instrument - (stope "mine by").

extensometer immediately before and after mining by the instrument location. Stress related deformation while instruments were located in stope abutments is ignored (prior to mining by).

The position of each instrument and anchor location is projected onto a true longitudinal view of the stope hanging wall, as shown in Figure 8.3. With each mining step after the extensometer has been mined by, the effective radius factor (ERF) value is calculated for each anchor location, with respect to the new abutments. For each mining step, initial stable deformation readings for each anchor are determined. Some time dependent creep may be occurring, however this is usually not significant for the short time periods between stope blasts, unless the anchor position is close to failure.

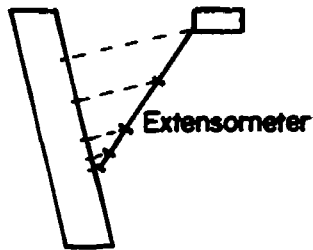
The calculated ERF value for each extensometer anchor and mining step is then plotted against total anchor deformation. Deformation is expressed as total movement from the collar, movement between anchors or microstrain between anchor points. Based on these graphs, insight into the rock mass response to mining as well as the effect of future mining can be made.

The previous section has shown how the effective radius factor of a point on a surface can be related to the elastic deformation of the point on or above the surface. This section will look at non-elastic and elastic deformation, collected in the field, and show how it relates to mining activity

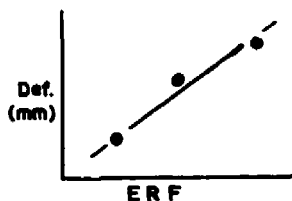
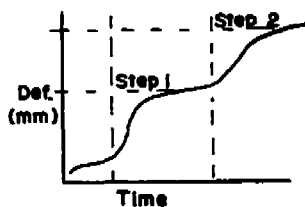
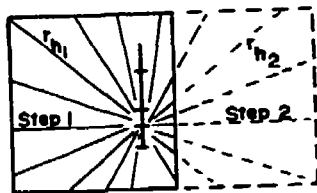
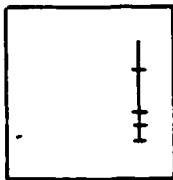
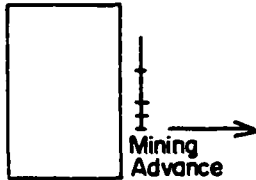
8.3 MOUNT ISA MINE

Data from several instrumented stoping blocks were collected from the Lead Mine at Mount Isa. A general description of the Mount Isa ore body is summarized from the brochure, Mount Isa Today (1990). The Mount Isa Mine (MIM) is located in the valley of the Leichhardt River in the northwestern side of Queensland, Australia. The ore body consists of deposits of

Vertical Section



Longitudinal Sections



GENERAL ANALYSIS APPROACH

Extensometer anchor locations are projected onto a true longitudinal view of the stope hanging wall

Initial mining places the extensometer on the stope abutment. Deformation during this stage is ignored.

The extensometer has been "mined by". Resulting deformation is obtained for each mining step

Effective radius factor values are calculated for each mining step.

$$ERF = \frac{.5}{\frac{1}{n} \sum_{\theta=1}^n \frac{1}{r_h}}$$

Initial stable deformations values for each extensometer anchor are determined for each mining step.

Deformation from collar or microstrain between anchors are plotted against the extensometer ERF value for each mining step.

Figure 8.3 General analysis approach for relating opening geometry, instrument location and resulting deformation with mining.

copper and silver-lead-zinc in parallel seams of a shale formation about 1000 metres thick.

The lead-silver-zinc ore body consists of multiple parallel beds dipping at about 70° to the west, as shown in schematic cross section in Figure 8.4. The orebody hanging walls consist of bedded shales of varied strength. Hanging wall stability and dilution are always a concern and a great deal of effort and research has gone into studying and instrumenting the stope hanging walls.

In general the ore body hanging wall consists of three predominant discontinuity sets, described by Windsor, Bywater and Worotnicki (1984):

- Bedding Planes are very continuous and weak with little or no cohesive strength and angles of friction typically in the order of 10°. The bedding planes are parallel and form the hanging wall surfaces.
- Steep north and south dipping joints which are continuous up dip but tend to terminate on bedding.
- Steep east dipping joints, often with calcite infilling.

The major controlling structure for the hanging walls is the spacing, strength and continuity of the bedding planes. A site specific classification system has been developed at the mine which is predominantly dependent on bedding plane spacing.

Three main mining methods are used in the silver-lead-zinc orebody consisting of cut and fill stoping, open stoping and bench stoping. In both the open and bench stoping mining methods, large open hanging walls may be exposed and the control of hanging wall dilution is a major concern.

A substantial amount of instrumentation data on hanging wall behaviour has been collected at the mine site. The closely spaced parallel ore bodies have made access for extensometer instrumentation relatively simple. Figure 8.5 is a typical cross section showing

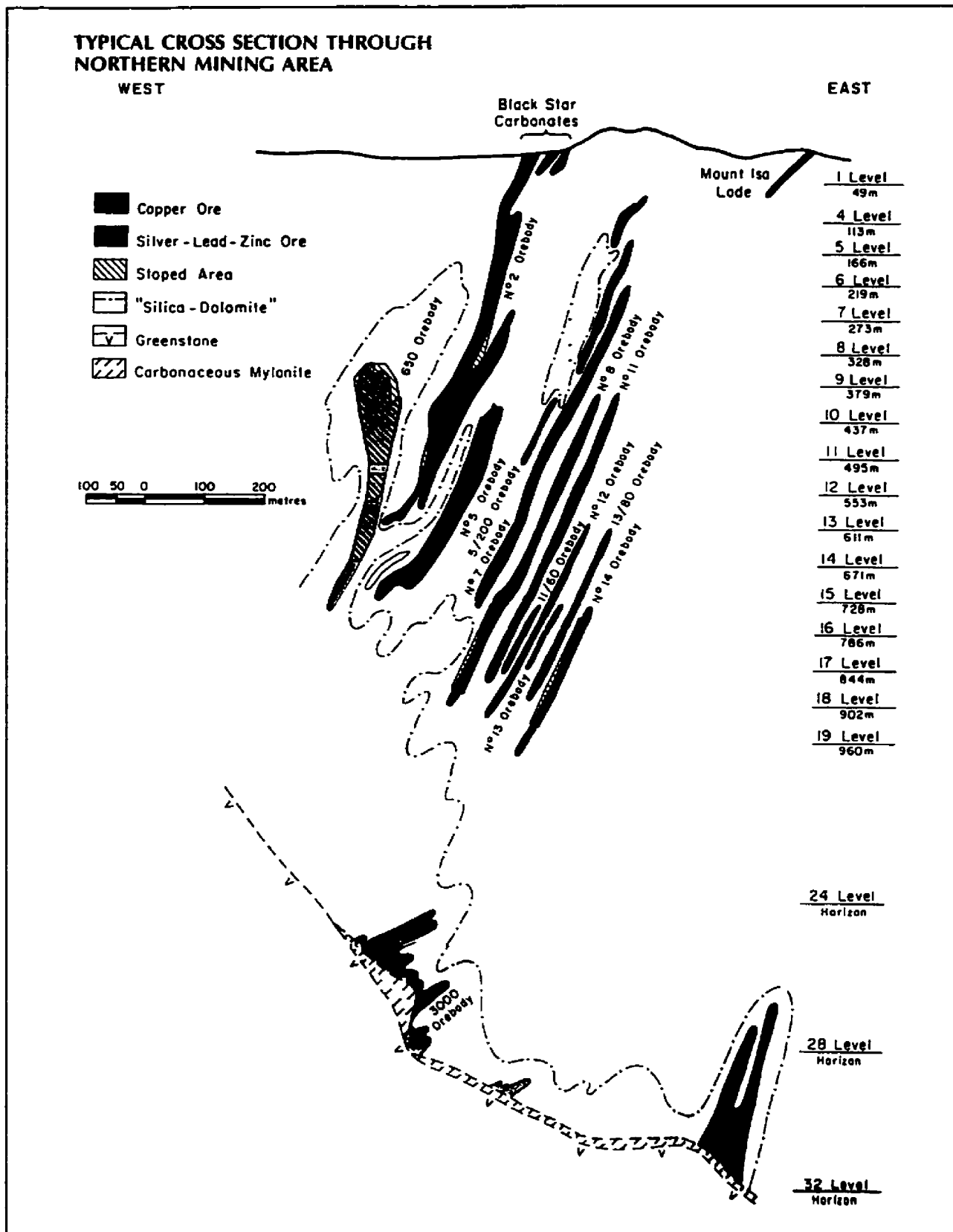


Figure 8.4 Typical cross section showing parallel ore zones at the Mount Isa lead mine. (Isa Today, 1990)

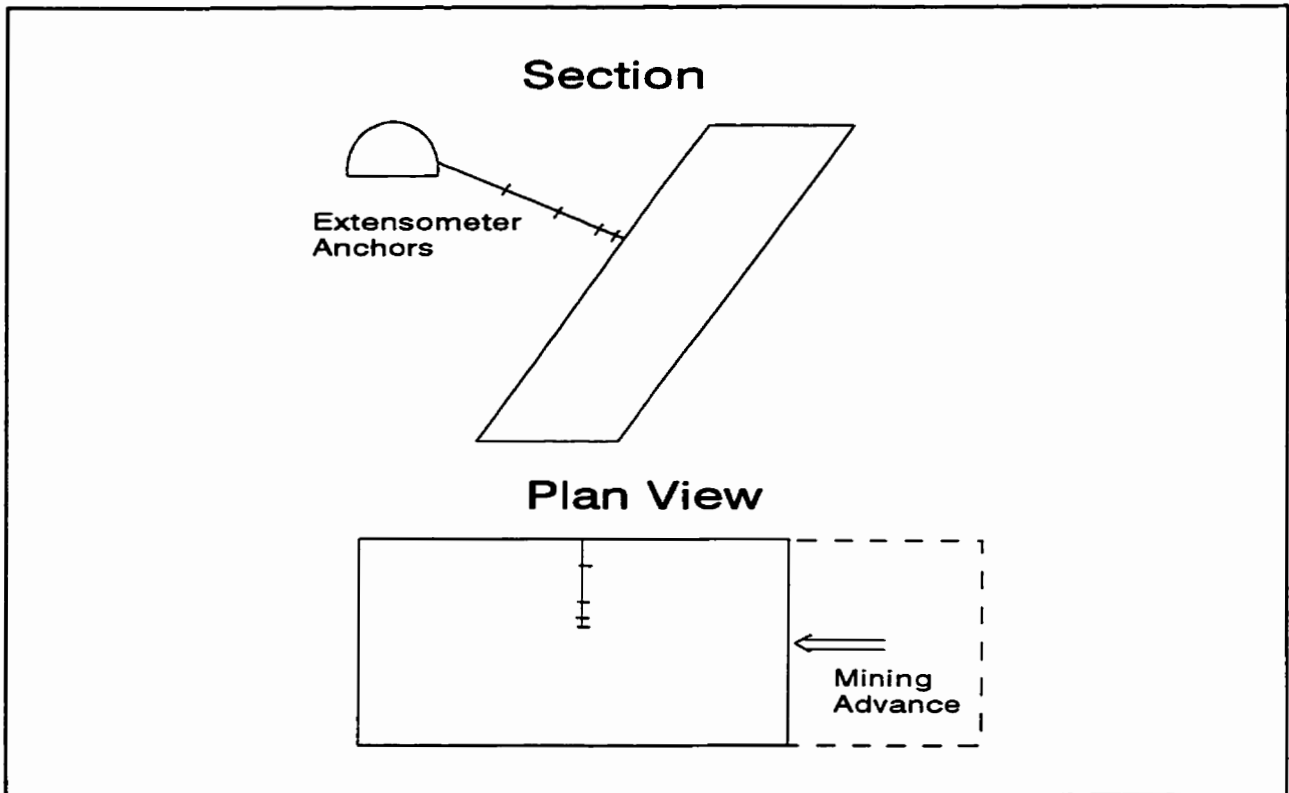


Figure 8.5 Typical hanging wall extensometer configuration.

the general layout for the hanging wall instrumented stopes.

Hanging wall deformation data have been obtained from numerous stopes and a summary of the available data for each area is given in the following sections. Unless otherwise noted, the instrumentation summary in each of the following sections is taken from internal "Mount Isa Memorandums" written by the author during the course of his studies. The instrumentation was installed and the data was gathered by staff at Mount Isa Mines.

8.3.1 Mount Isa Stope 5FP1

Instrumentation was installed from the 5HP1 12A level bench to monitor the hanging wall behaviour of the 5FP1 bench stope. Data from two extensometers were available and they showed the hanging wall deformation as mining advanced. Figure 8.5 shows a cross section of the general mining and instrumentation geometry. The data were obtained from internal Mount

Isa Mines documents including an instrumentation summary by Milne (1994). Each extensometer was installed with six anchors and the deepest anchor was located .5 metres from the hanging wall contact.

A bench stoping mining method was followed in this area, which is similar to a modified Avoca method. This mining area was in a highly stressed abutment and N-Fold modelling estimated stresses in the order of 40 MPa, normal to the ore body. The up dip extent of the stope was 53 metres and rock formed the abutment on all sides of the stope. The final instrumentation readings coincided with an open stope strike length of 43 metres.

The extensometers were read for about 3 months from February 26 to June 7, 1993, however, automatic data recording was not available in this area so there are gaps in the readings. When the first extensometer was undercut the bench stope was open to a strike length of 24 metres.

Figure 8.6 shows graphs of measured hanging wall deformation versus time, as well as versus the effective radius factor values for the extensometers. The limited data available were plotted as movement between anchors versus time, with the each blast indicated as a vertical line. Each blast resulted in a new ERF value for the extensometer location and movement between the collar and the bottom anchor was also plotted. A reasonable trend of increasing movement between the extensometer collar and bottom anchor versus ERF was obtained. Based on the graphs of deformation versus time, it would be difficult to estimate the expected deformation if an additional blast had been taken. Based on the deformation versus ERF graph, an approximation could be made on the effect of further mining on expected deformation.

8.3.2 Mount Isa Stope 5HP1

The 5HP1 stope is parallel to the 5FP1 stope and was placed in a stress shadow after

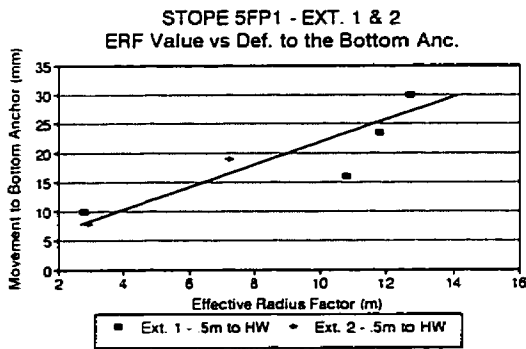
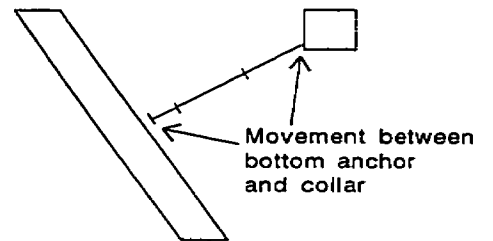
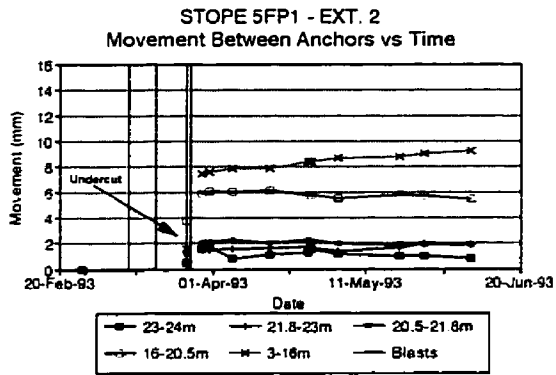
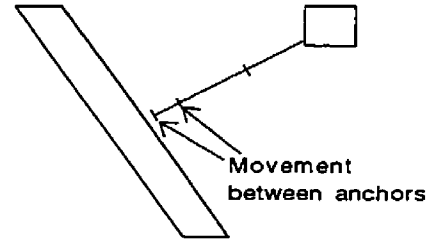
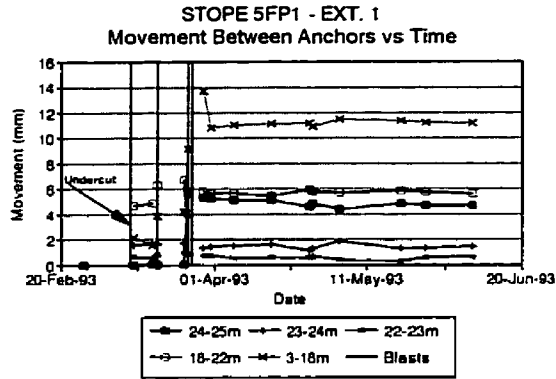


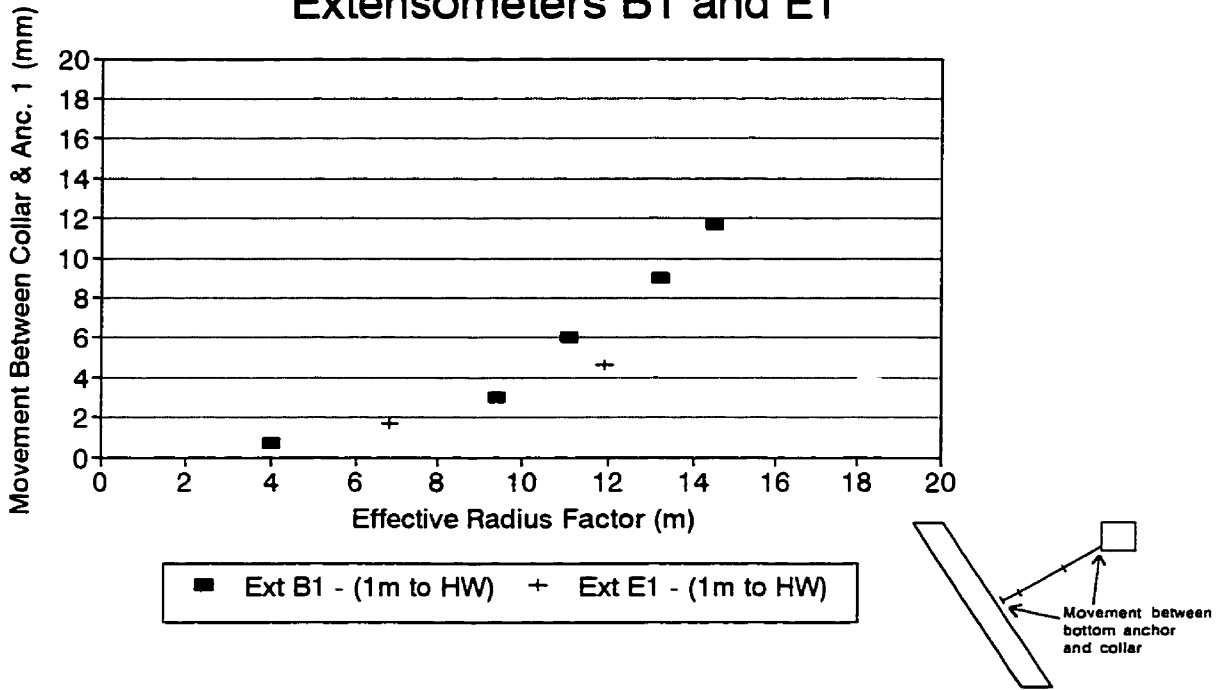
Figure 8.6 Deformation versus time and ERF values for mining the 5FP1 stope.

mining of the 5FP1 stope. Figure 8.5 shows the general instrumentation geometry in cross section. Instrumentation was installed from a hanging wall instrumentation drift to monitor hanging wall deformation, cable support load and blasting in the 5HP1 hanging wall panel (Villaescusa, 1996). Monitoring was conducted from the beginning of April to the middle of May, 1994 when mining cut off access to the instrumentation drift. Two of the instruments, extensometers B1 and E1, were located near the vertical centre of the stope and were read as mining activity changed the distance from the instruments to the supporting abutments. Prior to the loss of access, the maximum stope dimension was approximately 53 metres on strike and 55 metres up dip.

Extensometer B1 was the first one mined by, and showed a maximum of about 12mm movement between the collar and the deepest anchor, located just above the hanging wall contact, at a depth of 23 metres. A maximum strain of $2000\mu\epsilon$ was measured between the bottom two anchors. These movements are less than those recorded during the mining of the 5FP1 stope located in a parallel ore horizon. The mining of 5FP1 occurred prior to 5HP1 mining activity and the majority of the stresses normal to the ore body were blocked.

Figure 8.7 shows the change in movement between the collar and the deepest anchor as well as the microstrain between the bottom two anchors with the changing effective radius factor values with mining. Both instruments plotted together show consistent trends of increasing deformation with increasing ERF values. Based on the empirical relationship suggested in Section 7.3 (Eq. 7.10), complete relaxation of the immediate hanging wall, between the bottom two extensometer anchors, should occur at an ERF value approximately equal to the furthest anchor distance from the open face. There are 3 metres between the bottom 2 anchors, and the bottom anchor is up to about 1 metre from the open face. This suggests that movement between the bottom two anchors which occurs after an ERF of approximately 4 metres, is caused by non-

Deformation Vs Effective Radius Factor Extensometers B1 and E1



Microstrain vs Effective Radius Factor Extensometers B1 and E1

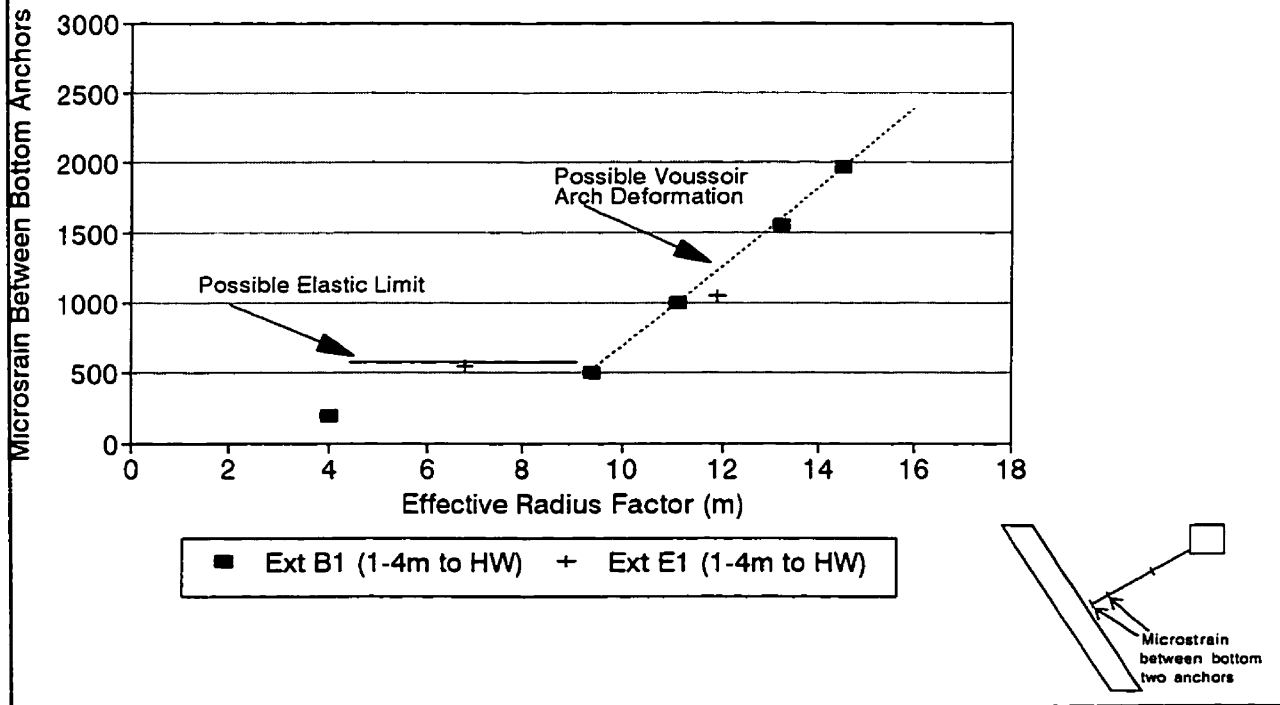


Figure 8.7 Deformation versus ERF values for mining in the 5HP1 stope.

elastic deformation. Movement between anchors stabilizes at about 500 microstrain at an ERF value of about 5 metres and remained stable until an ERF value of 9 metres. If 500 microstrain corresponds to complete relaxation between these anchors, and a rock mass modulus of 25 GPa and Poisson's ratio of .25 is estimated, an initial stress of 15 MPa was present normal to the ore body at the time of extensometer installation. This is based on Equation 7.10 presented in Section 7.3, relating stress and strain close to and normal to planar surfaces. This low stress estimate is reasonable in the stress shadow of stope 5FP1 and suggests elastic deformation is occurring up to an ERF value of 9 metres. When an ERF value of 9 metres is exceeded, microstrain increases rapidly indicating the hanging wall is no longer behaving elastically (Figure 8.7). There is a linear increase in strain with ERF values. This linear increase in strain may be associated to the deformation behaviour due to voussoir arch action.

It is interesting to note that if about 1200 microstrain are added to the measurements recorded, the microstrain versus ERF values correspond reasonably well to the data collected in the parallel stope 5FP1, shown in Figure 8.6. This 1200 microstrain would be a reflection of the higher stresses present during the mining of stope 5FP1 and would correspond to a stress difference of 30 MPa for a 25 GPa rock mass.

8.3.3 M665 Stoping Triplet

A detailed report was written concerning the rock mechanics aspects of mining the M665 stoping triplet which consists of a comprehensive summary of an extensively instrumented stoping block. The input data and a summary of mining activity were obtained from an internal MIM report. Much of the following summary is taken from an internal MIM File Note by Milne, 1994.

The M665 Triplet is located in the 8 orebody between levels 15B and 13. The study was

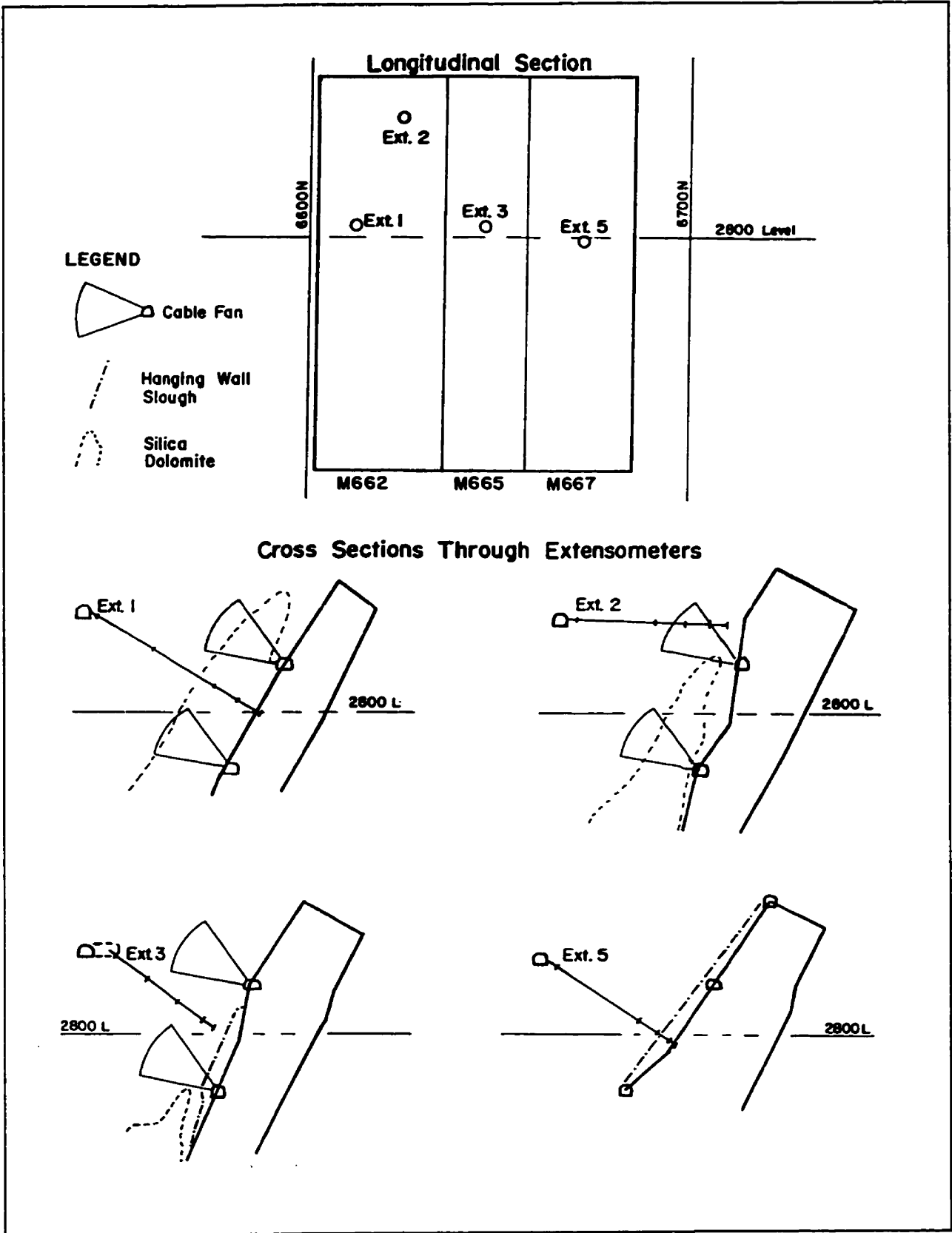


Figure 8.8 Hanging wall Instrumentation for the M665 Stopping Block (After MIM Internal Report, 1979)

designed to record the behaviour of the rock and backfill within this stoping block to assist in the establishment of design principles. The triplet consisted of three individual stopes M662, M665 and M667, shown in Figure 8.8. The mining sequence consisted of Mining M667 followed by M662. During the mining of M662, M667 was backfilled. M665 was then mass blasted into the open M662 stope. Maximum open stope dimensions were about 105 metres vertical and 55 metres on strike (stopes M662 and M665 together).

This instrumented stope study included 9 extensometers, a rock noise event counter, as well as CSIRO overcoring at two separate stages of mining. Modelling was also done to estimate the elastic rock response to mining. A detailed history of blasting and a visual assessment of hanging wall performance was also made. Stress measurements prior to mining indicated stresses perpendicular to the ore body with a magnitude of approximately 24 MPa.

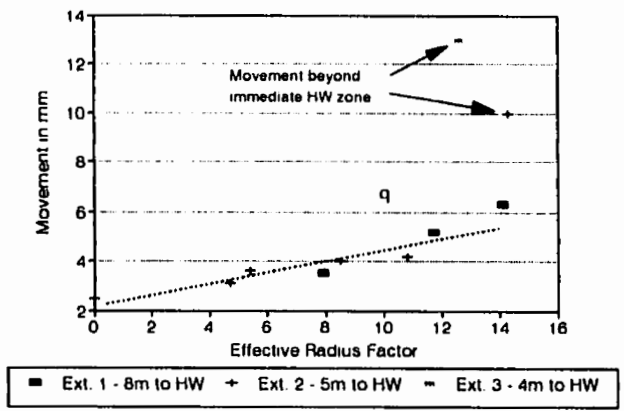
The instrumentation of interest in this review are the extensometers located in the stope hanging wall recording deformation due to mining. Four extensometers, 1, 2, 3 and 5 were located in the stope hanging wall and recorded deformation due to mining by the instrument anchors. Extensometer 3 was located above stope M665 and was undercut only after the mass blasting of this stope resulting in only one ERF value and corresponding deformation. The ERF value for Extensometer 3, after the mass blast of stope M665, was determined by treating the backfilled abutment of stope M667 the same as rock. This is not a conservative assumption, however, little deformation can be expected at the immediate stope abutment (Chapter 9). Figure 8.8 shows the location of these instruments on longitudinal and cross sections.

The deformation between the reference anchor and the anchor closest to the hanging wall was also averaged for each significant blast. This movement was plotted against the ERF value on four graphs shown in Figure 8.9. The data from the extensometer anchors located closest to the hanging wall were analysed. Deformation was assessed as total movement between the

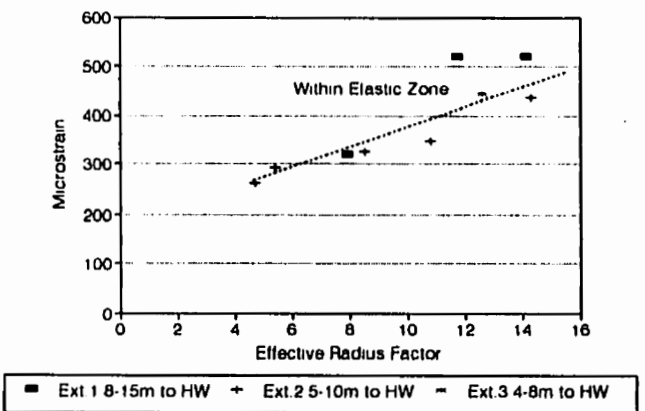
Figure 8.9 Extensometer deformation above the M665 open stope, plotted against the ERF value.

M665 TRIPLET - EFFECTIVE RADIUS FACTOR Vs DEFORMATION

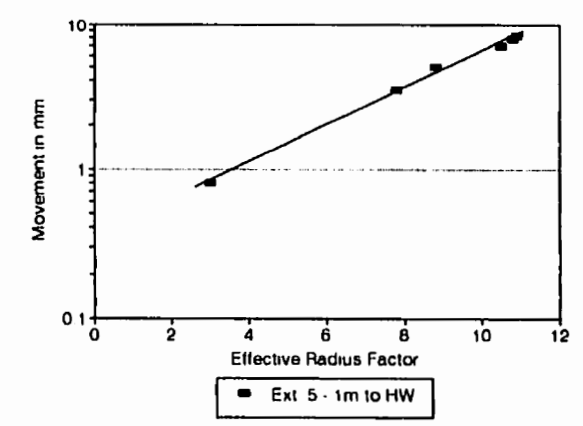
ERF Value versus Movement from Collar to the Bottom Anchor (4 to 8m from HW)



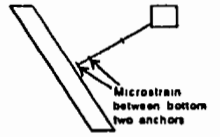
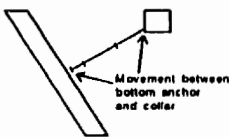
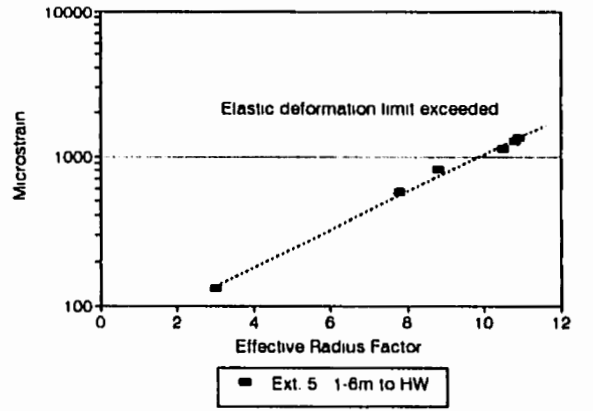
ERF Value versus Microstrain Between the Bottom 2 Anchors within 15m of HW



ERF Value versus Movement from Collar to the Bottom Anchor 1m to HW



ERF Value versus Microstrain Between the Bottom 2 Anchors (1 to 6m from HW)



reference anchor and the anchor closest to the hanging wall as well as microstrain between the two anchors closest to the hanging wall. Data from extensometer 5 were plotted separately since the bottom anchor was only about 1 metre from the hanging wall. Extensometers 1, 2 and 3 were plotted together since these instruments monitored a zone of rock between 4 to 15 metres from the hanging wall.

The bottom anchor in Extensometer 5 was located about 1 metre above the free stope surface and showed an exponential increase in movement, relative to the collar, with increasing radius factor. The bottom anchors in Extensometers 1, 2 and 3 were located 4 to 8 metres from the open hanging wall and showed a linear increase in movement with increasing ERF values. These graphs compare the immediate (1 metre) and more deep seated (4 to 8 metre) hanging wall deformation behaviour.

The plots of microstrain between the bottom two anchors versus ERF values both show a consistent trend of increasing microstrain with ERF values. For extensometers 1, 2 and 3 the bottom two anchors are between 4 to 15 metres from the hanging wall. A linear increase in microstrain with increasing ERF values is observed. Movements should be within the elastic range up to approximately an ERF value of 15 (Section 7.3), corresponding to an anchor depth 15 metres from the hanging wall. An upper limit to elastic strain can be estimated based on Equation 7.10 and the following approximate rock mass properties:

- $E = 25 \text{ GPa}$
- $\nu = .25$
- $\sigma = 24 \text{ MPa}$

This results in a calculated maximum elastic strain of approximately $780 \mu\epsilon$. Extensometers 1, 2 and 3 show a maximum of under 600 microstrain and are therefore indicating elastic deformation between 4 and 15 metres from the open stope hanging wall.

For extensometer 5, microstrain between anchors 1 to 6 metres from the hanging wall

is recorded. An exponential increase in microstrain with increasing ERF values is observed indicating elastic deformation limits have been exceeded within 1 to 6 metres of the hanging wall. Based on guidelines presented in Section 7.3, movements should be within the elastic range until an ERF value of approximately 6 metres (depth of the deepest anchor) is exceeded. The second microstrain reading is at a ERF value of 8 metres and is approximately at the expected elastic limit.

The graphs indicate it should be possible to extrapolate overall surface deformations over a stope hanging wall based on limited extensometer data. The two plots of microstrain versus ERF values also show an increasing trend of deformation with mining (Fig. 8.9). In the case of the three extensometers where the bottom anchor is 4 to 8 metres from the hanging wall, a relatively linear relationship between strain and ERF values is apparent. The scatter in data is likely due to the 4 to 8 metre range in the relative position of the bottom anchor. This trend is showing elastic movement and ideally would converge to a constant value, assuming elastic deformation continued. In the case of extensometer 5, where the bottom anchor is only 1 metre from the hanging wall, an exponential increase in strain with the ERF value is apparent. This exponential increase in strain is an indication of a less stable immediate hanging wall condition and the magnitude of strain exceeds the expected elastic limits due to stress relaxation normal to the opening. The instrumentation measurements of strain indicate that the load on the installed cable support would not have been high (less than 45 KN).

8.3.4 80G3 Bench Stope Instrumentation

An extensive hanging wall instrumentation program was implemented for the mining of the initial panel stope in the 8 ore body (Figure 8.10). The 80G3 panel stope between levels 18E and 19E, at a depth of about 870 metres, were the first panel stopes in 8 ore body and were

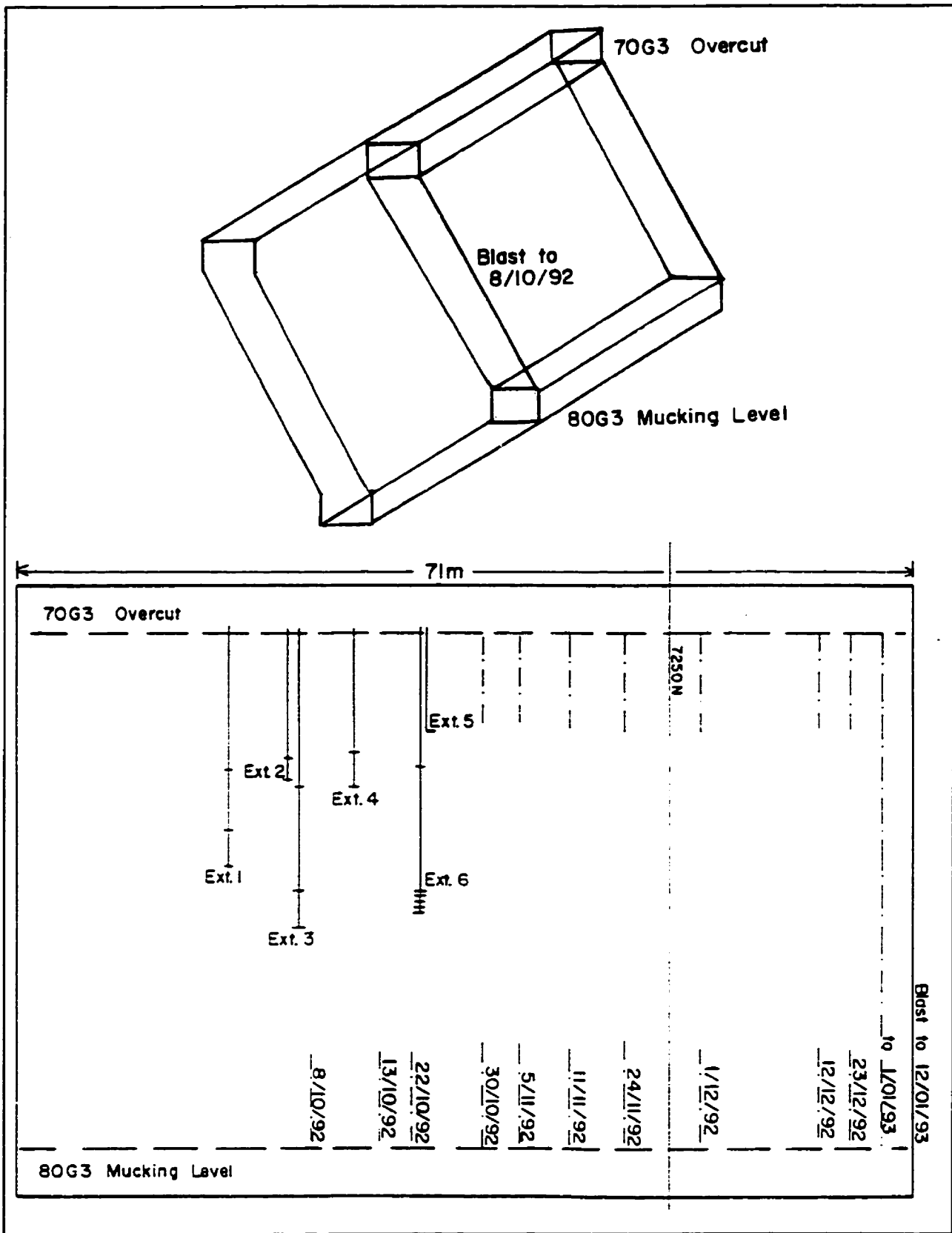


Figure 8.10 Mt. Isa Mine - Stope 80G3 longitudinal view showing extensometer locations and blasting steps.

considered "trial stopes". Stresses in the area of this study were relatively high. Previous mining in the 8 ore body consisted of sub-level open stoping with relatively small hanging wall strike lengths exposed. In order to determine the behaviour of the large 8 ore body hanging wall, an instrumentation program consisting of 6 extensometers was implemented (Villaescusa, 1992 - internal MIM memorandum). The information for this summary was taken from Villaescusa, 1992 and a instrumentation summary by Milne (1994) both internal MIM documents.

The final open stope strike length was 71 metres and the up dip bench dimension was 50 metres. Cable support was installed at sub levels so the total unsupported up dip length was 42 metres. The cable support did not influence the calculation of the ERF values and did little to influence deformation between the sub levels. No significant hanging wall stability problems were noted during the mining of this stope.

Stress modelling was conducted in the 80G3 panel area using the N-Fold computer model. Pre mining stresses in the area were approximately 50 MPa. Mapping was done in the area and it indicated bedding plane breaks in the immediate 5m of hanging wall were in the order of 4 to 5 breaks per metre. Based on ground condition, blasting and stress, a hanging wall stability assessment was made which indicated good hanging wall conditions. Six extensometers on 4 rings were installed to monitor the behaviour of this panel stope hanging wall. The extensometer rings were 5 metres apart and were located in the first half of the stope excavated (Figure 8.10). The bearing and dip of each extensometer hole was surveyed every 5 metres down the hole. The hole and anchor locations are shown in long and cross section in Figure 8.10 and 8.11. The first extensometer had 5 anchors and the other five had 6 anchors each. The monitoring of the hanging wall was divided into one metre wide bands and extensometer anchors were installed to monitor movement at the centre of these bands. The bands were

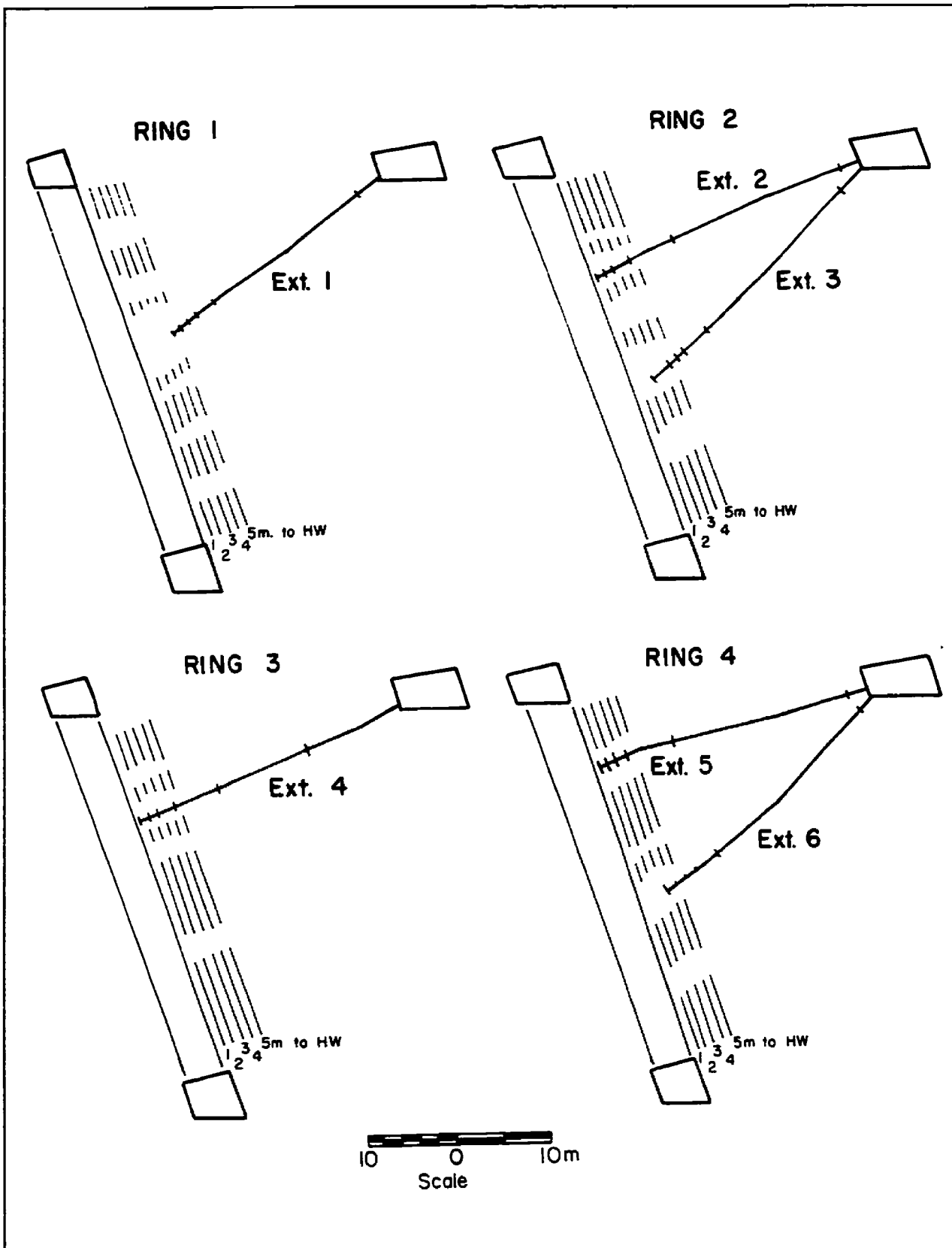


Figure 8.11 Mt. Isa Mine, stope 80G3 - Cross sections showing extensometer locations (After MIM Internal Memo)

defined as a distance from the hanging wall (Figure 8.11).

The measured extensometer deformation has been related to the extensometer anchor distance from the supporting abutment. With each blast and new stope limits, the ERF value at each extensometer location has been assessed. Graphs of the movement from the collar to each anchor, as well as the strain measured between anchors, were analysed with respect to the change in the ERF value with mining. It was found that the graphs of total movement between the extensometer collar and each anchor were not very informative. These graphs represented an average of all the movement occurring in a wide zone from the hanging wall and combined non-elastic movement occurring near the open hanging wall with elastic deformation near the instrument collar. For this reason graphs of total movement between the instrument collar and each anchor have not been included.

Microstrain measured between anchor points was calculated and gives more insight into hanging wall behaviour. Figures 8.12 and 8.13 show microstrain between anchors at .5 to 1.5m, 1.5 to 2.5m, 2.5 to 4.5m, 4.5 to 6.5m, 6.5 to 9.5m and 10 to 30m from the open hanging wall, plotted against the ERF value.

An upper limit to elastic strain, normal to the opening, can be estimated based on equation 7.10 and the following rock mass properties:

- $E = 25 \text{ GPa}$
- $\nu = .25$
- $\sigma = 50 \text{ MPa}$, normal to the hanging wall

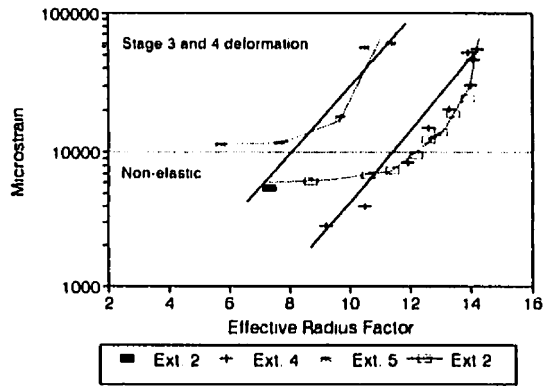
An upper limit to elastic strain, normal to the opening, is approximately 1600 microstrain.

Six graphs of increasing microstrain with ERF value are shown in Figures 8.12 and 8.13. These graphs are plotted on both normal and log scales and show four stages of deformation. These four stages of deformation are defined below:

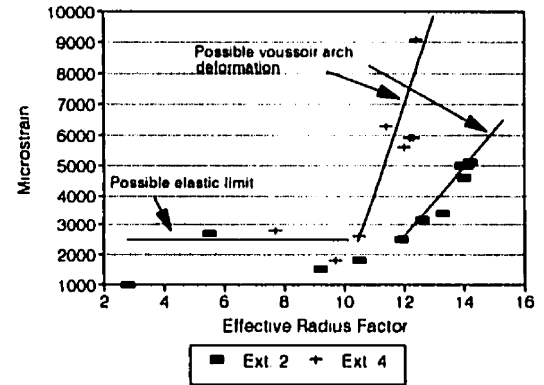
- Stage 1 deformation is defined as deformation occurring below the elastic limit of about

Figure 8.12 80G3 Slope - Microstrain between anchors .5m to 6.5m from the hanging wall, plotted against the ERF value.

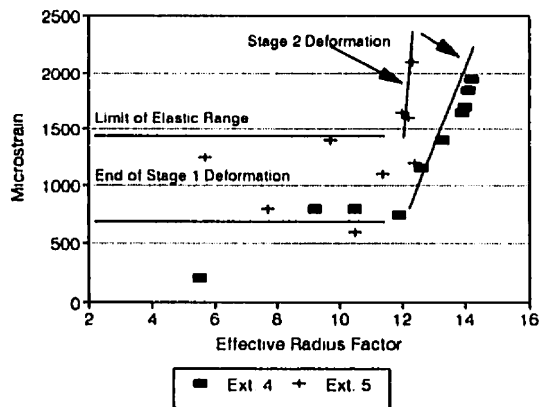
Effective Radius Factor vs MStrain
Between .5 and 1.5m From HW



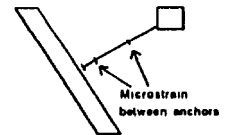
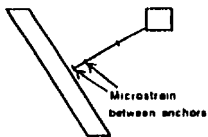
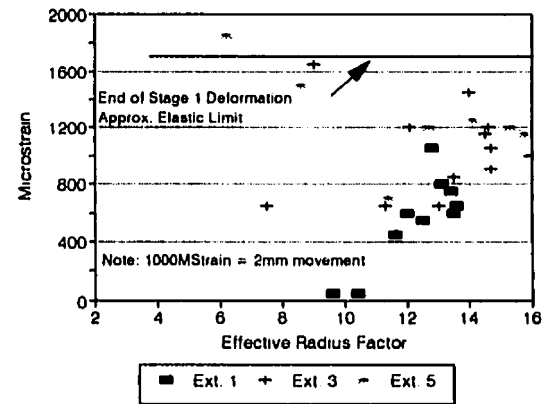
Effective Radius Factor vs MStrain
Between 1.5 and 2.5m From HW



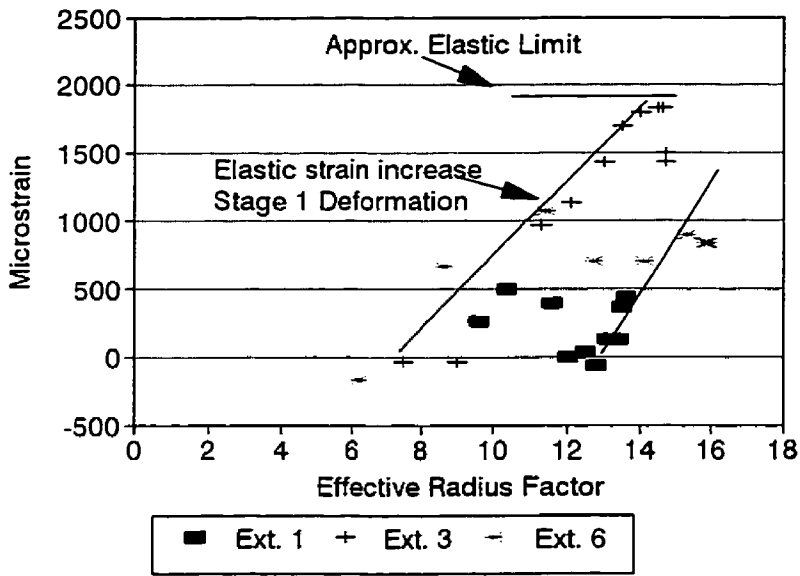
Effective Radius Factor vs MStrain
Between 2.5 and 4.5m From HW



Effective Radius Factor vs MStrain
Between 4.5 and 6.5m From HW



Effective Radius Factor vs MStrain Between 6.5 and 9.5m From HW



Effective Radius Factor vs MStrain Between 10.0 and about 30m From HW

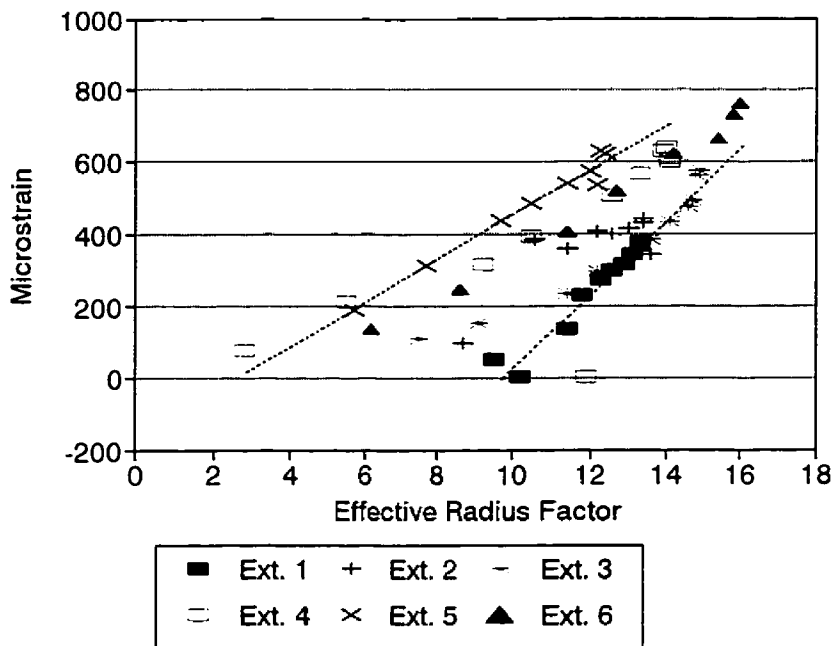


Figure 8.13 80G3 Slope - Microstrain between anchors 6.5m to 30m from the hanging wall, plotted against the ERF value.

1600 microstrain.

- Stage 2 deformation plots as a linear increase of microstrain above the elastic limit
- Stage 3 deformation plots as an exponential increase in microstrain with increasing ERF and shows as a straight line on a semi-log plot.
- Stage 4 deformation appears as an exponential increase in microstrain when plotted on a log scale.

Closest to the hanging wall contact, between .5 and 1.5 metres, the rate of increase in microstrain with the ERF value is exponential on semi-log paper (Fig 8.12). The recorded movements were well beyond the expected elastic range for strain normal to the excavation. This is defined as stage 4 deformation and continued stability of the immediate hanging wall with this rate of movement is unlikely. The final readings between these anchors indicated the ground had already opened 6 centimetres between anchors one metre apart.

Between 1.5 and 2.5 metres from the hanging wall (Figure 8.12), the microstrain between anchors increased exponentially with the ERF value. The magnitude of strain exceeds the predicted elastic limit and this rate of increasing movement also indicates that the rock is no longer behaving elastically.

Between 2.5 to 4.5 metres and 4.5 and 6.5 metres (Fig. 8.12), the measured microstrain between anchors is relatively constant between about 600 and 1500 microstrain, until an ERF value of about 10 metres. This plateau in measured microstrain between anchors represents the limit of elastic relaxation of the hanging wall and is close to the elastic limit of 1600 microstrain predicted from equation 7.10. It is interesting to note that after an ERF value of about 12 metres, the microstrain between 2.5 and 4.5 metres from the hanging wall starts to increase linearly from the maximum elastic limit. This indicates that this zone of rock was just starting to leave the elastic deformation range at the completion of this stope mining. The start of stage 2 deformation is indicated in this graph. Stage 2 deformation is likely related to a voussoir arch

mode of movement.

The zone of rock between anchors at 4.5 and 6.5 metres is shown in Figure 8.12.

The majority of strain readings within this zone, recorded by three of the extensometers, plateau at approximately the maximum estimated elastic limit of 1600 microstrain. This graph is showing movement at the limit of stage 1 deformation and was possibly starting to show stage 2 deformation where strain was increasing linearly with the ERF value. It should be noted that 1000 microstrain is only 1 millimetre of movement over 1 metre, so some data scatter should be expected.

In the two remaining zones, 6.5 to 9.5 metres and 10 to 30 metres from the hanging wall, a relatively linear increase in microstrain with ERF values was recorded. The maximum values of microstrain recorded in these zones were below the maximum estimated elastic limit indicating all movement recorded was stage 1 deformation. This deformation is simply reflecting the elastic response of the rock mass to the increasing open stope geometry. In this zone, even though movements greater than 10 mm between anchors are measured and strain is increasing linearly, there is no instability indicated.

This instrumentation program gave very detailed data on the deformation behaviour of the immediate hanging wall of the 80G3 panel stope.

8.3.5 Summary

Data from four detailed instrumentation studies have been obtained from Mount Isa Mines. The deformation was plotted as movement or strain versus increasing ERF values. The most valuable information was obtained from looking at microstrain between anchors versus ERF values. Total movement between the instrument collar and each anchor produced data which was an average of several stages of movement occurring at different distances from the open

hanging wall.

In each study an upper limit to elastic strain was approximated based on stresses estimated normal to the hanging wall, the rock mass modulus and Poisson's ratio (Equation 7.10). Based on the rate of strain change with increasing ERF values and the estimated elastic strain limit, four stages of deformation have been identified and are listed below:

- Stage 1. Elastic strain deformation below the estimated elastic limit. This elastic strain may appear to increase linearly with ERF values or asymptotically converge to a constant maximum value.
- Stage 2. Linearly increasing strain with increasing ERF values. The value of strain in this stage exceeds the estimated elastic maximum.
- Stage 3. Exponentially increasing strain with increasing ERF values.
- Stage 4. This stage of deformation immediately precedes failure and shows as an exponential increase in strain, when plotted on a log scale.

8.4 BRUNSWICK MINE

The Brunswick mine is located near Bathurst in New Brunswick, Canada. The mine produces 10,500 t/day lead-zinc-copper-silver ore. Figure 8.14 shows a longitudinal view of the mine with the study area indicated.

A geomechanics research project, sponsored by Brunswick Mining, the Noranda Technology Centre and the Mining Research Directorate, was carried out at the mine in 1992-93. The study was conducted to examine the geomechanics problems associated with mining in the highly stressed conditions that are found in the sill pillars (Hudyma et al., 1994). Data from this study is taken from Hudyma et al., (1995) and much of the following discussion is taken from Milne et al. (1996).

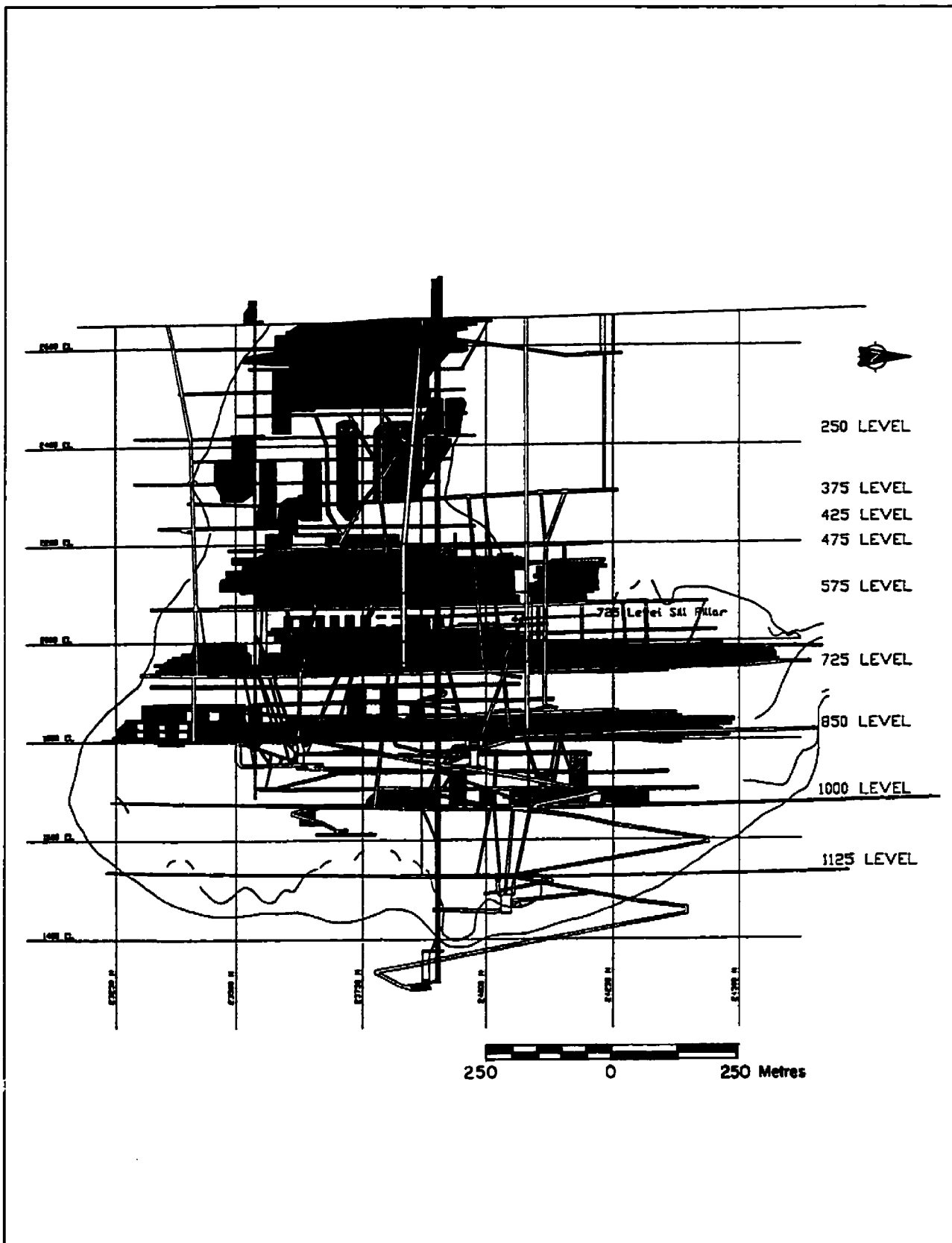


Figure 8.14 Vertical longitudinal projection of the Brunswick Mine main ore zone (MOZ). (Internal Brunswick Mine report)

In the area of the study the orebody is about 5 to 10 m wide and dips approximately 70 to 75° to the west. Stresses in the sill pillar area were estimated from modelling to be about 70 MPa and the intact unconfined compressive strength of the ore is about 220 MPa.

The conventional instrumentation program in this study consisted of 11 extensometers, 10 CANMET strain gauges (Herget, 1991) as well as ground movement monitors (GMM's), closure stations and borehole camera logging. Figure 8.15 gives isometric, plan and longitudinal views of the instrumentation in the study area. The extensometers were installed to monitor hanging wall and footwall behaviour with mining. Due to hanging wall instability, the final stope blast was a large mass blast. For all but extensometer 2, this prevented data from being collected on deformation with incremental mining steps. Extensometer no. 2 was undercut at an early stage and it was possible to follow the increasing deformation of the hanging wall with continued mining. Figure 8.16 shows a cross sectional view of extensometer no. 2 and Figure 8.17 shows longitudinal views of several mining steps and the ERF values corresponding to the

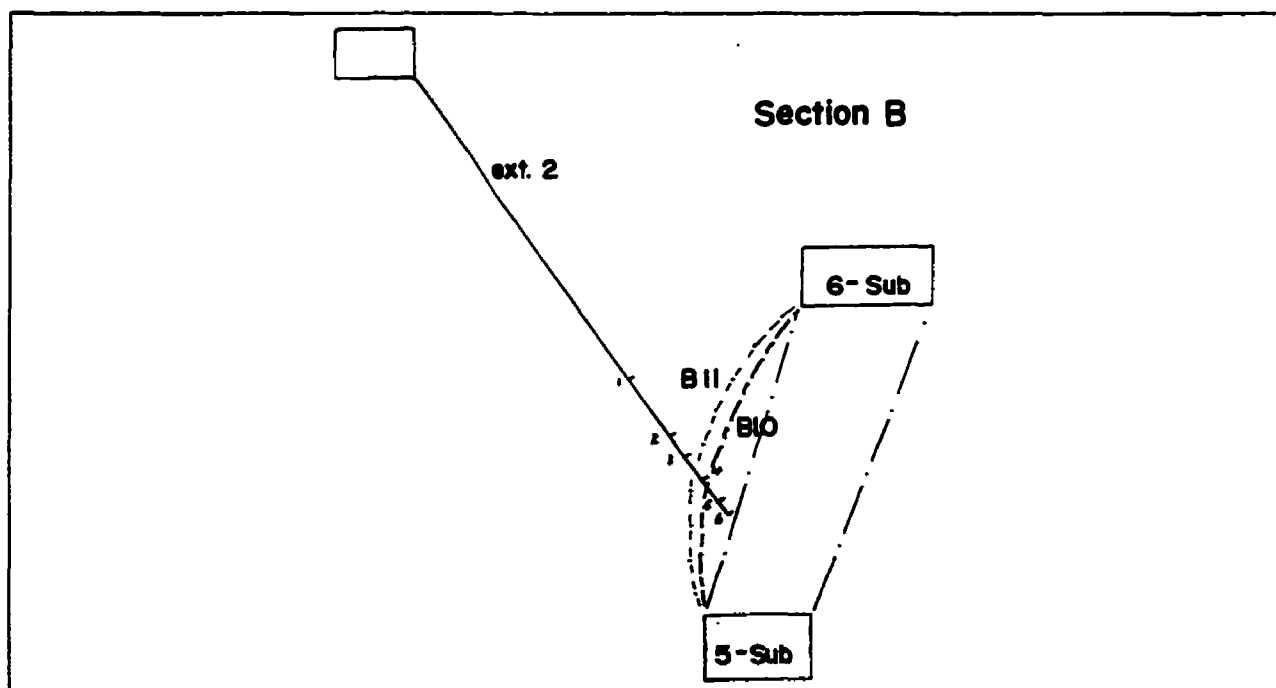


Figure 8.16 Cross section view of extensometer no. 2.

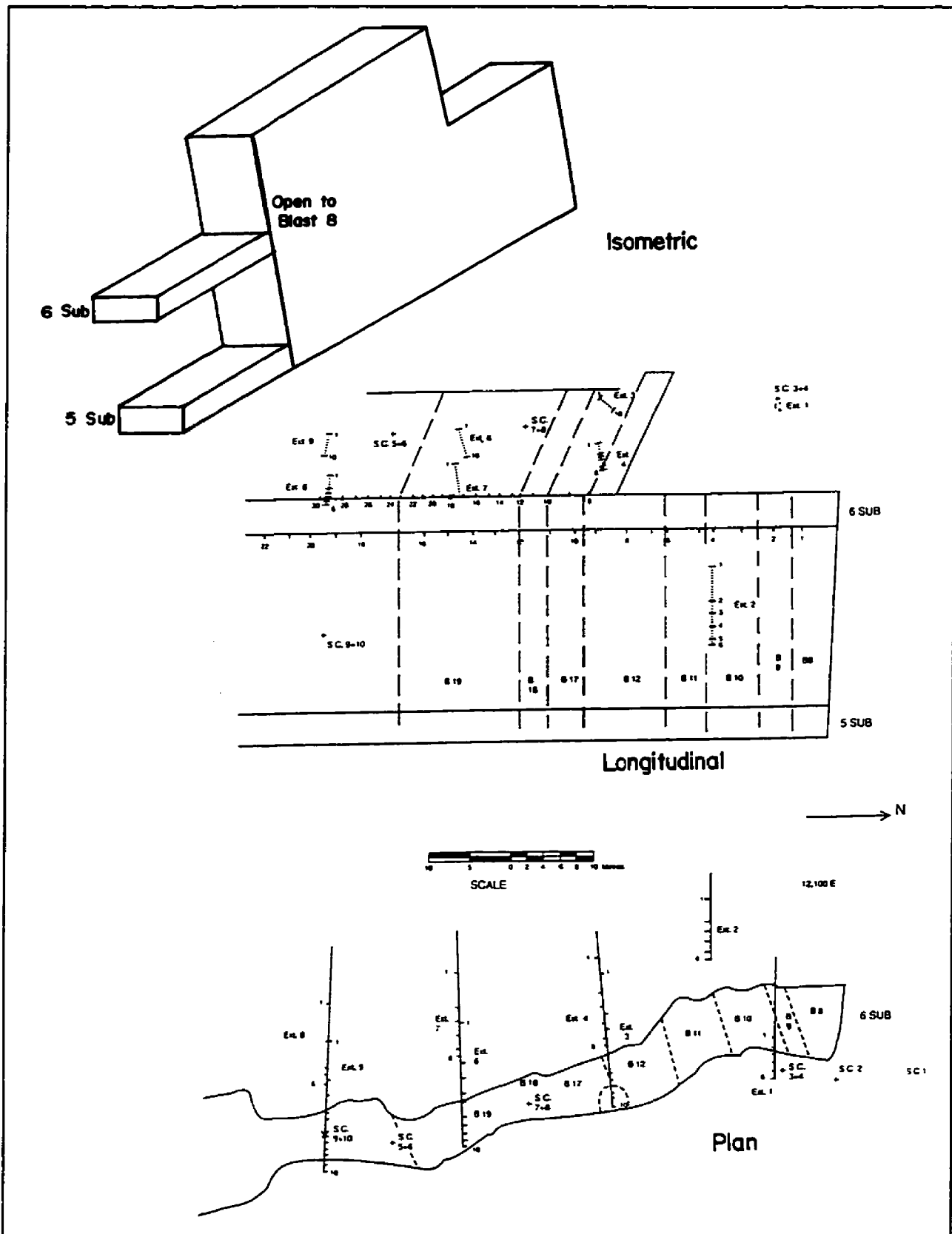


Figure 8.15 Brunswick Mine, isometric, longitudinal and 6 sub level plan view of instrumentation locations and blast steps.

BRUNSWICK MINE
16N Stope - 725 Level Sill Pillar
Looking West

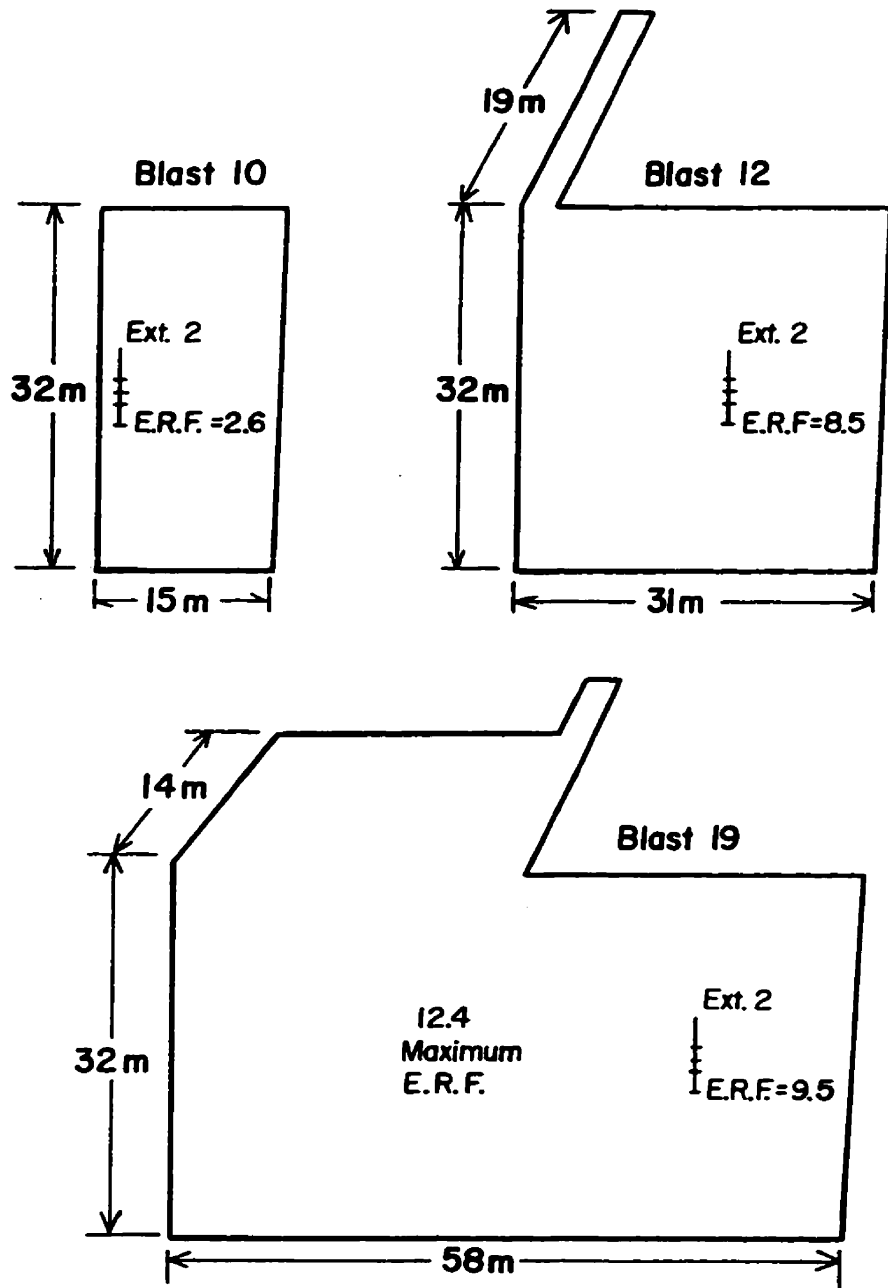


Figure 8.17 Brunswick Mine 16N stope looking west showing longitudinal views of three stages of mining and the corresponding ERF values for the hanging wall extensometer (From Milne et al., 1996).

bottom anchor of extensometer no. 2. The final stope was mined to 58m on strike and about 45m up dip. Cable support was installed from the sub-level, but extensive dilution accompanied the final stope blast. Figure 8.18 shows the deformation between the collar and extensometer anchors as well as the microstrain between anchors plotted against the ERF values for the major blasts. Both graphs show a linear log-normal relationship with ERF values. It should be noted that the strain measured between the bottom two anchors reaches a maximum value of about 15000 microstrain, well in excess of elastic strain values. Also, the strain level at which cable support yields has also been exceeded.

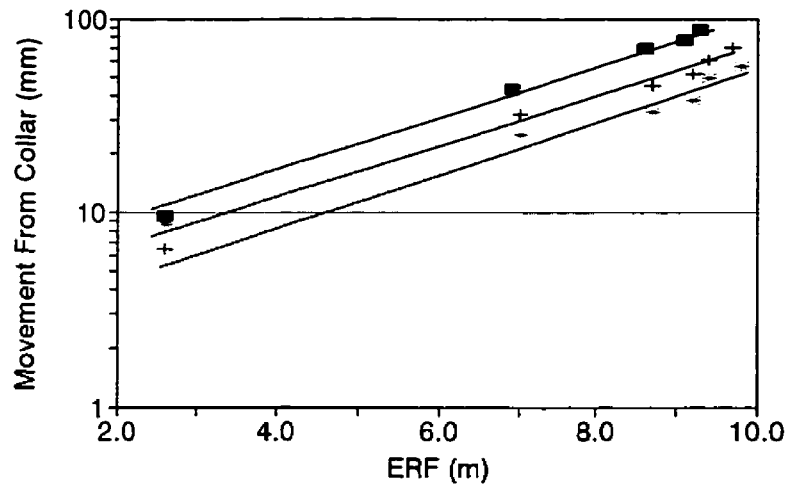
The final mining step, blast 19, resulted in extensive hanging wall failure over much of the stope. A maximum effective radius factor value at the centre of the hanging wall of 12.4 was calculated. If the trend in strain versus effective radius factor values shown in Figure 8-18 can be extrapolated, a maximum strain value for the immediate hanging wall of 50,000 microstrain would be projected from the available data. It is evident that strain levels of this magnitude could not be supported by the hanging wall rock as indicated by the extensive hanging wall dilution observed for this stope.

8.5 SUMMARY

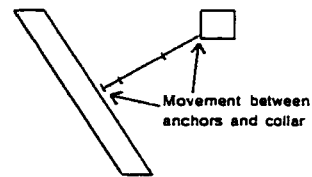
Data has been analysed for instrumented stope hanging walls at Brunswick Mine and Mount Isa. In both cases the predominant hanging wall structure consisted of parallel bedding or foliation. This structure influenced the mode of deformation, however, the procedure for analysing the data is valid for any structural environment. A strong foliation or bedding discontinuity set is commonly oriented parallel to open stope hanging walls.

A procedure has been presented for analysing and interpreting field deformation data

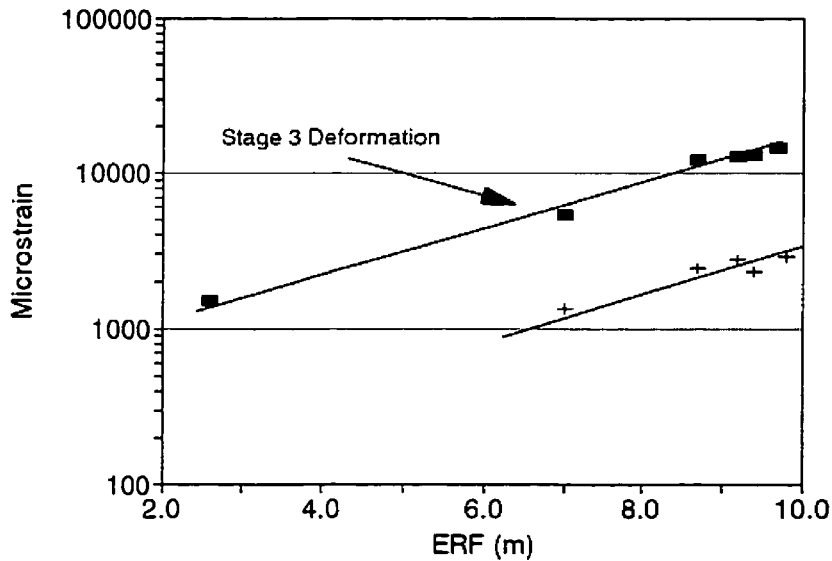
Brunswick Mine - 725 Sill Stopes 13-16N Movement From the Collar vs ERF Values



■ 1m to HW + 3m to HW - 8m to HW



MStrain Between Anchors vs ERF Values



■ 1-3m from HW + 3 to 8m from HW

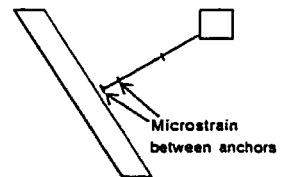


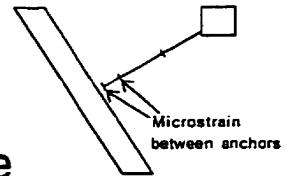
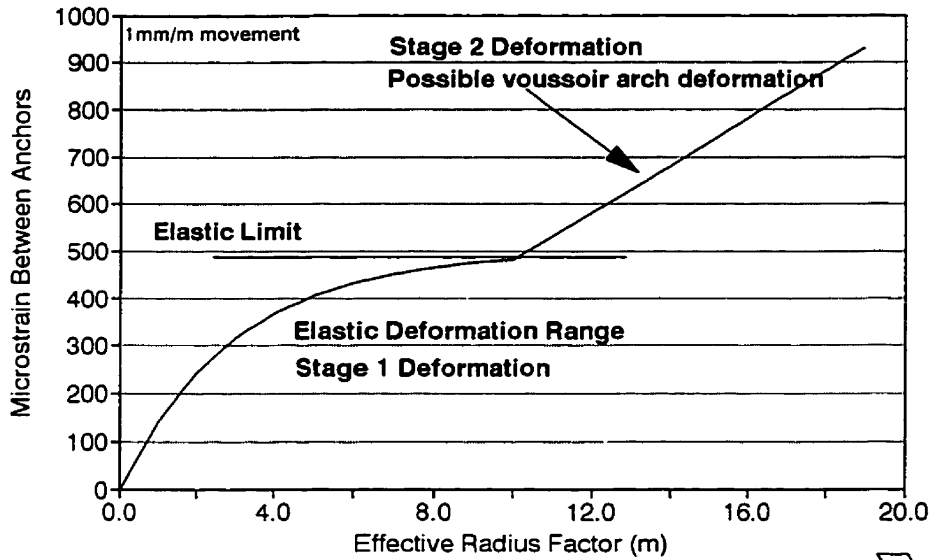
Figure 8.18 Collar to anchor deformation and microstrain between anchors, plotted against the ERF value (From Milne et al., 1996).

based on surface geometry. Based on the data collected, there appears to be four phases of deformation prior to failure and it is apparent that there is a different mechanism driving the movement in each phase. Figure 8.19 is an idealized graph of microstrain between anchors versus ERF values for the four suggested phases of deformation. To determine where these phases of movement are occurring in the rock mass, movement between anchors must be assessed. Movement between anchors is best shown as a strain or microstrain. It is interesting to note that the most valuable information has been obtained when the extensometer data has been plotted as microstrain between anchors. The most common mine site practice is to plot deformation data as total movement between the collar and each anchor. This averages out overall hanging wall deformation and makes interpretation difficult.

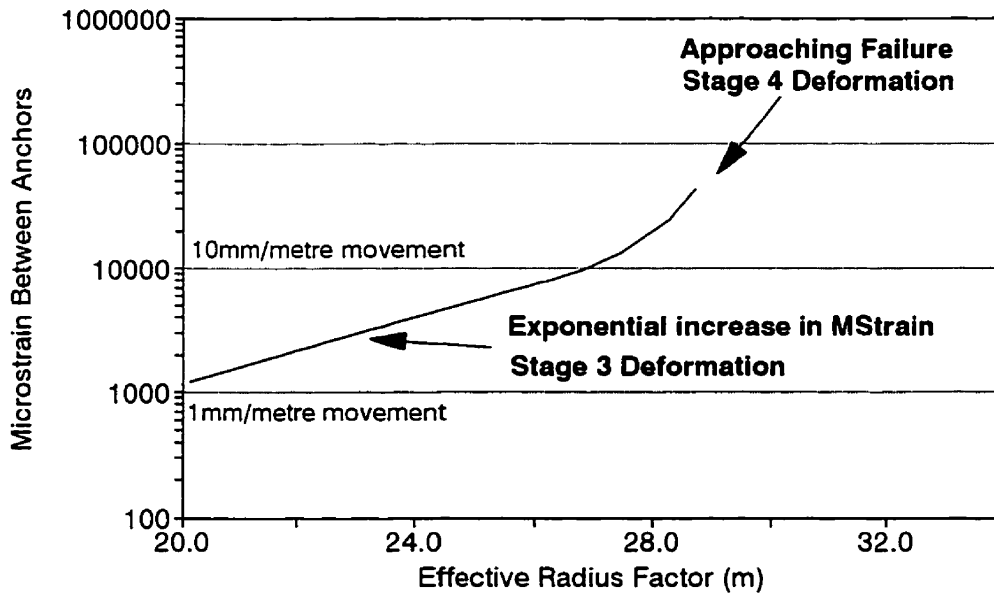
The first phase of deformation consists of elastically driven relaxation of the rock mass which asymptotically converges to a constant strain. This constant strain is a function of the rock mass modulus (in relaxation), Poisson's ratio and the field stress acting normal to the opening surface prior to excavation (Eq. 7.10). Change in stress parallel to a hanging wall will have an influence on deformation normal to the hanging wall, however, modelling has indicated that this effect is minor (Section 7.3). In most cases, an estimate of stress normal to the stope hanging wall is available. Also, an initial estimate of rock mass modulus can be made based on rock mass classification. These parameters, as well as an estimate of Poisson's ratio (commonly between .2 and .3), allow the engineer to set a minimum estimate of stable deformation, below which there is little cause for concern. Initial movement during this phase of deformation can be quite rapid and could otherwise cause concern. It will assist the ground control engineer if an estimate of maximum elastic deformation is available.

The second phase of deformation shows a linear relationship between microstrain and the ERF value and is likely caused by a voussoir arch deformation mechanism. The stability along

Theoretical Microstrain vs Effective Radius Factor Values



Theoretical Microstrain vs Effective Radius Factor Values



Note: Magnitudes of microstrain for stages of deformation are only possible ranges.

Figure 8.19 Graph showing the theoretical stages of hanging wall deformation versus ERF values

structures such as discrete wedges is decreasing and the potential for failure along isolated blocks is increasing. Overall failure of the surface, unless initiated along pre-existing structure, is unlikely based on the available data.

The third deformation phase consists of an exponential increase in deformation with the ERF value. A linear plot of deformation versus ERF values can be obtained using a semi-log plot. A voussoir arch deformation mechanism may be occurring, coupled with a delamination along bedding or foliation. Increased deformation would be due to both an increase in the ERF value and a decrease in beam thickness. Stability of the overall surface cannot be relied on in this phase and movement should be monitored closely. With experience, stable deformation limits may be determined to allow the prediction of failure.

The fourth phase appears as an even more rapid increase in rate of movement with ERF values. Failure is imminent and there is likely significant creep between stope blasts. Once this phase of movement is reached, it is likely that overall surface failure to the depth at which this movement phase is occurring, is simply a matter of time.

It is important to determine the distance from the hanging wall that each phase of deformation is occurring. If phase 4 deformation is only occurring between anchors within 2 metres of the opening surface, only failure within this zone is imminent. If phase 1 or 2 deformation is occurring at more than 3 metres from the hanging wall, there is little concern for stability for the rock mass more than 3 metres from the opening. From the data collected at Mount Isa Mine and Brunswick Mine, the following instrumented zones were showing the following stages of deformation:

Mount Isa Mine

Stope 5FP1

Ext. 1	- .5 to 3.5m from HW	Stage 1?
Ext. 2	- .5 to 4.0m from HW	Stage 1?

Stope 5HP1			
Ext. 1	- 1 to 4.0m from HW	Stage 1 and 2	
Ext. 2	- 1 to 4.0m from HW	Stage 1 and 2	
M665 Triplet			
Ext. 1, 2 and 3	- 4 to 15.0m from HW	Stage 1	
Ext. 5	- 1 to 6.0m from HW	Stage 3	
80G3 Stope			
Ext. 2, 4 and 5	- .5 to 1.5m from HW	Stage 3 and 4	
Ext. 2 and 4	- 1.5 to 2.5m from HW	Stage 1 and 2	
Ext. 4 and 5	- 2.5 to 4.5m from HW	Stage 1 and 2	
Ext. 1, 3 and 5	- 4.5 to 6.5m from HW	Stage 1	
Ext. 1, 3 and 6	- 6.5 to 9.5m from HW	Stage 1	
Ext. 1, 2, 3, 4, 5, and 6	- 10 to 30.0m from HW	Stage 1	
Brunswick Mine			
Stope 13-16N			
Ext. 2	- 1 to 3m from HW	Stage 3	
Ext. 2	- 3 to 8m from HW	Stage 3	

It should be noted that most of the data collected were obtained with automatic data logging systems. It would have been unlikely that manual readings, taken on a weekly basis, would have allowed this detailed interpretation of deformation behaviour.

Instrumentation data is usually only available at one or two locations on an opening surface. Based on the ERF values for the surface, the different phases of deformation can be extrapolated to areas without instrumentation. It is feasible that phase three deformation may be occurring near the centre of a surface while stage two movement is present closer to the surface abutments. Figure 8-20 shows the potential development of deformation on an increasing hanging wall surface. As well as assisting in the prediction of failure, an estimate of the degree of deformation in different areas of a hanging wall allows the engineer to better optimize the installation of support. In areas where little or no deformation is predicted, little or no load on support would be generated.

Development of Deformation Stages

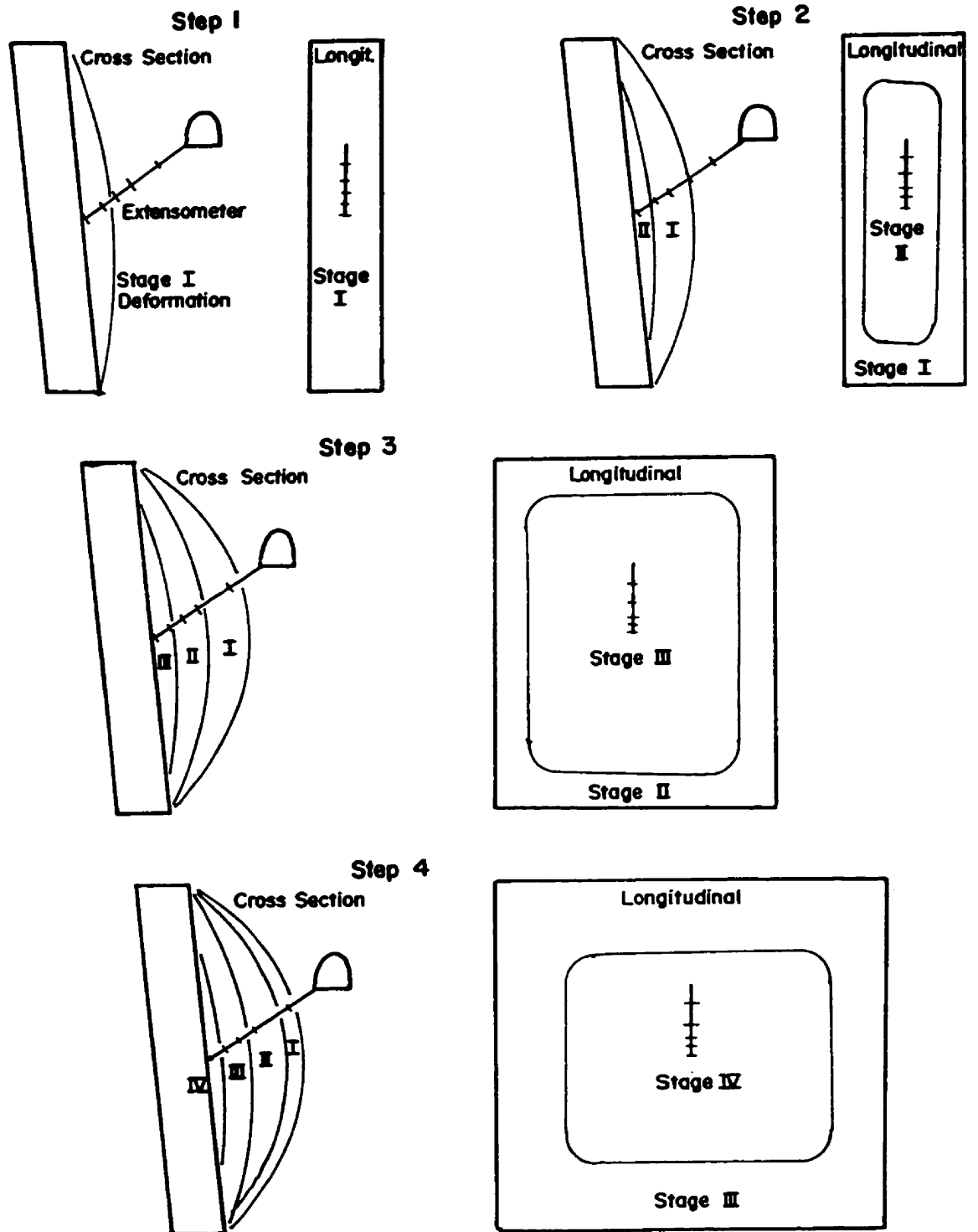


Figure 8.20 Proposed development of deformation stages.

CHAPTER 9

INFLUENCE OF BACKFILL ON HANGING WALL DEFORMATION

9.1 INTRODUCTION

The use of backfill to increase the stability of underground openings is common, however, it is difficult to assess its effectiveness. In principle, the addition of backfill restricts the deformation of the opening surfaces and this results in an increase in stability. The stability graph design technique is one of many opening design techniques which base stability on the hydraulic radius of the surface under consideration (Chapter 2). When mining is conducted against backfill, there can be questions concerning the relevant opening geometry which should be used for design. Potvin, (1988) suggested guidelines for assessing opening geometry next to backfill:

- For mining adjacent to a backfilled stope, the hydraulic radius of a back should ignore the presence of backfill, since it is unlikely the fill will be tight to the back.
- For a hanging wall adjacent to a backfilled stope, the backfilled stope is commonly treated like a rock abutment.

The reasoning behind these guidelines reflects the mechanism of support provided by backfill. For hydraulic and even broken rock fill, there is a component of active pressure applied to any surface which is steeper than the angle of internal friction of the fill. For sand fill the angle of internal friction can be treated as approximately 35° to 37° , however, for hydraulic fill any surface steeper than about 15° would have active pressure applied. Also, very significant levels of passive support would be exerted by even a low modulus backfill after limited hanging wall deformation. A value of .29 GPa is given by Brady and Brown (1985) for the modulus of 8% cemented sandfill. For a 10 metre wide stope, backfilled with this material,

a hanging wall movement of 1 centimetre would mobilize almost .3 MPa of pressure against the hanging wall. This far exceeds the support which could be applied by any reasonable cable bolting pattern. For this reason, backfill support for hanging walls are often treated the same as rock abutments.

This assessment of surface stability against backfilled stopes is valid for mining and completely filling a stope before adjacent mining. Figure 9.1 is a plan view of an opening showing the general shape of expected hanging wall deformation. The deformation would be at a maximum at centre span and roughly follow an arch, decreasing to zero at the rock abutments. If this open stope is then backfilled, the hanging wall deformation profile is effectively 'frozen' in place. This is an optimistic simplification which considers any backfill compression insignificant compared to the scale of hanging wall deformation. This assumption is most accurate for weak hanging wall / stiff backfill situations. Mining is then conducted adjacent to the backfilled opening. Since only limited movement has occurred at the edge of the backfill, due to backfill compression, the backfill abutment can be treated the same as a rock abutment for predicting deformation of the second stope. This accounts for the effectiveness of backfill for hanging wall stability.

This approach is no longer valid if a continuous mining and backfilling operation is used to develop a moving window of open ground, such as with a modified Avoca mining method. The difference between these two situations is best described by looking at the expected hanging wall deformations. Figure 9.2 is a plan view showing steps of a continuous mining backfilling procedure. Step one shows the idealized hanging wall deformation profile after opening a 20 metre span. Step two shows the first half of this deformation profile 'frozen' in place with the additional of backfill. Another 10 metres of rock is mined creating a 20 metre moving window of open hanging wall. In this scenario, the backfill abutment has moved and is intuitively less

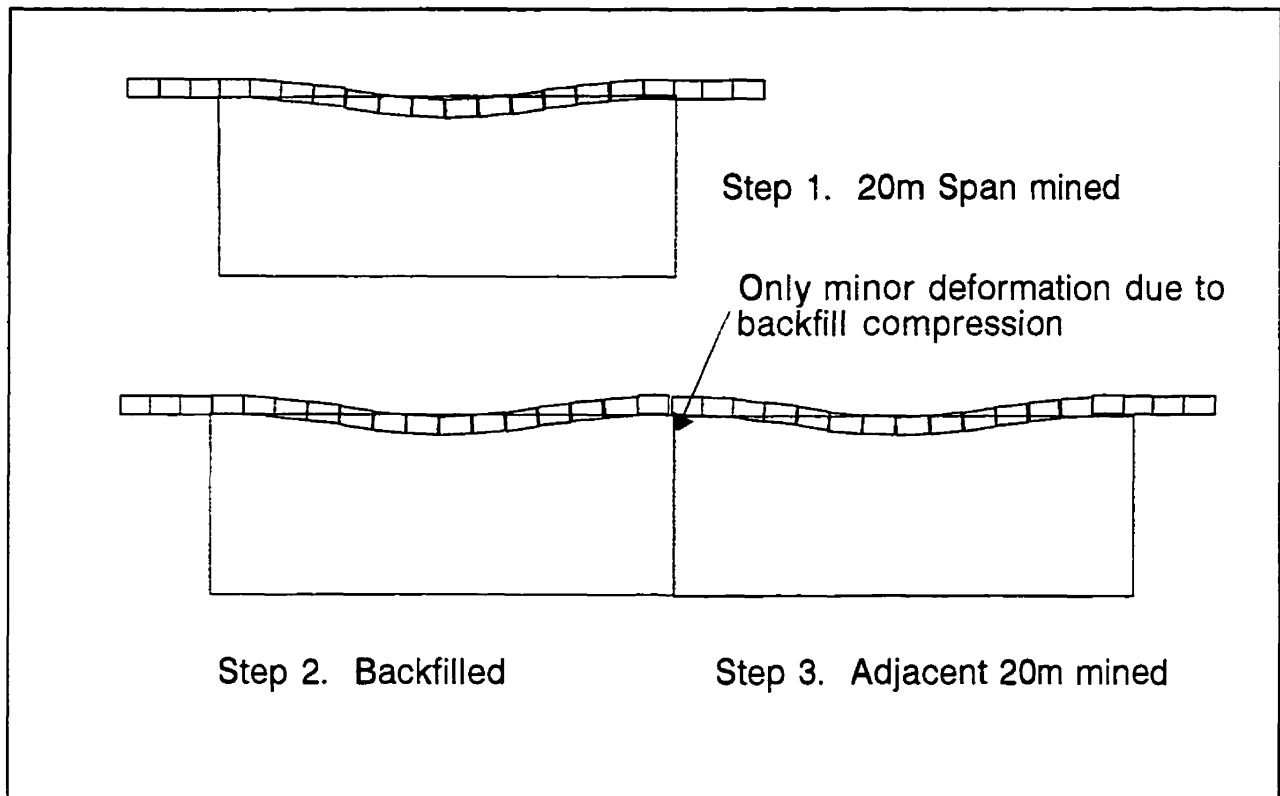


Figure 9.1 Plan view of expected form of hanging wall deformation with backfilling only after stope completion.

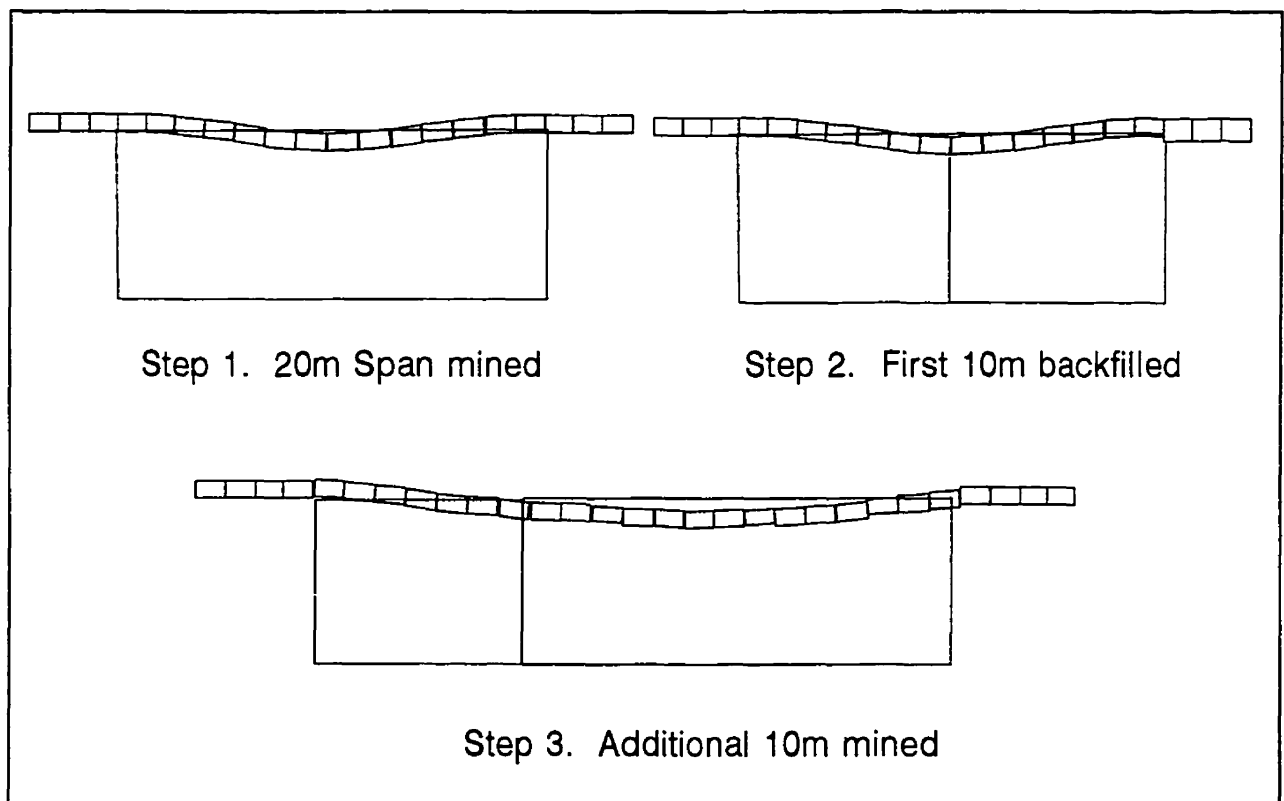


Figure 9.2 Plan view of expected form of hanging wall deformation with a continuously advancing backfill abutment.

stable than the backfill abutment which hasn't moved, shown in Figure 9.1.

9.2 HANGING WALL DEFORMATION IN A CONTINUOUS BACKFILLING CYCLE

In order to estimate the hanging wall stability and deformation of a moving window of open ground, some method of assessing the influence of the progressing backfilled abutment is required. Figure 9.3 shows an idealized plan view of a hanging wall deformation profile with a backfilled abutment. An initial span was opened and then half this span was backfilled. The span was then increased to its original size with additional mining, however, the backfilled abutment has a locked in deformation. A new arching deformation profile will develop. The effective point of zero deformation for this arch, on the backfilled abutment, will be some distance 'x' behind the backfill front. The final span will have an effective span 'x' metres greater than the open span shown. With each subsequent mining and backfilling cycle the value of 'x' will increase, though it will tend to converge to a constant value.

In Figure 9.3 the deformation arch for the two mining steps has been drawn with the same radius of curvature. This may or may not be a valid assumption, however, it can be taken as a reasonable initial estimate. An iterative procedure can be followed with numerous backfill and mining steps, assuming a constant radius of curvature for the deformation arch. The effective final span converges to the sum of the opening span after blasting plus the opening span after backfilling. In other words, the effective span is a sum of the maximum and minimum opening spans developed during the mining and backfilling cycle. Figure 9.4 gives an example of the iterative procedure used to determine the effective span.

In both Figure 9.3 and 9.4, hanging wall deformation due to compression of backfill has been ignored. It has been assumed that the magnitude of backfill compression would be

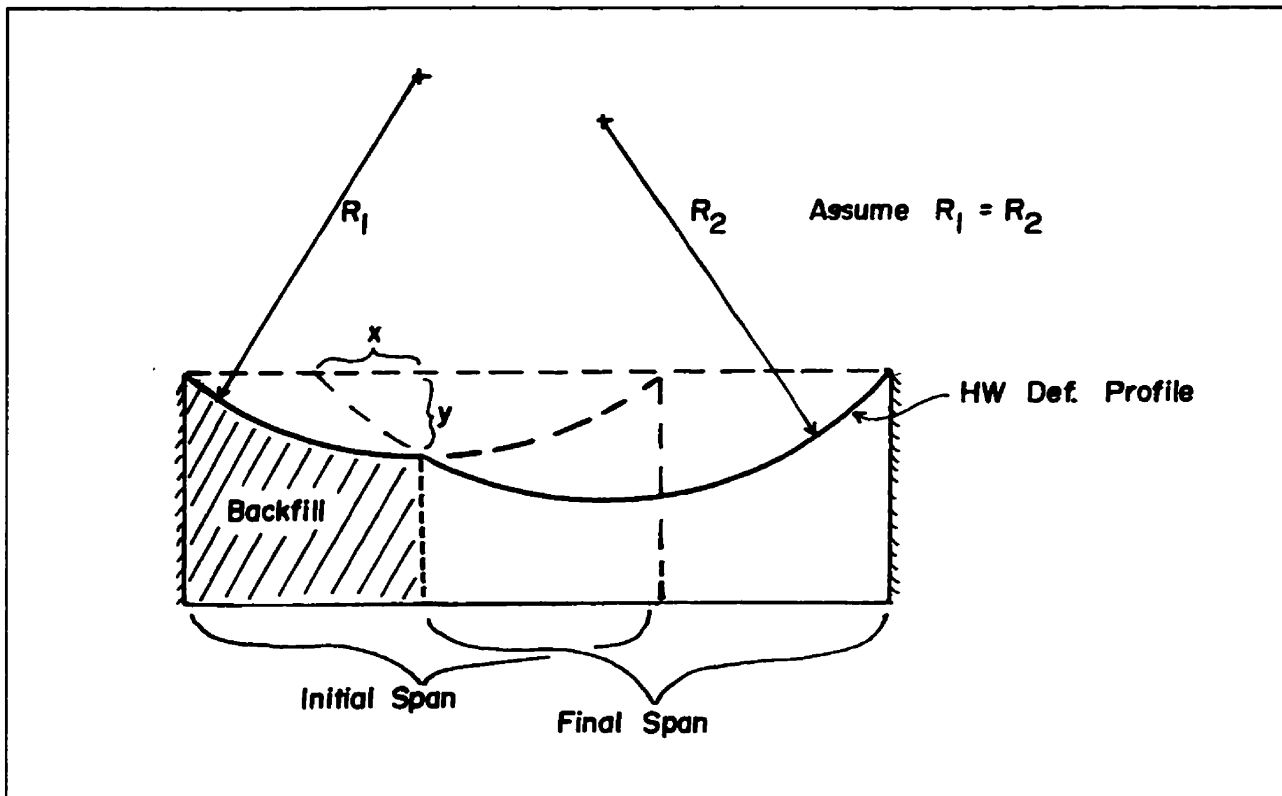


Figure 9.3 Plan view of a hanging wall deformation arch after a backfilling step (Ignoring backfill compression).

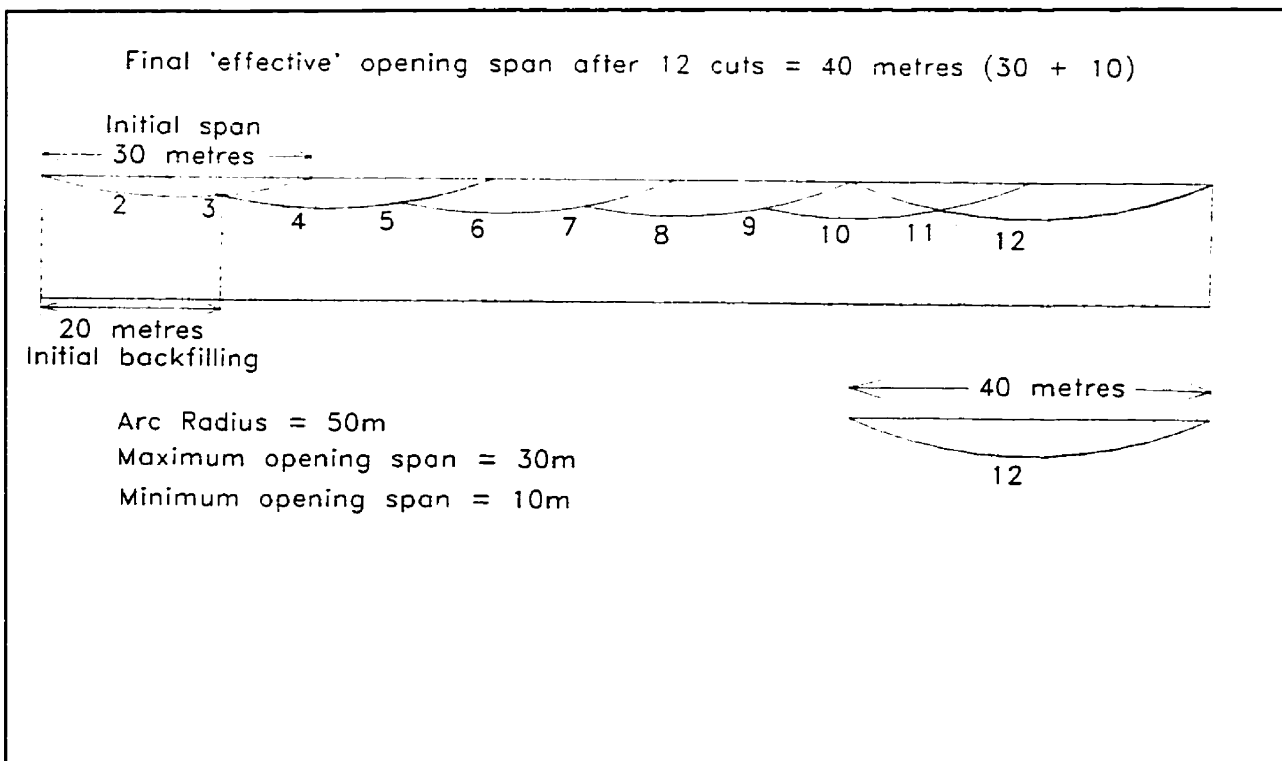


Figure 9.4 Plan view of projected deformation for a backfilling cycle with a 30 metre open span, backfilled to 10 metres then opened to 30 metres.

negligible compared to the deformation of the open hanging wall. After large amounts of hanging wall deformation have occurred, this approximation is reasonable. Figures 8.6 and 8.18 show maximum hanging wall deformation of 30 millimetres and 80 millimetres respectively. If a .29 GPa modulus backfill with a width of 10 metres is assumed, this magnitude of movement, in a backfilled stope, would generate .9 MPa to 2.3 MPa of support pressure, sufficient to support 37 to 100 metres of dead weight. This is far greater than the pressure required to support any hardrock mining hanging wall. Standard effective hanging wall support commonly consists of steel cables installed on a 2 metre by 2 metre pattern. This can support the dead weight of approximately 3.4 metres of rock which would be equivalent to approximately one millimetre of backfill compression, given the conditions mentioned above. For most cases of hanging wall deformation, one millimetre of backfill abutment compression is not significant.

Figure 9.5 shows a typical modified Avoca style mining method. Based on graphical construction and the assumptions listed above, the hanging wall deformation profile of a modified Avoca mining cycle would be equivalent to the deformation profile of a larger span against rock abutments. This larger equivalent span would be equal to the maximum opening span prior to backfilling plus the minimum opening span which occurs after backfilling.

With this first estimate of the effective span against a continuously advancing backfill front, the effective radius factor for the opening surface can be calculated. Instead of treating the backfill front as a rock abutment, which is highly unconservative, the effective backfill abutment can be assumed to act some distance 'x' behind the backfill front. The first estimate of this value 'x' should be equivalent to the minimum opening strike length after backfilling. The next section discusses case histories of hanging wall deformation against a moving backfill front.

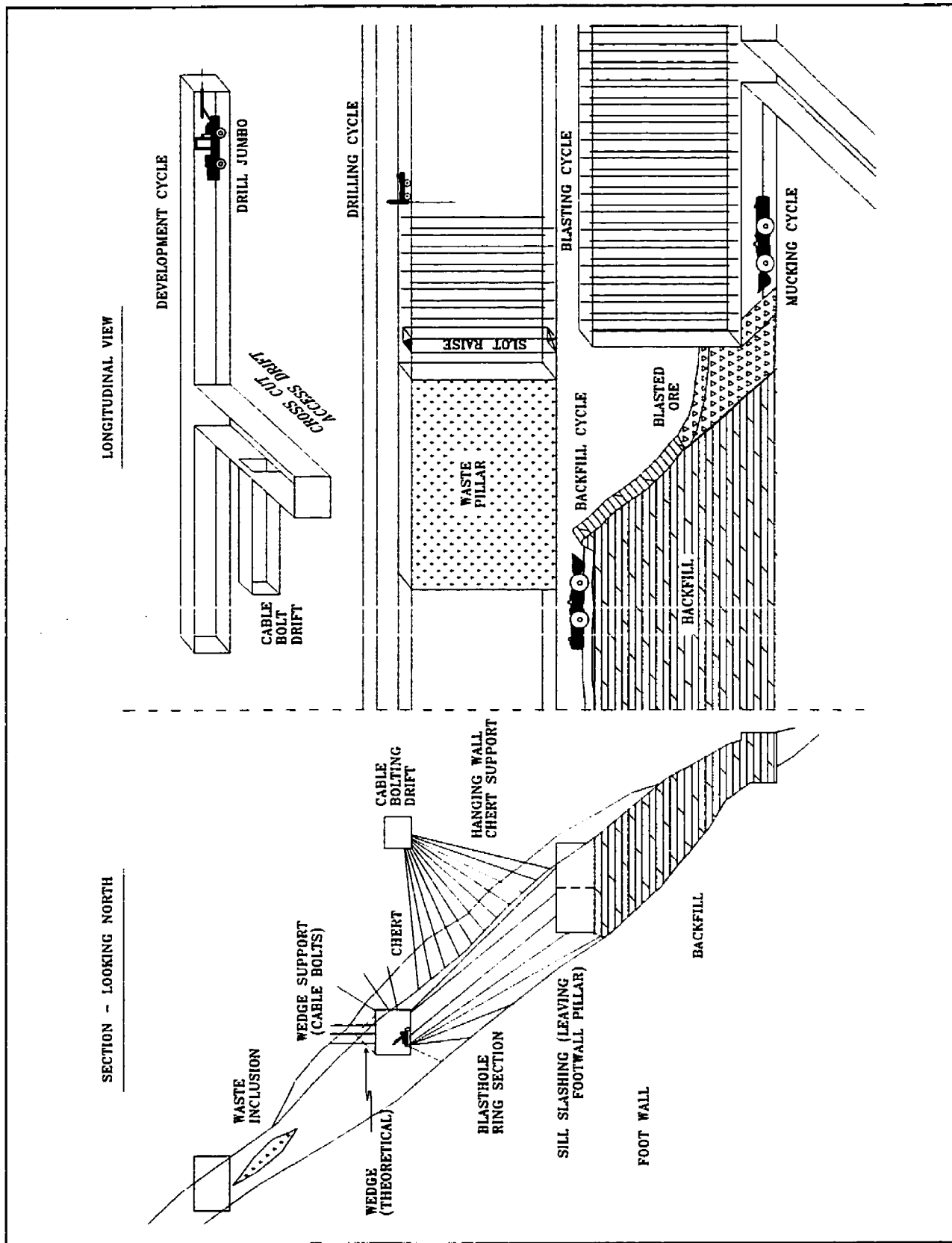


Figure 9.5 Views of the Modified Avoca mining method used at Winston Lake Mine (From Winston Lake Mine - Inmet Mining Corp.).

9.3 WINSTON LAKE MINE CASE HISTORIES

Winston Lake Mine, Division of Inmet Mining Corporation is located in Northern Ontario near the town of Schreiber. The Winston Lake orebody consists of massive sphalerite dipping 40 to 60 degrees east. The footwall and hanging wall are gabbro with a weak highly chloritized ore contact. Between the ore and hanging wall gabbro, a zone of banded chert-rhyolite-tuff is often present with a thickness between about 0 and 5 metres. In wide orebody zones the chert disappears and in thin ore zones it reaches its maximum. The orebody ranges from 5 to 17 metres in thickness. Each of the case histories discussed deal with a chert hanging wall. Classification values have been previously determined for the chert hanging wall material and are given below (Milne & Jacob, 1990):

RQD 100%

J_n 12 (Three joint sets plus random)

J_r 1.0 (Planar and smooth joint surfaces)

J_a 1.0 (Clean joint surfaces)

$Q' = 8$

The mine uses a quasi Avoca-longhole mining method and there are twenty metres vertical between overcut and undercut drifts, as shown in Figure 9.5.

Winston Lake Mine was chosen as one of the first detailed support cases for the MRD (Mining Research Directorate) project on hard rock support. Details on this study are taken from an internal Noranda report (Milne and Jacob, 1990). The study consisted of three phases and a report summarizing the findings was completed in January 1993 (Maloney and Kaiser). The first and third phases of this study include hanging wall deformation monitoring which is summarized in the following two sections.

9.3.1 Phase 1, Winston Lake Hanging Wall Deformation, Stope 565#4

The first phase of the MRD study included hanging wall instrumentation consisting of Interfels and wireflex extensometers, as well as borehole camera holes. This study was conducted in the 565 #6 stope. One of the main concerns in the study was assessing the stability of the chert hanging wall. Extensive cable support was installed from a cable bolt drift and an estimate of the effectiveness of both the backfill and cable support was of interest.

In this review, the hanging wall deformation data from the four extensometers are compared to the blasting and backfilling records which determine the area of exposed hanging wall. Figure 9.6 shows the blasting and backfilling progress on a true longitudinal section. The backfill positions given represent the toe of the backfill which slopes at approximately a 37° angle. The toe positions of the cable support is also given, however, the cable performance cannot be assessed since there are no instrumented unsupported areas to compare with.

To assess the hanging wall behaviour, it is first necessary to estimate the hanging wall area in contact with the broken rock fill. With the relatively low ore body dip between 40° to 60°, contact with the broken rock fill can be expected somewhere below the top of the fill level. Figure 9.7 is a schematic of the ore body hanging wall and fill sloping at a 37° angle of repose showing that hanging wall contact with the backfill should be in the order of at least 6 metres below the top of the backfill. Due to the undulating nature of the hanging wall, backfill to hanging wall contact may be in the order of only 10% (Winston Lake Engineering Staff, Personal Communication).

The extensometer data showed the deformation was highly localized to weak bedding plane features and was very dependent on the thickness of chert present. Figure 9.8 shows the extensometer location in section and in plan. To determine the effect of the backfill, the effective radius factor value for each extensometer was plotted against microstrain between

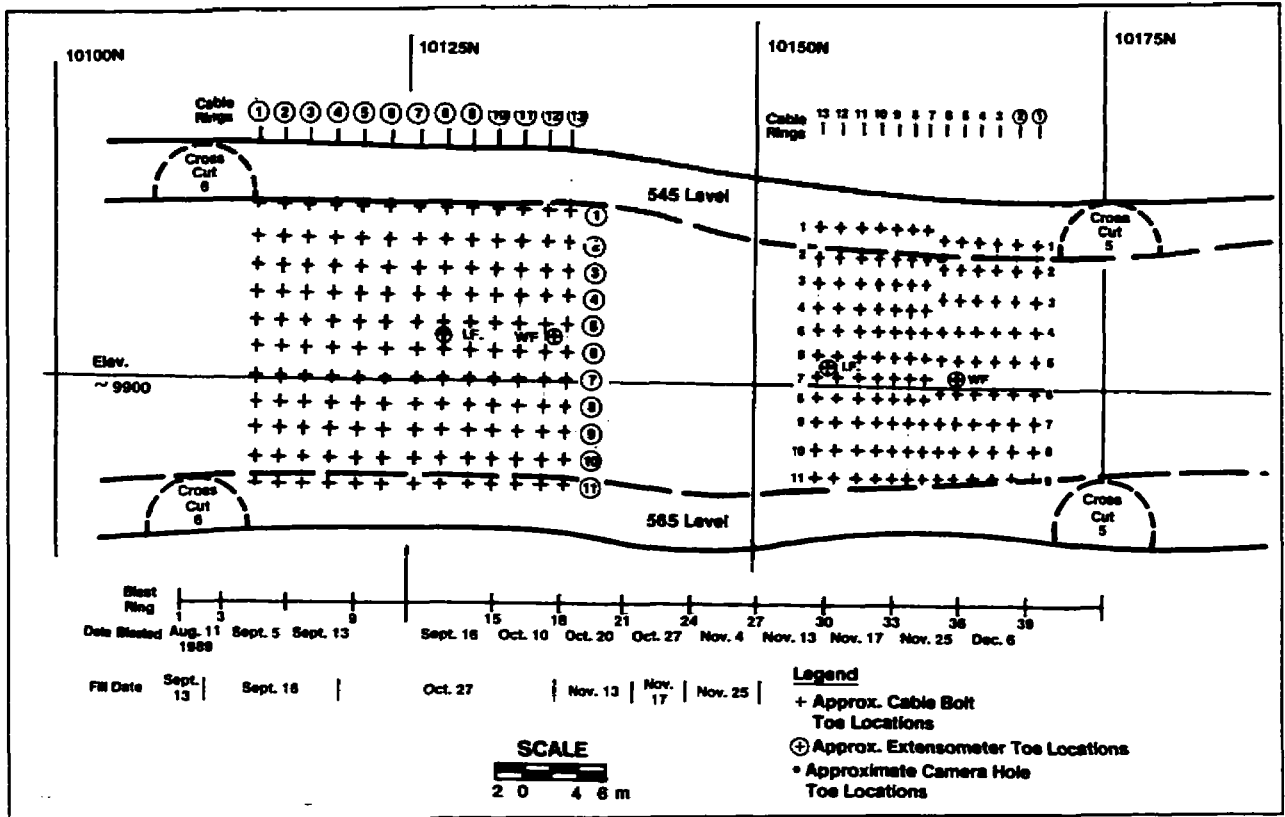


Figure 9.6 True longitudinal view of the 565#6 stope showing extensometer toe locations and approximate cable bolt locations.

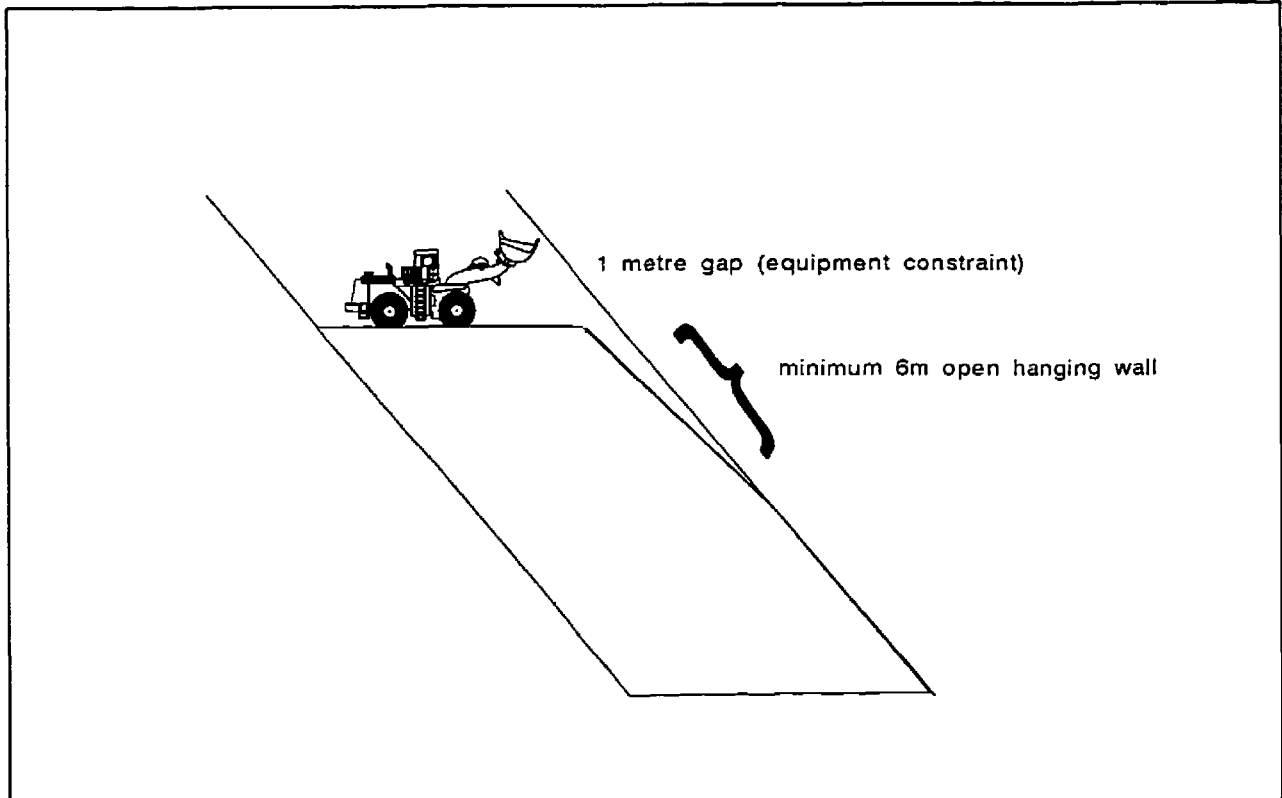


Figure 9.7 Cross section showing 60° dipping hanging wall and 37° sloping fill.

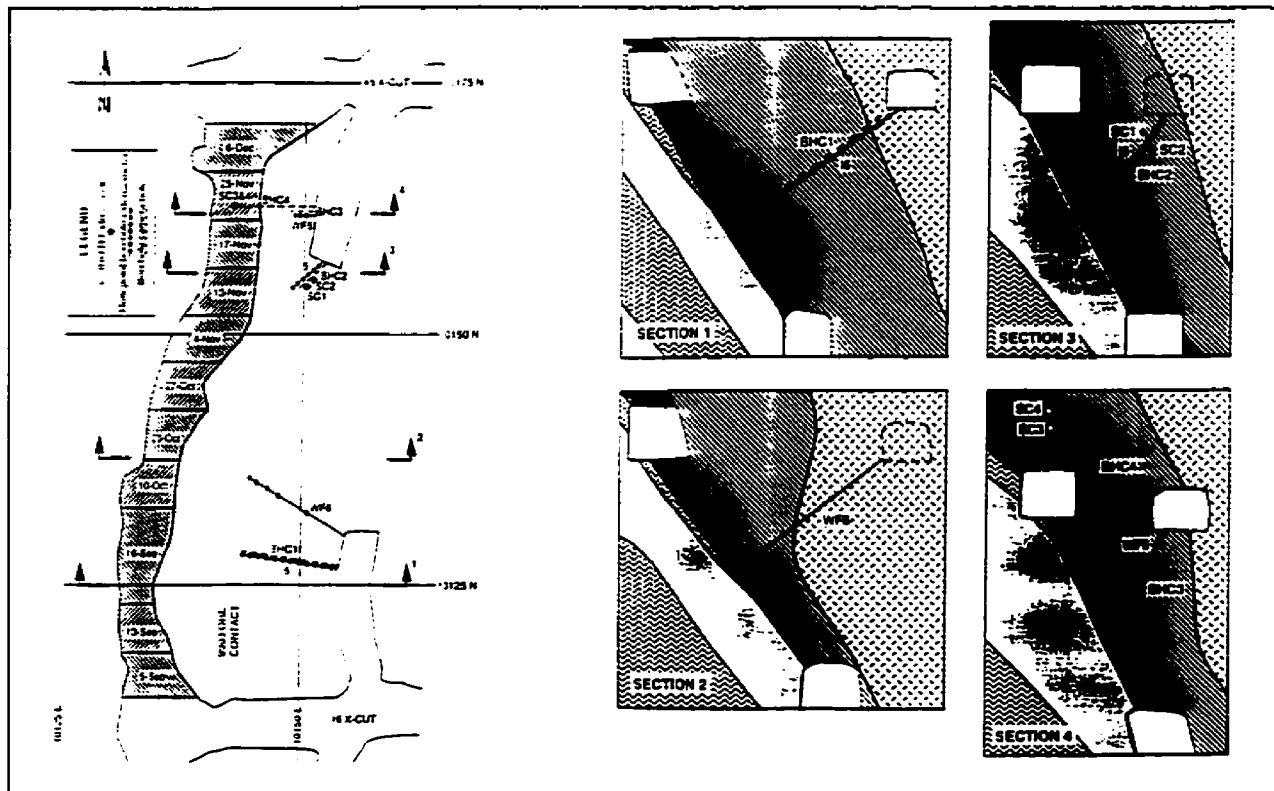


Figure 9.8 Plan and cross section views of the instrumentation installed in the 565 #6 stope. (From Maloney and Kaiser, 1993).

anchors. Three different approaches were taken to obtain the ERF values for the extensometers and are summarized below:

1. The backfill was treated like a rock abutment.
2. The backfill was ignored on strike and assumed to provide support 6 metres below the fill base.
3. The support from the backfill was assumed to lag 20 metres behind the backfill front on strike, and support from the base of the backfill was assumed to act 6 metres below the backfill surface, to account for the backfill angle of repose.

As discussed in the previous section, an initial estimate of the effective on strike span of the moving exposed hanging wall may be approximated by the open strike length after backfilling plus the maximum strike length prior to backfilling. On average, the open span after blasting plus 20 metres approximates this.

Figure 9.9 shows the three different assumptions used to calculate ERF values for the

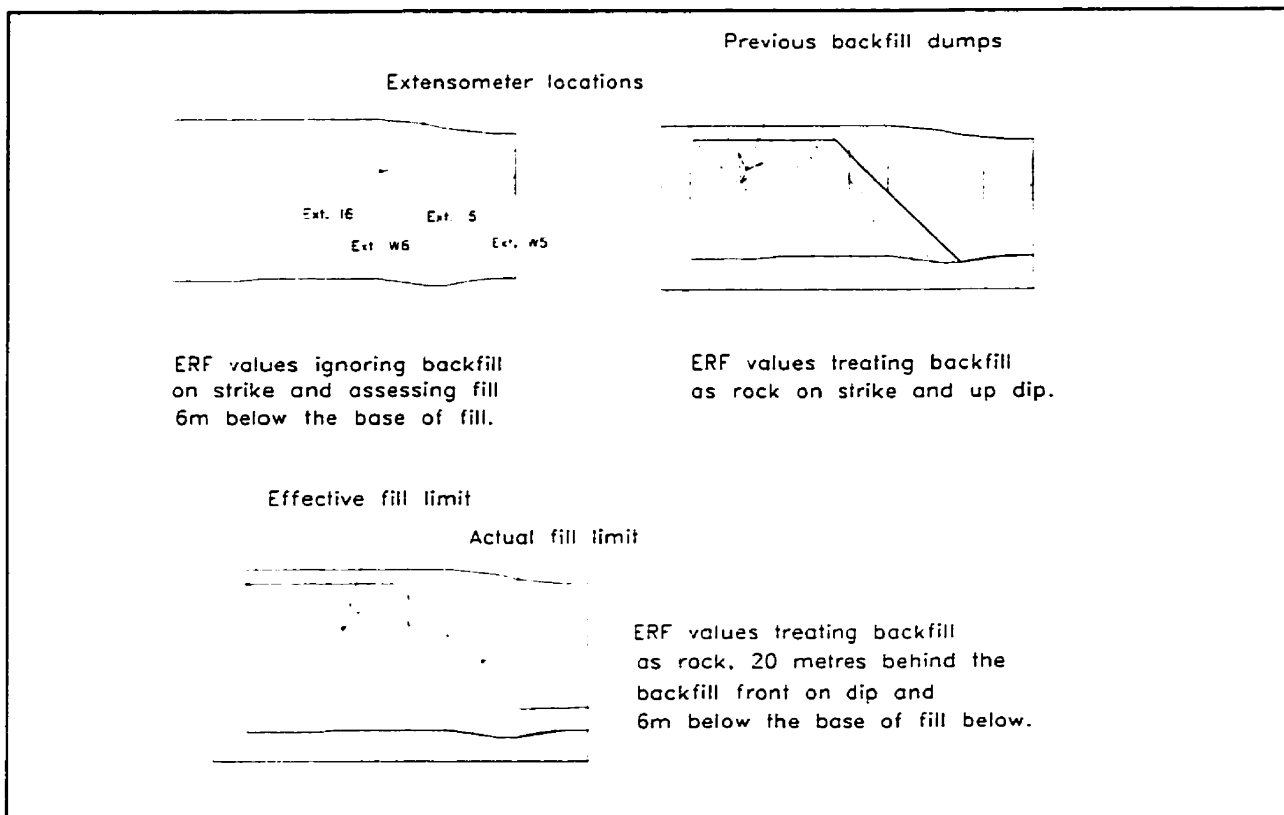


Figure 9.9 Mining as of November 25th, 1989 showing longitudinal view of 3 methods of interpreting the effect of backfill on the effective radius factor.

extensometer locations. Figures 9.10 to 9.12 show the microstrain versus ERF values for extensometers I565#6, W565#6 and I565#5. W565#5 did not warrant plotting due to insufficient data. In each of the three figures, the ERF values were calculated using the three approaches for assessing backfill listed above.

In Figure 9.10, when backfill was considered as effective as a rock abutment there was a minor steepening of the microstrain versus ERF value in extensometer W565 #6. This indicates that the effective open stope geometry is greater than that bounded by the backfill limit. In Figure 9.11, when backfill was ignored, there was a minor flattening of the microstrain versus ERF values. This indicates that the effective stope geometry was overestimated when the influence of backfill was ignored. In Figure 9.12 the slope of the microstrain versus ERF value was too shallow to show any significant difference between the 3 methods used to assess backfill

Figure 9.10 ERF values versus microstrain between the bottom anchors of extensometer W565#6. ERF values are based on three methods of assessing the effect of backfill.

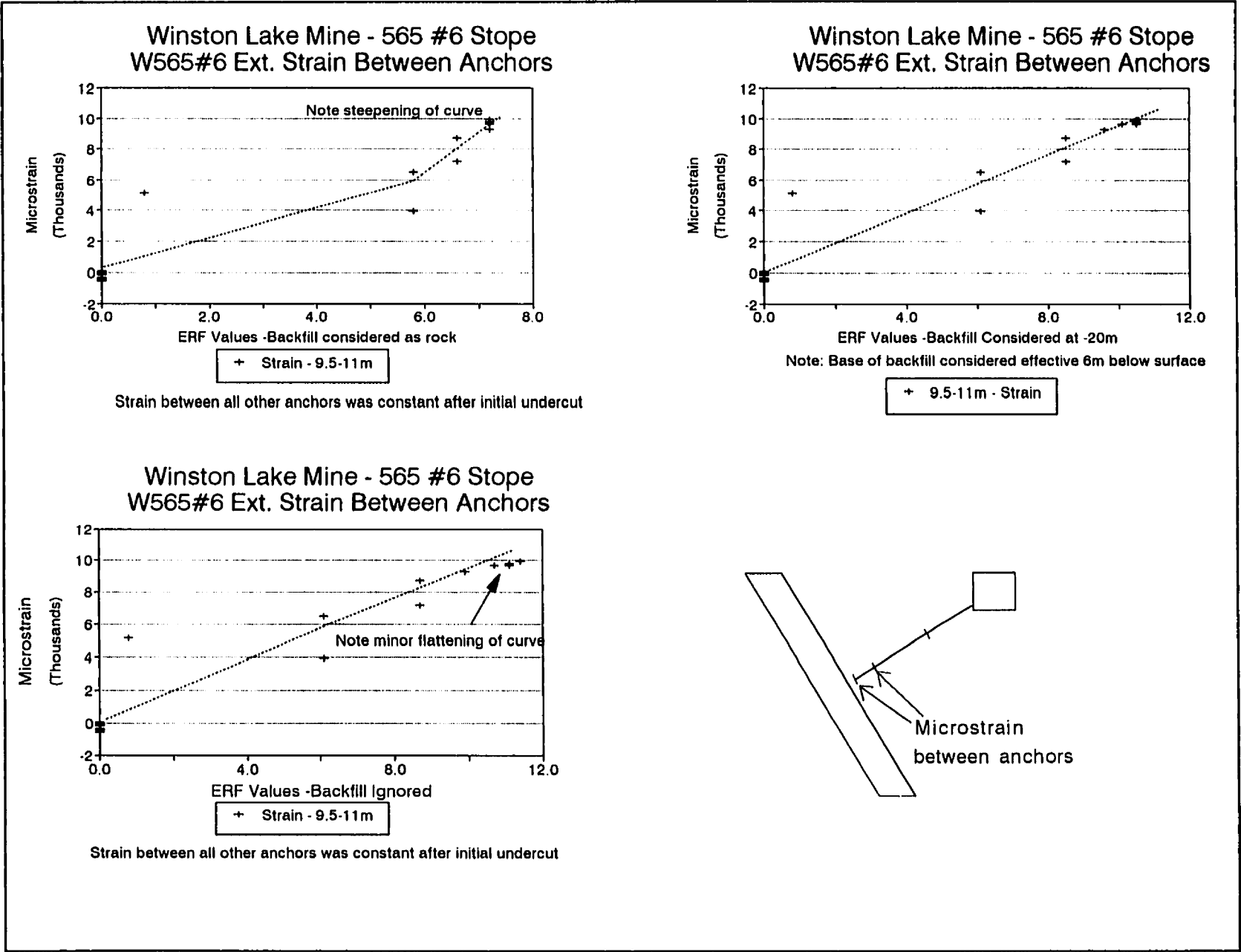
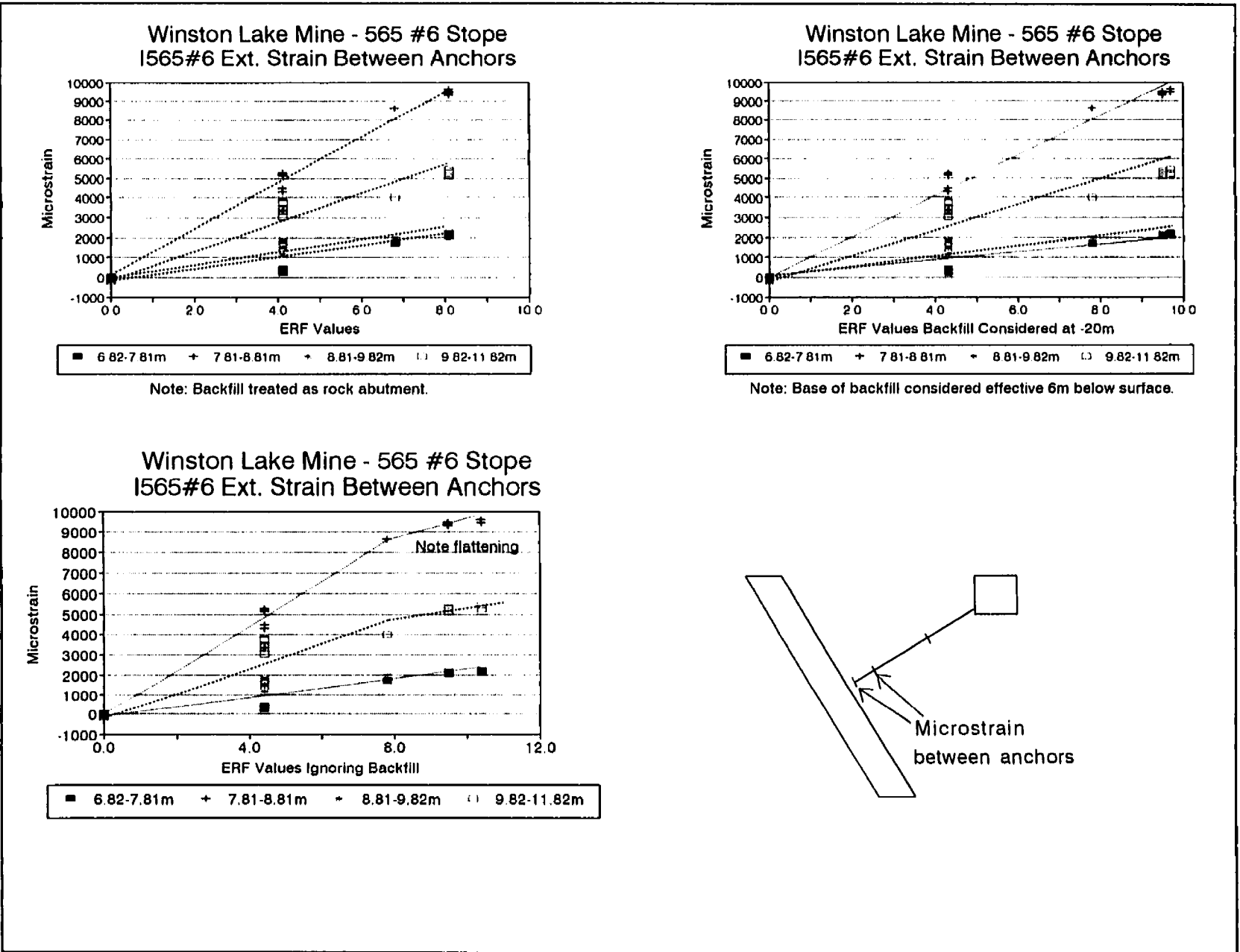
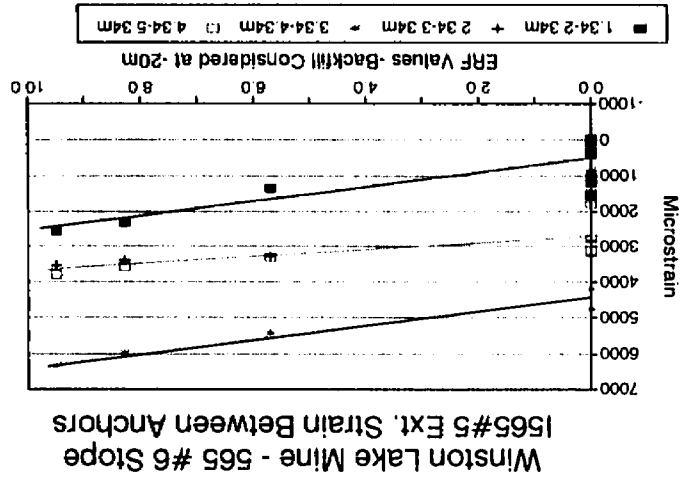


Figure 9.11 ERF values versus microstrain between anchors of extensometer I565#6. ERF values are based on three methods of assessing the effect of backfill.





Note: Base of backfill considered effective 5m below surface

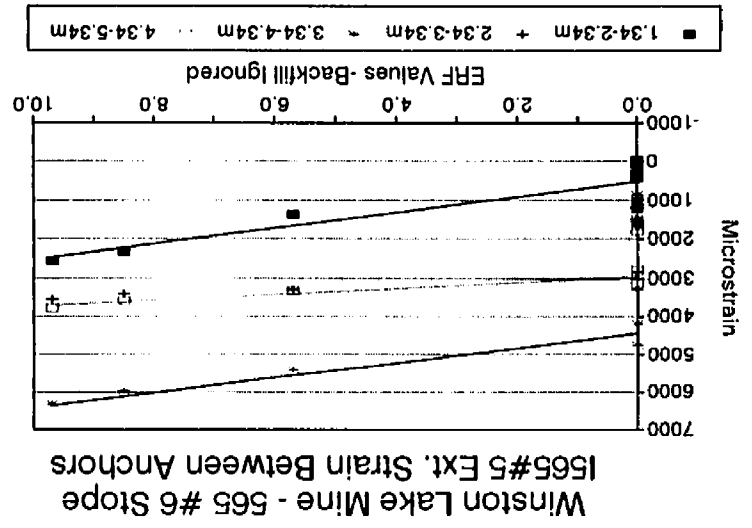
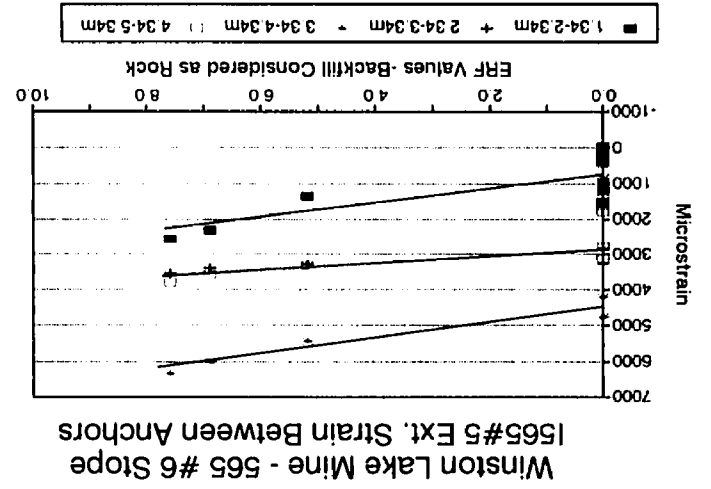
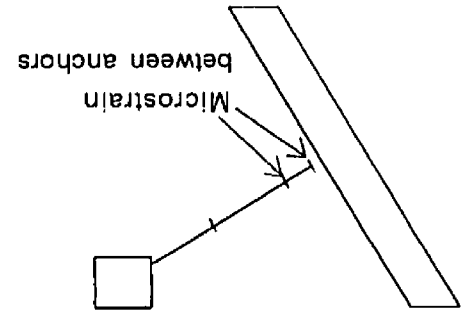


Figure 9.12 ERF values versus microstrain between the bottom anchors of extensometer I565#5. ERF values are based on three methods of assessing the effect of backfill.

and calculate the ERF values.

In this study, only the microstrain between anchors was investigated, not the total movement from the collar. The collars for these extensometers were located in the hanging wall cable bolt drift, which was well within the influence zone of the stoping block. Significant stress related collar movements were occurring with mining which disguised the actual movement of the immediate hanging wall.

Intuitively, backfill cannot provide as effective a support as intact rock. Also, backfilling does provide some support and limits movement since hanging wall dilution does occur if backfill is placed too late. In all three instruments, a relatively linear relationship was obtained between hanging wall strain and the ERF value calculated with the backfill influence located 20 metres behind the filling front and 6 metres below the base of the fill. The data set, unfortunately, is not conclusive since the three methods of assessing backfill only resulted in up to a 30% change in the ERF value calculation.

9.3.2 Phase 3, Winston Lake Hanging Wall Deformation, Stope 530#8

The third phase of the Winston Lake study included hanging wall instrumentation of interest located in Stope 530 #8. As in the first phase of the study summarized above, hanging wall deformation data from three extensometers (W1, W2 and W3), are compared to blasting and backfilling records to assess the influence of backfill. Figure 9.13 shows the location of these instruments on plan and section.

Two additional factors influence hanging wall movements above this stope:

1. Extensometers W1 and W2 were installed in a section of the hanging wall cable bolted with cables with barrel and wedge grips, which significantly increases cable support stiffness. The other section of the hanging wall was supported with birdcage cables which would be expected to allow greater hanging wall deformation.

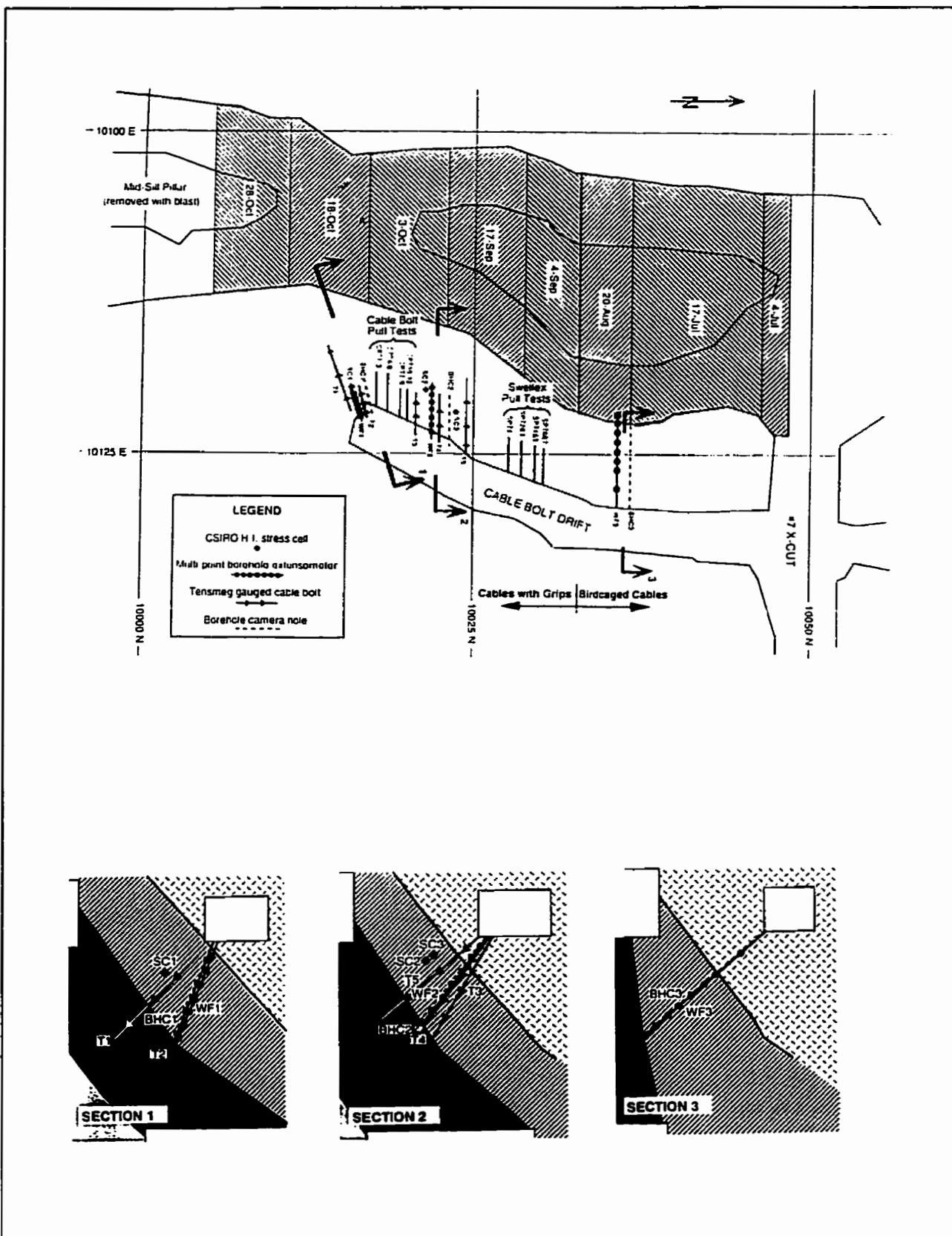


Figure 9.13 Plan and cross section views of the instrumentation installed in the 530 #8 stope (From Maloney and Kaiser, 1993).

2. The chert hanging wall above extensometers 530W1 and 530W1 was undercut by a failure over approximately a 15m strike length of the chert pillar between the 530 sill drift and cable bolt drift. The loss of this pillar undercutting the base of the hanging wall creates a small brow which increases the surrounding ERF values in the area. The effect of the brow was included in the calculation of the ERF values.

The influence of backfill on the ERF values was assessed in the same fashion by trying three approaches for quantifying backfill effect:

1. backfill was treated as a rock abutment
2. backfill on strike was ignored and below was assumed to provide support 6 metres below the fill base.
3. backfill support was considered to lag 20 metres behind the fill front and 6 metres below the fill base.

In each of the three extensometers, significant movement occurred prior to undercutting the instruments, possibly reflecting the unstable nature of the back of the undercut. Also, in each case the bottom 1 to 2 anchors, representing 1 to 2 metres of hanging wall, were lost after undercutting. The data from extensometers W1 and W2 showed the overriding influence of the cable grips used. After movement coinciding with initial undercutting, little or no movement occurred in the hanging wall. Data from these instruments were not analysed. Extensometer W3, however, was located above the birdcage cabled section of the hanging wall and showed continued hanging wall movement concentrated between the bottom remaining two anchors, 7 to 8 metres from the collar, and 4 to 6 metres from the collar. This movement probably coincides with zones of dilating foliation planes in the chert.

Backfilling in this stope occurred after all but one of the stope blasts, and blasts typically advanced the face about 6 metres. Open spans on strike were kept small, in the order of 15 metres. Figure 9.14 shows the three approaches for assessing the backfill effect.

When the backfill limit is treated like a rock abutment, a small moving window of open hanging wall results in the extensometers being exposed for only 2 or 3 blasts. The maximum

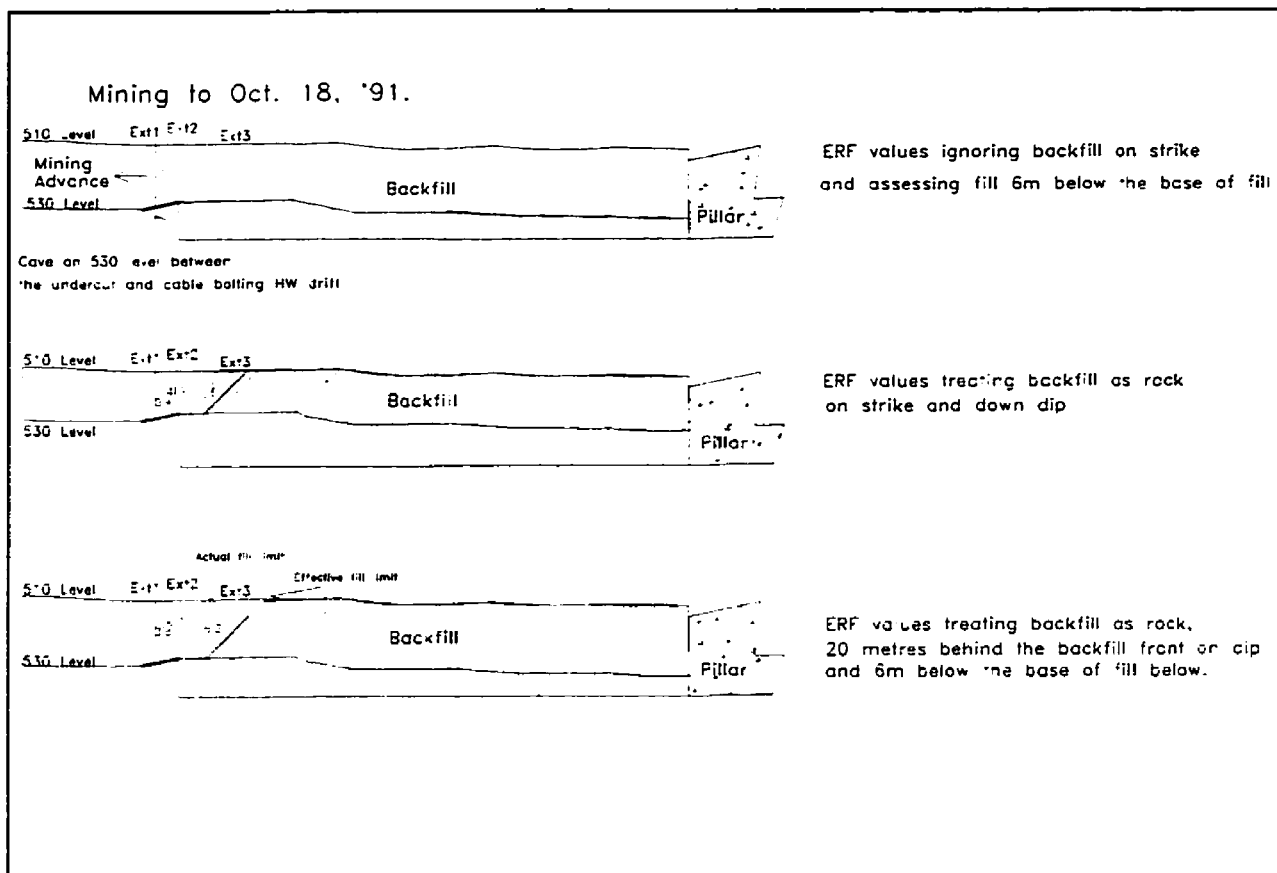


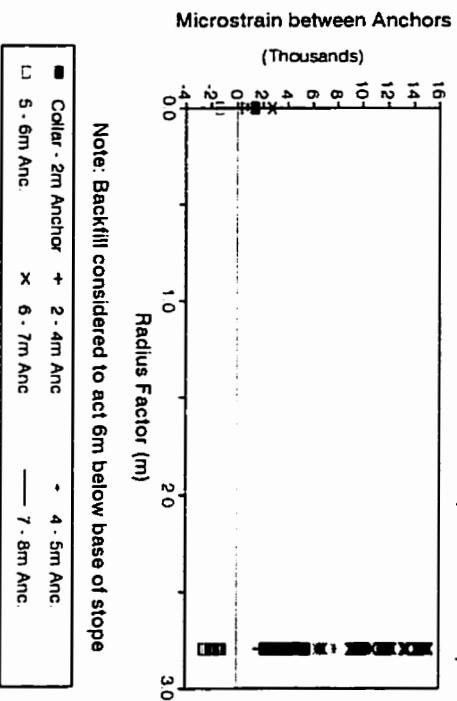
Figure 9.14 Longitudinal view of stope 530 #8 showing 3 methods of interpreting the effect of backfill on the effective radius factor.

radius factor is reached with initial exposure, or after the subsequent blast. If treating the backfill front as an abutment was a realistic approach, maximum movement would be reached after undercutting and only minor movement related to time dependent creep would be expected. Extensometer W3, located in the birdcaged cable section of the hanging wall, showed significant continued movement with each blast until the backfill front was well past the instrument location (Figure 9.15).

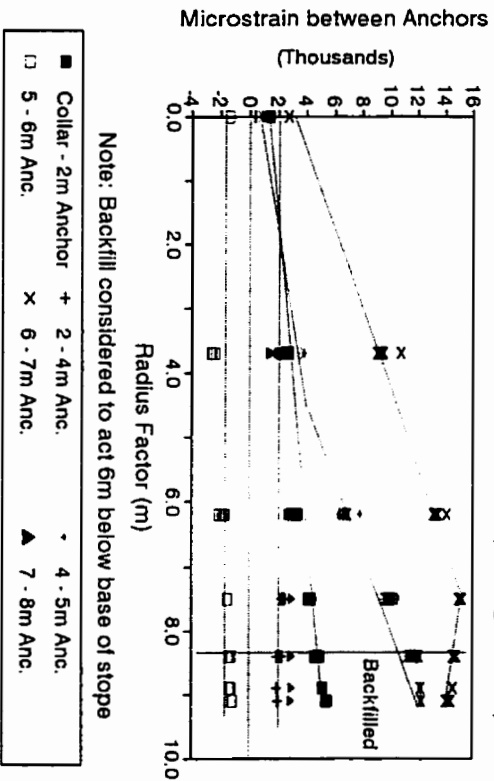
Figure 9.15 shows the other two techniques for interpreting the backfill influence. When the effect of fill was considered to act 6 metres below the fill base on dip and 20 metres behind the fill face on strike, a linear relation was obtained between strain and the ERF value until backfilling passed the instrument location. After fill was located below the extensometer, strain

Figure 9.15 ERF values versus microstrain between Ext. 530 #3 anchors. ERF values are based on 3 methods of assessing backfill effect.

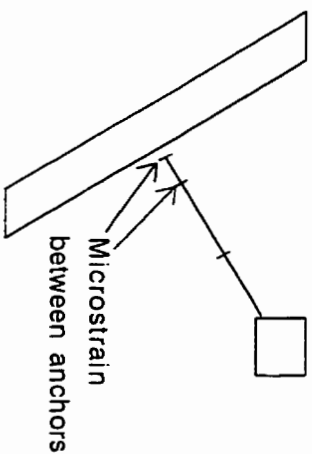
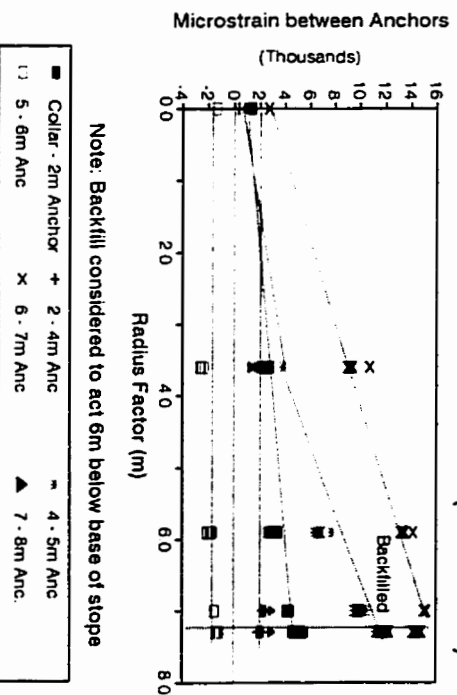
Winston Lake Mine - 530#8 Stope Ext.3
MStrain vs Radius Factor (Fill as rock)



Winston Lake Mine - 530#8 Stope Ext.3
MStrain vs Radius Factor (Fill Ignored)



Winston Lake Mine - 530#8 Stope Ext.3
MStrain vs Radius Factor (Fill + 20m)



between the bottom two anchors decreased indicating the lowermost anchor was resting on fill and the anchor a metre above was still moving down and was not yet seeing the effect of the fill.

In the case where the backfill was ignored when calculating the ERF value, a linear relationship was also obtained until backfilling passed the instrument location. There is little difference between the case where the influence of fill was ignored on strike or considered to lag 20 metres behind the fill front.

The instrumented hanging wall deformation data does not conclusively indicate the most accurate method of assessing the influence of backfill on hanging wall deformation and stability. The data does suggest that the common practise of treating the backfill front like a rock abutment is overly optimistic and could result in unstable designs.

9.4 SUMMARY

This section has attempted to quantify the effective open hanging wall geometry when one or more slope abutments consist of an advancing backfill front. Current empirical design procedures generally treat a backfill abutment the same as a rock abutment (Potvin, 1988; Hutchison & Diederichs, 1996). This is far from a conservative assumption, when the backfill abutment is continuously moving. The other extreme would be to ignore the presence of backfill, however, practical experience and documented case histories show this to be an unrealistic approach.

An hypothesis was put forward that for an advancing backfill front on strike, the effective on strike slope dimension should be a function of the open slope geometry before and after backfilling. The proposed effective open hanging wall geometry on strike is a sum of the open strike length before backfilling and after backfilling. This gives a design strike length greater

than the strike length ever exposed during the mining / backfilling cycle. The following example illustrates two extremes where the same maximum stope strike length is allowed:

Case 1

A stope is mined on strike to a length of 25 metres, 20 metres of backfill is added along strike to reduce the open length of ground to only 5 metres on strike. Blasting advances until a strike length of 25 metres is again open. In this case between 5 and 25 metres of ground is open on strike (the strike length exposed never exceeds 25 metres). As this cycle continues the effective open strike length becomes 30 metres (25m + 5m).

Case 2

In this case the stope is also mined to a maximum strike length of 25 metres. Backfill is then added to reduce the open strike length to 20 metres and blasting again advances the face. In this case between 20 to 25 metres of ground is always open on strike and it would be expected that a less stable condition would result than in case 1. The proposed effective open strike length becomes the sum of these two values to give a 45 metre effective strike length.

The available instrumentation data and stability assessment suggest that treating the backfill limits the same as rock abutments is overly optimistic. The data suggests it is realistic to assume the effect of the backfill lags behind the actual backfill front, however, sufficient data are not available to conclusively indicate how much this lag should be. Figure 9.4 presents a realistic initial approach for assessing a continuously moving backfill front. Effective support from a backfill front acts at a distance behind the actual location of the backfill front. The effective final opening strike length is taken as the sum of the maximum and minimum opening strike lengths developed during the mining and backfilling cycle.

The next chapter investigates the use of the radius factor term for assessing surface

geometry for surface stability design.

CHAPTER 10

RADIUS FACTOR AND SURFACE STABILITY ANALYSIS

10.1 INTRODUCTION

The previous chapters have shown a relationship between theoretical and actual surface deformation and the surface effective radius factor (ERF) values. The maximum surface movement can be expected to coincide to the location of the maximum ERF value, which is equal to the surface radius factor (RF). As movement on a surface increases past the elastic limit, general dilation of fractures reduces the overall stability of a surface. This chapter looks at relating increasing RF values to reduced surface stability.

A link has been shown between HR and RF in Chapter 5. Several design techniques have been developed which relate rock mass conditions to hydraulic radius and surface stability which include the following:

- Laubscher Design Method (Laubscher, 1990) (Sect. 2.2.5)
- Mathews' Design Method (Mathews et al, 1981) (Sect. 2.2.6)
- Dilution Design Method (Pakalnis, 1987) (Sect. 2.2.7)
- Modified Stability Graph Method (Potvin, 1988) (Sect. 2.2.8)
- Bench Stability Method (Villaescusa, 1996) (Sect. 2.2.9)

The Modified Stability Graph method is an empirical design technique which has had widespread application in Canadian hard rock mines. This approach is based on an initial database of 176 unsupported and 59 cable supported case histories. Supported case histories refer to stopes where cable bolts have been used for support. Figures 2.9 and 2.10 summarize this graphical design technique. It consists of a graph divided into stable, support required and unstable or caving zones. The graph plots surface hydraulic radius on the X axis versus a parameter, Stability Number N, which quantifies the strength and stresses acting on the rock

mass. This design technique has been modified by Nickson, (1992) with an additional 13 unsupported and 46 supported case histories. The next section looks at the original database to see if the radius factor term can replace the hydraulic radius term.

10.2 MODIFIED STABILITY GRAPH DATABASE

The Potvin and Nickson databases were combined and produced the modified stability graph. No change was recommended in the design transition zone between stable and unstable without support. A new transition zone between stable and unstable surfaces was developed for cable supported surfaces.

Before investigating the possibility of replacing the hydraulic radius with radius factor it is of value to consider the ratio between the HR and RF values with an increasing width to length ratio. Figure 10.1 shows a graph of the ratio between HR and RF values, expressed as a percentage, versus the length to width ratio of a rectangular surface. The majority of stope surfaces have a length to width ratio of between one to ten. Narrow stope backs may be an exception to this, however, both the RF and HR values for these surfaces would be small. The RF and HR values are equal at a length to width ratio of approximately 3.0. For a square surface the RF value is greater than the HR value ($HR = 90\% RF$). For a length to width ratio of ten, the HR value is greater than the RF value ($RF = 86\% HR$).

In order to assess the possibility of replacing the hydraulic radius term on the X axis of the modified stability graph, information on the dimensions of the surfaces analysed is required. Only the surface hydraulic radius is provided in the original design work (Potvin, 1988). A progress report (Potvin, 1987), however, provided detailed stope dimension data on a portion of the original data to allow calculation of RF values. The database collected by Nickson (1992)

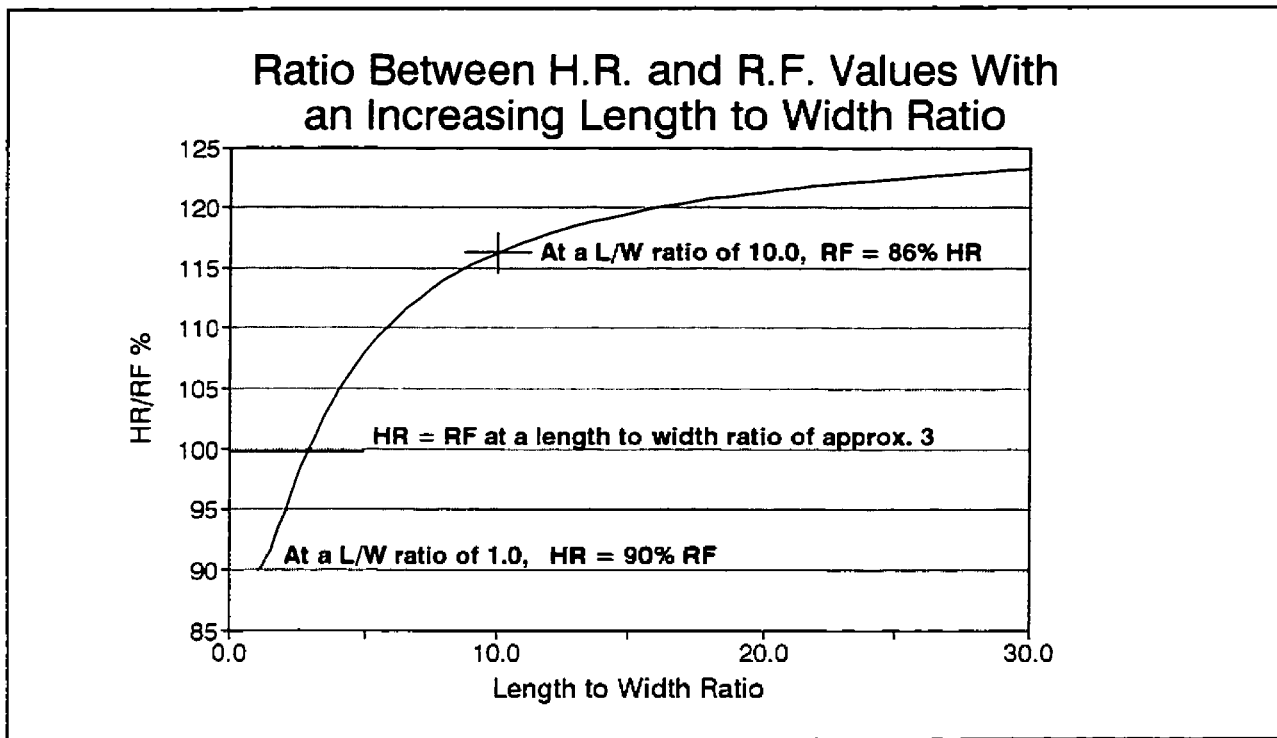
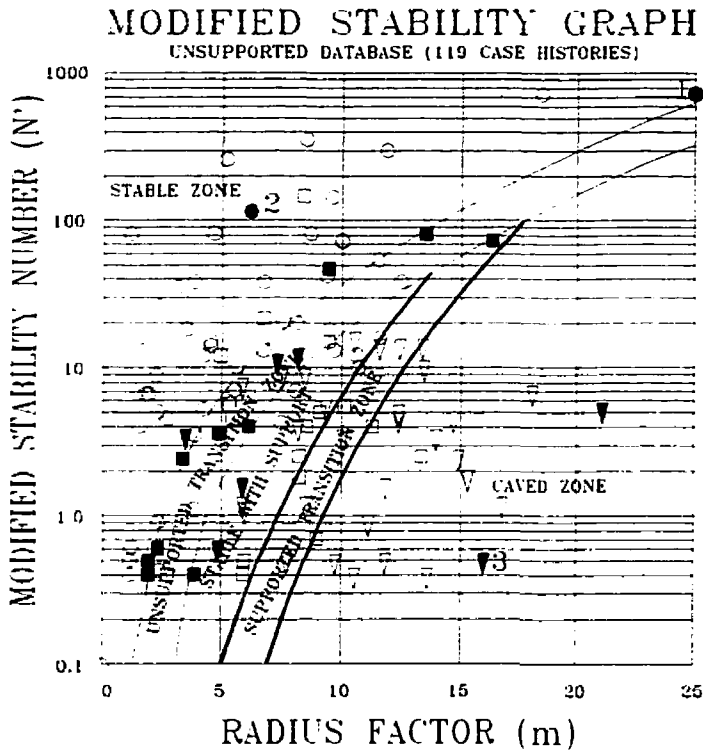
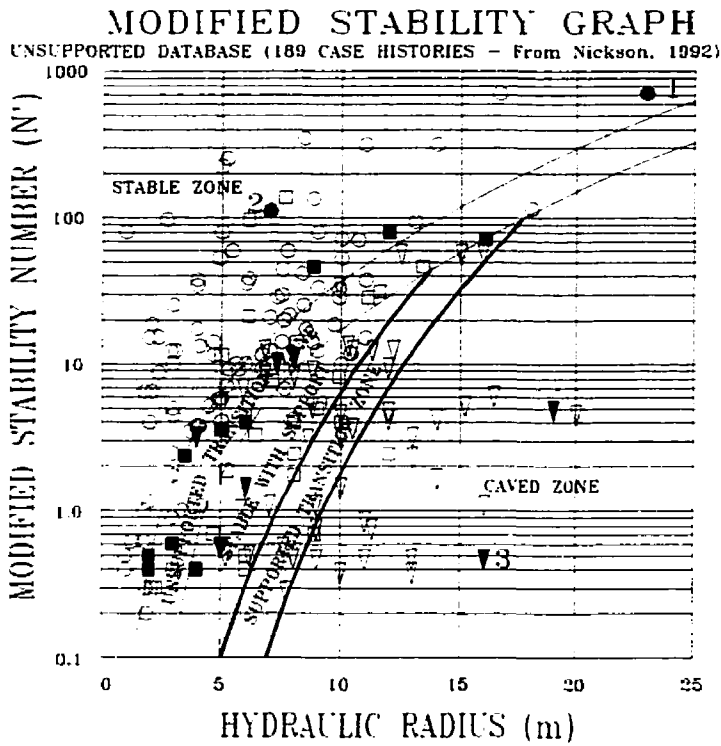


Figure 10.1 Graph of the ratio between HR and RF values plotted against an increasing surface length to width ratio.

also included detailed slope dimensioning. In all cases, the HR value was recalculated with the geometry data provided. If the recalculated HR value differed from the tabulated value by more than 10%, the case history was not considered. From the 189 unsupported case histories collected by Potvin and Nickson, slope dimensions for 119 case histories allowed determination of RF values (Figure 10.2). From the 103 combined supported case histories, 65 cases included slope dimensions for determining RF values (Figure 10.3).

Figures 10.2 and 10.3 show the original unsupported and supported database plotted on the modified stability graph. The available data were plotted versus both the hydraulic radius and the radius factor and several highlighted case histories are shown. These were chosen to show the shift along the x-axis between the graphs plotted with hydraulic radius compared to those plotted with radius factor. On both the supported and unsupported modified stability graphs, points were labelled 1, 2 and 3 which show cases where the RF value was greater, less



Without Cables	
Ref. Points:	General Points
● Stable	○ Stable
■ Unstable	□ Unstable
▼ Caved	▽ Caved
Labelled Points	
● 1	RF > HR
▼ 2	RF < HR
▼ 3	RF = HR

Figure 10.2 Unsupported case histories plotted on the modified stability graph using hydraulic radius and radius factor (After Milne et al., 1996).

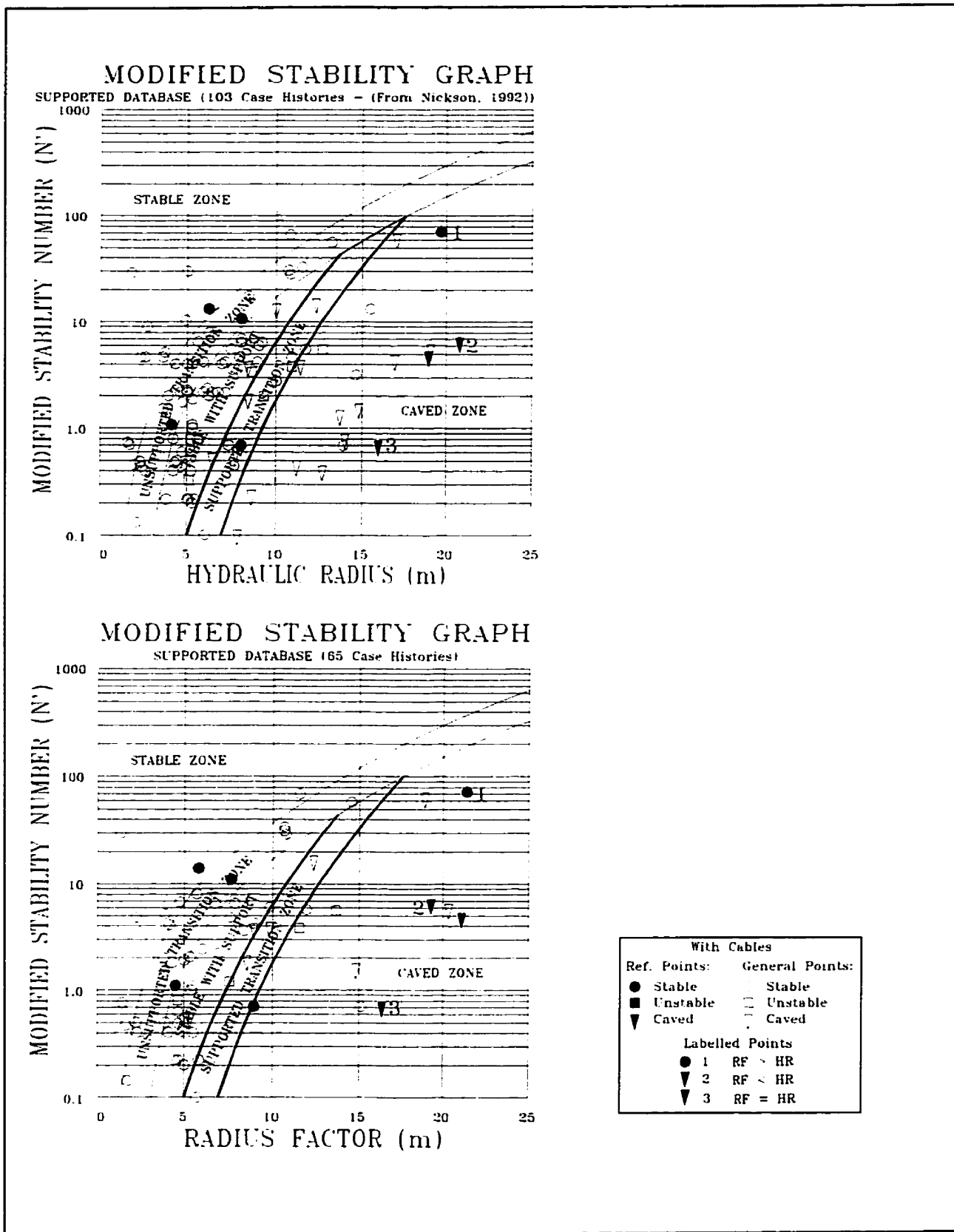


Figure 10.3 Supported case histories plotted on the modified stability graph using hydraulic radius and radius factor (After Milne et al., 1996).

than and approximately equal to the HR value.

Based on an inspection of the case histories plotted with the RF value, the same design zones between stable, stable with support and unstable are applicable. Since converting HR values to RF values results in up to either a 10 to 15% increase or decrease in magnitude, no clear trends developed which would justify changing the design boundaries. Except for large surfaces ($HR \geq 10m$), the change from HR to RF values would result in up to a one metre change. A change in plus or minus one metre for the HR value on the modified stability graph is within the tolerance of the design technique.

With the available data it appears that the radius factor term could replace the hydraulic radius with the modified stability graph design method, without adjusting the design limits. There is little advantage, however, to using the RF term instead of HR for simple rectangular surface geometries. For irregular surfaces the RF term simplifies the difficulty associated with determining a representative HR value (Figures 4.4 and 5.2). Cut and fill mining with irregular stope boundaries and isolated post pillars is ideally suited for analysis with the RF term. Also, for surfaces cut by raises, the RF value provides a more realistic surface assessment (Figure 5.6). The next section will consider several case histories where the RF value provides a more realistic assessment of surface geometry for stability design.

10.3 CASE HISTORIES

Several case histories assessing the modified stability graph design method with the RF term have been documented (Milne et al., 1996) and much of this section is taken from that paper.

Limitations to the modified stability graph design technique have been highlighted in the

past. Potvin and Milne (1992) discussed difficulties associated with assessing back stability in areas cut by raises. The hydraulic radius term cannot account for these more complex geometries. Three case histories of back instabilities from a mine in Northern Canada are presented in this section. In each case, back instability occurred in areas where the modified stability graph analysis predicted stability. These cases were associated with the presence of a raise, the approach of a brow or the intersection of a cross drift. In some instances the ground fall was also influenced by inclusions of waste in the ore back, which weakened the overlying strata. Each of these cases are re-analysed using the radius factor as well as hydraulic radius terms. Data for these case histories has been obtained from an internal Noranda Technology Centre report (Milne, 1991) (Milne et al., 1996).

10.3.1 565 # 8 Ground Fall

Figure 10.4 shows views of a 230 tonne ground fall which occurred above the 565 #8 stope. This failure was triggered by a stope blast in the adjacent advancing brow. Remote mucking was being conducted from a supported area of the stope and there was no access in the unstable area.

A hydraulic radius of approximately 3.1m can be estimated for this area and a maximum radius factor of 3.6m can be determined, which takes into account the advancing mining front. A stability number, N, of 2.0 is determined for this area based on the following input parameters (Section 2.2.8):

$$Q' = 20$$

$$A \text{ factor} = .1 \text{ (Stress } \approx 50\% \text{ of UCS)}$$

$$B \text{ factor} = .5 \text{ (45}^\circ \text{ foliation)}$$

$$C \text{ factor} = 2 \text{ (horizontal back)}$$

$$N = 2.0$$

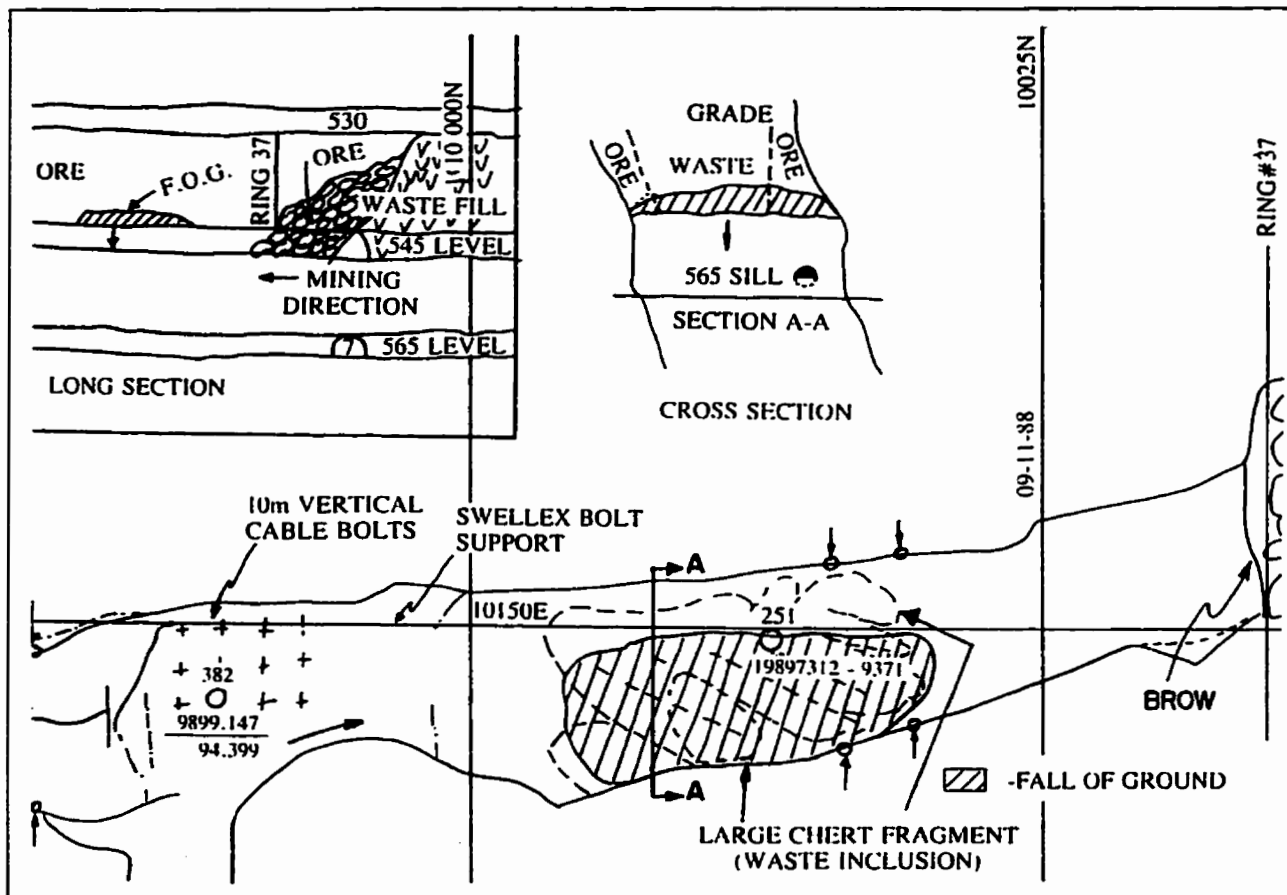


Figure 10.4 Plan and sectional view showing the 565 #8 ground fall (From Internal Noranda Technology Centre report)

Figure 10.5 shows a plot representing the stability of this stope area based on the HR and RF values. No support was installed in this area, nor was it indicated based on the modified stability graph using hydraulic radius. Based on the RF plotted stability for this area, however, some uncertainty for the unsupported stability of this area would have been indicated.

10.3.2 565 #6 Ground Fall

Figure 10.6 shows views of a 550 tonne ground fall on the 565 level. The ground fall was suspected to have been initiated with blasting in an adjacent raise. Support in this area consisted of 2.4 metre swellex bolts and no cable support was installed.

A hydraulic radius of approximately 2.3m is estimated for this area. The block size in

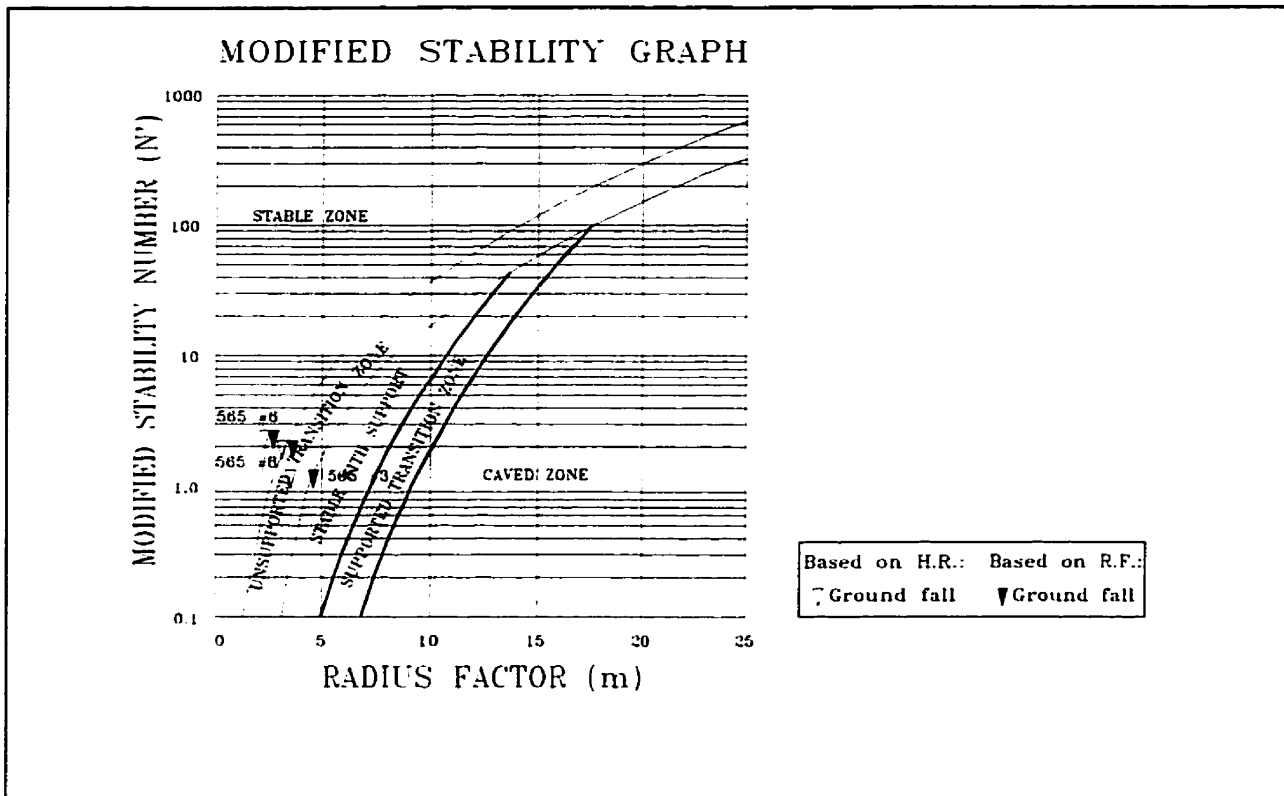


Figure 10.5 Modified stability graph plot of case histories, based on both the surface radius factor and hydraulic radius.

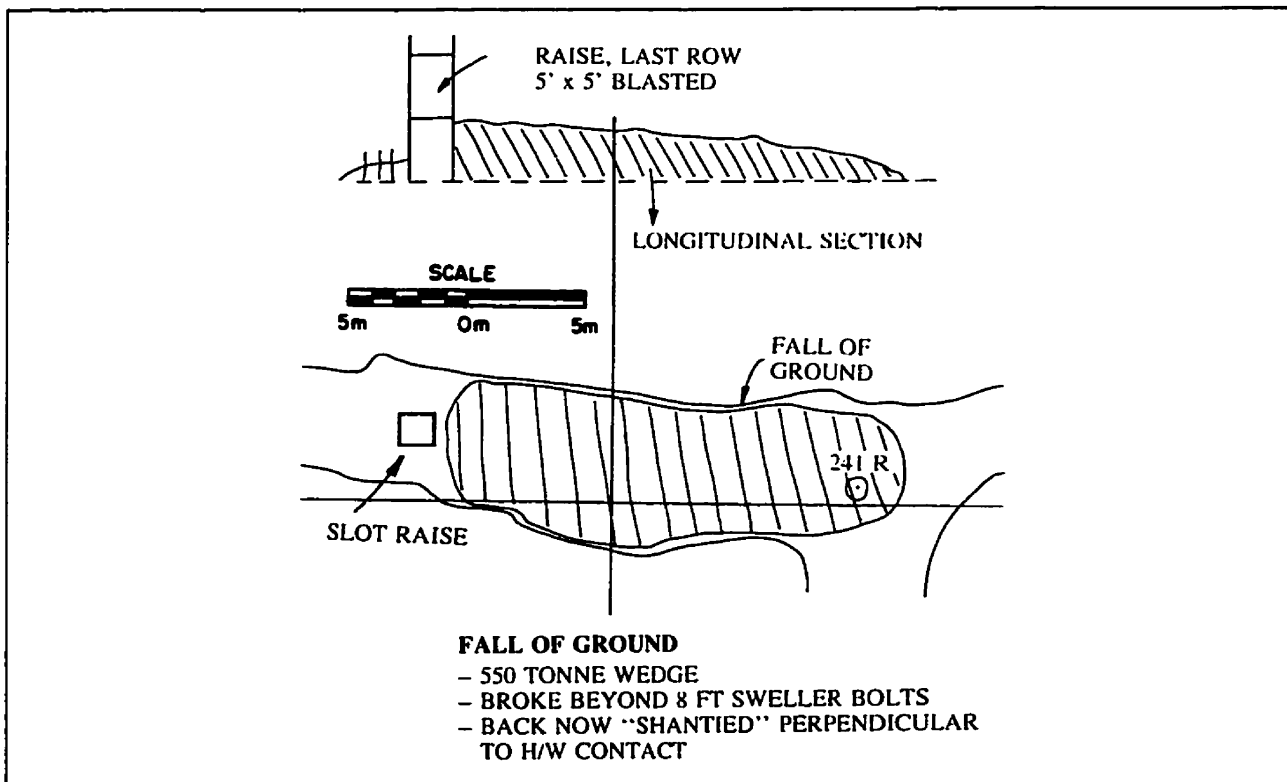


Figure 10.6 Plan and cross section views of the 565 #6 ground fall (From NTC Internal report)

this area is approximately .5 metres. A radius factor of 2.7m, calculated .5 metres from the raise at centre span, gives the maximum realistic RF value for this area. A larger RF value could be determined closer to the raise, however, the RF value should be determined at least one block size diameter away from a raise. A stability number of 2.4 is determined for this area based on the following parameters:

$$Q' = 20$$

$$A \text{ factor} = .1 \text{ (Stress} = 50\% \text{ of UCS)}$$

$$B \text{ factor} = .6 \text{ (} 50^\circ \text{ foliation)}$$

$$C \text{ factor} = 2 \text{ (horizontal back)}$$

$$N = 2.4$$

The modified stability graph plot of this point clearly indicates no support was required in this area (Figure 10.5). Based on the radius factor plot, cable support still would not have been indicated, however, the plotted value has moved towards the transition zone where support may be indicated.

10.3.3 565 #3 Ground Fall

Figure 10.7 shows a plan and cross sectional view of this 150 tonne ground fall. Swellex support had been installed in this area, however, cable support was not installed due to the limited opening span.

A hydraulic radius of 3.5m can be estimated for the back in this area. This ground fall occurred at a 'T' intersection with a cross cut drift. The hydraulic radius cannot account for this geometry, whereas the maximum radius factor of 4.6m includes the influence of this cross cut. A stability number of 1.2 is determined from the following parameters:

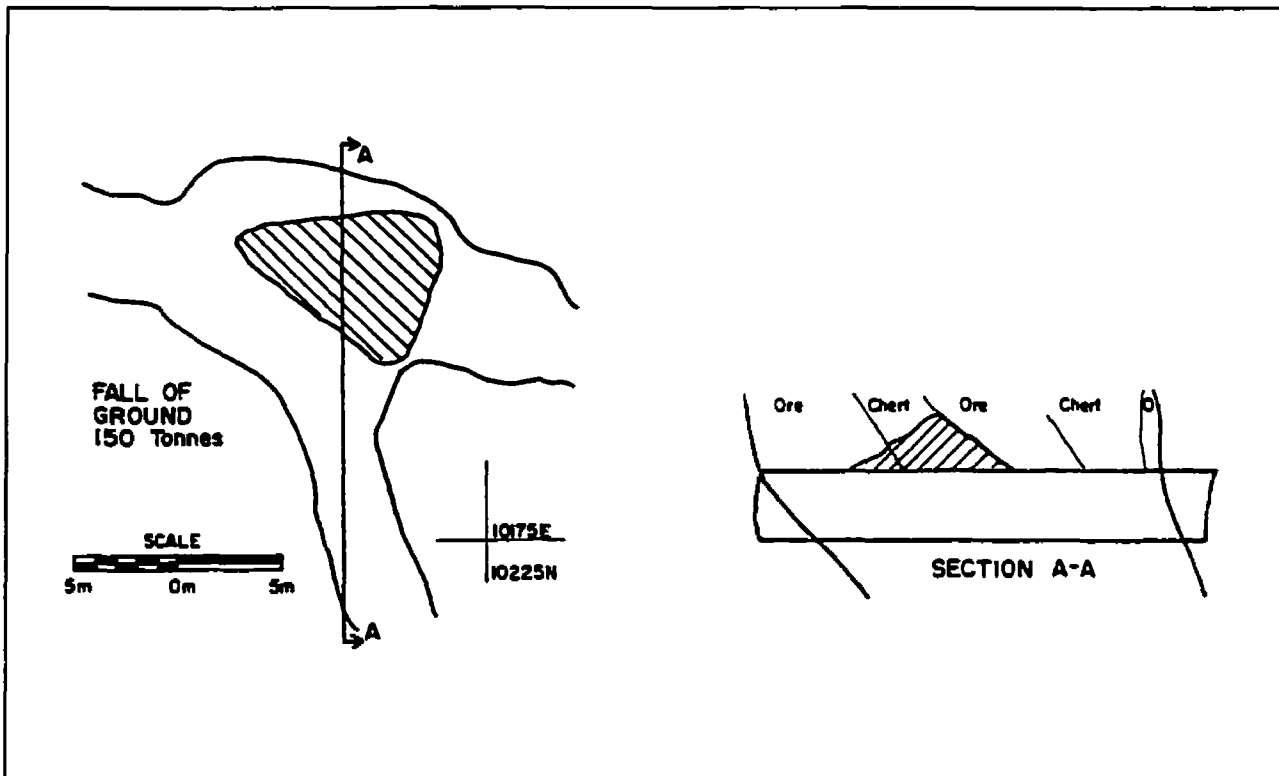


Figure 10.7 Plan and cross section showing the 565 #3 ground fall (From NTC Internal report).

$$Q' = 20$$

$$A \text{ factor} = .1 \text{ (Stress } \approx 50\% \text{ of UCS)}$$

$$B \text{ factor} = .3 \text{ (35}^\circ \text{ foliation)}$$

$$C \text{ factor} = 2.0 \text{ (horizontal back)}$$

$$N = 1.2$$

The hydraulic radius plot of this point is in the transition zone where cable support may be required, however, the radius factor plot indicates the need for cable support. A chert inclusion in the back of this ground fall contributed to the instability in this area.

10.4 SUMMARY

The hydraulic radius term has been used extensively for the empirical design of stable

surfaces in underground mines. The term can be expressed as a function of the minimum distance to supporting abutments. A new parameter, radius factor, is based on a much more accurate calculation of the distance to abutments and better reflects the stability of complex geometries. Overall surface stability can be better assessed with the radius factor value. The relative stability of any point on a surface can also be quantified with the effective radius factor term.

The case histories presented show that using the radius factor term can provide a more conservative and accurate estimate of stability for complex opening geometries. The method is not foolproof, as indicated in section 10.3.2. There are still factors such as anomalous geological conditions, characterized by the presence of faults or weak inclusions (Potvin and Milne, 1992), which the design method can not be expected to account for.

The radius factor allows a more rigorous assessment of surface geometry and could be applied to other empirical design techniques.

CHAPTER 11

SURFACE FAILURE GEOMETRY AND EFFECTIVE RADIUS FACTOR VALUES

11.1 INTRODUCTION

The previous chapters have shown a relationship between the stability of a surface and the maximum effective radius factor, or radius factor value for the surface. Given limited surface deformation data, a correlation has also been determined between the ERF value on a surface and the relative surface deformation. This chapter considers the geometry of a surface after failure and the RF and ERF values.

Field data concerning surface geometry after failure has been collected at Brunswick Mine Ltd. and Placer Dome Inc.'s Detour Lake Mine. The Brunswick Mine study assesses data collected during a research project sponsored by Brunswick Mining, the Noranda Technology Centre (NTC) and the Mining Research Directorate and details of the study are presented in Section 8.4. The Detour Lake Mine data is from a research project conducted between the mine and the Canada Centre for Mineral and Energy Technology (CANMET). The findings from these case histories are summarized in this chapter.

11.2 THEORETICAL FAILURE GEOMETRY

Failure of an underground surface can be governed by a block failure, stress failure or a ravelling failure mechanism, as shown in Figure 11.1. The shape of a block failure is generally controlled by the strength and orientation of joints or shears in the rock mass. A ravelling failure can occur when the rock mass block size is small relative to the surface

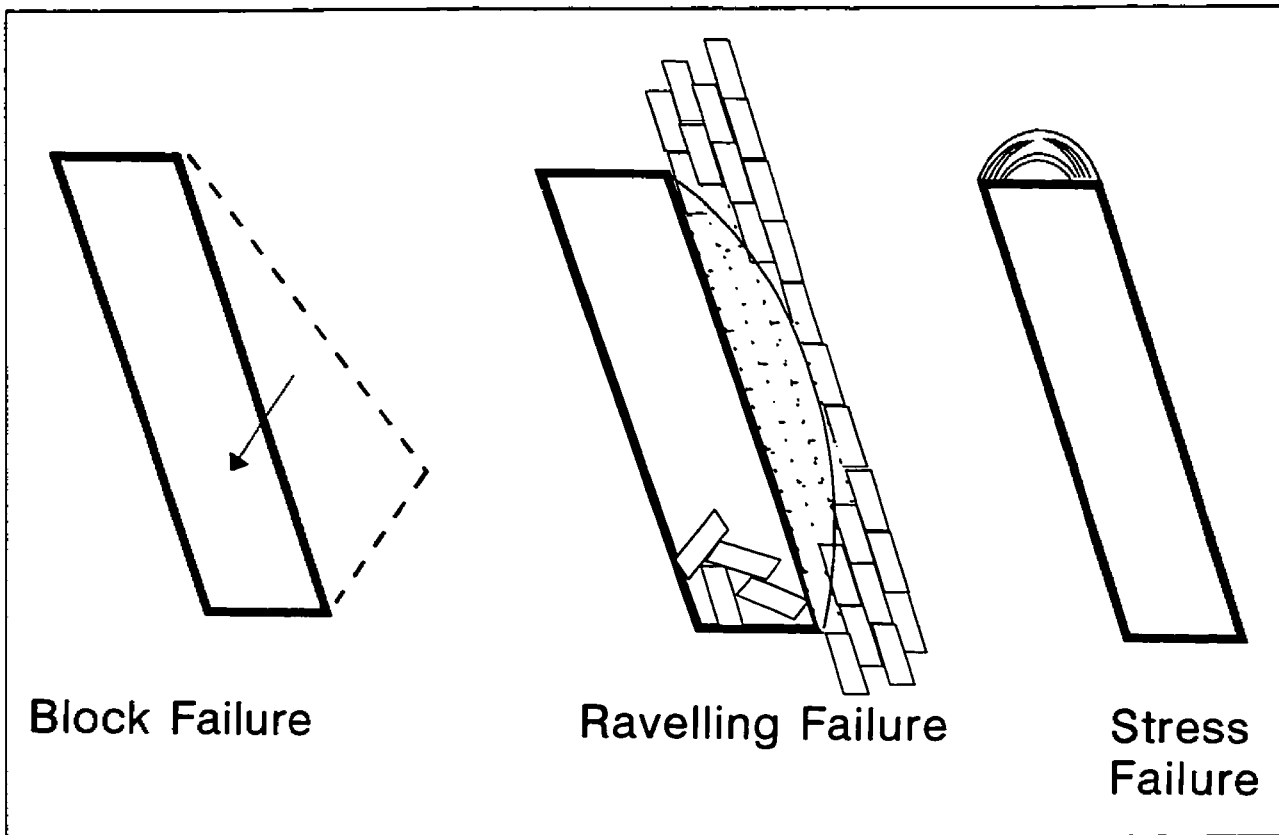


Figure 11.1. Examples of a block failure and a ravelling failure.

geometry. The geometry of a ravelling or stress failure takes a general arched shape but is influenced by several parameters:

- The geometry of the small blocks which are failing may reflect the final failure surface geometry.
- Clamping stresses may be present at some distance from the open surface. The profile of these stresses may influence the failure geometry.
- Failure may progress to a stabilizing arch.

The influence of these factors on the geometry of a ravelling failure is discussed to determine if they can be related to the ERF term.

11.2.1 Influence of Block Geometry on Ravelling Failures

The initial stages of a failure may take the form of a block failure, possibly with several

blocks contributing to the failure. As the failure progresses to a ravelling failure, the block size relative to the failure or surface geometry becomes small, as shown in Figure 11.2. On a small scale the independent block geometry is apparent, however, on a large scale a curved or arched failure surface is generated.

11.2.2 Influence of Field Stresses on Ravelling Failures

A lack of clamping stress is often a factor in a ravelling failure. Adjacent to large openings, tensile field stresses are often modelled close to and parallel to the opening. These tensile stresses cannot actually be generated in a fractured rock mass, however, modelled tensile stresses indicate that fractures may open and that the rock mass is no longer being clamped together. This zone of modelled elastic tensile stresses, where clamping stresses parallel to the opening are absent, is often referred to as a relaxation zone around an opening. As the opening

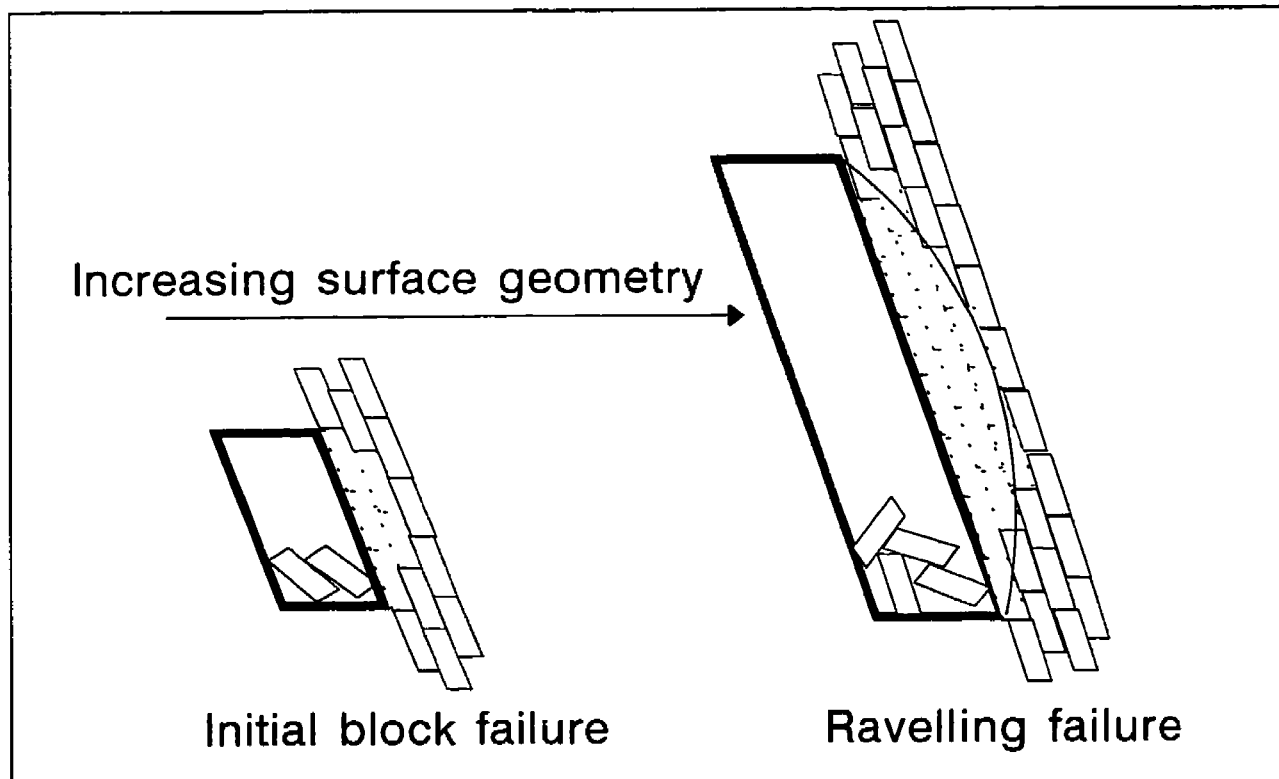


Figure 11.2 General failure geometry generated by a ravelling surface failure.

surface extent increases, the depth of the relaxation zone increases. At some point when the relaxation zone is large enough relative to the rock mass block size, ravelling failure can initiate.

Section 7.3 compared the depth of modelled tensile stresses parallel to an opening and the surface effective radius factor value. A linear relationship was obtained between the maximum depth of tensile stresses parallel to an opening and the surface radius factor value (Figure 7.12), determined for various opening geometries and field stress ratios. Given that the potential for a ravelling failure increases with the depth of surface relaxation, a relationship between depth of ravelling failure and surface radius factor values is worth investigating.

11.2.3 Influence of Arching Action on Ravelling Failures

When clamping stresses no longer exist in a fractured rock mass and the rock mass block size is small relative to the zone of relaxation, a voussoir type arching action is required for the rock mass to be self supporting. Sections 2.3.6 and 3.2.6 goes into some detail on voussoir arch theory. Voussoir arch action generates a self supporting compressive arch in the rock mass. This compressive arch has the geometry of a parabola (Brady and Brown, 1985). In sections 5.3.1 and 5.3.2, an arch corresponding to surface effective radius factor values was generated. This arch closely followed the geometry of a parabola indicating that it may be possible to relate the geometry of voussoir arching action generated above a surface and the relative ERF values on the surface.

The next section looks at failure geometries measured in the field.

11.3 BRUNSWICK MINE HANGING WALL INSTABILITY

A geomechanics research project was conducted between Brunswick Mining, NTC and

the Mining Research Directorate during 1992 and 1993. The study consisted of the mining of an extensively instrumented hanging wall. Details of this study are presented in section 8.4. Hanging wall instability necessitated termination of the stope prior to the planned completion geometry. This section assesses the magnitude of hanging wall slough with increasing hanging wall surface geometry.

11.3.1 Stability Analysis

The stope hanging wall consisted of a weak sericitic schist. In areas of relatively low induced stress, the rock mass had the following properties:

- RQD = 90%
- J_n = 9 (3 Joint sets)
- J_r = 1.0 (Smooth joint surfaces)
- J_a = 4.0 (Chloritic infilling of foliation surfaces)

$$Q' = 4.0$$

In areas of high stress near stoping blocks, the observed RQD was much lower due to stress induced failure along foliation.

The following factors can be applied for the modified stability graph analysis:

- Q' = 4.0
- A = 1.0 (Stress Factor, Low Stress)
- B = .3 (Joint orientation factor - joints parallel to the hanging wall)
- C = 6.4 (Hanging wall dipping at 75°)

$$N = 7.7 \text{ (Stability Number)}$$

Eight major blasts opened up this stope and the geometry after each of these blasts is shown in Figure 8.15. With each hanging wall geometry after major blasts, a surface radius factor value has been calculated. These values are plotted on the modified stability graph for RF values and are shown in Figure 11.3. Significant hanging wall slough corresponded to opening up this stope. Figure 11.4 shows the estimated hanging wall failure geometry with

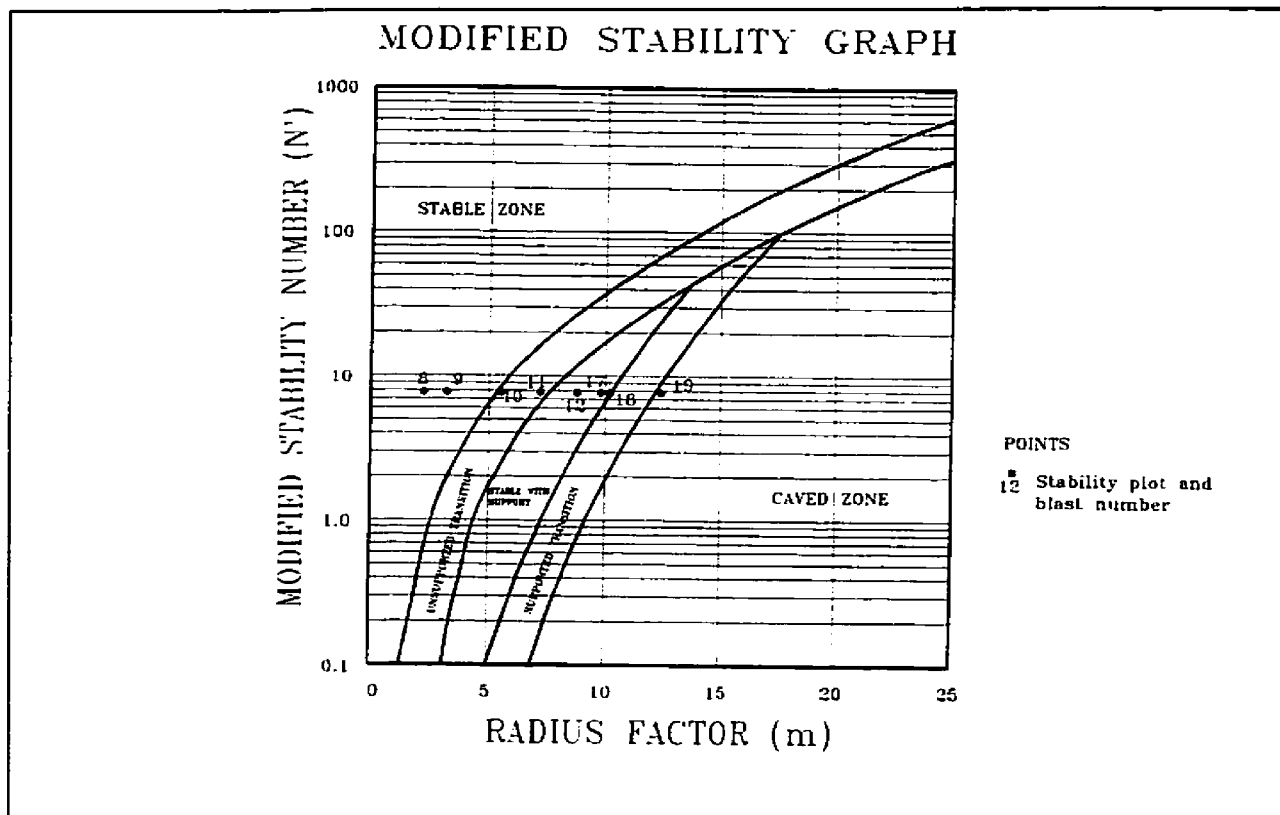


Figure 11.3 Stability plot of the 16N stope hanging wall after major blasts.

major blasts, based on extensometer data.

11.3.2 Failure Radius of Curvature

As shown in Figure 11.4, the general interpreted failure geometry follows an arched shape. It is possible to quantify this geometry in terms of a radius of curvature. Simply expressing the hanging wall slough as a maximum or average number of metres of slough does not effectively quantify the degree of instability. One metre of slough above a three metre wide drift indicates extensive failure and unstable conditions whereas one metre of failure on the hanging wall of a 30 metre by 50 metre stope is often considered quite minor. The degree of arching associated with a failure takes into account the overall surface geometry as well as the maximum depth of slough.

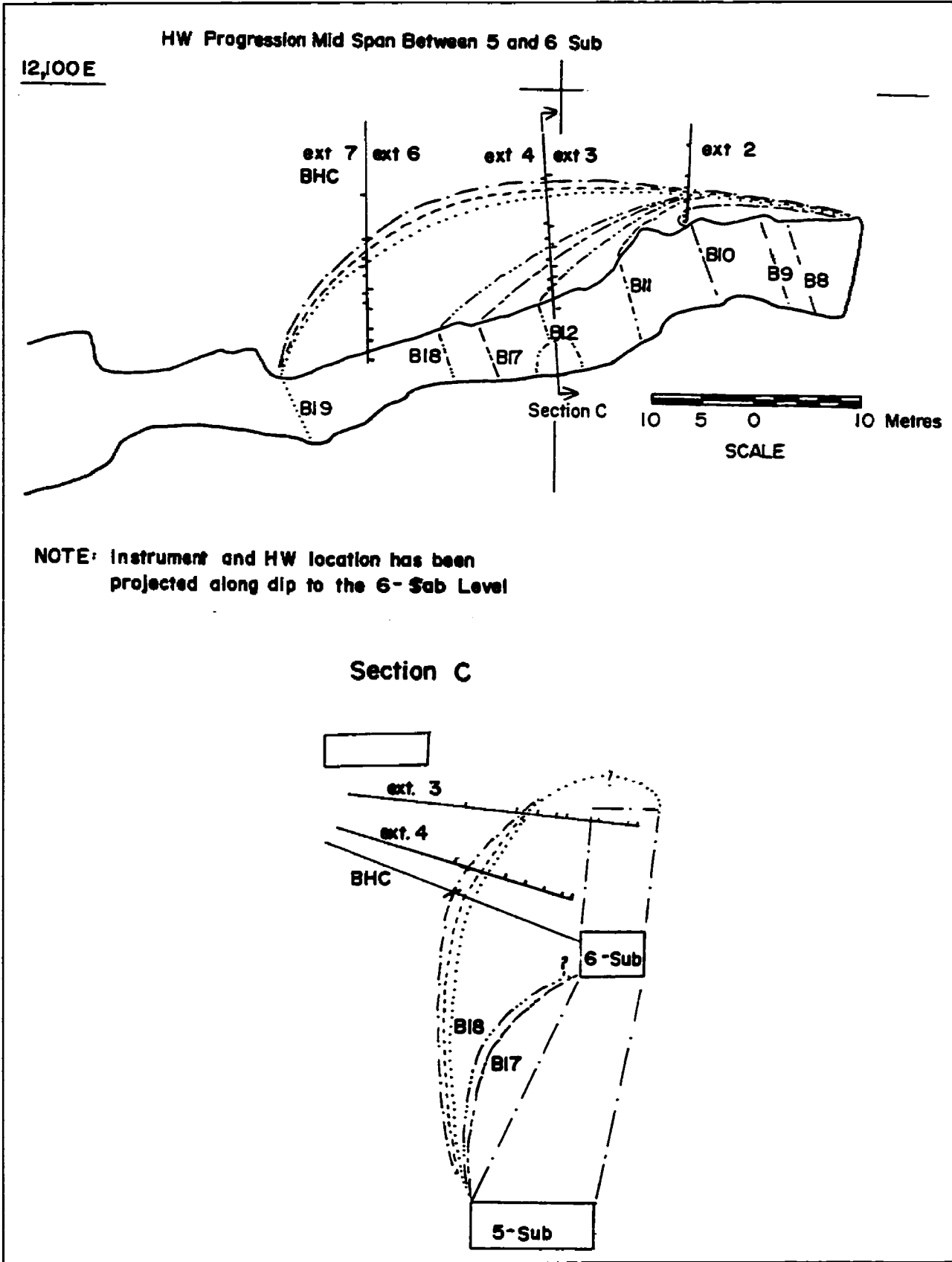


Figure 11.4 Plan and cross section views of hanging wall sloughing with mining.

Figure 11.5 shows the approach for determining the radius of curvature of a failure surface. The radius of curvature (RC) should generally be determined for the minimum opening span since the minimum span has the greatest influence on opening stability (Section 5.3.2). To attempt to account for the effect of two way spanning, the parameter relating to span can be replaced by radius factor since RF is equal to one quarter the span of a circular opening.

Based on the minimum opening span and the estimated metres of hanging wall slough, a radius of curvature for the estimated failure can be determined for each blast. Table 11.1 presents the surface RF value, minimum span, maximum metres of slough and corresponding radius of curvature. This radius of curvature has been plotted against the overall surface radius factor in Figure 11.6. The radius of curvature of the failed surface was relatively constant relative to the opening geometry and ranged between 15 to 21.5 metres. The next section looks

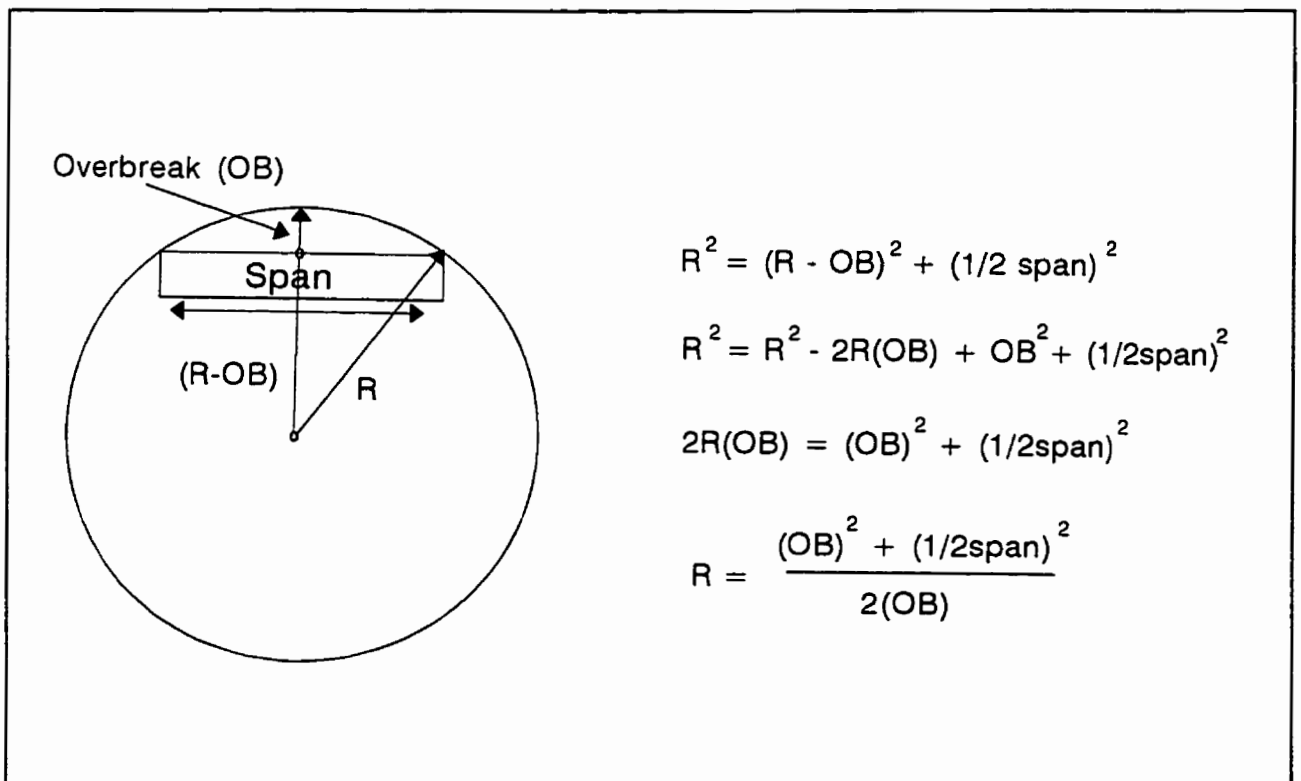


Figure 11.5. Relationship between maximum surface slough or overbreak and failure radius of curvature.

Table 11.1
Stope 16N - HW Slough for Major Blasts

Blast	RF (m)	Min Span (m)	Max. Slough (m)	Rad. of Curvature (Min Span)	Rad. of Curvature (RF Value)
8	2.2		0	Inf.	Inf.
9	3.4		0	Inf.	Inf.
10	5.5	16m	2m	17.0m	31.3m
11	7.2	23m	4.5m	21.5m	26.8m
12	8.8	23.5m	4.5m	21.5m	39.0m
17	9.8	24m	6m	15.0m	35.0m
18	10.2	24m	6m	15.0m	37.7m
19	12.5	32m	8m	20.0m	42.4m

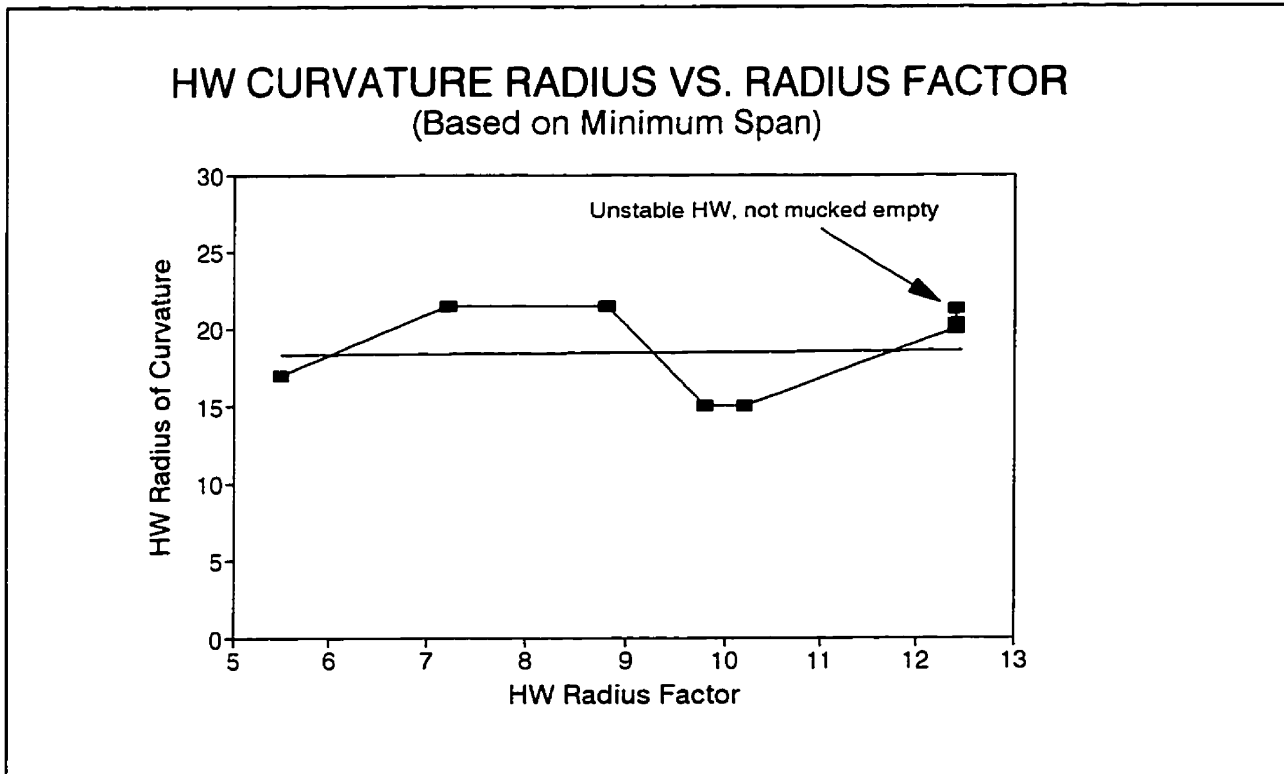


Figure 11.6. Hanging wall radius of curvature versus surface radius factor for the Brunswick Mine 16N stope.

at the estimated hanging wall depth of slough with the expected zone of relaxation.

11.3.3 Hanging Wall Depth of Relaxation

Section 7.4 has related the maximum depth of relaxation above a surface to the surface radius factor value. The relationship was determined for conditions where the principal stresses were oriented parallel and perpendicular to the opening surface with the stress ratio K varying from 1.5 to 2.5.

At the Brunswick mine, sill pillar stope 16N, pre-mining stress measurements indicated a stress ratio K of approximately 3.0, with the maximum stress oriented normal to the ore body (Kanduth et al. 1992). This stress ratio can be expected to have increased as mining progressed in the sill pillar. Figure 11.7 shows the depth of failure versus surface RF values for the major blasts in the 16N stope. These values are plotted on the graph showing maximum depth of relaxation versus RF values for various stress ratios. The initial hanging wall slough coincides well with the depth of relaxation for a stress ratio of 3:1. Subsequent blasts show an increase in the depth of slough corresponding to increased hanging wall relaxation. An increased depth of hanging wall relaxation is a result of an increase in the stress ratio due to continued mining.

11.3.4 Summary

The Brunswick Mine 16N sill pillar stope had extensive hanging wall failure delineated by several hanging wall extensometers. Two methods were considered for quantifying the failure extent. A surface radius of curvature was determined based on the maximum depth of failure and the minimum surface span. A relatively constant radius of curvature for the failure geometry indicated that increased arching action with depth of failure was not a stabilizing mechanism.

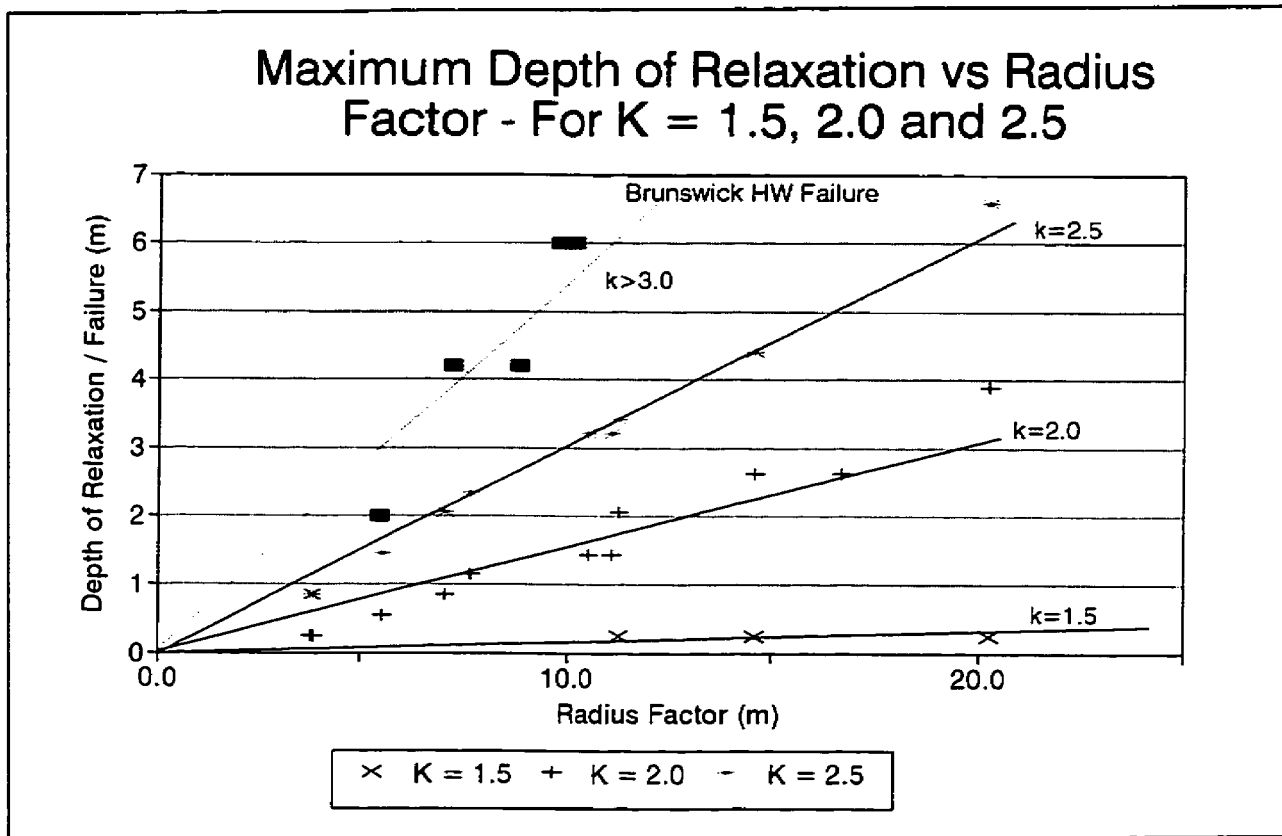


Figure 11.7. Maximum extent of hanging wall failure compared to maximum expected extent of hanging wall relaxation.

The depth of failure was also plotted against the surface radius factor. The resulting points are reasonably close to the depth of relaxation expected for the sill pillar stress regime. This suggests that the limit of the hanging wall failure was controlled by the initial compressive stresses parallel to the hanging wall coinciding with the limit of the relaxation zone. It may have been possible to predict the maximum failure depth based on the opening geometry and stress regime, however, whether or not failure would occur requires a more in depth assessment such as the modified stability graph analysis. The extensive hanging wall failure was influenced by the high stress ratio encountered in the sill pillar and the lack of supporting arching action, possibly due to the small rock mass block size relative to the hanging wall extent.

11.4 DETOUR LAKE MINE DILUTION SURVEY

Placer Dome Inc.'s Detour Lake Mine (DLM) is a 2800 tonne per day gold mine located north of Timmins, Ontario, Canada. Mining is carried out using mechanized cut and fill and longhole stoping (Pakalnis & al., 1993). The ore body is near vertical and has a width of approximately 6 metres in the study area. In 1992 the mine entered into a research agreement with the Canada Centre for Mineral and Energy Technology (CANMET) to study dilution in one of their sub level retreat (SLR) stopes. The general findings of this study are presented by Pakalnis, Dunne and Cooke (1994). The findings from this study which pertain to dilution and the ERF values have been previously documented (Milne et al., 1996; Milne and Mah, 1994) and much of this section is taken from that paper.

Figure 11.8 is a longitudinal view of the West SLR stope showing the frequent and irregularly spaced pillars left for hanging wall support. The majority of this stope was mined open with the addition of fill only near the end of the stope life for long term regional support.

Due to the sub-level retreat mining method, dilution was only a concern when it occurred near the retreating mining front. The throw of the muck is about 15m so any hanging wall dilution which occurred more than 15m away from the trailing mining front would likely not be mucked.

During the course of mining, the Cavity Monitoring System (CMS) laser surveys were conducted to determine stope dimensions and the degree of hanging wall dilution (Miller et al., 1992). Only limited data was obtained from the CMS surveys because of the narrow stope geometry and limited access, however, useful trends were obtained. The effective radius factor term proved to be a useful method of evaluating the stability of the zone of open hanging wall near the retreating mining front.

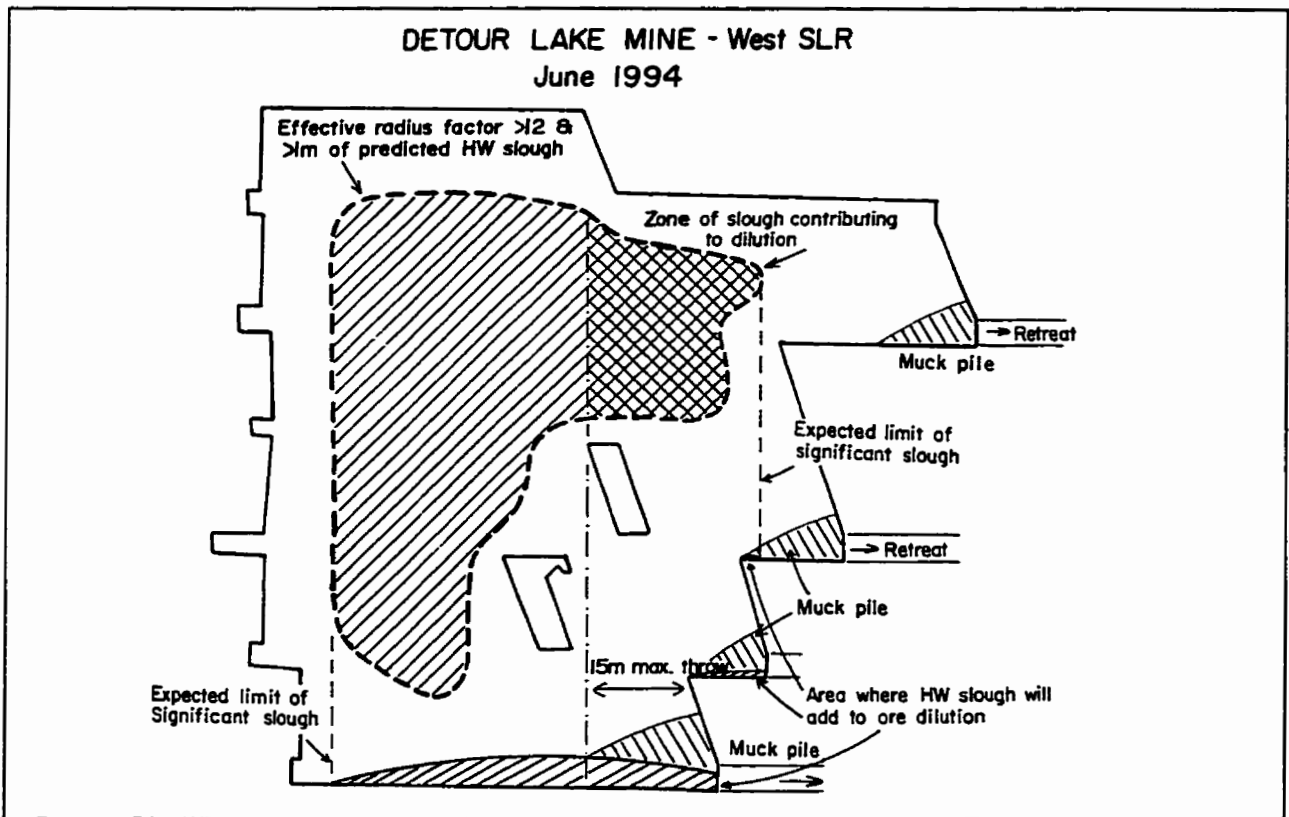


Figure 11.8. Longitudinal view of the west sub-level retreat stope at Detour Lake mine. The area where the ERF values are greater than 12m and significant dilution can be expected is highlighted (After Milne et al., 1996).

The metres of slough were estimated at points on a grid pattern corresponding to the CMS surveyed areas. The ERF values for the grid points were also determined and the metres of slough versus ERF values were plotted. Figure 11.9 shows the ERF values versus metres of hanging wall slough for areas corresponding to supported sub-level drifts and to the unsupported areas between sub-levels. The CMS surveys indicated that little hanging wall sloughing occurred along supported sub level horizons. It was found, however, that sloughing of up to about two metres occurred when the effective radius factor values exceeded 12 metres between sub levels. One metre of slough is equivalent to about 15% dilution.

Figure 11.9 shows the area of the hanging wall where the effective radius factor values exceeded 12 metres and resulting slough could be mucked with ore. Understanding what areas of the hanging wall will produce significant dilution levels enables the mine to adjust the mining

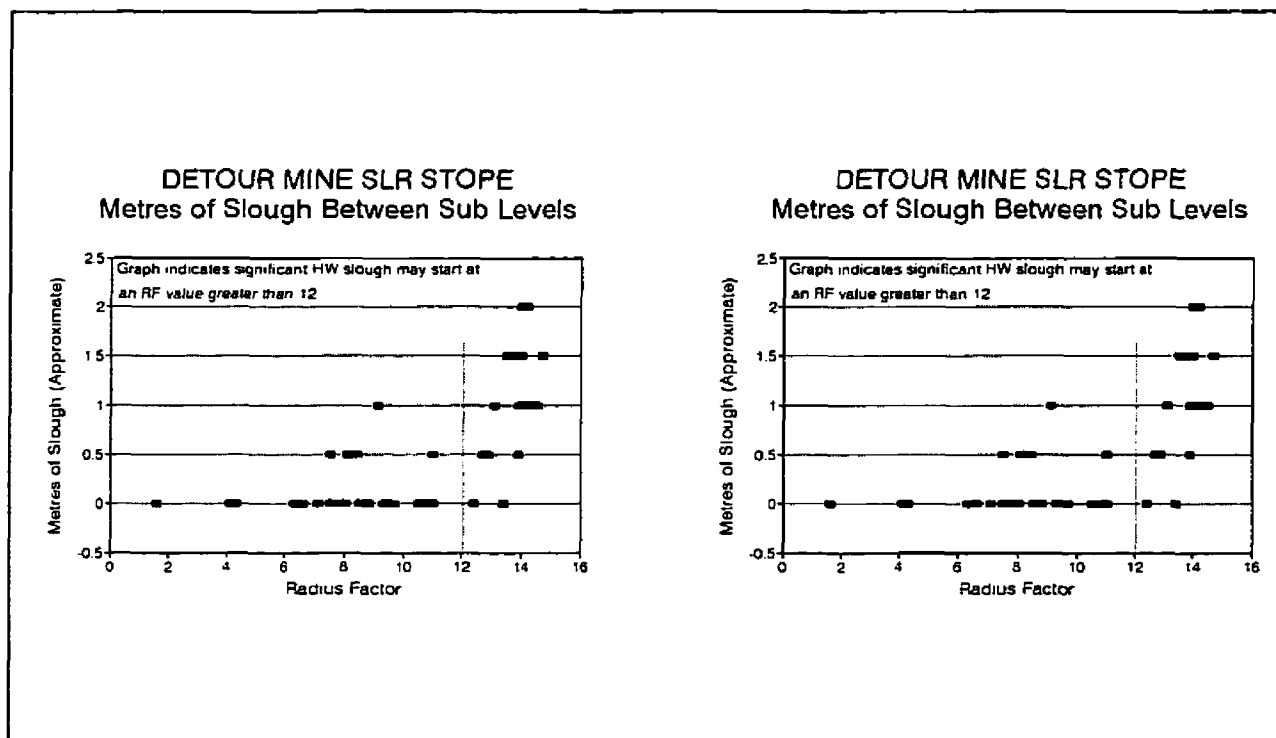


Figure 11.9. Metres of slough versus ERF values for the unsupported hanging wall between sub-levels and for supported sub-levels.

retreat front and relocate pillars to minimize mucking this dilution with ore.

11.5 SUMMARY

Case histories have been presented which show that the maximum depth of failure can be related to the surface radius factor value and that the relative magnitude of failure at a point on a surface corresponds to the effective radius factor value of that point. The case histories investigated pertain to a ravelling failure mechanism for a relaxed hanging wall surface. The approach would not be valid for a block or wedge failure, or a failure driven by high stresses such as in a narrow stope back or drift.

At the Brunswick mine, 725 level 16N stope, a comparison of the maximum depth of hanging wall failure and the surface RF value provided insight into the failure mechanism. The

failure depth with increasing RF values corresponded very closely to the maximum expected depth of relaxation for the stress ratio in the highly stressed sill pillar. In similar hanging wall conditions, the maximum probable failure depth can be estimated by stress conditions and the surface RF value. This will allow the stope hanging wall geometry and support extent to be designed to prevent significant dilution.

At Detour Lake mine CMS survey data coupled with hanging wall ERF values have shown a trend between depth of dilution and surface ERF values. ERF values greater than 12 metres corresponded to as much as two metres of slough whereas .5 metres of slough or less were common in areas where the ERF values were less than 12 metres. This has allowed the mine to plan their extraction to minimize the tonnes of dilution mucked, (Dunne and Pakalnis, 1996).

CHAPTER 12

CONCLUSIONS

12.1 INTRODUCTION

The objective of this thesis was to develop an improved method of quantifying surface geometry for assessing surface stability and deformation. Two new terms have been introduced; The radius factor was developed as a term to assess the overall stability of a surface and the effective radius factor was developed to assess the relative deformation of a point on a surface. The majority of the existing database for the modified stability graph design method, collected by Potvin (1988) and Nickson (1992), was re-analysed substituting the radius factor term for hydraulic radius. Modelled elastic deformations and field measured deformations have been compared to surface effective radius factor values and definite relationships have been determined which will assist in the interpretation of field data and linking deformation to stability design. The deformation data has been limited to hanging wall cases where the predominant structure was oriented parallel to the opening surface and the stress state was generally in a state of relaxation. The trends and relationships presented should be applied to similar cases. The stability design study using the modified stability graph has been conducted on stope backs and hanging walls and shows general applicability.

12.2 CONCLUSIONS

The findings of this study can be grouped into five main categories:

1. Stability design and surface geometry

2. Modelled deformation and surface geometry
3. Field deformation and surface geometry
4. Depth of the modelled tensile zone and depth of failure around an opening and
5. Influence of stiff backfill on effective opening geometry.

Each of these categories relies on the radius factor or effective radius factor term to assess opening surface geometry. Using the same terms for stability design and the interpretation of field deformation monitoring helps the field engineer relate deformation with approaching movement. This will allow the on site engineer to start linking stability and support design based on allowable stable deformation limits.

12.2.1 Stability Design and Surface Geometry

The existing database for the modified stability graph design method consists of 189 unsupported and 103 supported case histories (Nickson, 1992). Of these cases, 119 unsupported and 65 supported cases have been re-analysed, substituting radius factor for hydraulic radius. Due to the similarity between the RF and HR terms for assessing regular surface geometries, no changes to the design transition zones between stable and caved were warranted.

Specific case histories of failures, where the hydraulic radius factor did not adequately assess surface geometry, were re-analysed using the radius factor term (Milne et al., 1996). These case histories included failures influenced by the presence of raises and brows. The RF term reflected these features and the resulting plots more closely reflected the instability in these cases.

12.2.2 Modelled Deformation and Surface Geometry

The ERF term has been found to be an effective tool in assessing the relative amount of

deformation on a surface. It does not give an absolute prediction of movement, but with limited data it can extrapolate future movement with increased opening geometry and give a distribution of movement on a surface.

The following relationships were found between modelled deformations above an opening surface and the corresponding ERF value on the surface:

- A linear relationship has been found between deformation modelled at points above a surface and the ERF value at the points.
- Modelled strains between two points perpendicular to an opening surface were found to converge to a constant value. The constant value was reached when the maximum distance from the surface to the furthest point was less than the corresponding ERF value on the surface.
- The maximum elastic strain modelled between two points perpendicular to an opening surface was found to be a function of the stress normal to the surface, the rock mass modulus of elasticity and Poisson's ratio (Eq. 7.10).

An on site ground control engineer can use the preceding relationships to quickly determine a probable deformation distribution over the opening surface and determine if measured deformations are exceeding probable elastic limits. The relationships were not developed as a replacement to numerical modelling. They were developed to show that the theoretical elastic deformation behaviour at a point above an opening surface can be linked to the ERF value of the point and the overall RF value of the surface.

12.2.3 Field Deformation and Surface Geometry

Field extensometer data has been collected at Brunswick Mine, Winston Lake Mine and Mount Isa Mine. The deformation data has been analysed with respect to increasing opening size and ERF values for the instrument locations on the opening surface. It has been found that the best data can be obtained by plotting microstrain between anchors against the increasing ERF value for the instrument location. The field data analysis has shown four phases of strain

deformation characterized by the rate of movement with respect to increasing ERF values.

These four stages are summarized below:

- Phase one deformation consists of elastically driven relaxation of the rock mass. Measured microstrain between extensometer anchors converges to a constant strain. This constant strain value can be related to the elastic properties of the rock mass and the premining stress normal to the opening.
- Phase two deformation shows a linear relationship between microstrain and the ERF value, likely related to a voussoir arch deformation mechanism. Based on available data, overall failure of the surface is unlikely unless initiated along pre-existing structure.
- Phase three deformation shows an exponential increase in deformation with the ERF value. A linear plot is obtained using semi-log plot. A voussoir arch deformation mechanism coupled with an increased delamination of the hanging wall along foliation may be the mechanism causing this deformation. Stability of the overall surface cannot be relied on in this phase of movement. With experience, stable deformation limits may be determined to allow the prediction of failure.
- The fourth phase of deformation shows as a rapid increase in the rate of movement leading to imminent failure. There is likely significant time dependent movement between blasts. It is likely that overall surface failure to the depth at which this movement phase is occurring, is simply a matter of time.

The four phases of strain deformation delineated above do not always occur adjacent to an opening surface. There is a general trend where the higher phase of deformation occurs closest to the opening surface.

Based on an interpretation of instrumentation data it is possible to delineate zones of approaching failure through to zones of elastic deformation. This assists the engineer in designing effective support where it is most needed, as well as predicting zones of potential instability.

12.2.4 Depth of Modelled Tensile Stress and Potential Failure

Modelling was conducted to compare the radius factor of a surface to the maximum depth of modelled tensile stress. This zone of modelled tensile stress or relaxation is often cited as

one of the main reasons for instability (Pakalnis, 1991). A linear relationship was determined between the maximum depth of elastically modelled tensile stress and the RRF value of a surface. The slope of the linear relationship varied with the stress ratio K , where K equals the in-situ stress normal to the surface divided by the stress parallel to the surface.

Field data from a hanging wall failure at Brunswick mine showed the depth of failure corresponded to the expected depth of modelled tensile stress based on the increasing surface radius factor and the field stress ratio. The modelled relationship between surface radius factor, field stress ratio and depth of the modelled tensile zone indicates a maximum failure depth which can be expected in a low stress hanging wall failure.

Data from Detour Lake Mine also showed a link between the ERF value on a surface and the measured depth of surface slough. Based on limited data from the CMS system, significant surface slough was measured beyond a limiting ERF value.

The ability to predict the potential depth of failure and probable areas of slough on a surface will greatly assist in the effective design of surface support and pillar placement.

12.2.5 Influence of Backfill on Effective Opening Geometry

The analysis of Winston Lake mine field data indicates that the common practice of treating an advancing backfill front the same as a rock abutment is overly optimistic. The data suggests it is realistic to assume the stabilising effect of the backfill lags behind the actual backfill front. Data suggests that the effective span against a moving backfill front should be equal to the sum of the maximum and minimum opening spans developed during the mining and backfilling cycle. Even this approach is not conservative since it ignores the influence of the backfill compressing. For stiff backfill in relatively weak hanging wall environments, this approximation is reasonable.

12.2.6 Summary

This study has developed two new terms for assessing the geometry of an opening surface. These terms have been successfully linked to surface deformation, surface stability and depth of failure. This allows the engineer to start relating the magnitude of deformation with the approach of instability. The ability to predict the relative deformation of different locations on a surface allows the engineer to design support for different areas of the surface.

The radius factor and effective radius factor have been shown to accurately assess the stability of more complex geometries than can be realistically expected from the hydraulic radius term. This allows for a more accurate stability design of complex geometries.

12.3 FUTURE WORK

This study has presented methods for linking the interpretation of instrumentation data with the empirical stability design of an opening surface. Further field studies should be conducted where instrumentation is installed to monitor movement with the purpose of determining the stabilizing effect of cable support, post pillars and backfill. Since this study has presented a method of linking measured deformation with the approach of instability, relative surface stability can be assessed in terms of movement rather than just a subjective stable, unstable or caved designation. This will allow the stabilizing influence of different support measures to be quantified.

Empirical relationships have been found for relating modelled elastic deformation, and maximum depth of induced tensile stress above openings, to the corresponding ERF and RF values on the opening surface. Additional research should be conducted to determine if closed form solutions for elastic deformations around openings can be related to the RF and ERF terms.

The radius factor has been found to be an improved method of assessing geometry with the modified stability graph design method. The databases from other empirical design techniques should be re-analysed substituting radius factor for hydraulic radius and equivalent span to see if similar improvements can be made.

12.4 FINAL REMARKS

The design approach presented for interpreting surface deformation has been applied in the field for hanging wall surfaces with low induced stresses. The methodology presented for interpreting data relies on the extrapolation of measured field data and needs to be calibrated at operating mines to develop on site deformation guidelines. The replacement of radius factor for hydraulic radius has taken advantage of the large amount of data available from the original calibration of the modified stability graph design technique. The design method using the radius factor term will provide a useful initial stability assessment and, with increased application, specific design criteria can be developed at individual mines.

BIBLIOGRAPHY

- Barton, N., Lien, R. and Lunde, J. 1974. Engineering classification of rock masses for the design of tunnel support. *Rock Mech.* vol 6, pp. 189-236.
- Barton, N. 1989. Cavern design for Hong Kong rocks, Proceedings of the seminar rock cavern - Hong Kong, Inst. of Min. & Metall., pp. 179-202.
- Bawden, W., Personal Conversation, February, 1996.
- Bawden, W. and Milne, D. 1987. Geomechanical mine design approach at Noranda Minerals. Proceedings of the International Symposium on Rock Mechanics, A.A. Balkema, Montreal, Canada, pp. 799-803.
- Beer, G. and Meek, J. L. 1982. Design curves for roofs and hangingwalls in bedded rock based on voussoir beam and plate solutions. *Trans. Instn. Min. Metall.* Vol 91, pp. A18-22.
- Bieniawski, Z.T. 1974. Geomechanics classification of rock masses and its application in tunnelling. Proc. Third International Congress on Rock Mechanics, ISRM, Denver, Vol. 11A, pp. 27-32.
- Bieniawski, Z.T. 1978. Determining rock mass deformability: Experience from case histories. *Int. J. Rock Mech. Min. Sci. and Geomech. Abst.*, 15, pp. 237-247.
- Brady, B.H.G. and Brown, E.T. 1985. *Rock mechanics for underground mining*, London, George Allen @ Unwin, 527 pp.
- Bucky, P. B. 1934. Effect of approximately vertical cracks on the behaviour of horizontally lying roof strata, *Trans. of the Amer. Inst. of Mining & Metall. Eng.*, Vol 109, pp 212-229.
- Clark, L. 1996. A numerical modelling study on the zone of relaxation around open stope hanging walls, Internal UBC Document.
- Coulomb, C.A. 1776. Essai sur une application des règles de maximis et minimis à quelques problèmes de statique, relatifs à l'architecture. *Mémoires de Mathématique et de Physique, l'Académie royale des Sciences* 7, 343-82.
- Crouch, S.L. and Starfield, A.M.. 1983. *Boundary element methods in solid mechanics*, George, Allen & Unwin, London, 322 pp.
- Deere, D.U. 1964. Technical description of rock cores for engineering purposes, *Rock Mechanics and Engineering Geology*. Vol. 1, No. 1, pp17-22

- Denkhaus, H.G., Critical review of strata movement theories and their application to practical problems, *Journal of the South African Institute of Mining and Metallurgy*, March 1964, Vol. 64, 23pp.
- Diedericks, M., 1994. NTBEAM Program, Geomechanics Research Centre, Sudbury, Ontario
- Dunne, K. and Pakalnis, R. 1996. Dilution aspects of a sublevel retreat stope at Detour Lake mine. *North American Rock Mechanics Symposium*, Montreal.
- Dunncliff, J. 1988. *Geotechnical instrumentation for monitoring field performance*. New York: Wiley.
- Evans, W. H. 1941. The strength of undermined strata, *Trans. Instn. Min. Metall.*, 50, pp 475-532.
- Felderer, M. 1995. An empirical open stope design method using the radius factor, B.A.Sc thesis. The University of British Columbia, p44.
- Goodman, R. E. 1989. *Introduction to rock mechanics*, John Wiley & Sons, Toronto, 562 pp..
- Goodman, R.E. and Shi G. H. 1985. *Block theory and its application to rock engineering*, Prentice-Hall, Englewood Cliffs, NJ.
- Goris, J.M., 1990. Laboratory evaluation of cable bolt supports, *Proc. 92nd Annual General Meeting of CIM*.
- Hadjigeorgiou, J., Leclair, J. and Potvin, Y. 1995. An update of the stability graph method for open stope design, *97th AGM-CIMM*, Halifax, Canada.
- Hausch, D. 1995. Personal conversation.
- Hoek, E. and Brown, E.T., 1980. *Underground excavations in rock*. Institute of Mining and Metallurgy, London, 527 pp.
- Hoek, E. 1994. The challenge of input data for rock engineering, *ISRM News Journal*, Vol. 2, No. 2, pp. 23-24.
- Hoek, E., Kaiser, P.K. and Bawden, W.F. 1995. *Support of underground excavations in hard rock*. Rotterdam; Balkema.
- Herget, G., *Monitoring of Excavation Performance*, MRL 91-082 (TR) 1991.
- Hutchinson, D.J. 1992. A field investigation of cable bolt reinforcement of open stopes at Ansil mine. PhD Thesis, Department of Civil Engineering, University of Toronto.
- Hutchinson, D.J. and Diedericks, M., 1996. *Cablebolting in underground mines*. BiTech Publishers Ltd., Richmond, 406 pp.

- Itasca 1992. Itasca Program documentation, Minneapolis, Minnesota, 1992.
- Jaeger, J.C. and Cook, N.G.W. 1984. Fundamentals of rock mechanics, Chapman and Hall Ltd., London, 593 pp.
- Kanduth, H., Germain, P. and Jacob, D. 1992. Internal NTC Report., 29 pp.
- Kirsch, G. 1898. Die theorie der elastizitat und die bedürfnisse der festigkeitslehre. eit. Ver. Deut. Ing. 42, 797-807.
- Lang, B., Pakalnis, R. and Vongpaisail, S. 1991. Span design in wide cut and fill stopes at Detour Lake Mine, 93rd AGM-CIMM, Calgary, Canada.
- Laubscher, D.H. and Taylor, 1976. The importance of geomechanics classification of jointed rock masses in mining operations. Proceedings of the Symposium for Rock Engineering, Johannesburg, pp. 119-128.
- Laubscher, D.H. 1977. Geomechanics classification of jointed rock masses - mining applications. Transactions, Institute of Mining and Metallurgy, section A, Vol. 86, pp. A1-A7
- Laubscher, D.H. 1990. A geomechanics classification system for the rating of rock mass in mine design. Journal of South African Inst. of Mining and Technology. Vol. 90, No. 10, pp 257-273.
- Logan, A.S., Villaescusa, E., Stampton, V.R., Struthers, M.A. and Bloss, M.L. 1993. Geotechnical instrumentation and ground behaviour monitoring at Mount Isa. Proceedings Geotechnical Instrumentation and Monitoring in Open Pit and Underground Mining, Balkema, Rotterdam, pp 321-329
- Lunder, P, 1994. Noranda Technology Centre, internal computer program.
- Maloney, S. and Kaiser, P.K., 1993. Field investigation of hanging wall support by cable bolt pre-reinforcement at Winston Lake Mine. Internal report, Geomechanics Research Centre, Sudbury.
- Mathews, K.E., Hoek, E., Wyllie, D. and Stewart, S.B. 1981. Prediction of stable excavation spans for mining below 1000 metres in hard rock, Canada: CANMET, Dept. of Energy, Mines and Resources, DSS Serial No. OSQ80-00081, DSS File No. 17SQ.23440-0-9020.
- McGaughey, J. Personal Communication, February, 1994.
- Merrill, R. H. 1954. Design of underground mine opening, oil shale mine, Rifle, Colorado. Rep. Invest. U.S. Bur. Mines 5089, 56 pp.
- Merritt, A.H. 1972. Geologic prediction for underground excavations. Proc. First North American Rapid Excavation and Tunnelling Conference, AIME, New York, pp. 115-132.

- Miller, F., Jacobs, D. and Potvin, Y. 1992. Cavity monitoring system update and applications, 94th CIM Annual General Meeting, Montreal, Paper #106.
- Milne, C., Nov. 1995. Personal Conversation.
- Milne, D. 1988. Suggestions for standardization of rock mass classification, MSc Dissertation, Imperial College, University of London, pp. 123.
- Milne, D. 1991. Internal Noranda Technology Centre Report.
- Milne, D. and Jacob, D. 1990. Winston Lake Mine Support study data - Phase 1. Internal Noranda Technology Centre Report.
- Milne, D. and Mah, S. 1994. Detour Lake Mine Borehole Camera Logging and Instrumentation Review, Internal Report.
- Milne, D. and Milne, C. 1993. Closure program for stress change estimation, Internal software development, Milne & Milne Engineering.
- Milne, D., Pakalnis, R. and Lunder, P. 1996. Approach to the quantification of hanging-wall behaviour, Trans. Inst. Min. Metall., Vol. 105, pp. A69-A74.
- Milne, D. Pakalnis, R. and Felderer, M. 1996. Surface geometry assessment for open stope design, North American Rock Mechanics Symposium, Montreal.
- Nickson, S.D. 1992. Cable support guidelines for underground hard rock mine operations. M.A.Sc thesis. The University of B.C., p. 223.
- Obert, L. and Duval W. 1967. Rock mechanics and the design of structures in rocks, Wiley, New York.
- Page, C. 1988. Personal conversation.
- Pakalnis, R., Miller, H., Vongpaisal, S., Madill, T. 1987. An empirical approach to open stope design, ISRM Proceedings, Montreal.
- Pakalnis, R.C.T. 1991. Three dimensional modelling - an applied approach. Proceedings of the Second Canadian Conference on Computer Applications in the Mineral Industry, Edited by R. Poulin, R.C.T. Pakalnis and A.L. Mular, Vancouver, Canada, pp. 619-630.
- Pakalnis, R. and Vongpaisal, S. 1993. Mine design an empirical approach, Proceedings International Congress on Mine Design, Kingston, Canada, pp. 455-467, Rotterdam: Balkema.
- Pakalnis, R., Dunne, K. and Cook, K. 1995. Design guidelines for sublevel retreat mining method, CANMET report, DSS Serial No. 23440-2-9142/01-SQ, 117pp.

- Pakalnis, R., Vongpaisal, S., Lang, B., Cook, K. 1993. Ground stability guidelines for cut and fill mining of wide ore bodies, Dept. of Energy Mines and Resources, Canada, DSS File No. 14SQ.23440-49-9145, p. 274.
- Potvin, Y. 1987. Progress Report, Internal Noranda Technology Centre Report.
- Potvin, Y. 1988. Empirical open stope design in Canada, Ph.D. thesis. The University of British Columbia, p. 350.
- Potvin, Y. Hudyma, M.R., Miller, H.D.S. Design guidelines for open stope support. CIM Bulletin, June 1989.
- Potvin, Y. and Milne, D. 1992. Empirical cable bolt support design, Proceedings Rock Support in Mining and Underground Construction, pp. 269-275, Rotterdam: Balkema.
- Stacey, T.R. and Page, C.H. 1986. Practical handbook for underground rock mechanics, Trans Tech Publications, Clausthal-Zellerfeld, pp. 144.
- Terzaghi, K. 1946. Rock defects and loads on tunnel supports. Rock Tunnelling with Steel Supports, Editors R.V. Proctor and T. White. Commercial Shearing and Stamping co., Youngstown, pp. 15-99.
- Thompson, A.G. and Windsor, C.R. 1993. Theory and strategy for monitoring the performance of rock reinforcement, Proc. Australian Conf. on Geotechnical Instrumentation and Monitoring in Open Pit and Underground Mining, Kalgoorlie, Rotterdam: Balkema.
- Timoshenko, S. P. 1940. Theory of plates and shells, New York, McGraw-Hill Book Co., 220 pp.
- Timoshenko, S. P. and Goodier J. N. 1958. Theory of elasticity, Wiley, New York, 567 pp.
- Thomas, B.T. and Finney, R.L. 1984. Calculus and analytic geometry, Reading, Addison-Wesley, 1041 pp.
- Villaescusa, E. 1996. Excavation design for bench stoping at Mount Isa mine, Queensland, Australia. Trans. Instn Min. Metall., London, pp. A1-A10.
- Wickham, G.E., Tiedemann, H.R. and Skinner, E.H. 1974. Ground support prediction model-RSR concept. Proceedings of the North American Rapid Excavation and Tunnelling Conference vol 1, pp. 43-64.
- Wiles, T. Map3D, Version 35, User's Manual, Copper Cliff, Ont., 162 pp.
- Windsor, Bywater and Worotnicki, 1984. Instrumented and observed behaviour of N663 trial stope, Race Course Area, Mount Isa Mines, Project Report No. 23, CSIRO Confidential Report, 53 pp.

- Windsor, C.R. 1993. Measuring stress and deformation in rock masses - A keynote lecture. Proc. Australian Conf. on Geotechnical Instrumentation and Monitoring in Open Pit and Underground Mining, Kalgoorlie, Rotterdam: Balkema.
- Woodruff, 1966. Methods of working coal and metal mines, Vol. 1, Pergamon Press, London, 538 pp.
- Wright, F. D. 1972. Arching action in cracked roof beams, Fifth international strata control conference, London, 7 pp.
- Wright, F.D. 1973. Roof control through beam action and arching, SME - Mining Engineering Handbook, The Amer. Inst. of Mining & Metall. & Petrol. Eng. 16 pp.

APPENDIX A

CONVERGENCE PROGRAM

APPENDIX A

CONVERGENCE PROGRAM - VERSION 1.0

The program 'converge.exe' has been designed to assist in the interpretation of closure station data. For input, the program takes three values of strain, a direction angle for each strain, Young's Modulus and Poisson's ratio. A default value for Poisson's ratio is set at .2, however, the user should realize that this value can have a significant effect on results. It has been suggested that Poisson's ratio for a rock mass can be significantly greater than for an intact sample.

Program output consists of principal strain values and orientation, as well as principal stresses. The theory used for obtaining principal strains and orientation is based on a matrix inversion and solution taken from "Introduction to Rock Mechanics" by Goodman (1989). The resolution of principal stresses from strains applies the Kirsch solution taken from "Rock Mechanics for Underground Mining" by Brady & Brown, (1985). This solution assumes a circular drift geometry and an elastic rock mass response. The drift will not have a circular cross section, however, and this will produce some inaccuracy. When the elastic response of the rock mass appears to have been exceeded, the orientation and magnitude of principal strains may still provide useful data.

The program is designed to take spreadsheet input with a format shown below and given in the file 'sample.prn'.

	28.00	152.00	0.00	75.00
20-Jul-92	0.00	0.00	0.00	
22-Jul-92	-80.58	-7.27	-35.09	
27-Jul-92	-142.84	3.63	-39.22	
31-Jul-92	-76.91	69.03	49.54	
05-Aug-92	-402.89	-108.99	-103.20	
10-Aug-92	-168.48	159.85	80.50	
17-Aug-92	-162.99	56.31	1.03	

19-Aug-92	-161.15	76.29	12.38
03-Sep-92	263.71	570.38	334.37
29-Sep-92	304.00	519.52	470.60
20-Oct-92	651.94	156.22	460.28
09-Nov-92	688.57	319.70	532.52
12-Dec-92	3083.91	-2317.85	-1120.77
07-Jan-93	1640.85	-1732.94	-1159.98
04-Feb-93	1871.59	-1849.19	-1133.15
09-Feb-93	2153.61	-2332.38	-1376.71
03-Mar-93	2021.76	-2336.02	-1440.69

The first column consists of the dates at which measurements were taken. The first column adjacent to the dates are the measurements in microstrain. The value at the top of the second column, 28, is the corresponding measuring direction, in degrees, measured counter-clockwise from horizontal. 152 is the measuring direction for the second column of microstrain measurements and 0 (horizontal) is the third measuring direction for the final column of microstrain measurements. The single value in the fifth column, 75.00, is the input value of Young's Modulus, given in GPa.

This format must be followed for all input files. There must be no spaces in the date column, however, as many spaces as desired can be used between data entries. Do not skip any data entries; ie, input a date without corresponding measurements - this would throw the data reading out of sync. The program is designed to take input from exported .prn files from QPRO spreadsheet files. The program has the option of using a default value for Poisson's ratio of .2 or any other value the user assumes.

The program displays results on the screen and the user has the option of creating a spreadsheet file '.sss' or a print file, '.ppp'. To provide complete screen and print output, the program asks for a station name, the viewing direction for the orientations (N,S,E etc.) and the measuring length of each strain measuring direction. (The viewing direction can be put in with the file execution step).

The spreadsheet file consists of 6 columns of data. The first column repeats the reading dates, column 2 and 3 are the major and minor principal strain values and column 4 is the maximum principal strain (and stress) direction. Columns 5 and 6 are the principal stress values. No identification or background data is provided with the spreadsheet file and it is designed to be imported into a spreadsheet.

This program has been developed by Milne & Milne Engineering in conjunction with the UBC Mining-Geotechnical Group. Assistance has been provided by the Noranda Technology Centre and Energy Mines and Resources. If you find this program of use, please send 12 chocolate chip cookies (no nuts please) to Milne & Milne Engineering, 2609 W. 22 ave., Vancouver, B.C.. V6L 1M3.

C & D Milne.

APPENDIX B

MATHEMATICAL DERIVATION OF THE RADIUS FACTOR TERM

APPENDIX B

MATHEMATICAL DERIVATION OF THE RADIUS FACTOR TERM

As has been previously discussed, the harmonic radius of any surface is equal to the radius factor (RF), when calculated from the surface centre using equation 5.1. This same equation can be applied at any point on a surface to determine an effective radius factor value (ERF).

The harmonic average radius from a point on a surface can be determined numerically from the AutoCad 'LISP' routine developed by Lunder, (1994). The numerical solution for the harmonic radius of a surface consists of the integration of Equation 5.3 given below:

$$\frac{1}{r_h} = \frac{\int_0^{2\pi} \frac{1}{r_\theta} d\theta}{\int_0^{2\pi} d\theta} \quad (\text{Eq. B.1})$$

Analytical solutions for the harmonic radius value have been developed for rectangular and circular surfaces and are presented in the following section (Hausch, 1995).

B.1 RECTANGULAR SURFACE

Figure B.1 shows a rectangular surface of length L and width W. The surface is broken into 8 sections by horizontal and vertical lines through the calculation point for the harmonic radius and with diagonal lines connecting the rectangle corners and the calculation point. Each of the lines sectioning the surface form limits for integrating the harmonic radius about a point with the coordinants (x,y).

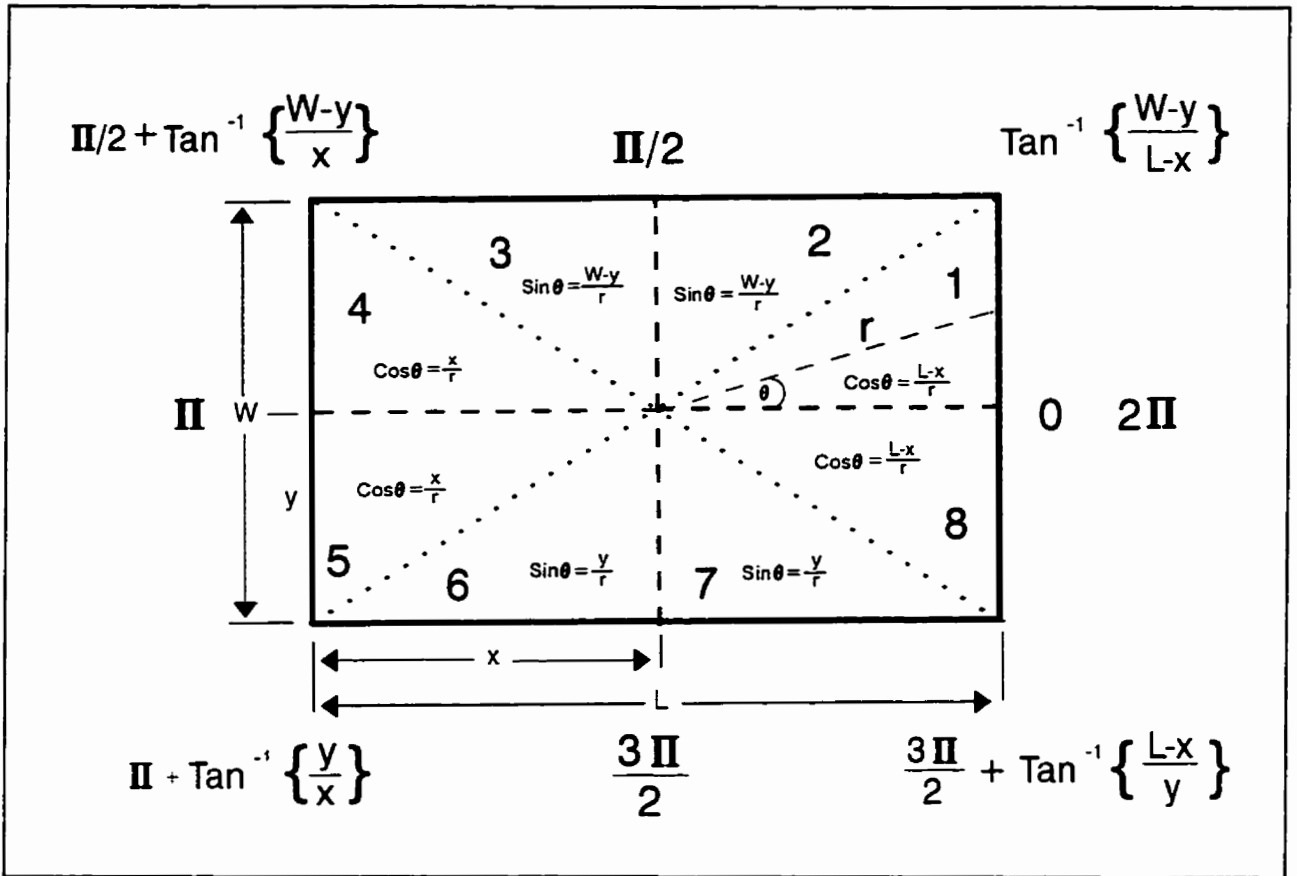


Figure B.1 A rectangular surface broken into sections for integration.

In each of the 8 sections, a trigonometric equation relates the distance from the calculation point to the abutment at an angle θ , with respect to the perpendicular distance to the abutment. The angles of the sectioning lines are shown in Figure B.1 and are expressed in terms of the rectangle geometry and the calculation point. The steps for the integration of these equations to determine average harmonic radius for the first two sections are given below:

Section 1

$$\text{Cos}\theta = \frac{L-x}{r} \dots\dots\dots \frac{1}{r} = \frac{\text{Cos}\theta}{L-x} \tag{Eq. B.2}$$

$$\frac{1}{r_h} = \frac{1}{\int d\theta} \int \frac{1}{r} d\theta = \left(\frac{1}{L-x} \right) \left(\frac{1}{\int_{0^\circ}^{\text{Tan}^{-1} \left(\frac{W-y}{L-x} \right) d\theta} } \right) \int_{\theta=0^\circ}^{\theta=\text{Tan}^{-1} \left(\frac{W-y}{L-x} \right)} \text{Cos}\theta d\theta \tag{Eq. B.3}$$

$$\frac{1}{r_h} = \left(\frac{1}{L-x}\right) \left[\frac{1}{\tan^{-1}\left(\frac{W-y}{L-x}\right) - \tan^{-1}0^\circ} \right] \left[\sin\left(\tan^{-1}\left(\frac{W-y}{L-x}\right)\right) - \sin 0^\circ \right] \quad (\text{Eq. B.4})$$

Section 2

$$\sin\theta = \frac{W-y}{r} \dots\dots\dots \frac{1}{r} = \frac{\sin\theta}{W-y} \quad (\text{Eq. B.5})$$

$$\frac{1}{r_h} = \frac{1}{\int d\theta} \int \frac{1}{r} d\theta = \left(\frac{1}{W-y}\right) \left(\frac{1}{\int_{\theta=\tan^{-1}\left(\frac{W-y}{L-x}\right)}^{\theta=\frac{\pi}{2}} d\theta} \right) \int_{\theta=\tan^{-1}\left(\frac{W-y}{L-x}\right)}^{\theta=\frac{\pi}{2}} \sin\theta d\theta \quad (\text{Eq. B.6})$$

$$\frac{1}{r_h} = \left(\frac{1}{W-y}\right) \left(\frac{1}{\left[\frac{\pi}{2} - \tan^{-1}\left(\frac{W-y}{L-x}\right)\right]} \right) \left[-\cos\left(\frac{\pi}{2}\right) - \left(-\cos\left(\tan^{-1}\left(\frac{W-y}{L-x}\right)\right)\right) \right] \quad (\text{Eq. B.7})$$

Section 3

$$\sin\theta = \frac{W-y}{r} \dots\dots\dots \frac{1}{r} = \frac{\sin\theta}{W-y} \quad (\text{Eq. B.8})$$

$$\frac{1}{r_h} = \frac{1}{\int d\theta} \int \frac{1}{r} d\theta = \left(\frac{1}{W-y}\right) \left(\frac{1}{\int_{\frac{\pi}{2}}^{\frac{\pi}{2} + \tan^{-1}\left(\frac{W-y}{x}\right)} d\theta} \right) \int_{\frac{\pi}{2}}^{\frac{\pi}{2} + \tan^{-1}\left(\frac{W-y}{x}\right)} \sin\theta d\theta \quad (\text{Eq. B.9})$$

$$\frac{1}{r_h} = \left(\frac{1}{W-y}\right) \left(\frac{1}{\left[\frac{\pi}{2} + \tan^{-1}\left(\frac{W-y}{x}\right) - \frac{\pi}{2}\right]} \right) \left[-\cos\left(\frac{\pi}{2} + \tan^{-1}\left(\frac{W-y}{x}\right)\right) - \left(-\cos\left(\frac{\pi}{2}\right)\right) \right] \quad (\text{Eq. B.10})$$

Section 4

$$\cos\theta = \frac{x}{r} \dots\dots\dots \frac{1}{r} = \frac{\cos\theta}{x} \quad (\text{Eq. B.11})$$

$$\frac{1}{r_h} = \frac{1}{\int d\theta} \int \frac{1}{r} d\theta = \left(\frac{1}{x}\right) \left(\frac{1}{\int_{\Pi}^{(\frac{\Pi}{2} + \tan^{-1}(\frac{W-y}{x}))} d\theta} \right) \int_{\Pi}^{(\frac{\Pi}{2} + \tan^{-1}(\frac{W-y}{x}))} \cos\theta d\theta \quad (\text{Eq. B.12})$$

$$\frac{1}{r_h} = \left(\frac{1}{x}\right) \left(\frac{1}{[\Pi - (\frac{\Pi}{2} + \tan^{-1}(\frac{W-y}{x}))]} \right) [\sin\Pi - \sin(\frac{\Pi}{2} + \tan^{-1}(\frac{W-y}{x}))] \quad (\text{Eq. B.13})$$

The integration of the other 4 sections around the rectangle follow the pattern given above and are not shown. The equations can easily be entered into a spreadsheet program to obtain ERF values for any point on a rectangle if the AutoCad routine is not available. The analytical solution for a circular surface follows:

B.2 CIRCULAR SURFACE

Figure B.2 shows a circular surface with a radius given as R centred at coordinants 0,0. The equation for the circle described is simply as follows:

$$x^2 + y^2 = R^2 \quad (\text{Eq. B.14})$$

Due to symmetry, it is apparent that for a given distance from the centre of a circle, the average harmonic radius and corresponding ERF values will be a constant. At the centre of the circle the average harmonic radius will obviously be equal to the radius of 1. For all other points within the circle, the analytical solution for the harmonic radius is not as straight forward. Figure B.2 shows a point within the circle a distance Δ from the centre. For points on the circle for all values of x greater than Δ , the equation for the circle can be expressed as follows:

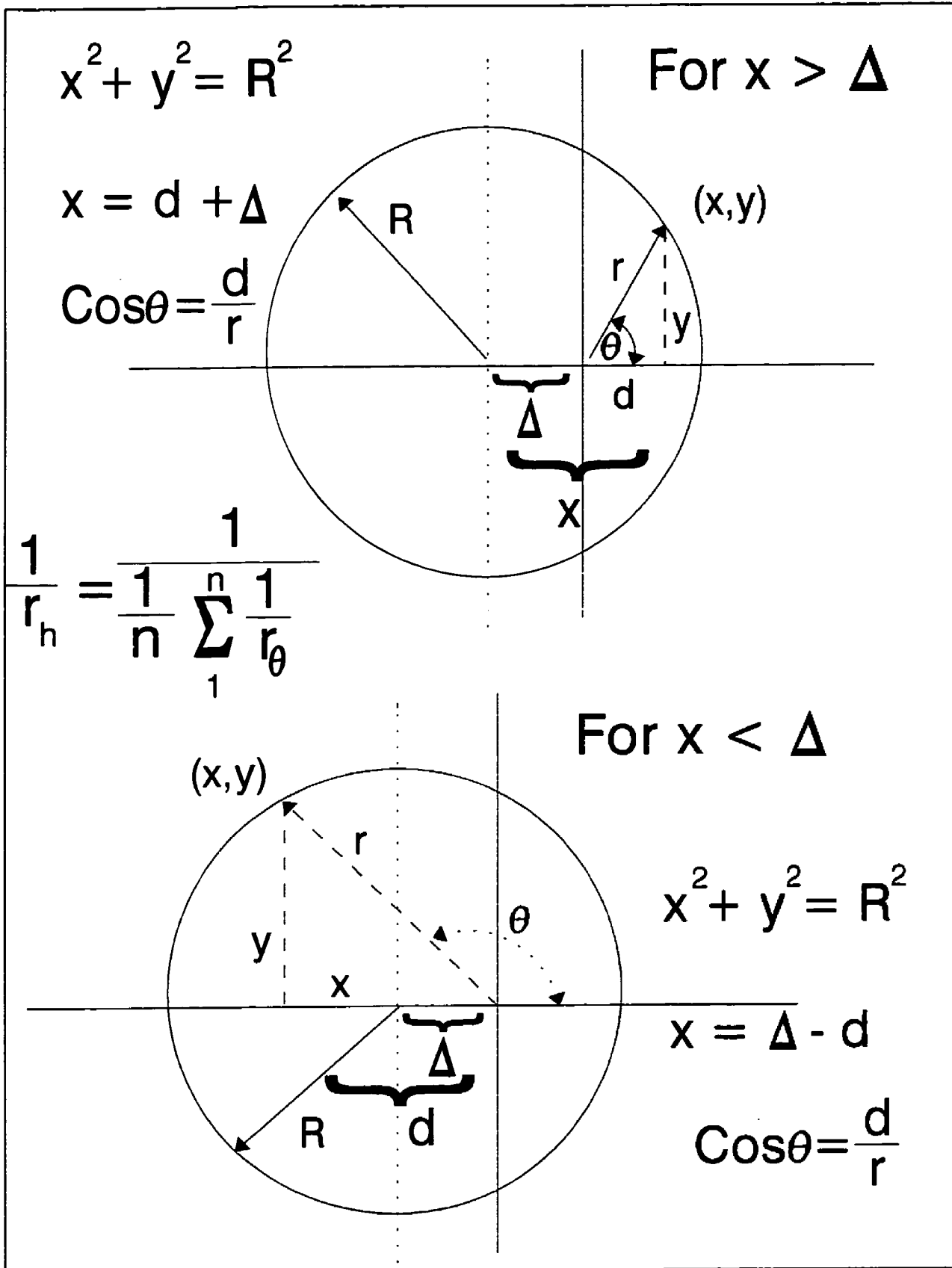


Figure B.2 Harmonic radius calculation for a circle for points not at the centre.

$$(d+\Delta)^2 + y^2 = R^2 \quad (\text{Eq. B.15})$$

where $(d+\Delta) = x$

For the points on the circle where x is less than Δ , the equation is shown below:

$$(d-\Delta)^2 + y^2 = R^2 \quad (\text{Eq. B.16})$$

where $(\Delta-d) = x$

This is simply a shifting of the y axis to pass through the calculation point for the harmonic radius.

To determine the average harmonic radius, a solution for the integration given in Equation 5.3 is required. For simplicity the integration will be done separately for values of $x > \Delta$ and $x < \Delta$, based on Equations B.15 and B.16.

$x > \Delta$

For this section of the circle, the distance r from the calculation point to the circle perimeter is given by the following equation:

$$r^2 = d^2 + y^2 \quad (\text{Eq. B.17})$$

Combining with Equation B.15 gives:

$$r = \sqrt{R^2 - 2d\Delta - \Delta^2} \quad (\text{Eq. B.18})$$

From Figure B.2 it is apparent that r can also be expressed as follows:

$$\text{Cos}\theta = \frac{d}{r} = \frac{d}{\sqrt{R^2 - 2d\Delta - \Delta^2}} \quad (\text{Eq. B.19})$$

Squaring both sides and equating to zero gives:

$$d^2 + 2d\Delta \text{Cos}^2\theta - (R^2 - \Delta^2)\text{Cos}^2\theta = 0 \quad (\text{Eq. B.20})$$

Solving the quadratic equation for d gives:

$$d = \frac{-2\Delta \cos^2\theta \pm \sqrt{4\Delta^2 \cos^4\theta + 4(R^2 - \Delta^2)\cos^2\theta}}{2} \quad (\text{Eq. B.21})$$

Since d must be positive this simplifies to:

$$d = -\Delta \cos^2\theta + \cos\theta \sqrt{\Delta^2 \cos^2\theta + R^2 - \Delta^2} \quad (\text{Eq. B.22})$$

From equation B.19, 1/r can be expressed as follows:

$$\frac{1}{r} = \frac{1}{-\Delta \cos\theta + \sqrt{R^2 - \Delta^2(1 - \cos^2\theta)}} \quad (\text{Eq. B.23})$$

Therefore:

$$\frac{1}{r_h} = \int \frac{1}{r} d\theta = \frac{1}{\int_{0^\circ}^{\frac{\pi}{2}} d\theta} \frac{d\theta}{-\Delta \cos\theta + \sqrt{R^2 - \Delta^2(1 - \cos^2\theta)}} \quad (\text{Eq. B.24})$$

Which equals:

$$\frac{1}{r_h} = \frac{1}{\frac{\pi}{2}} \int_{0^\circ}^{\frac{\pi}{2}} \frac{d\theta}{-\Delta \cos\theta + \sqrt{R^2 - \Delta^2(1 - \cos^2\theta)}} \quad (\text{Eq. B.25})$$

$x < \Delta$

For this section of the circle, the distance r from the calculation point to the circle perimeter can be expressed by combining Equations B.16 and B.17 giving the following:

$$r = \sqrt{R^2 + 2d\Delta - \Delta^2} \quad (\text{Eq. B.26})$$

From Figure B.2, r can also be expressed as follows:

$$\cos\theta = \frac{-d}{r} = \frac{-d}{\sqrt{R^2 + 2d\theta - \Delta^2}} \quad (\text{Eq. B.27})$$

Squaring both sides and equating to zero gives:

$$d^2 - 2d\Delta \cos^2\theta - (R^2 - \Delta^2)\cos^2\theta = 0 \quad (\text{Eq. B.28})$$

Solving the quadratic equation for d gives:

$$d = \frac{2\Delta \cos^2\theta \pm \sqrt{4\Delta^2 \cos^4\theta + 4(R^2 - \Delta^2)\cos^2\theta}}{2} \quad (\text{Eq. B.29})$$

Since d must be positive this simplifies to:

$$d = \Delta \cos^2\theta - \cos\theta \sqrt{\Delta^2 \cos^2\theta + (R^2 - \Delta^2)} \quad (\text{Eq. B.30})$$

From equation B.27, 1/r can be expressed as follows:

$$\frac{1}{r} = \frac{1}{-\Delta \cos\theta + \sqrt{\Delta^2 \cos^2\theta + R^2 - \Delta^2}} \quad (\text{Eq. B.31})$$

Due to symmetry this expression can be integrated between 0° and π/2 and expressed as follows:

$$\frac{1}{r_h} = \int \frac{1}{r} d\theta = \frac{1}{\int_{\frac{\pi}{2}}^{\pi} d\theta} \int_{\frac{\pi}{2}}^{\pi} \frac{d\theta}{-\Delta \cos\theta + \sqrt{\Delta^2 \cos^2\theta + R^2 - \Delta^2}} \quad (\text{Eq. B.32})$$

Which equals:

$$\frac{1}{r_h} = \frac{2}{\pi} \int_{\frac{\pi}{2}}^{\pi} \frac{d\theta}{-\Delta \cos\theta + \sqrt{\Delta^2 \cos^2\theta + R^2 - \Delta^2}} \quad (\text{Eq. B.33})$$

Combining the integration between π/2 and π for x > Δ and x < Δ and dividing by 2 will give the inverse of the average harmonic radius of the circle at a point Δ from the centre. This combined integral from equations B.33 and B.25 follows:

$$\frac{1}{r_h} = \int \frac{1}{r} = \frac{1}{2} \left(\frac{2}{\Pi} \right) \int_0^{\frac{\Pi}{2}} \left(\frac{1}{\Delta \cos \theta + \sqrt{\Delta^2 \cos^2 \theta + R^2 - \Delta^2}} \right) + \frac{1}{\sqrt{\Delta^2 \cos^2 \theta + R^2 - \Delta^2} - \Delta \cos \theta} d\theta \quad (\text{Eq. B.34})$$

By multiplying the numerator and denominator of both the terms in the main integral by the term under the square root, a common denominator for the two terms is obtained, as follows:

$$\frac{1}{r_h} = \frac{2}{\Pi} \int_0^{\frac{\Pi}{2}} \frac{\sqrt{R^2 - \Delta^2 + \Delta^2 \cos^2 \theta}}{R^2 - \Delta^2} d\theta \quad (\text{Eq. B.35})$$

This can be further simplified to the following term:

$$\frac{1}{r_h} = \frac{2}{\Pi(R^2 - \Delta^2)} \int_0^{\frac{\Pi}{2}} \sqrt{R^2 - \Delta^2 \sin^2 \theta} d\theta \quad (\text{Eq. B.36})$$

For R equals 1, a solution for this integration is available in tables and can be expressed as shown below.

$$\frac{1}{r_h} = \frac{2}{\Pi(1 - \Delta^2)} \left(\frac{\Pi}{2} \right) \left[1 - \left(\frac{1}{2} \right)^2 \Delta^2 - \left(\frac{1 \cdot 3}{2 \cdot 4} \right) \frac{\Delta^4}{3} - \left(\frac{1 \cdot 3 \cdot 5}{2 \cdot 4 \cdot 6} \right) \frac{\Delta^6}{5} \dots \right] \quad (\text{Eq. B.37})$$

For values of R not equal to 1, multiply the solution in equation B.37 by R. The r_h value can be approximated by the first two terms in the series and the result will be accurate to within two per cent near the centre of the circle and accurate to 10% within 90% of the circle centre. The simplified equation follows:

$$\frac{1}{r_h} = \frac{1}{R^2 - \Delta^2} \left[R^2 - \left(\frac{1}{2} \right)^2 \Delta^2 \right] \quad (\text{Eq. B.38})$$

where Δ is set to the distance from the circle centre divided by the circle radius.

A further simplification yields equation 6.29 which approximates the r_h value within 80% of the

circle centre.

$$\frac{1}{r_h} = \frac{R^2}{R^2 - \Delta^2} \quad (\text{Eq. B.39})$$

The analytical solution for determining the harmonic radius for any point in a circle has been shown and coincides with numerical solutions obtained using the AutoCad Lisp program. Analytical solutions for more complex shapes may be possible but their determination would serve no practical purpose.

APPENDIX C

AUTOCAD PROGRAM FOR DETERMINING ERF VALUES

APPENDIX C

AUTOCAD PROGRAM FOR DETERMINING ERF VALUES

The following AutoCad 'Lsp' program has been written by Per Lunder while at the Noranda Technology Centre (Lunder, 1994). The program (HHRC.lsp), calculates ERF values at a specified point or on a grid pattern on an opening surface. The program will incorporate the influence of supporting pillars as well as raises and brows.

To use the program, the opening surface must be entered as a series of polylines within AutoCad. The colour of the polylines differentiates between abutments (white), pillars (blue) and raises and brows (red). To run the program the 'lsp' program must first be loaded in autocad. When running the program the user is prompted to indicate the plines to be considered in the ERF calculation for the surface, as well as where the values should be calculated.

The program listing is given below:

```
;*-----  
;* HHRC 1.0c3  
;* Copyright (c) 1994  
;* Conceived: Doug Milne (UBC)  
;* Author: P.J. Lunder (NTC)  
;*-----  
;* FILE: HHRC.LSP  
;* FUNCTIONS: HHRC everything else local  
;*-----  
;*  
;* This program calculate the radius factor of an area based upon  
;* the harmonic radius of the surface.  
;*  
;* Raises and/or pillars can be considered, raises must have colour  
;* red and pillars colour blue (optional)  
;*  
;* A closed polyline must be picked to designate the area in which  
;* the radius factors must be calculated  
;*  
;*
```

```

.*
.*
;
-----
;=====
=====

```

```

(defun gethrnum (ptt hr-ent-pl hr-rse-pl hr-pil-pl angdiv
/
  ct ang tpt d hrsm entptls pilptls rseptls entpt1 pilpt1 rsept1
  dsrse dspil dswal )

```

```

(setq ct 0 ang 0.0 hrsm 0.0)

```

```

(while (< ct angdiv)

```

```

  (setq tpt (polar ptt ang 0.00000001))

```

```

  (foreach n hrc-ent-pl
    (if (setq d (intlst ptt (polar ptt ang 1000.0) n))
      (setq entptls (cond (entptls (cons d entptls)) (t d))
      )
    )
  )
)

```

```

(if entptls
  (setq entpt1 (clopt ptt tpt entptls T)
    q1 ptt q2 tpt lsts entptls
  )
)

```

```

(if hrc-rse-pl
  (progn
    (foreach n hrc-rse-pl
      (if (setq d (intlst ptt (polar ptt ang 1000.0) n))
        (setq rseptls (cond (rseptls (cons d rseptls)) (t d))
        )
      )
    )
    (if rseptls (setq rsept1 (clopt ptt tpt rseptls T)))
  )
)

```

```

(if hrc-pil-pl
  (progn
    (foreach n hrc-pil-pl
      (if (setq d (intlst ptt (polar ptt ang 1000.0) n))
        (setq pilptls (cond (pilptls (cons d pilptls)) (t d))
        )
      )
    )
  )
)

```

```

    )
  )
)
(if pilptls (setq pilpt1 (clopt ptt tpt pilptls T)))
)
)

```

```

(setq
  dsrse (if rsept1 (distance pt1 rsept1) 100000.0)
  dspil (if pilpt1 (distance pt1 pilpt1) 100000.0)
  dswal (if entpt1 (distance pt1 entpt1) 100000.0)
)

```

```

(cond
  (rsept1
    (cond
      ((and (<= dsrse dswal)(<= dsrse dspil))
        (grdraw ptt rsept1 1 1)
      )
      (t
        (if (<= dspil dswal)
          (progn
            (grdraw ptt pilpt1 5 1)
            (setq hrsm (+ hrsm (/ 1 dspil)))
          )
          (progn
            (grdraw ptt entpt1 3 1)
            (setq hrsm (+ hrsm (/ 1 dswal)))
          )
        )
      )
    )
  )
)
)
)
)
)

```

```

(pilpt1
  (if (<= dspil dswal)
    (progn
      (grdraw ptt pilpt1 5 1)
      (setq hrsm (+ hrsm (/ 1 dspil)))
    )
    (progn
      (grdraw ptt entpt1 3 1)
      (setq hrsm (+ hrsm (/ 1 dswal)))
    )
  )
)

```

```

)
)

(entpt1
  (grdraw ptt entpt1 3 1)
  (setq hrsm (+ hrsm (/ 1 dswal)))
)

)

(setq
  entpts nil
  rsepts nil
  pilpts nil
  rsept1 nil
  entpt1 nil
  pilpt1 nil
  ct (1+ ct)
  ang (+ ang angdel)
)

)
hrs

);while
;-----
;=====
=====
(defun getents (/ done tmp tlst)

  (while (not done)

    (setq tmp (car (entsel
      "\nSelect Items to Hydraulically Radiate <Enter when done> : "
    )))

    (cond
      ((null tmp) (setq done T))

      ((if
        (or (= (itas 0 (entget tmp)) "POLYLINE") (= (itas 0 (entget tmp)) "LINE"))

        (cond
          ((= (itas 62 (entget tmp)) 1)

```

```

(if (member tmp #hrc-rse)
  (progn
    (if (= (length #hrc-rse) 1)
      (setq #hrc-rse nil)
      (progn
        (foreach n #hrc-rse
          (if (not (equal tmp n))
            (setq tlst (cons n tlst))
          )
        )
        (setq #hrc-rse tlst tlst nil)
      )
    )
    (redraw tmp 1)
  )
  (progn
    (setq #hrc-rse (cons tmp #hrc-rse))
    (redraw tmp 3)
  )
)
)
)

```

```
((= (itas 62 (entget tmp)) 5)
```

```

(if (member tmp #hrc-pil)
  (progn
    (if (= (length #hrc-pil) 1)
      (setq #hrc-pil nil)
      (progn
        (foreach n #hrc-pil
          (if (not (equal tmp n))
            (setq tlst (cons n tlst))
          )
        )
        (setq #hrc-pil tlst tlst nil)
      )
    )
    (redraw tmp 1)
  )
  (progn
    (setq #hrc-pil (cons tmp #hrc-pil))
    (redraw tmp 3)
  )
)
)
)

```

```
(t
```

```

(if (member tmp #hrc-ent)
  (progn
    (if (= (length #hrc-ent) 1)
      (setq #hrc-ent nil)
      (progn
        (foreach n #hrc-ent
          (if
            (not (equal tmp n))
            (setq tlst (cons n tlst))
          )
        )
        (setq #hrc-ent tlst tlst nil)
      )
    )
    (redraw tmp 1)
  )
  (progn
    (setq #hrc-ent (cons tmp #hrc-ent))
    (redraw tmp 3)
  )
)
)
)
)
)

```

```

(princ "PICK A POLYLINE OR A LINE OK. ")

```

```

))))

```

```

;-----
;=====
;=====

```

```

(defun c:hrc( / #hrc-ent #hrc-rse #hrc-pil
  hrc-ent-pl hrc-rse-pl hrc-pil-pl
  k1 k2 xdiv ydiv angdiv xdel ydel angdel xt yt pt1 ahrsum hrsum
)

```

```

(getents)

```

```

(if #hrc-ent

```

```

  (progn
    (foreach n #hrc-ent (setq hrc-ent-pl (cons (gplst n) hrc-ent-pl)))

```

```

    (if #hrc-rse
      (foreach n #hrc-rse (setq hrc-rse-pl (cons (gplst n) hrc-rse-pl)))
    )

```

```

(if #hrc-pil
  (foreach n #hrc-pil (setq hrc-pil-pl (cons (gplst n) hrc-pil-pl)))
)

(setq
  k1 (gpnt 1 "" nil "\nPick 1st corner :")
  k2 (gcrn 0 "" k1 " and now 2nd corner :")
)

(if (null k2)

  (progn
    (setq
      angdiv (gint 1 "" "\nNumber of Ang Divisions: ")
      txht (grel 1 "" "\nText Height: ")
      angdel (/ (* 2 PI) angdiv)
      pt1 k1
    )

    (redraw)
    (setq hrsum (gethrnum pt1
      hr-ent-pl
      hr-rse-pl
      hr-pil-pl
      angdiv

    ))
    (setq
      ahrsum
      (cond
        ((> hrsum 0)(* (/ 1 hrsum) angdiv 0.5))
        (t -1.0)
      )
    )
    (txt-mk pt1 txht (rtos ahrsum 2 1) '((62 . 2)(72 . 1)(73 . 2)) nil)

  )

  (progn
    (setq
      xdiv (gint 1 "" "\nNumber of X Divisions: ")
      ydiv (gint 1 "" "\nNumber of Y Divisions: ")
    )
  )
)

```

```

angdiv (gint 1 "" "\nNumber of Ang Divisions: ")
txht (grel 1 "" "\nText Height: ")
xdel (/ (- (car k2) (car k1)) xdiv)
ydel (/ (- (cadr k2)(cadr k1)) ydiv)
pt1 k1
angdel (/ (* 2 PI) angdiv)
xt 0
yt 0
)

(while (<= xt xdiv)

  (while (<= yt ydiv)

    (redraw)

    (setq
      hrsum
      (gethrnum
        pt1
        hr-ent-pl
        hr-rse-pl
        hr-pil-pl
        angdiv)
      )
    )

    (setq
      ahrsum
      (cond
        ((> hrsum 0)(* (/ 1 hrsum) angdiv 0.5))
        (t -1.0)
      )
    )
    (txt-mk pt1 txht (rtos ahrsum 2 1) '((62 . 2)(72 . 1)(73 . 2)) nil)

    (setq
      pt1 (list (car pt1) (+ (cadr pt1) ydel))
      yt (1+ yt)
      ahrsum nil
    )
  )
)

(setq
  pt1 (list (+ (car pt1) xdel) (cadr k1))
  xt (1+ xt)
  yt 0
)

```

```

)

);xt
)
)

)
(princ "\nNO AREA TO HYDRAULICALLY RADIUS SELECTED! ")
)
(princ)
)
;-----
;=====
;=====
;THESE ARE ALL PATCHED FROM ELSEWHERE
;-----
(defun clopt (pt0 ptz ptlst near / pt1 pt2 tpt tmlst chkang tmpang)

  (if (and pt0 ptz ptlst)

    (if (= (length ptlst) 1)

      (setq pt1
        (if (atom (caar ptlst))(car ptlst)(clopt pt0 ptz (car ptlst) near))
      )

      (progn
        :shorten the list to points

        (setq chkang (angle pt0 ptz))

        (if (equal chkang (* 2 pi) 0.03)
          (setq chkang (- chkang (* 2 pi)))
        )

        (while ptlst

          (setq
            tpt
            (if
              (atom (caar ptlst))(car ptlst)
              (clopt pt0 ptz (car ptlst) near)
            )
          )
        )
      )
    )
  )

```

```

    tmpfst (cons tpt tmpfst)
    ptlst (cdr ptlst)
  )
)

(setq ptlst tmpfst tmpfst nil)

(while ptlst
  (setq tmpang (angle pt0 (car ptlst)))
  (if (equal tmpang (* 2 pi) 0.03)(setq tmpang (- tmpang (* 2 pi))))

  (if (equal chkang tmpang 0.1)
    (setq tmpfst (cons (car ptlst) tmpfst))
  )

  (setq ptlst (cdr ptlst))
)

(setq
  pt1 (car tmpfst)
  ptlst (cdr tmpfst)
)

(while ptlst
  (setq pt2 (car ptlst))

  (if near
    (if
      (> (distance pt0 pt1) (distance pt0 pt2))
      (setq pt1 pt2)
    )
    (if
      (< (distance pt0 pt1) (distance pt0 pt2))
      (setq pt1 pt2)
    )
  )

  (setq ptlst (cdr ptlst))
)
pt1
)
)
nil
)
)

```

```

;=====
;=====
;
;-----
(defun inpoly (pt ename rad / intlen)

  (if
    (and pt ename rad
      (equal (itas 0 (entget ename)) "POLYLINE")
      (bittst (itas 70 (entget ename)) 1)
    )

    (progn
      (setq intlen (intlst pt (polar pt pi rad) (gplst ename)))

      (if
        (or (not intlen)(= (/ (length intlen) 2) (/ (length intlen) 2.0)))
        nil
        T
      ))
      nil
    ))
;=====
;=====
;
;-----
(defun intlst (pt1 pt2 tlst / intpt ct itlst lt)

  (if (and pt1 pt2 tlst)

    (progn

      (setq ct 0 lt (length tlst))

      (while (< ct (1- lt))
        (setq
          intpt (inters pt1 pt2 (nth ct tlst)(nth (1+ ct) tlst))
          ct (1+ ct)
        )
        (if intpt (setq itlst (cons intpt itlst)))
      )

      itlst
    )
    nil
  ))

```

```

;=====
;
;-----
(defun tan (t1) (/ (sin t1)(cos t1)))
;=====
;-----
(defun asin (t1 t2)(atan t1 (sqrt (- (* t2 t2)(* t1 t1)))))
;=====
;-----
(defun acos (t1 t2) (atan (sqrt (- (* t2 t2)(* t1 t1))) t1))
;=====
;-----
(defun dtr (t1) (* (/ t1 180.0) pi))
;=====
;-----
(defun rtd (t1) (/ (* t1 180.0) pi))
;=====
;-----
(defun midpt (p1 p2)
  (if (and p1 p2)
      (mapcar '(lambda (x) (/ x 2.0))(mapcar '+ p1 p2))
      nil
  ))
;-----
(defun gkwd (init kw prmp)
  (initget init kw)
  (getkeyword prmp)
)
;=====
;-----
(defun gpnt (init kw pt1 prmp)
  (initget init kw)
  (if pt1 (getpoint pt1 prmp)(getpoint prmp))
)
;=====
;-----
(defun gcrn (init kw pt1 prmp)
  (initget init kw)
  (getcorner pt1 prmp)
)

```

```

)
;=====
=====
;-----
(defun grel (init kw prmp)
  (initget init kw)
  (getreal prmp)
)
;=====
=====
;-----
(defun gint (init kw prmp)
  (initget init kw)
  (getint prmp)
)
;=====
=====
;-----
(defun gdis (init kw pt1 prmp)
  (initget init kw)
  (if pt1 (getdist pt1 prmp)(getdist prmp))
)
;=====
=====
;-----
(defun bittst (num bitchk)
  (if num (not (zerop (logand num bitchk))) nil)
)
;=====
=====
;
(defun gplst (ename / tlst pt1 vert plc pt2 en)

  (if ename

    (cond

      ((= (itas 0 (entget ename)) "POLYLINE")
        (setq
          en ename
          vert (entget ename)
          plc (bittst (itas 70 vert) 1)
          ename (entnext ename)
          vert (entget ename)
          pt1 (trans (itas 10 vert) en 1)
          pt2 pt1
        )
      )
    )
  )

```

```

    (while (/= (itas 0 vert) "SEQEND")
      (setq
        pt1 (trans (itas 10 vert) en 1)
        tlst (cons pt1 tlst)
        ename (entnext ename)
        vert (entget ename)
      )
    )
    (if plc (setq tlst (cons pt2 tlst)))
    (reverse tlst)
  )

  ((= (itas 0 (entget ename)) "LINE")
    (setq vert (entget ename))
    (list (trans (itas 10 vert) ename 1)(trans (itas 11 vert) ename 1))
  )

  (t nil)

)
nil
))
;=====
;=====
;
;-----
(defun egss (ss indx) (entget (ssname ss indx)))
;=====
;=====
;-----
(defun itas (eass lst) (cdr (assoc eass lst)))
;
;-----
(defun txt-mk (pt1 ht txt codlst xdat / zax)

  (if (and pt1 ht txt)
    (progn

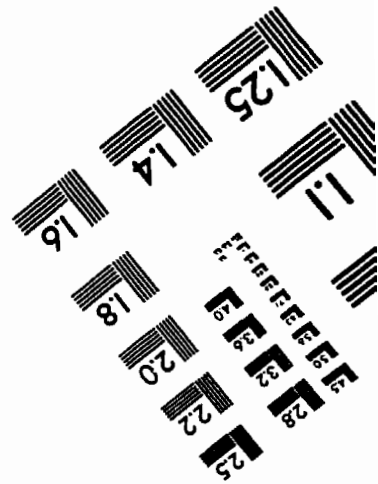
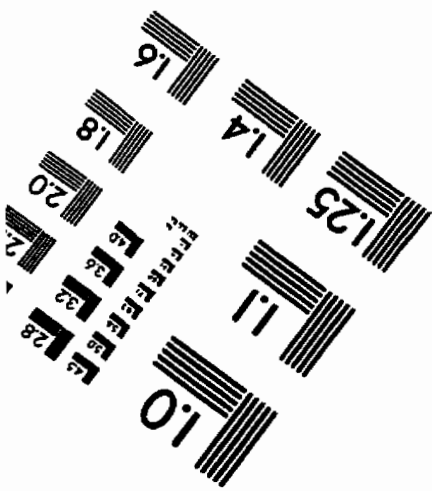
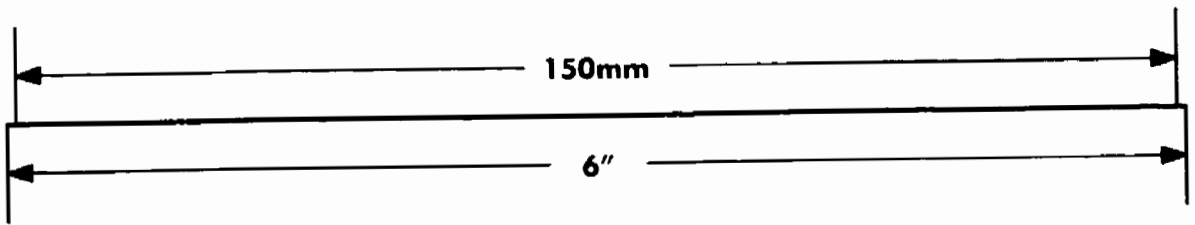
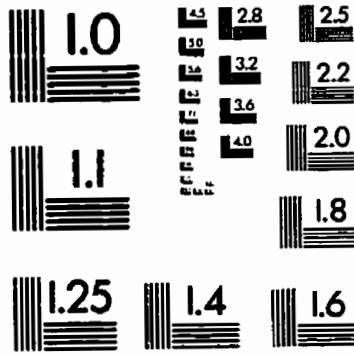
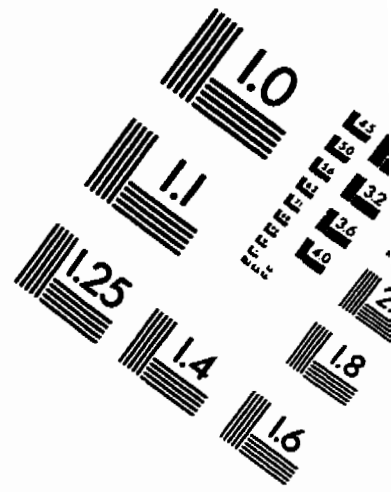
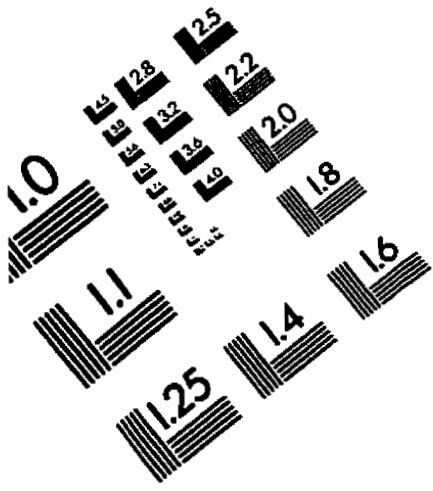
      (setq zax (mapcar '- (trans '(0 0 1) 1 0)(getvar "UCSORG"))))

    (entmake
      (append
        (list
          (cons 0 "TEXT")
          (cons 1 txt)
          (cons 40 ht)
          (cons 10 (trans pt1 1 zax))
        )
      )
    )
  )
)

```

```
(cons 11 (trans pt1 1 zax))
;(cons 72 1)
;(cons 73 2)
(cons 210 zax)
)
codlst xdat
))))
;=====
=====
;
```

IMAGE EVALUATION TEST TARGET (QA-3)



APPLIED IMAGE, Inc
 1653 East Main Street
 Rochester, NY 14609 USA
 Phone: 716/482-0300
 Fax: 716/288-5989

© 1993, Applied Image, Inc., All Rights Reserved